



UNIVERSITÀ  
DEGLI STUDI  
DI PADOVA

Sede Amministrativa: Università degli Studi di Padova

Dipartimento di Ingegneria Industriale

CORSO DI DOTTORATO DI RICERCA IN INGEGNERIA INDUSTRIALE  
CURRICOLO: INGEGNERIA DELL'ENERGIA  
CICLO XXIX

**DEVELOPMENT OF AN OPEN SOURCE ENVIRONMENT FOR THE AERO-STRUCTURAL  
OPTIMIZATION OF WIND TURBINES**

**Coordinatore:** Ch.mo Prof. Paolo Colombo

**Supervisore:** Ch.mo Prof. Ernesto Benini

**Dottorando:** Andrea Dal Monte



Alla mia famiglia che mi ha sempre sostenuto,  
agli amici leali su cui posso contare,  
a Vivy che ha sempre creduto in me.



# Abstract

An advanced open source optimization environment, for the design of Horizontal and Vertical Axis Wind Turbines, is hereby presented: several geometric parameters can be used as design variables while the proposed objective functions allow to run a multi-disciplinary study considering structural and aerodynamic analysis and the impact of the design on the total cost.

In order to improve the performances of the considered wind turbine model, the airfoils can be parametrized in several ways and both in-house functions and open source tools are integrated in the optimization environment, based on DAKOTA. A BEM code evaluates the aerodynamic performances of the HAWT blades and it can be coupled with both FEM analysis and functions for the analysis of the cost of energy. The open source CFD code OpenFOAM has also been included, as a module, in the overall environment: a CFD analysis can be run in a completely automatic way, from the definition of the geometry, through the generation of the mesh and the solving phase to the post-processing analysis.

The proposed optimization environment succeeded in improving the performances of both the considered Horizontal and Vertical Axis Wind Turbines in terms of structural, aerodynamic and cost objective functions.



# Contents

<b>Abstract</b>	I
<b>List of Figures</b>	IX
<b>List of Tables</b>	XXI
<b>General Introduction</b>	1
<b>I The Open Source Software for Engineering Analysis</b>	<b>1</b>
<b>Introduction and Background</b>	<b>3</b>
<b>1 CFD - Governing Equations</b>	<b>7</b>
1.1 The Mass Conservation Equation . . . . .	7
1.2 Lagrangian and Eulerian Approaches . . . . .	8
1.3 The Momentum Equations . . . . .	11
1.4 The Energy Equation . . . . .	12
1.5 Additional equations . . . . .	15
1.5.1 The Equation of State . . . . .	16
1.5.2 The Newtonian Fluid Hypothesis . . . . .	16
1.6 The Conservative Form of the Governing Equations of the Flow . . . . .	18
1.7 Forms of the General Transport Equation . . . . .	18
1.8 Discretization of Partial Differential Equations . . . . .	20
1.9 Explicit and Implicit Methods . . . . .	21
1.10 CFD for Rotating Machines . . . . .	22
1.10.1 Multi Reference Frame Model . . . . .	22
1.10.2 Relative Velocity Formulation . . . . .	23

1.10.3	Absolute Velocity Formulation . . . . .	24
1.10.4	MRF Domains and Limitations . . . . .	24
<b>2</b>	<b>The Open Source Codes</b>	<b>27</b>
2.1	Free Software Foundation . . . . .	28
2.2	GNU General Public License . . . . .	28
2.2.1	GNU GPLv3 Terms and Conditions . . . . .	29
2.2.2	Use of Licensed Software . . . . .	29
2.3	GNU Lesser General Public License . . . . .	30
2.3.1	GNU LGPL Terms and Conditions . . . . .	30
2.4	The 3-Clause BSD License . . . . .	30
2.5	XFOIL . . . . .	31
2.6	RFOIL . . . . .	32
2.7	Dakota . . . . .	33
2.7.1	MOGA Algorithm . . . . .	34
2.8	OpenFOAM . . . . .	35
2.8.1	OpenFOAM Solvers . . . . .	37
2.9	SALOME . . . . .	38
2.10	ParaView . . . . .	39
<b>3</b>	<b>Validation of a compressible CFD model for an external aerodynamic analysis</b>	<b>41</b>
3.1	Reference Values and Moment Center . . . . .	42
3.2	Geometric Model . . . . .	43
3.3	Mesh Setting . . . . .	47
3.3.1	Surface Mesh Generation . . . . .	47
3.3.2	Volume Mesh Generation . . . . .	51
3.4	Boundary Conditions Setup . . . . .	55
3.4.1	ANSYS Fluent Boundary Conditions . . . . .	55
3.4.2	OpenFOAM Boundary Conditions . . . . .	56
3.5	Solution Strategies . . . . .	58
3.5.1	ANSYS Fluent Solution Strategy . . . . .	58
3.5.2	OpenFOAM Solution Strategy . . . . .	59
3.6	Discussion of Results . . . . .	61
3.6.1	Lift, Drag and Pitching Moment Polars Comparison . . . . .	61



3.6.2	Static Pressure Coefficient Comparison . . . . .	65
3.6.3	Total Pressure Losses Comparison . . . . .	70
3.6.4	Friction Lines . . . . .	75
3.7	PIV Analysis . . . . .	81
<b>Conclusions</b>		<b>91</b>
<b>Nomenclature Part I</b>		<b>93</b>
 <b>II Development of an Optimization Environment for the Horizontal Axis Wind Turbine Design</b>		 <b>95</b>
<b>Introduction and Background</b>		<b>97</b>
<b>4</b>	<b>BEM Theory for Horizontal Axis Wind Turbine</b>	<b>101</b>
4.1	1D Momentum Theory for an Ideal Wind Turbine . . . . .	101
4.2	Effects of Rotation . . . . .	107
4.3	The Classical Blade Element Momentum Method . . . . .	110
4.4	BEM Method Algorithm . . . . .	114
4.5	Corrections to the Classical Blade Element Momentum Method . . . . .	115
4.6	Annual Energy Production . . . . .	117
<b>5</b>	<b>Proposal for a Coupled Aerodynamic-Structural Wind Turbine Blade Optimization</b>	<b>119</b>
5.1	The Case Study . . . . .	119
5.2	Description of the BEM Code . . . . .	122
5.2.1	BEM Code Validation . . . . .	123
5.3	Description of the Structural Model . . . . .	123
5.4	Design Variables . . . . .	126
5.5	Formulation of the Optimization Problem . . . . .	127
5.6	The Multi-Objective Genetic Algorithm . . . . .	129
5.7	Description of the Optimization Process . . . . .	133
5.8	First Optimization: Settings and Results . . . . .	133
5.9	Second Optimization: Settings and Results . . . . .	134
5.10	Discussion of the Optimization Results . . . . .	136

<b>6</b>	<b>Parametric Aero-Structural Optimization of a Small Wind Turbine</b>	<b>141</b>
6.1	Description of Wind Turbine . . . . .	141
6.2	Airfoil Parametrization . . . . .	143
6.3	Optimization Variables and Constraints . . . . .	145
6.4	Objective Functions . . . . .	145
6.4.1	Aerodynamic Fitness Function . . . . .	145
6.4.2	Structural Fitness Function . . . . .	148
6.4.3	Cost Fitness Function . . . . .	150
6.5	Optimization Strategy . . . . .	151
6.6	Twist Angles Distribution Optimization . . . . .	152
6.6.1	Results of the Twist Angle Analysis . . . . .	153
6.7	Penalties and Corrections Adopted . . . . .	155
6.7.1	Penalty for Thin Profiles . . . . .	155
6.7.2	Correction for the Start-Up Inertia of the Wind Turbine . . . . .	156
6.8	AEP70 - Shape Optimization of the Blade Airfoils . . . . .	157
6.8.1	AEP70-Opt1: Optimization of the Root Airfoil of the Blade . . . . .	158
6.8.2	AEP70-Opt2: Optimization of the Primary Airfoil of the Blade . . . . .	160
6.8.3	AEP70-Opt3: Optimization of the Tip Airfoil of the Blade . . . . .	162
6.9	Results of the AEP70 Optimization . . . . .	164
6.10	AEP75 - Shape Optimization with LCOE . . . . .	165
6.10.1	The Levelized Cost of Energy . . . . .	165
6.10.2	Optimization Strategy . . . . .	168
6.10.3	AEP75-Opt1: Optimization of the Tip Airfoil of the Blade . . . . .	169
6.10.4	AEP75-Opt2: Optimization of the Primary Airfoil of the Blade . . . . .	171
6.10.5	AEP75-Opt3: Optimization of the Root Airfoil of the Blade . . . . .	173
6.11	Results of the AEP75 Optimization . . . . .	175
<b>7</b>	<b>Validation of a Numerical Model of a Horizontal Axis Wind Turbine with Experi-</b>	
	<b>mental Data Using Two CFD Codes</b>	<b>177</b>
7.1	Objectives . . . . .	178
7.2	Methods . . . . .	178
7.3	Results . . . . .	180
	<b>Conclusion</b>	<b>183</b>

**III Development of an Optimization Environment for the Vertical Axis Wind Turbine Design 191**

**Introduction and Background 193**

**8 Parametric Aero-Structural Optimization of a VAWT Airfoil 195**

    8.1 Case Study . . . . . 195

    8.2 Analysis of the Airfoil Parametrization . . . . . 196

        8.2.1 Parametrization ParA (5 Variables) . . . . . 196

        8.2.2 Parametrization ParB (8 Variables) . . . . . 197

        8.2.3 Parametrization ParC (9 Variables) . . . . . 197

        8.2.4 Parametrization ParD (8 variables) . . . . . 198

    8.3 Airfoil Optimization for the Design Point (OptA) . . . . . 199

    8.4 Description of the Genetic Pool and Adopted Constraints . . . . . 200

    8.5 Objective Functions . . . . . 201

    8.6 Penalties Applied . . . . . 204

    8.7 Setting of XFOIL for the Polars Evaluation . . . . . 205

    8.8 Optimization Strategy . . . . . 205

    8.9 Parallel Computing Implementation and Scalability Test . . . . . 206

    8.10 Results of Optimization A . . . . . 208

    8.11 Discussion of Optimization A Results . . . . . 217

    8.12 General Airfoil Optimization (OptB) . . . . . 218

    8.13 Results of Optimization B . . . . . 219

        8.13.1 OptB1 - Results of the Free+Forced Transition Analysis . . . . . 220

        8.13.2 OptB1 - Effects of the Angle of Pitch Variation . . . . . 228

        8.13.3 OptB1 - Pareto Front Analysis . . . . . 230

        8.13.4 OptB2 - Results of the Free Transition Analysis . . . . . 231

        8.13.5 OptB3 - Results of the Forced Transition Analysis . . . . . 235

    8.14 Discussion of Optimization B Results . . . . . 240

**9 An Automatic Numerical Analysis of a VAWT 243**

    9.1 Case Study . . . . . 243

9.2	Geometry Generation and Meshing Procedure . . . . .	244
9.3	Setting of the CFD Numerical Model . . . . .	246
9.4	The CFD Module . . . . .	248
9.5	Discussion of the Numerical Analysis Results . . . . .	250
9.5.1	Results for Tip Speed Ratio 4.5 . . . . .	250
9.5.2	Results for Tip Speed Ratio 2.0 . . . . .	254
	<b>Conclusion</b>	<b>257</b>
	<b>Nomenclature Part III</b>	<b>259</b>
	<b>Conclusion and Future Work</b>	<b>261</b>
	<b>Bibliography</b>	<b>263</b>
	<b>Appendices</b>	<b>273</b>
<b>A</b>	<b>PIV Results for the Optimized Tiltortor Configuration</b>	<b>273</b>
<b>B</b>	<b>HAWT: Global Shape Optimization</b>	<b>277</b>
B.0.1	Global Optimization Results . . . . .	278
B.1	Corrections to the Optimization Process . . . . .	279
B.1.1	Robustness of the BEM Code . . . . .	279
B.1.2	Additional Constraints . . . . .	280
<b>C</b>	<b>Incorrect Settings of the XFOIL Analysis</b>	<b>281</b>
<b>D</b>	<b>VAWT Optimization Tool - User Manual</b>	<b>289</b>
D.1	Structure of the code . . . . .	289
D.2	Optimization files . . . . .	290
D.3	Analysis files . . . . .	291
D.4	Computer Setup . . . . .	292
D.5	How to Run an Optimization . . . . .	292

# List of Figures

1.1	Mass flow in the fluid element . . . . .	8
1.2	Models of flow: finite volume and infinitesimal fluid element approaches . . . . .	10
1.3	Stress components in the x-direction of a fluid particle . . . . .	11
1.4	Components of the heat flux vector . . . . .	13
1.5	Example of a discrete grid of points . . . . .	20
1.6	Stationary and Rotating Reference Frames . . . . .	23
1.7	MRF, stationary and rotating zones . . . . .	24
2.1	License compatibilities . . . . .	27
2.2	GPLv3 logo. . . . .	28
2.3	LGPLv3 logo. . . . .	30
2.4	The logo of XFOIL. . . . .	31
2.5	The logo of ECN. . . . .	32
2.6	The logo of Dakota. . . . .	33
2.7	The logo of OpenFOAM. . . . .	35
2.8	OpenFOAM folder structure . . . . .	36
2.9	Overview of the OpenFOAM structure . . . . .	37
2.10	The logo of SALOME. . . . .	38
2.11	The logo of ParaView. . . . .	39
3.1	Subdivision of the tiltrotor surface in patches: nose (blue), fuselage (violet), wing-fuselage junction (red), wing and nacelle (orange and yellow), sponsons (cyan), tail (green), empennages (brown) . . . . .	43
3.2	The bounding box represents the fluid domain of the wind tunnel. Surface subdivision: inlet (green), outlet (cyan), symmetry plane (violet), symmetry (yellow and missing surfaces) . . . . .	44

3.3	CAD model of the support system of the tiltrotor. Fixed pylon (cyan), rotating pylon(red), wiring (green) and tunnel floor (yellow) . . . . .	44
3.4	Comparison between the junction geometry provided by RUAG (on the left) and the simplified geometry for the meshing operations (on the right) . . . . .	45
3.5	Characteristic points on the fuselage and support: main balance center (A) and wing rotation axis centre (C) . . . . .	45
3.6	The whole geometry is composed by fuselage and ventral pylon. The configuration is shown at null pitch angle (on the left) and with non-null incidence angle (on the right)	46
3.7	Imported and cleaned geometry of ERICA tiltrotor model. Active edges (green), and suppressed edges (blue, dashed) . . . . .	47
3.8	View of the surface mesh over the supporting pylon (on the left) and over the aircraft nacelle (on the right) . . . . .	49
3.9	Detail of the empennage trailing edge worst surface elements (on the left) and closeup of the mesh refinement around the empennage-fuselage junction (on the right) . . . . .	50
3.10	Prismatic mesh over the empennage-fuselage junction without BL correction (on the left) and after application of BL automatic reduction (on the right) . . . . .	51
3.11	Close-up of the volume mesh near the horizontal tailplane: comparison of mesh obtained without (on the left) and with (on the right) the refinement shell . . . . .	52
3.12	Close-up of the volume mesh near the mid wing: comparison of mesh obtained without (on the left) and with (on the right) the refinement shell . . . . .	52
3.13	Longitudinal section of the volume mesh: comparison of mesh obtained without (on top) and with (on bottom) the refinement shell . . . . .	53
3.14	Overall longitudinal section of the volume mesh: comparison of mesh obtained without (on top) and with (on bottom) the refinement shell . . . . .	54
3.15	Lift and drag coefficients comparison of OpenFOAM simulations against ANSYS Fluent results and wind tunnel data . . . . .	64
3.16	Pitching moment polar and aircraft aerodynamic efficiency: comparison of OpenFOAM simulations against ANSYS Fluent results and wind tunnel data . . . . .	64
3.17	Contour plots of the static pressure coefficient $C_P$ over the full scale tiltrotor model at various incidences (front view): comparison of the Fluent (on the left), OpenFOAM (on the right) results . . . . .	66

3.18	Contour plots of the static pressure coefficient $C_P$ over the full scale tiltrotor model at various incidences (front view): comparison of the Fluent (on the left), OpenFOAM (on the right) results . . . . .	67
3.19	Contour plots of the static pressure coefficient $C_P$ over the full scale tiltrotor model at various incidences (front view): comparison of the Fluent (on the left), OpenFOAM (on the right) results . . . . .	68
3.20	Contour plots of the static pressure coefficient $C_P$ over the full scale tiltrotor model at various incidences (front view): comparison of the Fluent (on the left), OpenFOAM (on the right) results . . . . .	69
3.21	Total pressure losses visualization of the full scale tiltrotor with null deflection of the control surfaces at various incidences: comparison of OpenFOAM (on the right) and Fluent (on the left) results . . . . .	71
3.22	Total pressure losses visualization of the full scale tiltrotor with null deflection of the control surfaces at various incidences: comparison of OpenFOAM (on the right) and Fluent (on the left) results . . . . .	72
3.23	Total pressure losses visualization of the full scale tiltrotor with null deflection of the control surfaces at various incidences: comparison of OpenFOAM (on the right) and Fluent (on the left) results . . . . .	73
3.24	Total pressure losses visualization of the full scale tiltrotor with null deflection of the control surfaces at various incidences: comparison of OpenFOAM (on the right) and Fluent (on the left) results . . . . .	74
3.25	Friction lines over the tiltrotor model at various angle of incidence (front view): comparison of OpenFOAM (on the right) and Fluent (on the left) results . . . . .	76
3.26	Friction lines over the tiltrotor model at various angle of incidence (front view): comparison of OpenFOAM (on the right) and Fluent (on the left) results . . . . .	77
3.27	Friction lines over the tiltrotor model at various angle of incidence (rear view): comparison of OpenFOAM (on the right) and Fluent (on the left) results . . . . .	78
3.28	Friction lines over the tiltrotor model at various angle of incidence (rear view): comparison of OpenFOAM (on the right) and Fluent (on the left) results . . . . .	79
3.29	Detail of the friction lines in the wing-fuselage connection zone at $\alpha = 12.38^\circ$ . . . . .	80
3.30	Detailed comparison of the friction lines (from Fluent analysis) in the rear part of the fuselage at $\alpha = -1.89^\circ$ and $\alpha = 12.38^\circ$ . . . . .	80
3.31	Graphical illustration of the considered planes for the PIV analysis . . . . .	81

3.32	Velocity contours in the wake of the baseline model, case $\alpha = -2^\circ$ : the comparison among PIV data, ANSYS Fluent and OpenFOAM analysis is illustrated for the considered planes. . . . .	84
3.33	Velocity contours in the wake of the baseline model, case $\alpha = 0^\circ$ : the comparison among PIV data, ANSYS Fluent and OpenFOAM analysis is illustrated for the considered planes	85
3.34	Velocity contours in the wake of the baseline model, case $\alpha = +2^\circ$ : the comparison among PIV data, ANSYS Fluent and OpenFOAM analysis is illustrated for the considered planes . . . . .	86
3.35	Velocity contours in the wake of the baseline model, case $\alpha = -2^\circ$ : the comparison among ANSYS Fluent and OpenFOAM analysis is illustrated for the considered planes	87
3.36	Velocity contours in the wake of the baseline model, case $\alpha = -2^\circ$ : the comparison among ANSYS Fluent and OpenFOAM analysis is illustrated for further planes (2050mm, 2150mm, 2250mm 2350mm) . . . . .	88
3.37	Contours of the x-component of the vorticity in the baseline model, case $\alpha = -2^\circ$ : the comparison among PIV data, ANSYS Fluent and OpenFOAM analysis is illustrated for the considered planes . . . . .	89
4.1	Streamlines distribution in the considered 1D model; velocity and pressure distributions upstream and downstream . . . . .	102
4.2	Circular control volume around the wind turbine . . . . .	103
4.3	Alternative volume around the wind turbine . . . . .	104
4.4	Power and trust coefficients $C_P$ and $C_T$ as function of the axial induction factor $a$ . . .	106
4.5	Expansion of the wake and velocity jump for the 1D ideal wind turbine model . . . . .	106
4.6	The turbulent-wake state induced by the unstable shear flow at the edge of the wake .	107
4.7	Schema of a 3 blade rotor . . . . .	107
4.8	Triangles of velocities in a section of the blade . . . . .	108
4.9	Triangle of velocities with induced velocities for a section of the blade . . . . .	109
4.10	Control volume adopted for the 3D model analysis . . . . .	110
4.11	Velocities at the rotor plane . . . . .	111
4.12	Loads on the blade . . . . .	112
4.13	Linear variation of the loads with the radius . . . . .	115
4.14	Expressions for $C_T$ versus the axial induction factor $a$ . . . . .	116
4.15	Probability of wind speed and power curve . . . . .	118



5.1	Scheme of the subdivision of the blade layout in the chordwise direction . . . . .	120
5.2	Exploded drawing of the analyzed rotor blade geometry, showing the subdivision in 9 areas spanwise and 8 zones chordwise . . . . .	121
5.3	Experimental and numerical power production as a function of the wind speed for the AOC 15/50 wind turbine . . . . .	124
5.4	Shell 181 configuration . . . . .	124
5.5	A detail of the adopted in mesh in the root area . . . . .	125
5.6	Representation of the Bezier points and of the corresponding curve for the chord spanwise distribution of the AOC 15/50 blade . . . . .	126
5.7	Representation of the Bezier points and of the corresponding curve for the twist spanwise distribution of the AOC 15/50 blade . . . . .	127
5.8	Location of the reinforcements (all zones with the exception of 9 and 10, the Spar Web and the Spar Flange) inside the original AOC 15/50 blade (from Table 5.3) . . . . .	130
5.9	Genetic pool of the original AOC 15/50 blade . . . . .	130
5.10	Functional diagram of the S.O.C.R.A.TE. optimization process; the algorithm is based upon the coupling of the commercial code Ansys, an in-house made BEM code and the commercial code Matlab . . . . .	132
5.11	Evolution of the Pareto front for the first optimization process . . . . .	134
5.12	Genetic pool of the 135 <sup>th</sup> individual of the 27 <sup>th</sup> generation (first optimization) . . . . .	134
5.13	Evolution of the Pareto front for the second optimization process . . . . .	135
5.14	Genetic pool of the 146 <sup>th</sup> individual of the 24 <sup>th</sup> generation (second optimization) . . . . .	136
5.15	Comparison between the chord distributions for both the original AOC 15/50 blade and the (second) optimized one . . . . .	137
5.16	Comparison between the twist distributions for both the original AOC 15/50 blade and the (second) optimized one . . . . .	138
5.17	Comparison between the angle of attack distributions for both the original AOC 15/50 blade and the (second) optimized one . . . . .	138
5.18	Comparison between the aerodynamic force distributions evaluated in 12 blade sections for both the original AOC 15/50 blade and the (second) optimized one . . . . .	138
5.19	Comparison of the flexural rigidity distribution for the original AOC 15/50 blade, the (second) optimized one and the (second) optimized geometry coupled with the original Sandia layout . . . . .	139

5.20	Comparison between the surface density distribution for the original AOC 15/50 blade and the optimized solutions . . . . .	140
6.1	Scheme of the optimization algorithm for a Horizontal Axis Wind Turbine . . . . .	142
6.2	S814: Bezier parametrization and extended polar . . . . .	144
6.3	S812: Bezier parametrization and extended polar . . . . .	144
6.4	S813: Bezier parametrization and extended polar . . . . .	144
6.5	AOC 15/50 power curve: experimental data versus BEM results using XFOIL and RFOIL polars . . . . .	146
6.6	Experimental data versus <i>Flat plate theory</i> and <i>Viterna method</i> . . . . .	147
6.7	Weibull curve n.1 of the considered wind speed distribution ( $V_{ave} = 7.0$ m/s) . . . . .	147
6.8	Weibull curve n.2 of the considered wind speed distribution ( $V_{ave} = 7.5$ m/s) . . . . .	147
6.9	Exploded drawing of the analysed rotor blade geometry, showing the subdivision in 9 areas spanwise and 8 zones chordwise . . . . .	150
6.10	Twist angle distribution for a Weibull mean wind speed mean of 5.0 m/s (left) and 5.5 m/s (right) . . . . .	153
6.11	Twist angle distribution for a Weibull mean wind speed mean of 6.0 m/s (left) and 6.5 m/s (right) . . . . .	153
6.12	Twist angle distribution for a Weibull mean wind speed mean of 7.0 m/s (left) and 7.5 m/s (right) . . . . .	154
6.13	Structural zones of the blade profiles . . . . .	155
6.14	Effect of the proposed penalty functions on the power curve calculated by the BEM code	157
6.15	<i>AEP70 – Opt1</i> : Pareto front convergence for the root airfoil optimization . . . . .	158
6.16	<i>AEP70 – Opt1</i> : Solution A power curve and airfoil parametrization . . . . .	159
6.17	<i>AEP70 – Opt1</i> : Solution B power curve and airfoil parametrization . . . . .	159
6.18	<i>AEP70 – Opt1</i> : Solution C power curve and airfoil parametrization . . . . .	159
6.19	<i>AEP70 – Opt2</i> : Pareto front convergence for the primary airfoil optimization . . . . .	160
6.20	<i>AEP70 – Opt2</i> : Solution A power curve and airfoil parametrization . . . . .	161
6.21	<i>AEP70 – Opt2</i> : Solution B power curve and airfoil parametrization . . . . .	161
6.22	<i>AEP70 – Opt2</i> : Solution C power curve and airfoil parametrization . . . . .	161
6.23	<i>AEP70 – Opt3</i> : Pareto front convergence for the tip airfoil shape optimization . . . . .	162
6.24	<i>AEP70 – Opt3</i> : Solution A power curve and airfoil parametrization . . . . .	163
6.25	<i>AEP70 – Opt3</i> : Solution B power curve and airfoil parametrization . . . . .	163
6.26	<i>AEP70 – Opt3</i> : Solution C power curve and airfoil parametrization . . . . .	163

6.27	Levels 1 and 2 of the SCBS. . . . .	165
6.28	Capital Expenditures for the land-based wind reference project, NREL 2014. . . . .	166
6.29	<i>AEP75 – Opt1</i> : Pareto front convergence of the tip airfoil shape optimization . . . . .	169
6.30	<i>AEP75 – Opt1</i> : Solution A power curve and airfoil parametrization . . . . .	170
6.31	<i>AEP75 – Opt1</i> : Solution B power curve and airfoil parametrization . . . . .	170
6.32	<i>AEP75 – Opt1</i> : Solution C power curve and airfoil parametrization . . . . .	170
6.33	<i>AEP75 – Opt2</i> : Pareto front convergence of the primary airfoil shape optimization . . . . .	171
6.34	<i>AEP75 – Opt2</i> : Solution A power curve and airfoil parametrization . . . . .	172
6.35	<i>AEP75 – Opt2</i> : Solution B power curve and airfoil parametrization . . . . .	172
6.36	<i>AEP75 – Opt2</i> : Solution C power curve and airfoil parametrization . . . . .	172
6.37	<i>AEP75 – Opt3</i> : Pareto front convergence of the primary airfoil shape optimization . . . . .	173
6.38	<i>AEP75 – Opt3</i> : Solution A power curve and airfoil parametrization . . . . .	174
6.39	<i>AEP75 – Opt3</i> : Solution B power curve and airfoil parametrization . . . . .	174
6.40	<i>AEP75 – Opt3</i> : Solution C power curve and airfoil parametrization . . . . .	174
7.1	AOC 15/50 3D model and adopted fluid domain with boundary conditions. . . . .	179
7.2	Power curve of AOC 15/50. Comparison between experimental and numerical data (OpenFOAM and Ansys FLUENT). . . . .	180
7.3	Contribution of the different sections of the blade to the total torque for different velocities (before stall). . . . .	180
7.4	Comparison of the pressure distribution on the blade surface and the velocity flow field between ANSYS Fluent (on the left) and OpenFOAM (on the right). . . . .	181
8.1	Results of the parametrization <i>ParA</i> on the NACA0015 (left) and S812 (right) airfoils . . . . .	196
8.2	Results of the parametrization <i>ParB</i> on the NACA0015 (left) and S812 (right) airfoils . . . . .	197
8.3	Results of the parametrization <i>ParC</i> on the NACA0015 (left) and S812 (right) airfoils . . . . .	198
8.4	Results of the parametrization <i>ParD</i> on the NACA0015 (left) and S812 (right) airfoils . . . . .	199
8.5	Flowchart of the <i>OptA</i> optimization process: the algorithm is based upon the coupling of the panel code XFOIL, the DMST model, functions for the parametrization and both the aerodynamic and structural analysis . . . . .	199
8.6	Range of the allowable movements of the <i>ParD</i> control points in <i>OptA</i> . . . . .	201
8.7	Upper and lower bounds for suction and pressure side curves on in <i>OptA</i> . . . . .	201
8.8	Aerodynamic polars of NACA0015, evaluated in XFOIL in both free and forced transition . . . . .	202
8.9	Extension of the aerodynamic polars using the Viterna method, for NACA0015 . . . . .	202

8.10	Angles of attack distribution during a revolution and related frequency for the NACA0015 airfoil . . . . .	203
8.11	Results of the scalability test of the optimization algorithm . . . . .	207
8.12	Resulting Pareto front for the <i>OptA</i> analysis . . . . .	208
8.13	<i>NACA0015</i> : Bezier parametrization of the airfoil . . . . .	209
8.14	The trend of $\alpha$ during a rotation, the related frequency distribution and the comparison between the polars in free and forced transition conditions are illustrated for <i>NACA0015</i> 209	
8.15	<i>A101</i> : Bezier parametrization of the airfoil . . . . .	210
8.16	The trend of $\alpha$ during a rotation, the related frequency distribution and the comparison between the polars in free and forced transition conditions are illustrated for <i>A101</i> airfoil210	
8.17	<i>A102B</i> : Bezier parametrization of the airfoil . . . . .	211
8.18	The trend of $\alpha$ during a rotation, the related frequency distribution and the comparison between the polars in free and forced transition conditions are illustrated for <i>A102B</i> airfoil211	
8.19	<i>A103B</i> : Bezier parametrization of the airfoil . . . . .	212
8.20	The trends of $\alpha$ during a rotation, the related frequency distribution and the comparison between the polars in free and forced transition conditions are illustrated for <i>A103B</i> airfoil212	
8.21	<i>A104</i> : Bezier parametrization of the airfoil . . . . .	213
8.22	The trends of $\alpha$ during a rotation, the related frequency distribution and the comparison between the polars in free and forced transition conditions are illustrated <i>A104</i> airfoil .	213
8.23	<i>A105B</i> : Bezier parametrization of the airfoil . . . . .	214
8.24	The trends of $\alpha$ during a rotation, the related frequency distribution and the comparison between the polars in free and forced transition conditions are illustrated for <i>A105B</i> airfoil214	
8.25	<i>A106</i> : Bezier parametrization of the airfoil . . . . .	215
8.26	The trends of $\alpha$ during a rotation, the related frequency distribution and the comparison between the polars in free and forced transition conditions are illustrated for <i>A106</i> airfoil215	
8.27	Power and thrust coefficients values of <i>NACA0015</i> airfoil for the considered range of tip speed ratio solidity . . . . .	216
8.28	Power and thrust coefficients values of <i>A102B</i> airfoil for the considered range of tip speed ratio solidity . . . . .	216
8.29	Power and thrust coefficients values of <i>A103B</i> airfoil for the considered range of tip speed ratio solidity . . . . .	216
8.30	<b>VAWT Optimization B</b> Flowchart . . . . .	218
8.31	Distribution of the angles of attack adopted in <i>Optimization B</i> . . . . .	219

8.32	Resulting Pareto front of the free+forced transition analysis in Optimization B . . . . .	220
8.33	<i>OptB1</i> : NACA0015 airfoil parametrization . . . . .	221
8.34	<i>OptB1</i> : NACA0015 airfoil, comparison of the polars for free and forced transitions . . . . .	221
8.35	<i>OptB1</i> : NACA0015 airfoil, power and thrust coefficients . . . . .	221
8.36	<i>OptB1</i> : B101 airfoil parametrization . . . . .	222
8.37	<i>OptB1</i> : B101 airfoil, comparison of the polars for free and forced transitions . . . . .	222
8.38	<i>OptB1</i> : B101 airfoil, power and thrust coefficients . . . . .	222
8.39	<i>OptB1</i> : B102 airfoil parametrization . . . . .	223
8.40	<i>OptB1</i> : B102 airfoil, comparison of the polars for free and forced transitions . . . . .	223
8.41	<i>OptB1</i> : B102 airfoil, power and thrust coefficients . . . . .	223
8.42	<i>OptB1</i> : B103 airfoil parametrization . . . . .	224
8.43	<i>OptB1</i> : B103 airfoil, comparison of the polars for free and forced transitions . . . . .	224
8.44	<i>OptB1</i> : B103 airfoil, power and thrust coefficients . . . . .	224
8.45	<i>OptB1</i> : B104 airfoil parametrization . . . . .	225
8.46	<i>OptB1</i> : B104 airfoil, comparison of the polars for free and forced transitions . . . . .	225
8.47	<i>OptB1</i> : B104 airfoil, power and thrust coefficients . . . . .	225
8.48	<i>OptB1</i> : B105 airfoil parametrization . . . . .	226
8.49	<i>OptB1</i> : B105 airfoil, comparison of the polars for free and forced transitions . . . . .	226
8.50	<i>OptB1</i> : B105 airfoil, power and thrust coefficients . . . . .	226
8.51	<i>OptB1</i> : B106 airfoil parametrization . . . . .	227
8.52	<i>OptB1</i> : B106 airfoil, comparison of the polars for free and forced transitions . . . . .	227
8.53	<i>OptB1</i> : B106 airfoil, power and thrust coefficients . . . . .	227
8.54	<i>OptB1</i> : B102 airfoil, power and thrust coefficients at $-5.0^\circ$ fixed pitch . . . . .	228
8.55	<i>OptB1</i> : B102 airfoil, power and thrust coefficients at $-2.0^\circ$ fixed pitch . . . . .	228
8.56	<i>OptB1</i> : B102 airfoil, power and thrust coefficients at $0^\circ$ fixed pitch . . . . .	229
8.57	<i>OptB1</i> : B102 airfoil, power and thrust coefficients at $+2.0^\circ$ fixed pitch . . . . .	229
8.58	<i>OptB1</i> : B102 airfoil, power and thrust coefficients at $+5.0^\circ$ fixed pitch . . . . .	229
8.59	<i>Optimization B</i> : solutions belonging to the Pareto front . . . . .	230
8.60	<i>Optimization B</i> : transposition of the considered solutions in the power coefficient - thickness space . . . . .	230
8.61	Pareto front for the airfoil optimization in free transition conditions . . . . .	231
8.62	<i>OptB2</i> : B201-FR airfoil parametrization . . . . .	232
8.63	<i>OptB2</i> : B201-FR airfoil, power and thrust coefficients . . . . .	232

8.64	<i>OptB2</i> : B202-FR airfoil parametrization . . . . .	232
8.65	<i>OptB2</i> : B202-FR airfoil, power and thrust coefficients . . . . .	233
8.66	<i>OptB2</i> : B203-FR airfoil parametrization . . . . .	233
8.67	<i>OptB2</i> : B203-FR airfoil, power and thrust coefficients . . . . .	233
8.68	<i>OptB2</i> : B204-FR airfoil parametrization . . . . .	234
8.69	<i>OptB2</i> : B204-FR airfoil, power and thrust coefficients . . . . .	234
8.70	<i>OptB2</i> : B205-FR airfoil parametrization . . . . .	234
8.71	<i>OptB2</i> : B205-FR airfoil, power and thrust coefficients . . . . .	235
8.72	Pareto front for the airfoil optimization in forced transition conditions . . . . .	235
8.73	<i>OptB3</i> : B301-FO airfoil parametrization . . . . .	236
8.74	<i>OptB3</i> : B301-FO airfoil, power and thrust coefficients . . . . .	236
8.75	<i>OptB3</i> : B302-FO airfoil parametrization . . . . .	237
8.76	<i>OptB3</i> : B302-FO airfoil, power and thrust coefficients . . . . .	237
8.77	<i>OptB3</i> : B303-FO airfoil parametrization . . . . .	237
8.78	<i>OptB3</i> : B303-FO airfoil, power and thrust coefficients . . . . .	238
8.79	<i>OptB3</i> : B304-FO airfoil parametrization . . . . .	238
8.80	<i>OptB3</i> : B304-FO airfoil, power and thrust coefficients . . . . .	238
8.81	<i>OptB3</i> : B305-FO airfoil parametrization . . . . .	239
8.82	<i>OptB3</i> : B305-FO airfoil, power and thrust coefficients . . . . .	239
8.83	<i>OptB3</i> : B306-FO airfoil parametrization . . . . .	239
8.84	<i>OptB3</i> : B306-FO airfoil, power and thrust coefficients . . . . .	240
9.1	Domain of the computational analysis . . . . .	244
9.2	Domain of the rotating mesh zone ( <i>Rotor</i> ) . . . . .	245
9.3	Detail of the structured mesh adopted around the airfoil . . . . .	246
9.4	Details of the structured mesh . . . . .	247
9.5	Comparison between normal forces calculated from CFD analysis, DMST model and experimental results for $\lambda = 4.5$ . . . . .	251
9.6	Comparison between tangential forces calculated from CFD analysis, DMST model and experimental results for $\lambda = 4.5$ . . . . .	251
9.7	Numerical velocity field, calculated with OpenFOAM, for $\lambda = 4.5$ . . . . .	252
9.8	Velocity field resulting from the PIV analysis for $\lambda = 4.5$ , [103] p. 60 . . . . .	253
9.9	Comparison between normal forces calculated from CFD analysis, DMST model and experimental results for $\lambda = 2.0$ . . . . .	254

9.10	Numerical velocity field, calculated with OpenFOAM, for $\lambda = 2.0$ . . . . .	255
9.11	Comparison between tangential forces calculated from CFD analysis, DMST model and experimental results for $\lambda = 2.0$ . . . . .	255
9.12	Velocity field resulting from the PIV analysis for $\lambda = 2.0$ , [103] p. 61 . . . . .	256
A.1	Velocity contours in the wake of the optimized model, case $\alpha = -2^\circ$ : the comparison among PIV data, ANSYS Fluent and OpenFOAM analysis is illustrated for the considered planes . . . . .	274
A.2	Velocity contours in the wake of the optimized model, case $\alpha = 0^\circ$ : the comparison among PIV data, ANSYS Fluent and OpenFOAM analysis is illustrated for the considered planes . . . . .	275
A.3	Velocity contours in the wake of the optimized model, case $\alpha = +2^\circ$ : the comparison among PIV data, ANSYS Fluent and OpenFOAM analysis is illustrated for the considered planes . . . . .	276
B.1	Wb1Opt0: Pareto front of the global optimization . . . . .	277
B.2	Wb1Opt0, Solution 1: power curve and airfoil 1 shape . . . . .	278
B.3	Wb1Opt0, Solution 2: power curve and airfoil 1 shape . . . . .	278
B.4	Wb1Opt0, Solution 3: power curve and airfoil 1 shape . . . . .	279
C.1	Pareto front resulting in the preliminary phase of optimization setting . . . . .	281
C.2	A251: Bezier parametrization of the airfoil . . . . .	283
C.3	A251 airfoil. The variation of $C_D$ and $C_L$ polars is presented for different setting of the XFOIL analysis . . . . .	283
C.4	A253: Bezier parametrization of the airfoil . . . . .	284
C.5	A253 airfoil. The variation of $C_D$ and $C_L$ polars is presented for different setting of the XFOIL analysis . . . . .	284
C.6	A254: Bezier parametrization of the airfoil . . . . .	285
C.7	A254 airfoil. The variation of $C_D$ and $C_L$ polars is presented for different setting of the XFOIL analysis . . . . .	285
C.8	A255: Bezier parametrization of the airfoil . . . . .	286
C.9	A255 airfoil. The variation of $C_D$ and $C_L$ polars is presented for different setting of the XFOIL analysis . . . . .	286
C.10	A256: Bezier parametrization of the airfoil . . . . .	287

C.11 A256 airfoil. The variation of $C_D$ and $C_L$ polars is presented for different setting of the XFOIL analysis . . . . .	287
D.1 Structure of the Optimization environment for Vertical Axis Wind Turbine . . . . .	289



# List of Tables

1.1	Conservative and Non-conservative forms of Navier-Stokes Equations . . . . .	10
1.2	OpenFOAM solvers and options for rotating machines . . . . .	22
3.1	Geometric reference values and pitching moment centre coordinates . . . . .	42
3.2	Quality parameters limits specified for ERICA surface mesh . . . . .	47
3.3	2D automeshing settings for the parches of ERICA tiltrotor model . . . . .	48
3.4	Quality statistic of the superficial mesh on the baseline tiltrotor configuration . . . . .	49
3.5	Mesh parameters for the inner volume . . . . .	53
3.6	Mesh parameters for the outer volume . . . . .	54
3.7	Flow conditions for the test case TN47 over 1/8 scaled tiltrotor [6] . . . . .	55
3.8	Adopted set of boundary conditions for ANSYS Fluent simulations of ERICA scaled model . . . . .	56
3.9	Setup of boundary conditions at wind tunnel inlet and outlet surfaces . . . . .	57
3.10	ANSYS Fluent solver setting and discretization used for CFD simulations . . . . .	58
3.11	ANSYS Fluent solution strategy adopted for the CFD simulations . . . . .	59
3.12	OpenFOAM numerical discretization schemes . . . . .	60
3.13	Results of the wind tunnel test over 1/8 scaled tiltrotor model . . . . .	61
3.14	Results of ANSYS Fluent CFD simulations . . . . .	62
3.15	Results of OpenFOAM CFD simulations . . . . .	63
3.16	Deviation (%) comparison between OpenFOAM and ANSYS Fluent against experimental data . . . . .	63
5.1	AOC 15/50 Wind Turbine characteristics . . . . .	119
5.2	Aerodynamic profiles characterizing the external geometry of the AOC 15/50 blade . . . . .	120
5.3	Layup schedule of the analyzed rotor blade . . . . .	121
5.4	Structural properties of the materials adopted in the AOC 15/50 blade . . . . .	125

5.5	Summary of the main optimization settings . . . . .	129
5.6	Scheme of the Crossover function . . . . .	131
5.7	Settings of the first optimization process . . . . .	134
5.8	Settings of the second optimization process . . . . .	135
5.9	Geometric features and load conditions of the original AOC 15/50 blade; no angle of attack is computed for the root section (being characterized by a junction between an airfoil and an oval section) and for the tip one (due to Prandtl's tip loss factor, see [41])	136
5.10	Geometric features and load conditions of the (second) optimized AOC 15/50 blade; no angle of attack is computed for the root section (being characterized by a junction between an airfoil and an oval section) and for the tip one (due to Prandtl's tip loss factor, see [41]) . . . . .	137
6.1	AOC 15/50 wind turbine characteristics . . . . .	141
6.2	AOC 15/50 chord and twist distributions . . . . .	142
6.3	Bezier control points describing both the pressure and suction sides of the baseline profiles	143
6.4	Adopted variables for the pressure and suction sides discretization of the aerodynamic profiles . . . . .	145
6.5	Constraints adopted for the proposed optimization . . . . .	145
6.6	Structural properties of the materials adopted in the AOC 15/50 blade . . . . .	148
6.7	Layup schedule of the analysed rotor blade . . . . .	149
6.8	Cases considered for the optimization of the twist angle distribution . . . . .	152
6.9	Upper and lower bounds of the Bezier points used in the twist optimization . . . . .	152
6.10	Genetic pool and fitness values of the considered points in Pareto front of <i>AEP70 – Opt1</i>	158
6.11	Genetic pool and fitness values of the considered points in Pareto front of <i>AEP70 – Opt2</i>	160
6.12	Genetic pool and fitness values of the considered points in Pareto front of <i>AEP70 – Opt3</i>	162
6.13	Results of the optimization for a Weibull distribution of the wind speed with a mean velocity of 7.0 <i>m/s</i> and Rayleigh distribution . . . . .	164
6.14	Summary of the main settings for <i>AEP75</i> optimization . . . . .	168
6.15	Constraints adopted for the <i>AEP75</i> optimization . . . . .	168
6.16	Genetic pool and fitness values of the considered points in Pareto front of <i>AEP75 – Opt1</i>	169
6.17	Genetic pool and fitness values of the considered points in Pareto front of <i>AEP75 – Opt2</i>	171
6.18	Genetic pool and fitness values of the considered points in Pareto front of <i>AEP75 – Opt3</i>	173
6.19	Results of the optimization for a Weibull distribution of the wind speed with a mean velocity of 7.5 <i>m/s</i> and Rayleigh distribution . . . . .	175

8.1	Characteristics of the VAWT model considered for the analysis . . . . .	195
8.2	Variables adopted in parametrization <i>ParA</i> . . . . .	196
8.3	Variables adopted in parametrization <i>ParB</i> . . . . .	197
8.4	Variables adopted in parametrization <i>ParC</i> . . . . .	198
8.5	Variables adopted in parametrization <i>ParD</i> . . . . .	198
8.6	Boundary constraints adopted in the proposed optimization . . . . .	200
8.7	An example of the XFOIL command list used to calculate the positive polar in forced transition conditions . . . . .	205
8.8	Main setting of the optimizer MOGA, used in <i>OptA</i> . . . . .	206
8.9	Shell script to check XFOIL processes and manage the parallel optimization . . . . .	207
8.10	Penalty coefficients adopted in <i>OptA</i> analysis . . . . .	208
8.11	<i>OptA</i> : considered individuals of the Pareto front . . . . .	208
8.12	Settings used in <i>Optimization B</i> . . . . .	219
8.13	<i>Optimization B</i> lower and upper extended boundaries . . . . .	219
8.14	<i>OptB1</i> : considered individuals of the Pareto front . . . . .	220
8.15	<i>OptB2</i> : considered individuals of the Pareto front . . . . .	231
8.16	<i>OptB3</i> : considered individuals of the Pareto front . . . . .	236
9.1	Case study considered in the analysis . . . . .	243
9.2	Operating conditions considered for the CFD analysis . . . . .	243
9.3	Setup of boundary conditions for the 2D CFD VAWT analysis . . . . .	247
9.4	Numerical setting of the 2D CFD VAWT analysis . . . . .	247
9.5	Numerical schemes adopted in the CFD analysis . . . . .	248
9.6	Shell script to setup and run the CFD analysis . . . . .	249
B.1	Genetic pool and fitness values of the considered solutions belonging to the Pareto front of <i>Wb1Opt0</i> . . . . .	278
C.1	Airfoils that present issues in the XFOIL calculation . . . . .	282

# General Introduction

The aim of the thesis is to cover the most important aspects of the multi-disciplinary optimization of the wind turbines, adopting an open source approach.

Nowadays, the open source codes are becoming increasingly important in the software selection process of the industrial companies. They have many advantages over the commercial software: the source code is accessible and it can be modified, the companies can implement by themselves the engineering models that they need and, hence, the cost reduction is relevant. However, many barriers are still impeding a wider use of them in the market: first, the complexity of the codes is higher than the commercial code as their stability in the calculation; the accuracy of the results is demonstrated to be good, however, the users need usually to spend more time in setting the analysis than commercial software. The learning curve of using open source codes is generally very long and that is why the companies look for experienced user. For these reasons, it is important and useful to propose standard procedures that take advantage of ready-to-use test cases for running the desired analysis.

The thesis aims to explore the open source software potential and to develop a fully open source environment for an optimization process. The proposed application field is the wind turbine design: the multi-disciplinary optimization of the performances of both Horizontal and Vertical Axis Wind Turbines will be discussed.

The first part of the thesis examines the open source tools available for the engineering analysis. Firstly, several types of copyleft licenses are presented with the terms and conditions that define the possibility to use them in order to build a new environment. In particular the GPL, LGPL and BSD licenses are presented. Sequentiality, the main features of the open source codes, adopted for the analysis of the thesis, are illustrated. XFOIL and RFOIL are panel codes that represent an excellent alternative to the CFD software in calculating the performances of airfoils. Dakota is a powerful optimization tool that contains the most important algorithm and methods to find the minimum of a function. Finally, a valid alternative to the commercial CFD codes is represented by the coupling of SALOME (a collection of geometric and meshing tools) with OpenFOAM (the most important open source CFD code) and

ParaView (used in the post processing phase). The advantages and disadvantages in using open source tools are illustrated.

The open source approach has, therefore, been tested for the aerodynamic analysis of a tiltrotor geometry in wind tunnel flow conditions. The study is part of the European research program DREAM-Tilt signed by the HIT09-UNIPD-RUAG consortium and the European community organism Clean Sky JU in the framework of the call for proposal, issued by the helicopter manufacturer AgustaWestland (AW). The study aims to highlight the accuracy and the stability aspects of open source codes (OpenFOAM) compared to commercial software (ANSYS Fluent). The results of OpenFOAM analysis are in good agreement with both ANSYS Fluent and experimental results.

The second part of the thesis focuses on the Horizontal Axis Wind Turbine design and optimization; at this stage of the research, the optimization loop has been implemented using both in-house codes and commercial software (ANSYS Mechanical and ANSYS Fluent). The starting point for the wind turbine design studies is represented by the structural optimization of the well-known Horizontal Axis Wind Turbine, AOC 15/50. The considered wind turbine, developed by Sandia National Laboratories, has been chosen since experimental and testing results (through which validate both structural and aerodynamic models) are freely available in literature. It has been possible to reproduce the composite layout stratification of the blade skin to validate the structural model and set the test-site conditions, in the numerical codes, to obtain the power curve with different aerodynamic analysis. Even though aerodynamic and structural optimizations of HAWT blades have been widely proposed by several authors, in reviewing the literature, the potential of an evolutionary algorithm based on the coupling of an aerodynamic model (based upon the BEM Theory) and a structural one (based on a FEM analysis) have been not often investigated. A first analysis on the Horizontal Axis Wind Turbine design (Chapter 5), hence, proposes an innovative coupled aerodynamic and structural optimization. The optimized sequence of the laminas has allowed to significantly reduce the total deformation at the blade tip with a registered increase in the flexural rigidity of the blade.

Sub-sequentially, a further optimization (described in Chapter 6) through genetic algorithm takes also into account the cost analysis, involving the use of different cost models available in literature. The combination of the Annual Energy Production and the Cost Of Energy represents one of the most popular optimization objectives for the HAWT definition. In the proposed analysis, the airfoil sequence of a wind turbine is designed by specifying the desired model for the Cost Of Energy and the condition of the installation site. The calculated airfoil shapes result in a sequence of cambered profiles; this, in addition to an optimized twist angles distribution, allowed to increase the Annual Energy Production density with the reduction of the Levelized Cost Of Energy of the considered blade.

In the third part of the thesis, the optimization environment has been made fully open source through the coupling of DAKOTA, the optimization tool developed by Sandia National Laboratories, with open source engineering codes and in-house functions for both the structural and aerodynamic analysis. The application field of Part III regards the optimization of Vertical Axis Wind Turbine airfoils (Chapter 8) and it has been carried during the research activity at Delft University of Technology. In these analysis, the aerodynamic function is evaluated as the average lift curve slope over the average drag coefficient over a rotation; the function, proposed by Ferreira et al., aims to maximize the optimal power output of the turbine by optimizing the shedding of the wake, which determines the energy conversion from the flow. In the optimization loop, a Double Multiple Stream Model and a panel code are included for the evaluation of the aerodynamic performances. The analysis results in increasing the aero-structural performances with an improvement of the power coefficient, assumed in a point of lower solidity.

A CFD validation is also carried in Chapter 9 through the implementation of automatic procedures that couple open source libraries for the geometry generation and the mesh creation with a fluid dynamic analysis in OpenFOAM.



---

## Part I

# The Open Source Software for Engineering Analysis





# Introduction and Background

Part I of the thesis deals with the implementation of a computational fluid dynamic analysis using open source tools. The presented study aims to highlight the accuracy and the stability aspects of the open source codes, specifically OpenFOAM, compared to the commercial software.

Firstly, a theoretical background of the Computational Fluid Dynamic (CFD) is provided in Chapter 1. The well known Navier-Stokes equations are derived with full attention to the principles which underlie the physics involved. They are presented in their conservative form, which represents the most suitable formulation for the implementation in a numerical analysis. The discretization of the equations on a computational grid and the differences between explicit and implicit methods are also illustrated. In addition, the theoretical formulation of a problem that involves rotating zone of fluids is also mentioned. The *Moving Reference Frame* technique allows to simplify the numerical analysis of the Horizontal Axis Wind Turbine, the topic addressed in Chapter 7.

Chapter 2 provides a general overview on the open source codes. Firstly, the concept of copyleft is explained and the most important types of open source license (GPL and LGPL) are presented. The open source codes, used in the thesis, are therefore briefly introduced. The panel codes XFOIL and RFOIL represent a high-accuracy alternative to the CFD analysis: they allow to evaluate the aerodynamic polars of an airfoil in a fast way. For this reason, they are suitable for the implementation in an optimization loop. A powerful collection of open source tools for the optimization is DAKOTA, a software developed by Sandia and released, for a few years, under a LGPL license. OpenFOAM represents the most important open source CFD code and its community of users continuously develops it. In order to generate a geometry, the 2D and 3D computational grids, the CAE software SALOME can be used. SALOME consists of several open source libraries and algorithms with a simple graphical interface. Finally, ParaView represents a great tool that helps the user to post-process the numerical results from FEM or CFD analysis, or simply to visualize a geometry.

The thesis aims to develop an open source environment for the wind turbines multi-disciplinary optimization. In the last decade, several tools for the design of both Horizontal and Vertical Axis Wind

---

Turbine have been proposed; QBlade [1] is one of the most important open source software (distributed under the GPL license) for the wind turbine design and calculation. It integrates the XFOIL/XFLR5 functionality to compute the polars and it includes them into the design process. It also contains several modules for the VAWT design calculation, the Viterna extrapolation, the structural Euler-Bernoulli beam module and the integration with the aeroelastic code FAST. The latter one is developed by NREL; FAST [2] is an aeroelastic CAE tool (distributed under the Apache License, Version 2.0) for simulating the coupled dynamic response of wind turbines. The tool allows the analysis of a wide range of wind turbine configurations, considering a different number of blades, pitch or stall regulation, rigid or teetering hub, upwind or downwind rotor, and lattice or tubular tower. It implements aerodynamic, hydrodynamic, control and electrical system and structural-dynamics models that can interact and be coupled. AeroDyn [3] is also developed by NREL and it represents a time-domain wind turbine aerodynamics module that has been coupled into FAST tool to enable aero-elastic simulation of horizontal-axis wind turbines. The cited tools are examples of multidisciplinary analysis of the wind turbine design and they take into account several aspects that should be considered in the design process. However, an optimization module is still not considered and they have not the flexibility to also include high-accuracy calculations evaluated with methods as the FEM and CFD codes.

Being the aero-dynamical study one the most important in the considered machine design, an extensive application of a CFD analysis (on a different topic, a tiltrotor external aerodynamic analysis), with open source codes, is presented in Chapter 3. The purpose is to test the capabilities of an open source CFD tool and compare the results with both numerical and experimental data. The work is part of the European research program DREAM-Tilt [4], signed by the HIT09-UNIPD-RUAG consortium and the European community organism Clean Sky JU in the framework of the call for proposal, issued by the helicopter manufacturer AgustaWestland (AW). Specifically, the analysis carried in Chapter 3 are complementary to the work accomplished in the framework of the DREAM-Tilt WP2, task 2.2: *Blind test assessment via CFD simulation of both the baseline and optimized tiltrotor geometry in wind tunnel flow conditions*, [4]. The analysis are based on the previous European research program Clean Sky Cfp (CODE-Tilt, [5]). In CODE-Tilt, the numerical model of the ERICA 1/8 scaled baseline geometry has been validated using experimental data available from a previous wind tunnel campaign, carried out at the Politecnico di Milano in the framework of the European project NICETRIP WP 4.5, [6]. Furthermore, the numerical prediction capabilities, at near-stall conditions, have been improved thorough numerical analysis carried in [7] for medium and high angles of attack. Finally, the numerical results have been compared against experimental data coming from a further dedicated experimental campaign, performed in June 2011 at the Politecnico di Milano wind tunnel, [8]. In addition, a

---

numerical validation with the open source OpenFOAM code has also been assessed in [9]. In the presented work, both the commercial software ANSYS Fluent and the open source code OpenFOAM have been tested in order to validate a CFD model of the tiltrotor baseline configuration, in wind tunnel conditions. The validation of the numerical models has been carried out on the 1/8 scaled tiltrotor geometry and it is described in detail in Chapter 3: the settings are reported in terms of boundary conditions, numerical schemes and simulation strategies. Finally, the obtained numerical results are compared against the experimental data. The global aerodynamic coefficients, flow distortion, total pressure losses and flow separation phenomena are analysed. In addition, a PIV analysis has also been carried in the framework of the DREAM-Tilt project [10]: the numerical results of ANSYS Fluent and OpenFOAM are compared with the PIV data in terms of velocity and vorticity field distributions.



# Chapter 1

## CFD - Governing Equations

The common known **Navier-Stokes equations** are a system of equations that govern the behaviour of the fluid flows. The following theory dissertation is reported in Anderson [11] and Versteeg [12] books.

The basic principles of Navier-Stokes equations are the conservation of three laws of the physics:

- **Conservation of mass:** the mass is conserved;
- **Newton's second law:** the rate of change of momentum equals the sum of the forces on a fluid;
- **First law of thermodynamic:** the energy rate of change is the sum of the rate of heat addition and the rate of work done on the fluid particles.

The underlying assumptions for the analysis are the following: the fluid is considered as a continuum and the macroscopic scale ( $> 1\mu m$ ) is adopted. The macroscopic properties of the fluid (such as pressure, velocity, density, temperature and their derivatives in space and time) will be calculated. All the considered proprieties are functions of space and time, hence  $\rho = \rho(x, y, z, t)$ ,  $u = u(x, y, z, t)$ , etc..

### 1.1 The Mass Conservation Equation

The mass conservation equation implicates to calculate the mass balance for the fluid element: *the rate of increase of mass in fluid element has to equal the net rate of flow of mass into fluid element.*

The rate of increase of mass is:

$$\frac{\partial}{\partial t}(\rho\delta x\delta y\delta z) = \frac{\partial\rho}{\partial t}\delta x\delta y\delta z$$

The net rate of flow of mass into fluid element is found by balancing the mass flow across its boundaries, as shown in Figure 1.1.

$$\begin{aligned}
 & \left( \rho u - \frac{\partial(\rho u)}{\partial x} \frac{1}{2} \delta x \right) \delta y \delta z - \left( \rho u + \frac{\partial(\rho u)}{\partial x} \frac{1}{2} \delta x \right) \delta y \delta z + \\
 & \left( \rho v - \frac{\partial(\rho v)}{\partial y} \frac{1}{2} \delta y \right) \delta x \delta z - \left( \rho v + \frac{\partial(\rho v)}{\partial y} \frac{1}{2} \delta y \right) \delta x \delta z + \\
 & \left( \rho w - \frac{\partial(\rho w)}{\partial z} \frac{1}{2} \delta z \right) \delta x \delta y - \left( \rho w + \frac{\partial(\rho w)}{\partial z} \frac{1}{2} \delta z \right) \delta x \delta y
 \end{aligned}$$

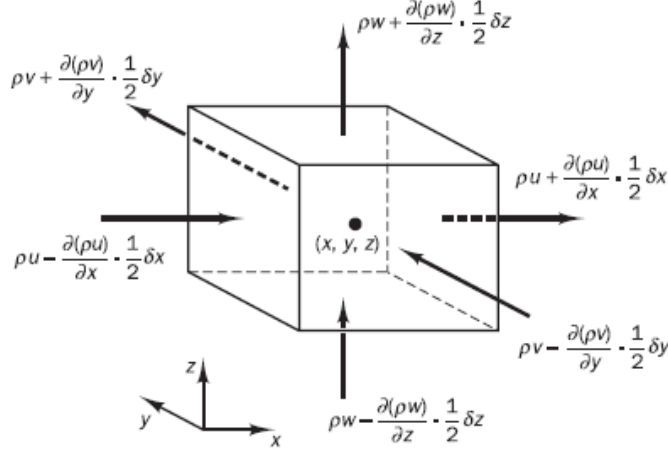


**Figure 1.1:** Mass flow in the fluid element

The two terms are equated and the expression is simplified dividing by  $\delta x \delta y \delta z$ . This leads to:

$$\frac{\partial \rho}{\partial t} + \frac{\partial(\rho u)}{\partial x} + \frac{\partial(\rho v)}{\partial y} + \frac{\partial(\rho w)}{\partial z} = 0$$

In vector notation, we obtain the **Continuity equation**: it is valid for an unsteady, three-dimensional and compressible fluid. The equation can be written using the divergence operator:

$$\frac{\partial \rho}{\partial t} + \text{div}(\rho \bar{u}) = 0 \tag{1.1}$$

For an incompressible fluid, the continuity equation assumes the simplified form:

$$\text{div}(\bar{u}) = \frac{\partial u}{\partial x} + \frac{\partial v}{\partial y} + \frac{\partial w}{\partial z} = 0 \tag{1.2}$$

## 1.2 Lagrangian and Eulerian Approaches

The momentum and energy conservation laws concern the changes of properties of a fluid particle. In the **Lagrangian approach** each property per unit of mass  $\phi$  is function of both position and time, hence  $\phi(x, y, z, t)$ .

The **Total or substantive derivative** of  $\phi$  with respect to time, following a fluid particle, defines

the rate of change of property  $\phi$  per unit of mass:

$$\frac{D\phi}{Dt} = \frac{\partial\phi}{\partial t} + \frac{\partial\phi}{\partial x} \frac{dx}{dt} + \frac{\partial\phi}{\partial y} \frac{dy}{dt} + \frac{\partial\phi}{\partial z} \frac{dz}{dt} \quad (1.3)$$

$$\frac{D\phi}{Dt} = \frac{\partial\phi}{\partial t} + \frac{\partial\phi}{\partial x} u + \frac{\partial\phi}{\partial y} v + \frac{\partial\phi}{\partial z} w = \frac{\partial\phi}{\partial t} + u * grad\phi \quad (1.4)$$

In Lagrangian approach the particle motion is tracked and the rate of change of  $\phi$  is computed for all the fluid particles. However, it is more common to consider a region fixed in space in order to develop the equations. This is the **Eulerian approach**.

The rate of changes of  $\phi$  per unit of volume for a fluid particle is defined as:

$$\rho \frac{D\phi}{Dt} = \rho \left( \frac{\partial\phi}{\partial t} + u * grad\phi \right) \quad (1.5)$$

The *substantive derivative* of  $\phi$  (which follows a fluid particle) is related to the *rate of change of  $\phi$*  (relative to a fluid element stationary in space) in the following way.

The generalization of the terms in the mass conservation equation for an arbitrary property  $\phi$  is:

$$\frac{\partial\rho\phi}{\partial t} + div(\rho\phi u) \quad (1.6)$$

The formula expresses the sum between the rate of change in time of  $\phi$  and the net flow of  $\phi$  out of the element, per unit of volume. It can be rewritten as:

$$\frac{\partial\rho\phi}{\partial t} + div(\rho\phi u) = \rho \left[ \frac{\partial\phi}{\partial t} + u * grad\phi \right] + \phi \left[ \frac{\partial\rho}{\partial t} + div(\rho u) \right] = \rho \frac{D\phi}{Dt} \quad (1.7)$$

where  $D/Dt$  and  $\partial/\partial t$  are physically and numerically different quantities. The meaning is:

*The sum of rate of increase of  $\phi$  for a fluid element and the net rate of flow of  $\phi$  out of the fluid element equals the rate of increase of  $\phi$  for a fluid particle.*

The substantial derivative represents the rate of change of a property of the given fluid element as it moves through space. The partial derivative, by contrast, represents the time rate of change of the property at the fixed point, due to transient fluctuations in the flowfield. Both conservative (divergence) and non-conservative forms of the rate of change can be used to express the conservation of the quantity  $\phi$ . For brevity, the non-conservative forms are used for the derivation of momentum and energy equations.

In order to derive the governing fluid equations, the adopted flow model could be either a *finite control volume* or an *infinitesimal fluid element*, fixed in the space or moving with the fluid. The



Equation	Var	Non-conservative	Conservative
x-momentum	$u$	$\rho \frac{Du}{Dt}$	$\frac{\partial \rho u}{\partial t} + \text{div}(\rho u u)$
y-momentum	$v$	$\rho \frac{Dv}{Dt}$	$\frac{\partial \rho v}{\partial t} + \text{div}(\rho v u)$
z-momentumz	$w$	$\rho \frac{Dw}{Dt}$	$\frac{\partial \rho w}{\partial t} + \text{div}(\rho w u)$
energy	$E$	$\rho \frac{DE}{Dt}$	$\frac{\partial \rho E}{\partial t} + \text{div}(\rho E u)$

**Table 1.1:** Conservative and Non-conservative forms of Navier-Stokes Equations

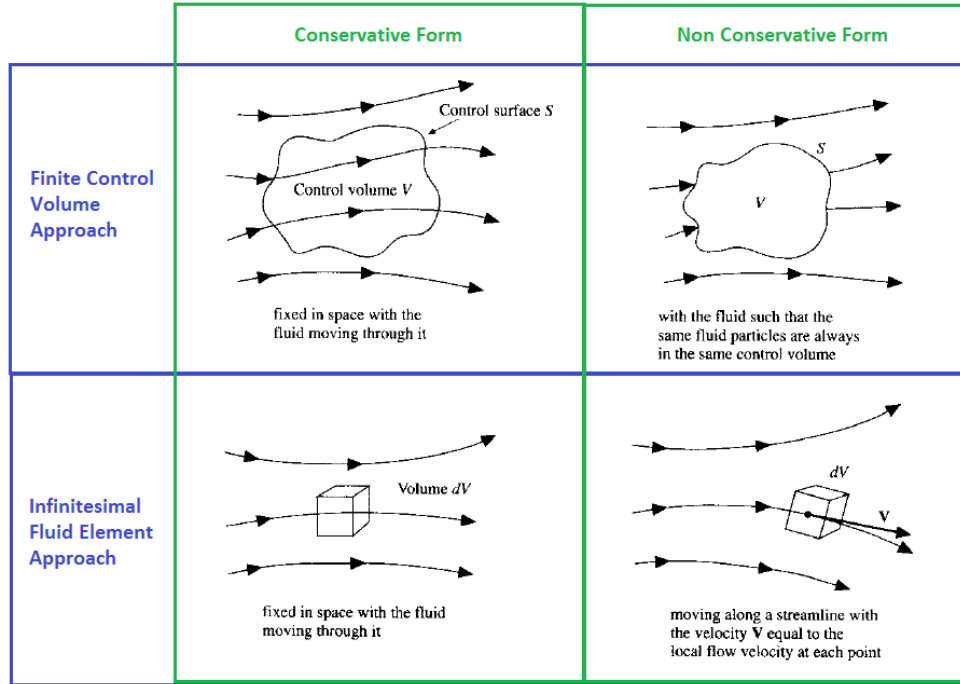


**Figure 1.2:** Models of flow: finite volume and infinitesimal fluid element approaches

various formulations lead to different forms of the governing equations, mathematically equivalent.

In the **Finite Control Volume** approach, a finite region of the flow is identified by a control volume and by a control surface. The control volume could be fixed in space or moving with the fluid. The fluid flow equations, directly obtained applying the fundamental physical principles, are in the integral form; a further manipulation allows to calculate the partial differential equations form. The governing equations, if calculated considering the control volume fixed in space, are in the conservative form; on the other hand, when considering the control volume moving with the fluid, the non-conservative form is obtained.

In a second model, an **Infinitesimal fluid element** of volume  $dV$  is considered: it may be fixed in space or moving with the fluid. In this case, the model leads directly to the fundamental equations in partial differential equation form. Again, considering the fluid element fixed in space leads to the conservation form, if the fluid element is moving, the non-conservation form is obtained.

In aerodynamic, the use of both the conservation or non-conservation forms is irrelevant. However, in Computational Fluid Dynamics the conservative form is more suited to be numerically solved.

### 1.3 The Momentum Equations

The Newton's second law, applied to a fluid particle, states: *the rate of increase of momentum of fluid particle is equal to the sum of forces on the fluid particle.*

The rates of increase of x,y and z-momentum per unit of volume are given by:

$$\rho \frac{Du}{Dt} \quad \rho \frac{Dv}{Dt} \quad \rho \frac{Dw}{Dt} \quad (1.8)$$

The forces acting on the fluid particle are classified as surface forces (pressure, viscous, gravity) and body forces (centrifugal, Coriolis, electromagnetic). In the momentum equation, the surface forces are usually highlighted, whereas the body forces are included in a source term. In a fluid particle both normal stresses (denoted by  $p$ ) and viscous stressed (denoted by  $\tau_{ij}$ ) are present. Figure 1.3 illustrates the stress components acting in the x-direction of the fluid particle.

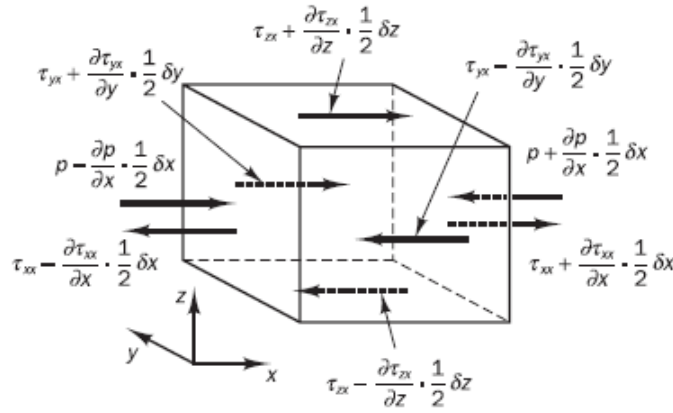


**Figure 1.3:** Stress components in the x-direction of a fluid particle

The net force in x-direction on left and right faces is:

$$\begin{aligned} & \left[ \left( p - \frac{\partial p}{\partial x} \frac{1}{2} \delta x \right) - \left( \tau_{xx} - \frac{\partial \tau_{xx}}{\partial x} \frac{1}{2} \delta x \right) \right] \delta y \delta z + \left[ - \left( p + \frac{\partial p}{\partial x} \frac{1}{2} \delta x \right) + \left( \tau_{xx} + \frac{\partial \tau_{xx}}{\partial x} \frac{1}{2} \delta x \right) \right] \delta y \delta z \\ & \left( - \frac{\partial p}{\partial x} + \frac{\partial \tau_{xx}}{\partial x} \right) \delta x \delta y \delta z \end{aligned} \quad (1.9)$$

The net force in x-direction on front and back faces is:

$$\begin{aligned}
 & -\left(\tau_{yx} - \frac{\partial\tau_{yx}}{\partial y}\frac{1}{2}\delta y\right)\delta x\delta z + \left(\tau_{yx} + \frac{\partial\tau_{yx}}{\partial y}\frac{1}{2}\delta y\right)\delta x\delta z \\
 & \qquad \qquad \qquad \frac{\partial\tau_{yx}}{\partial y}\delta x\delta y\delta z
 \end{aligned} \tag{1.10}$$

The net force in x-direction on up and bottom faces is:

$$\begin{aligned}
 & -\left(\tau_{zx} - \frac{\partial\tau_{zx}}{\partial z}\frac{1}{2}\delta z\right)\delta x\delta y + \left(\tau_{zx} + \frac{\partial\tau_{zx}}{\partial z}\frac{1}{2}\delta z\right)\delta x\delta y \\
 & \qquad \qquad \qquad \frac{\partial\tau_{zx}}{\partial z}\delta x\delta y\delta z
 \end{aligned} \tag{1.11}$$

The total force per unit of volume, due to the surface stresses, is:

$$\frac{\partial(-p + \tau_{xx})}{\partial x} + \frac{\partial\tau_{yx}}{\partial y} + \frac{\partial\tau_{zx}}{\partial z} \tag{1.12}$$

After including the body forces in a source term  $S_{Mx}$ , the **x-component of the momentum equation** is found by equalling 1.8 and 1.12:

$$\rho \frac{Du}{Dt} = \frac{\partial(-p + \tau_{xx})}{\partial x} + \frac{\partial\tau_{yx}}{\partial y} + \frac{\partial\tau_{zx}}{\partial z} + S_{Mx} \tag{1.13}$$

In the same way, the **y-component and the z-component** of the momentum equation are:

$$\rho \frac{Dv}{Dt} = \frac{\partial\tau_{xy}}{\partial x} + \frac{\partial(-p + \tau_{yy})}{\partial y} + \frac{\partial\tau_{zy}}{\partial z} + S_{My} \tag{1.14}$$

$$\rho \frac{Dw}{Dt} = \frac{\partial\tau_{xz}}{\partial x} + \frac{\partial\tau_{yz}}{\partial y} + \frac{\partial(-p + \tau_{zz})}{\partial z} + S_{Mz} \tag{1.15}$$

## 1.4 The Energy Equation

The first law of thermodynamic states: *the rate of change of energy of a fluid particle is equal to the rate of heat addition to the fluid particle plus the rate of work done on the particle.*

The rate of increase of energy  $E$  of a fluid particle per unit of volume is:

$$\rho \frac{DE}{Dt} \tag{1.16}$$

The second term of the right-hand side, the rate of work done by surface forces, is the product

of the forces with the velocity components in the direction of the force. Considering the x-direction, equations 1.9, 1.10 and 1.11 have to be multiply with the x-velocity component  $u$  and summed.

$$\left[ \frac{\partial(u(-p + \tau_{xx}))}{\partial x} + \frac{\partial(u\tau_{yx})}{\partial y} + \frac{\partial(u\tau_{zx})}{\partial z} \right] \delta x \delta y \delta z \quad (1.17)$$

For y-direction and z-direction the procedure is the same and leads to:

$$\left[ \frac{\partial(v\tau_{xy})}{\partial x} + \frac{\partial(v(-p + \tau_{yy}))}{\partial y} + \frac{\partial(v\tau_{zy})}{\partial z} \right] \delta x \delta y \delta z \quad (1.18)$$

$$\left[ \frac{\partial(w\tau_{xz})}{\partial x} + \frac{\partial(w\tau_{yz})}{\partial y} + \frac{\partial(w(-p + \tau_{zz}))}{\partial z} \right] \delta x \delta y \delta z \quad (1.19)$$

The terms containing the pressure, after the division by the volume  $\delta V$ , can be written in the vectorial form using the divergence operator:

$$-\frac{\partial(up)}{\partial x} - \frac{\partial(vp)}{\partial y} - \frac{\partial(wp)}{\partial z} = -\text{div}(p\bar{u})$$

Finally, by summing the equations 1.17, 1.18 and 1.19, the **Total rate of work done on the fluid particle by surface stresses** is:

$$\begin{aligned} [-\text{div}(p\bar{u})] + \left[ \frac{\partial(u\tau_{xx})}{\partial x} + \frac{\partial(u\tau_{yx})}{\partial y} + \frac{\partial(u\tau_{zx})}{\partial z} + \frac{\partial(v\tau_{xy})}{\partial x} + \right. \\ \left. \frac{\partial(v\tau_{yy})}{\partial y} + \frac{\partial(v\tau_{zy})}{\partial z} + \frac{\partial(w\tau_{xz})}{\partial x} + \frac{\partial(w\tau_{yz})}{\partial y} + \frac{\partial(w\tau_{zz})}{\partial z} \right] \end{aligned} \quad (1.20)$$

The heat flux vector  $\bar{q}$  represents the first term of the right-hand side: it is calculated from the components shown in Figure 1.4:

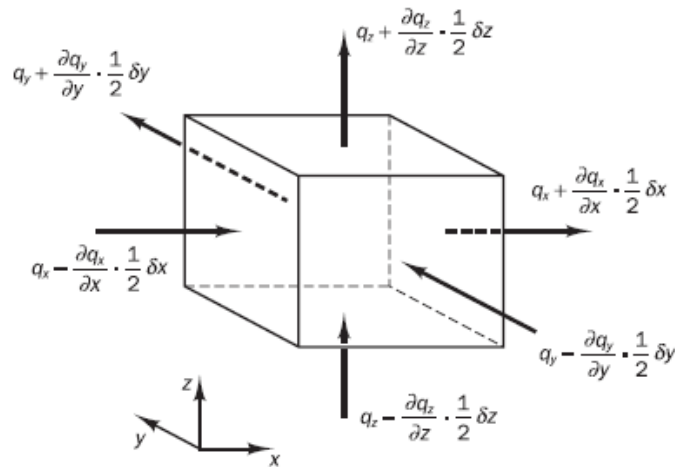


**Figure 1.4:** Components of the heat flux vector

The rate of heat transfer to the fluid particle in the x-direction is:

$$\left[ \left( q_x - \frac{\partial q_x}{\partial x} \frac{1}{2} \delta x \right) - \left( q_x + \frac{\partial q_x}{\partial x} \frac{1}{2} \delta x \right) \right] \delta y \delta z = -\frac{\partial q_x}{\partial x} \delta x \delta y \delta z$$

Similarly for y and z directions:

$$-\frac{\partial q_y}{\partial y} \delta x \delta y \delta z \quad -\frac{\partial q_z}{\partial z} \delta x \delta y \delta z$$

The sum of the components in the three directions, divided by the volume  $\delta V$ , leads to:

$$-\frac{\partial q_x}{\partial x} - \frac{\partial q_y}{\partial y} - \frac{\partial q_z}{\partial z} = -\text{div} \bar{q} \quad (1.21)$$

The heat conduction can be therefore related to the local temperature gradient through Fourier's law of heat conduction:

$$q_x = -k \frac{\partial T}{\partial x} \quad q_y = -k \frac{\partial T}{\partial y} \quad q_z = -k \frac{\partial T}{\partial z}$$

In vectorial notation:

$$\mathbf{q} = -k * \text{grad} T \quad (1.22)$$

Finally, the rate of heat addition to the fluid particle, due to heat conduction, is:

$$-\text{div} \mathbf{q} = \text{div}(k * \text{grad} T) \quad (1.23)$$

The left-hand side of energy equation concerns the specific energy  $E$  of the fluid.  $E$  is the sum of internal energy  $i$ , kinetic energy  $\frac{1}{2}(u^2 + v^2 + w^2)$  and potential energy.

The **Energy Equation** becomes:

$$\begin{aligned} \rho \frac{DE}{Dt} = & [-\text{div}(p\bar{u})] + \left[ \frac{\partial(u\tau_{xx})}{\partial x} + \frac{\partial(u\tau_{yx})}{\partial y} + \frac{\partial(u\tau_{zx})}{\partial z} + \frac{\partial(v\tau_{xy})}{\partial x} + \right. \\ & \left. \frac{\partial(v\tau_{yy})}{\partial y} + \frac{\partial(v\tau_{zy})}{\partial z} + \frac{\partial(w\tau_{xz})}{\partial x} + \frac{\partial(w\tau_{yz})}{\partial y} + \frac{\partial(w\tau_{zz})}{\partial z} \right] + \\ & \text{div}(k * \text{grad} T) + S_E \end{aligned} \quad (1.24)$$

where the effects of potential energy changes are included in the source term  $S_E$ , hence the specific energy is considered as:  $E = i + \frac{1}{2}(u^2 + v^2 + w^2)$ .

The energy equation can be rearranged in order to highlight the change in some terms.

The **Internal Energy Equation** is:

$$\begin{aligned} \rho \frac{Di}{Dt} = & -p \operatorname{div}(\bar{u}) + \operatorname{div}(k * \operatorname{grad}T) + \tau_{xx} \frac{\partial u}{\partial x} + \tau_{yx} \frac{\partial u}{\partial y} + \tau_{zx} \frac{\partial u}{\partial z} + \\ & \tau_{xy} \frac{\partial v}{\partial x} + \tau_{yy} \frac{\partial v}{\partial y} + \tau_{zy} \frac{\partial v}{\partial z} + \tau_{xz} \frac{\partial w}{\partial x} + \tau_{yz} \frac{\partial w}{\partial y} + \tau_{zz} \frac{\partial w}{\partial z} + S_i \end{aligned} \quad (1.25)$$

If the analysed fluid is incompressible  $i = cT$  ( $c$  is the specific heat),  $\operatorname{div}\bar{u} = 0$ .

The **Temperature Equation** becomes:

$$\begin{aligned} \rho c \frac{DT}{Dt} = & \operatorname{div}(k * \operatorname{grad}T) + \tau_{xx} \frac{\partial u}{\partial x} + \tau_{yx} \frac{\partial u}{\partial y} + \tau_{zx} \frac{\partial u}{\partial z} + \\ & \tau_{xy} \frac{\partial v}{\partial x} + \tau_{yy} \frac{\partial v}{\partial y} + \tau_{zy} \frac{\partial v}{\partial z} + \tau_{xz} \frac{\partial w}{\partial x} + \tau_{yz} \frac{\partial w}{\partial y} + \tau_{zz} \frac{\partial w}{\partial z} + S_i \end{aligned} \quad (1.26)$$

In the case of compressible flows, the energy equation is often expressed in terms of enthalpy. Since the specific enthalpy is  $h = i + p/\rho$  and the total enthalpy is defined as  $h_0 = h + \frac{1}{2}(u^2 + v^2 + w^2)$ , the relationship with the specific energy  $E$  is:

$$h_0 = i + \frac{p}{\rho} + \frac{1}{2}(u^2 + v^2 + w^2) = E + \frac{p}{\rho}$$

Hence the **Total Enthalpy Equation** is:

$$\begin{aligned} \frac{\partial \rho h_0}{\partial t} + \operatorname{div}(\rho h_0 \bar{u}) = & \operatorname{div}(k * \operatorname{grad}T) + \frac{\partial p}{\partial t} + \\ \left[ \frac{\partial(u\tau_{xx})}{\partial x} + \frac{\partial(u\tau_{yx})}{\partial y} + \frac{\partial(u\tau_{zx})}{\partial z} + \frac{\partial(v\tau_{xy})}{\partial x} + \frac{\partial(v\tau_{yy})}{\partial y} + \right. & \\ \left. \frac{\partial(v\tau_{zy})}{\partial z} + \frac{\partial(w\tau_{xz})}{\partial x} + \frac{\partial(w\tau_{yz})}{\partial y} + \frac{\partial(w\tau_{zz})}{\partial z} \right] & \end{aligned} \quad (1.27)$$

The presented equations 1.25, 1.26 and 1.27 represent alternative forms of the Energy Equation.

## 1.5 Additional equations

In order to describe the behaviour of a fluid, in the previous sections a system of 5 partial differential equations has been developed:

$$\left\{ \begin{array}{l} \text{mass conservation equation} \\ x - \text{momentum equation} \\ y - \text{momentum equation} \\ z - \text{momentum equation} \\ \text{energy equation} \end{array} \right.$$

However, 13 unknowns are present in the equations: the 3 components of the velocity vector  $u(u, v, w)$ , the 4 thermodynamic variables  $\rho, p, i$  and  $T$  and the 6 viscous stress  $\tau_{i,j}$ . In order to close the system further relationship between the thermodynamic variables and an hypothesis on the model of fluid are needed.

### 1.5.1 The Equation of State

The equation of state allows to relate the thermodynamic variables of the Navier-Stokes equations. The assumption of thermodynamic equilibrium has to be made in order to use the equation of state: this hypothesis is valid because of the instantaneous adjustment of the fluid to new conditions when a property changes rapidly from place to place.

**Equation of State** relates the two thermodynamic variables to two state variables:

$$p = p(\rho, T) \quad i = i(\rho, T)$$

$$p = \rho RT \quad i = C_V T \quad (1.28)$$

In the incompressible fluids, without density variation, there is no linkage between energy equation and the other 4 equations; hence, the flow can be solved considering only considering mass conservation and momentum equations (if not interested in heat transfer).

### 1.5.2 The Newtonian Fluid Hypothesis

The governing equations also contain, as unknowns, the viscous stress components  $\tau_{ij}$ . A model for viscous stress is therefore necessary in order to determine the conservation equations of the fluid flows. In three-dimensional flows, the local rate of deformation of a fluid element (assumed to be isotropic) is composed by the linear and volumetric deformation rates.

The rate of linear deformation presents 9 components:

$$s_{xx} = \frac{\partial u}{\partial x} \quad s_{yy} = \frac{\partial v}{\partial y} \quad s_{zz} = \frac{\partial w}{\partial z}$$

$$s_{xy} = s_{yx} = \frac{1}{2} \left( \frac{\partial u}{\partial y} + \frac{\partial v}{\partial x} \right) \quad s_{xz} = s_{zx} = \frac{1}{2} \left( \frac{\partial u}{\partial z} + \frac{\partial w}{\partial x} \right) \quad s_{yz} = s_{zy} = \frac{1}{2} \left( \frac{\partial v}{\partial z} + \frac{\partial w}{\partial y} \right)$$

The volumetric deformation is:

$$\frac{\partial u}{\partial x} + \frac{\partial v}{\partial y} + \frac{\partial w}{\partial z} = \text{div}u$$

In a **Newtonian Fluid**, the viscous stress are proportional to the rates of deformation:

$$\begin{aligned}
 \tau_{xx} &= 2\mu \frac{\partial u}{\partial x} + \lambda \operatorname{div}(u) & \tau_{yy} &= 2\mu \frac{\partial v}{\partial y} + \lambda \operatorname{div}(u) & \tau_{zz} &= 2\mu \frac{\partial w}{\partial z} + \lambda \operatorname{div}(u) \\
 \tau_{xy} = \tau_{yx} &= \mu \left( \frac{\partial u}{\partial y} + \frac{\partial v}{\partial x} \right) & \tau_{xz} = \tau_{zx} &= \mu \left( \frac{\partial u}{\partial z} + \frac{\partial w}{\partial x} \right) & \tau_{yz} = \tau_{zy} &= \mu \left( \frac{\partial v}{\partial z} + \frac{\partial w}{\partial y} \right)
 \end{aligned} \tag{1.29}$$

where the **dynamic viscosity**  $\mu$  relates the stress to the linear deformations and  $\lambda$  is the **bulk viscosity** that relates the stress to the volumetric deformation. The effects of  $\lambda$  are small and it can be approximated with  $\lambda = -\frac{2}{3}\mu$ ; for the incompressible fluid this term can be omitted.

The formulations of equation 1.29 can be used in the momentum equations ( 1.13, 1.14, 1.15) to obtain the **Navier-Stokes Equations**:

$$\rho \frac{Du}{Dt} = -\frac{\partial p}{\partial x} + \frac{\partial}{\partial x} \left[ 2\mu \frac{\partial u}{\partial x} + \lambda \operatorname{div}(\bar{u}) \right] + \frac{\partial}{\partial y} \left[ \mu \left( \frac{\partial u}{\partial y} + \frac{\partial v}{\partial x} \right) \right] + \frac{\partial}{\partial z} \left[ \mu \left( \frac{\partial u}{\partial z} + \frac{\partial w}{\partial x} \right) \right] + S_{Mx} \tag{1.30}$$

$$\rho \frac{Dv}{Dt} = -\frac{\partial p}{\partial y} + \frac{\partial}{\partial x} \left[ \mu \left( \frac{\partial u}{\partial y} + \frac{\partial v}{\partial x} \right) \right] + \frac{\partial}{\partial y} \left[ 2\mu \frac{\partial v}{\partial y} + \lambda \operatorname{div}(\bar{u}) \right] + \frac{\partial}{\partial z} \left[ \mu \left( \frac{\partial v}{\partial z} + \frac{\partial w}{\partial y} \right) \right] + S_{My} \tag{1.31}$$

$$\rho \frac{Dw}{Dt} = -\frac{\partial p}{\partial z} + \frac{\partial}{\partial x} \left[ \mu \left( \frac{\partial u}{\partial z} + \frac{\partial w}{\partial x} \right) \right] + \frac{\partial}{\partial y} \left[ \mu \left( \frac{\partial v}{\partial z} + \frac{\partial w}{\partial y} \right) \right] + \frac{\partial}{\partial z} \left[ 2\mu \frac{\partial w}{\partial z} + \lambda \operatorname{div}(\bar{u}) \right] + S_{Mz} \tag{1.32}$$

It is useful to rearrange the viscous stress terms, hiding the small contributions in the source term. For the x-momentum equation a compact form is:

$$\frac{\partial}{\partial x} \left( \mu \frac{\partial u}{\partial x} \right) + \frac{\partial}{\partial y} \left( \mu \frac{\partial u}{\partial y} \right) + \frac{\partial}{\partial z} \left( \mu \frac{\partial u}{\partial z} \right) + \left[ \frac{\partial}{\partial x} \left( \mu \frac{\partial u}{\partial x} \right) + \frac{\partial}{\partial y} \left( \mu \frac{\partial v}{\partial x} \right) + \frac{\partial}{\partial z} \left( \mu \frac{\partial w}{\partial x} \right) + \frac{\partial}{\partial x} (\lambda \operatorname{div}(\bar{u})) \right]$$

$$\operatorname{div}(\mu * \operatorname{grad}(u)) + [S_{Mx}]$$

The new source term becomes:

$$S_M = S_M + [S_{Mx}]$$

The **Navier-Stokes Equations in the finite volume method form** are:

$$\rho \frac{Du}{Dt} = -\frac{\partial p}{\partial x} + \operatorname{div}(\mu * \operatorname{grad}(u)) + S_{Mx} \tag{1.33}$$

$$\rho \frac{Dv}{Dt} = -\frac{\partial p}{\partial y} + \operatorname{div}(\mu * \operatorname{grad}(v)) + S_{My} \tag{1.34}$$



$$\rho \frac{Du}{Dt} = -\frac{\partial p}{\partial z} + \text{div}(\mu * \text{grad}(w)) + S_{Mz} \quad (1.35)$$

Adopting the Newtonian model for the viscous stresses in the **Energy Equation** leads to:

$$\rho \frac{Di}{Dt} = -p \text{div}(u) + \text{div}(k * \text{grad}(T)) + \phi + S_i \quad (1.36)$$

where the *dissipation function*  $\Phi$  represents a source of internal energy, due to deformation work on the fluid particle:

$$\Phi = \mu \left[ 2 \left[ \left( \frac{\partial u}{\partial x} \right)^2 + \left( \frac{\partial v}{\partial y} \right)^2 + \left( \frac{\partial w}{\partial z} \right)^2 \right] + \left( \frac{\partial u}{\partial y} + \frac{\partial v}{\partial x} \right)^2 + \left( \frac{\partial u}{\partial z} + \frac{\partial w}{\partial x} \right)^2 + \left( \frac{\partial v}{\partial z} + \frac{\partial w}{\partial y} \right)^2 \right] + \lambda (\text{div}(\bar{u}))^2$$

## 1.6 The Conservative Form of the Governing Equations of the Flow

The conservative (divergence form) of the system of equations governing the fluid flow of a Newtonian compressible fluid are:

- Continuity  $\frac{\partial \rho}{\partial t} + \text{div}(\rho \bar{u}) = 0$
- x-momentum  $\frac{\partial(\rho u)}{\partial t} + \text{div}(\rho u \bar{u}) = -\frac{\partial p}{\partial x} + \text{div}(\mu * \text{grad}(u)) + S_{Mx}$
- y-momentum  $\frac{\partial(\rho v)}{\partial t} + \text{div}(\rho v \bar{u}) = -\frac{\partial p}{\partial y} + \text{div}(\mu * \text{grad}(v)) + S_{My}$
- z-momentum  $\frac{\partial(\rho w)}{\partial t} + \text{div}(\rho w \bar{u}) = -\frac{\partial p}{\partial z} + \text{div}(\mu * \text{grad}(w)) + S_{Mz}$
- Energy  $\frac{\partial(\rho i)}{\partial t} + \text{div}(\rho i \bar{u}) = -p \text{div}(\bar{u}) + \text{div}(k * \text{grad}(T)) + \Phi + S_i$
- Equations of state  $p = p(\rho, T) \quad i = i(\rho, T)$

The resulting system is formed by 7 equations (5 PDEs + 2 algebraic) in 7 unknowns: the system is hence mathematically closed and can be solved by supplying auxiliary conditions (boundary and initial conditions).

## 1.7 Forms of the General Transport Equation

Observing the governing equations for a compressible Newtonian fluid, some similarity are evident. By introducing a general variable  $\phi$ , the conservative form of all fluid flow equations (also for scalar quantity) can be generalized in the **Transport Equation** form:

$$\frac{\partial(\rho \phi)}{\partial t} + \text{div}(\rho \phi \bar{u}) = \text{div}(\Gamma * \text{grad}(\phi)) + S_\phi \quad (1.37)$$

The rate of increase of  $\phi$  of fluid element plus the net rate of flow of  $\phi$  out of the fluid element equals the rate of increase of  $\phi$  due to diffusion plus the rate of increase of  $\phi$  due to sources.

Hence, on the left-hand side are the **rate of change of  $\phi$**  and the **convective term**; on the right-hand side are the **diffusive term** and the **source term**.

Equation 1.37) represents the starting point for the computational procedure in the Finite Volume Method; by setting  $\phi$  equal to  $1, u, v, e, i$  and assigning an appropriate values for diffusion coefficient  $\Gamma$  and the Source terms, the governing flow equations are obtained. The integration of 1.37) on a 3D control volume is:

$$\int_{CV} \frac{\partial(\rho\phi)}{\partial t} dV + \int_{CV} \text{div}(\rho\phi\bar{u})dV = \int_{CV} \text{div}(\Gamma * \text{grad}(\phi))dV + \int_{CV} S_\phi dV \quad (1.38)$$

Using *Gauss's divergence theorem*, the convective and the diffusive terms are rewritten over the bounding surface:

$$\frac{\partial}{\partial t} \left( \int_{CV} \rho\phi dV \right) + \int_A n \cdot (\rho\phi u) dA = \int_A n \cdot (\Gamma * \text{grad}(\phi)) dA + \int_{CV} S_\phi dV \quad (1.39)$$

where  $n$  is the component of vector in direction normal to surface element  $dA$ .

The physical meaning of the terms in transport equation is specified below:

- $\frac{\partial}{\partial t} \left( \int_{CV} \rho\phi dV \right)$  Rate of change of the total amount of property  $\phi$  in the control volume;
- $\int_A n \cdot (\rho\phi u) dA$  Net rate of decrease of property  $\phi$  in the fluid element due to convection;
- $\int_A n \cdot (\Gamma * \text{grad}(\phi)) dA$  Net rate of increase of property  $\phi$  in the fluid element due to diffusion;
- $\int_{CV} S_\phi dV$  Rate of increase of property  $\phi$  as results of sources in the fluid element.

In **steady state** problems the first term is null:

$$\int_A n \cdot (\rho\phi u) dA = \int_A n \cdot (\Gamma * \text{grad}(\phi)) dA + \int_{CV} S_\phi dV \quad (1.40)$$

In **time-dependent** problems a further integration with respect the time  $t$  over a small interval  $\Delta T$  is also necessary:

$$\int_{\Delta t} \frac{\partial}{\partial t} \left( \int_{CV} \rho\phi dV \right) dt + \int_{\Delta t} \int_A n \cdot (\rho\phi u) dA dt = \int_{\Delta t} \int_A n \cdot (\Gamma * \text{grad}(\phi)) dA dt + \int_{\Delta t} \int_{CV} S_\phi dV dt \quad (1.41)$$

## 1.8 Discretization of Partial Differential Equations

An analytical solution of the PDE involves closed-form expressions, which give the variation of the variable continuously throughout the domain; on the other hand, numerical solutions give the results only at some discrete points of the domain. An example of grid of points is shown in Figure 1.5: the spacing of the grid points in x and y directions is uniform,  $\Delta x$  and  $\Delta y$  are different. The finite difference method is widely used in CFD and it consists in replacing the partial derivative of the governing equations of fluid dynamic with algebraic difference quotients. The governing equations will become a system of algebraic equations, which can be solved at discrete grid points in the flow.

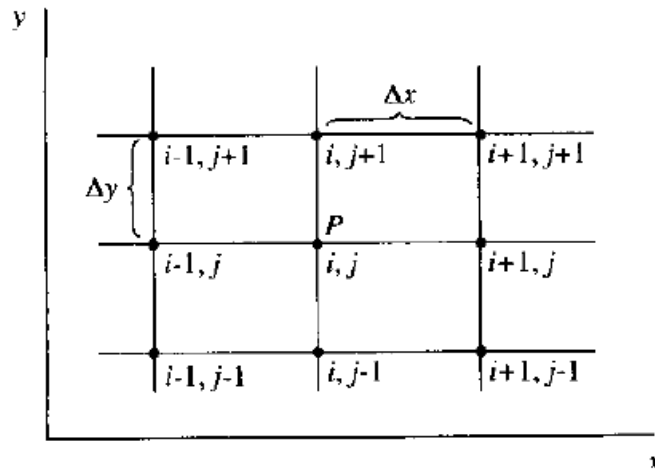


**Figure 1.5:** Example of a discrete grid of points

In the finite difference formulation, the expressions of the derivative are based on Taylor's series expansion. For example  $u_{i+1,j}$  represents the x-component of velocity at point  $(i + 1, j)$  and can be obtained from point  $(i, j)$  as:

$$u_{i+1,j} = u_{i,j} + \left(\frac{\partial u}{\partial x}\right)_{i,j} \Delta x + \left(\frac{\partial^2 u}{\partial x^2}\right)_{i,j} \frac{\Delta x^2}{2} + \left(\frac{\partial^3 u}{\partial x^3}\right)_{i,j} \frac{\Delta x^3}{6} + \dots \quad (1.42)$$

Equation 1.42 is mathematically correct if the number of terms at the right-hand side is infinite and the series converges as  $\Delta x$  tends to 0. In the numerical computations, the Taylor's series expansion has to be truncated, neglecting the high order terms. Depending on the truncation error, it is possible to define the accuracy of a numerical scheme as:

- First Order Accuracy  $u_{i+1,j} = u_{i,j} + \left(\frac{\partial u}{\partial x}\right)_{i,j} \Delta x$
- Second Order Accuracy  $u_{i+1,j} = u_{i,j} + \left(\frac{\partial u}{\partial x}\right)_{i,j} \Delta x + \left(\frac{\partial^2 u}{\partial x^2}\right)_{i,j} \frac{\Delta x^2}{2}$

The partial derivative  $\left(\frac{\partial u}{\partial x}\right)_{i,j}$  of Equation 1.42 can be calculated as :

$$\left(\frac{\partial u}{\partial x}\right)_{i,j} = \frac{u_{i+1,j} - u_{i,j}}{\Delta x} + o(\Delta x) \quad (1.43)$$

where  $o(\Delta x)$  represents the *high order terms* of  $\Delta x$ .

If the Taylor's series expansion is first expressed for direction  $(i + 1)$ , hence for direction  $(i - 1)$  and then the two expressions are compared, the following formulations are obtained:

- First Order Forward Difference:  $\left(\frac{\partial u}{\partial x}\right)_{i,j} = \frac{u_{i+1,j} - u_{i,j}}{\Delta x} + o(\Delta x)$
- First Order Rearward Difference:  $\left(\frac{\partial u}{\partial x}\right)_{i,j} = \frac{u_{i,j} - u_{i-1,j}}{\Delta x} + o(\Delta x)$
- Second Order Central Difference:  $\left(\frac{\partial u}{\partial x}\right)_{i,j} = \frac{u_{i+1,j} - u_{i-1,j}}{2\Delta x} + o(\Delta x)^2$
- Second Order Central Second Difference:  $\left(\frac{\partial^2 u}{\partial x^2}\right)_{i,j} = \frac{u_{i+1,j} - 2u_{i,j} + u_{i-1,j}}{(\Delta x)^2} + o(\Delta x)^2$

The y-direction formulations are similar. The mixed derivative can also be obtained by writing the x-derivative as a central difference of the y-derivative and then cast the y-derivative in terms of central differences:

- Second Order Mixed Derivative:  $\left(\frac{\partial^2 u}{\partial x \partial y}\right)_{i,j} = \frac{1}{4\Delta x \Delta y} (u_{i+1,j+1} + u_{i-1,j-1} - u_{i+1,j-1} - u_{i-1,j+1}) + o((\Delta x)^2, (\Delta y)^2)$

## 1.9 Explicit and Implicit Methods

In order to illustrate the differences between explicit and implicit methods a simple equation is taken as example:

$$\frac{\partial u}{\partial t} = \frac{\partial^2 u}{\partial x^2} \quad (1.44)$$

In equation 1.44, the forward difference and the central difference are used respectively for the time derivative and for the spatial derivative:

$$\frac{u_i^{n+1} - u_i^n}{\Delta t} = \frac{u_{i+1}^n - 2u_i^n + u_{i-1}^n}{(\Delta x)^2} \quad (1.45)$$

where the subscripts indicate the points in the spatial grid and the superscripts indicate the considered time step. The truncation error is  $o[\Delta t, (\Delta x)^2]$ .

The method to solve the equation takes the form of *marching solution* in step of time: the dependent variable at time  $t + \Delta t$  can be obtained **explicitly** directly from the known values at time  $t$ .

On the other hand, an implicit method consists in writing the equation in the Crank-Nicolson form: the spatial derivatives are calculated as average properties between the times  $n$  and  $(n + 1)$ .

$$\frac{u_i^{n+1} - u_i^n}{\Delta t} = \frac{1}{2} \frac{u_{i+1}^{n+1} + u_{i+1}^n - 2u_i^{n+1} - 2u_i^n + u_{i-1}^{n+1} + u_{i-1}^n}{(\Delta x)^2} \quad (1.46)$$

The unknowns at time  $n + 1$  are expressed not only in terms of the quantities at the previous time  $n$  but also in terms at time  $n + 1$ . Hence, a system of equations for every point of the grid to be solved simultaneously has to be implemented in order to obtain the solution for time  $n + 1$ . This represents the **implicit** finite difference solution.

The advantages and disadvantages of implicit and explicit methods can be summarized as:

**Explicit methods:**

- Advantages: simple to set up and program;
- Disadvantages: for a given  $\Delta x$ ,  $\Delta t$  must be less than limit imposed by stability constrains.

**Implicit methods:**

- Advantages: stability maintained over larger values of  $\Delta t$ . Hence, fewer time steps are needed to make calculations;
- Disadvantages: more complicated to set up and program. The matrix manipulation involves larger computer time per time step. Larger  $\Delta t$  implicates larger truncation errors.

## 1.10 CFD for Rotating Machines

A rotating machine such as a wind turbine, a pump or a water turbine could be evaluated with a Computational Fluid Dynamics analysis using different approaches, depending on the adopted time dependency, grid structure and computational domain features. As example, Table 1.2 highlights the most important solvers and strategies used in OpenFOAM.

	<b>Rotating regions only</b>	<b>Stationary and rotating regions</b>
<b>Steady</b>	SRFSimpleFoam	simpleFoam + fvOptions
<b>Transient</b>	SRFPimpleFoam	pimpleDyMFoam

**Table 1.2:** OpenFOAM solvers and options for rotating machines

### 1.10.1 Multi Reference Frame Model

The **Multiple Reference Frame** model (MRF) represents one of the most used approaches in order to set a fluid dynamic analysis of a rotating machine. The computational domain is divided in rotating

and stationary regions; the flow in moving zones is solved using the moving reference frame equations, while the stationary equation ( $\omega = 0$ ) is used for the stationary zone. At the interface zone, the fluxes are calculated using a local reference frame transformation. The equation for the rotating frame has to take into account the centripetal and the Coriolis forces [13]. As illustrated in Figure 1.6, a reference system is rotating steadily with angular velocity  $\omega$  relative to a stationary (inertial) reference frame.

The fluid velocities can be transformed from the stationary frame to the rotating frame using the relations between the velocities:

- Absolute velocity:  $\vec{v}$
- Relative velocity:  $\vec{v}_r = \vec{v} - \vec{u}_r$
- Whirl velocity:  $\vec{u}_r = \vec{\omega} \times \vec{r}$

where  $\vec{\omega}$  is the rotational axis and  $\vec{r}$  represents the position of a rotating point.

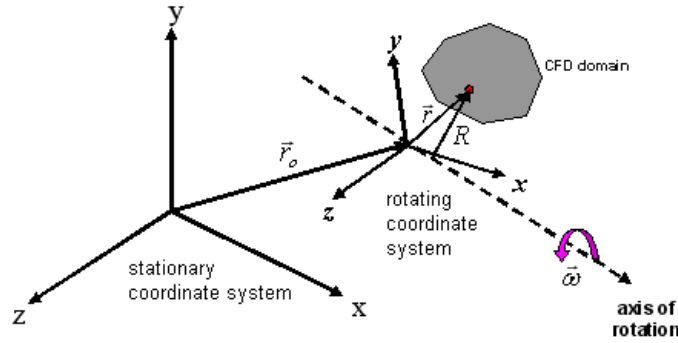


Figure 1.6: Stationary and Rotating Reference Frames

Once the equation of motion is determined in the rotating reference frame, additional terms appear for the acceleration in the momentum equations. This leads to two different formulations, the relative and the absolute velocity formulations.

### 1.10.2 Relative Velocity Formulation

In the relative velocity formulation, the momentum equations are expressed using the relative velocities as dependent variables. The governing equations of fluid flow for a steadily rotating frame are:

- Conservation of mass:  $\frac{\partial \rho}{\partial t} + \text{div}(\rho u) = 0$
- Momentum equation:  $\frac{\partial(\rho \vec{v}_r)}{\partial t} + \text{div}(\rho \vec{v}_r \vec{v}_r) + \rho(2\vec{\omega} \times \vec{v}_r + \vec{\omega} \times \vec{\omega} \times \vec{r}) = -\text{div}(p) + \text{div}(\tau_r) + \vec{F}$
- Conservation of energy:  $\frac{\partial(\rho E_r)}{\partial t} + \text{div}(\rho \vec{v}_r H_r) = \text{div}(k * \text{div}(T) + \tau_r * \vec{v}_r) + S_h$

As can be noticed, the momentum equation contains two additional acceleration terms: the Coriolis acceleration ( $2\vec{\omega} \times \vec{v}_r$ ) and the centripetal acceleration ( $\vec{\omega} \times \vec{\omega} \times \vec{r}$ ). In the formulation of  $\tau_r$  the relative velocity derivatives are used.

### 1.10.3 Absolute Velocity Formulation

In the absolute velocity formulation, the momentum equations is expressed using the absolute velocities as dependent variables. The governing equations of fluid flow for a steadily rotating frame are:

- Conservation of mass:  $\frac{\partial \rho}{\partial t} + \text{div}(\rho \vec{u}) = 0$
- Momentum equation:  $\frac{\partial(\rho \vec{v}_r)}{\partial t} + \text{div}(\rho \vec{v}_r \vec{v}) + \rho(\vec{\omega} \times \vec{v}) = -\text{div}(p) + \text{div}(\tau) + \vec{F}$
- Conservation of energy:  $\frac{\partial(\rho E)}{\partial t} + \text{div}(\rho \vec{v}_r H + \rho \vec{u}_r) = \text{div}(k * \text{div}(T) + \tau * \vec{v}) + S_h$

where the Coriolis and centripetal accelerations have been collapsed into a single term ( $\vec{\omega} \times \vec{v}$ ).

### 1.10.4 MRF Domains and Limitations

The Multiple Reference Frame model is often referred to as the *frozen rotor approach*. The method does not account for the relative motion of a moving zone with respect to adjacent zones and the grid remains fixed for the computation. In Figure 1.7 an example of a MRF typical domain is presented: the impeller is inside the rotating zone, while a stationary frame is used to model the fluid outside. The flow conditions are assumed to be steady-state at the interface between the two reference frames: the absolute velocity must be the same and the grid does not move.

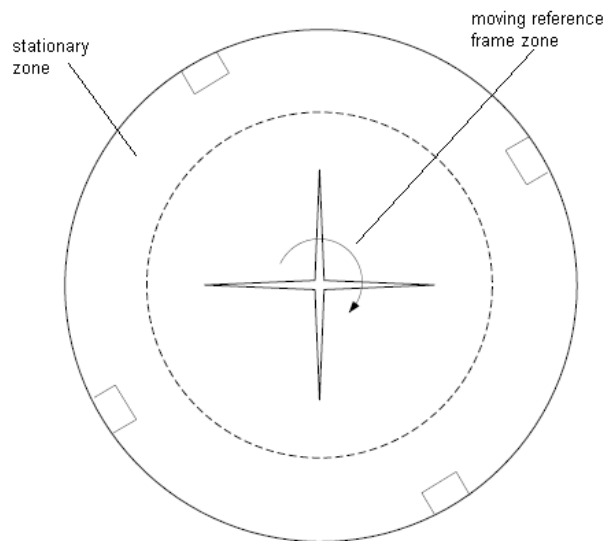


**Figure 1.7:** MRF, stationary and rotating zones

However, the MRF approach presents some limitations. The most important are: the component of the frame velocity normal to the boundary has to be zero (i.e. the interface has to be circular or parallel to the velocity vector), the use of multiple reference frames is meaningful only for steady flow and the translational and rotational velocities are assumed to be constant in time.





## Chapter 2

# The Open Source Codes

The present chapter aims to provide a brief description of the open source codes used in the thesis and an overview on the general licence condition for their use, development and distribution. Nowadays, several types of free licence are available, the most important are represented by the GNU GPL v3 and the GNU LGPL licences. Figure 2.1 shows an overview on the different licence compatibilities.

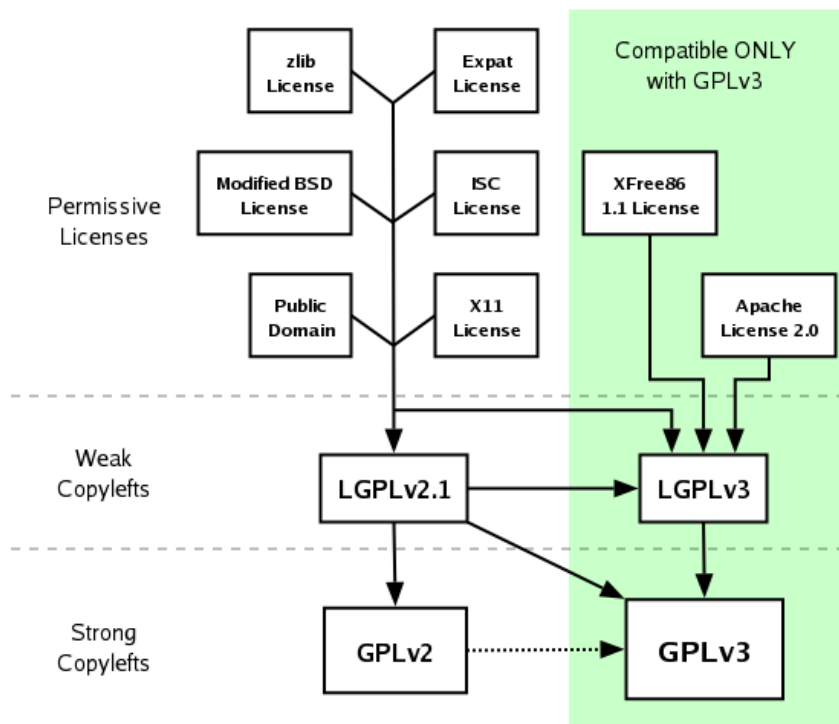


Figure 2.1: License compatibilities

## 2.1 Free Software Foundation

The Free Software Foundation (FSF) [14] is a non-profit organization founded by Richard Stallman in the 1985 to support the free software movement, which promotes the universal freedom to study, distribute, create and modify computer software. The FSF was incorporated in Massachusetts, USA, where it is also based. From its founding until the mid-1990s, FSF's resources were mostly used to employ software developers to write free software for the GNU Project. Since the mid-1990s, the FSF's employees and volunteers have mostly worked on legal and structural issues for the free software movement and the free software community.

## 2.2 GNU General Public License

The Free Software Foundation [14] is the author of the *GNU General Public License*. The conditions for the use and distribution of a code under these conditions are reported in the GNU website [15]. The GNU license is a copy-left for the free codes, introduced by Richard Stallman in the 1989 [16] as a licence for the codes of the GNU operative systems. Differently to the common copyright licence, the GPL has to remain free in all its distributions and modifications and has to guarantee the four essential freedoms [17]:

- **Freedom 0:** to run the program as one wish, for any purpose.
- **Freedom 1:** to study how the program works, and change it so it does the computing as one wish. Access to the source code is a precondition for this.
- **Freedom 2:** to redistribute copies so one can help his neighbour.
- **Freedom 3:** to distribute copies of a modified version to others. By doing this one can give the whole community a chance to benefit from the implemented changes. Access to the source code is a precondition for this.



Figure 2.2: GPLv3 logo.

### 2.2.1 GNU GPLv3 Terms and Conditions

The terms and conditions of the GPL must be made available to anybody receiving a copy of the work that has a GPL applied to it (the licensee). Any licensee who adheres to the terms and conditions is given permission to modify the work, as well as to copy and redistribute the work or any derivative version.

The licensee is allowed to charge a fee for this service, or do this free of charge. This latter point distinguishes the GPL from software licenses that prevent the commercial redistribution. The FSF argues that free software should not place restrictions on commercial use, and the GPL explicitly states that GPL works may be sold at any price. The GPL additionally states that a distributor may not impose *further restrictions on the rights granted by the GPL*. This forbids activities such as distributing of the software under a non-disclosure agreement or contract.

The programs distributed as pre-compiled binaries are required to be accompanied by a copy of the source code, a written offer to distribute the source code via the same mechanism as the pre-compiled binary, or the written offer to obtain the source code that the user got when they received the pre-compiled binary under the GPL.

Version 3 of the license allows making the source code available in additional ways including downloading source code from an adjacent network server or by peer-to-peer transmission.

The FSF does not hold the copyright for a work released under the GPL, unless an author explicitly assigns copyrights to the FSF. Only the individual copyright holders have the authority to sue when a license violation takes place.

### 2.2.2 Use of Licensed Software

The GPL software may be run for all purposes, including commercial purposes and even as a tool for creating proprietary software (using GPL-licensed compilers).

Users or companies, who distribute GPL-licensed works (e.g. software), may charge a fee for copies or give them free of charge: in order to non restrict the commercial use, distribution and redistribution, the GPL explicitly states that GPL works may be sold at any price. In purely private use, the software code may be modified and parts reused without requiring the source code to be released. For sales or distribution, the entire source code needs to be made available to end users, including any code changes and additions. In that case, copyleft is applied. However, software running as an application program under a GPL-licensed operating system such as Linux, is not required to be licensed under GPL or to be distributed with source-code availability

## 2.3 GNU Lesser General Public License

The conditions for the use and distribution of a code under the GNU *Lesser General Public License* are reported in the GNU website [18]. The GNU *Lesser General Public License* (LGPL) has been introduced by the Free Software Foundation in the 1991. It has been created to have a weaker copy-left than the GPL, in that it does not require own custom-developed source code to be made available under the same license terms.



Figure 2.3: LGPLv3 logo.

### 2.3.1 GNU LGPL Terms and Conditions

The only requirement of a software under LGPL is to be modifiable by end users via source code availability. For proprietary software, code under the LGPL is usually used in the form of a shared library such as a DLL, so that there is a clear separation between the proprietary and LGPL components. The LGPL is primarily used for software libraries, although it is also used by some stand-alone applications.

Differently from the GPL, the LGPL allows the work to be linked with a non-(L)GPLed program, regardless of whether it is free software or proprietary software. The non-(L)GPLed program can also be distributed under any terms if it is not a derivative work. For the derivative work, the program's terms must allow the *modification for the customer's own use and reverse engineering for debugging such modifications*. A standalone executable that dynamically links to a library through a '.so', '.dll' or similar medium is generally accepted as not being a derivative work as defined by the LGPL and it would fit the definition of a *work that uses the Library*. Essentially, if it is a *work that uses the library*, then it must be possible for the software to be linked with a newer version of the LGPL-covered program. The most commonly used method for doing so is to use a *suitable shared library mechanism for linking*.

## 2.4 The 3-Clause BSD License

As reported in [19], in a code with the BSD license, the redistribution and use in source and binary forms, with or without modification, are permitted when the following three conditions are met:

- Redistributions of source code must retain the above copyright notice, this list of conditions and the following disclaimer;
- Redistributions in binary form must reproduce the above copyright notice, this list of conditions and the following disclaimer in the documentation and/or other materials provided with the distribution;
- Neither the name of the copyright holder nor the names of its contributors may be used to endorse or promote products derived from this software without specific prior written permission.

## 2.5 XFOIL

XFOIL represents one of the main and well-known tools for the design and analysis of subsonic isolated airfoils. The code has been developed at MIT by Drela [20] and it has been presented in 1986. It consists of a collection of several routines for the analysis in inviscid and viscous conditions.



**Figure 2.4:** The logo of XFOIL.

As reported in the official web site [21], the most important functions are:

- Viscous (or inviscid) analysis of an existing airfoil. It allows forced or free transition, lift and drag predictions, Karman-Tsien compressibility correction and fixed or varying Reynolds and/or Mach numbers;
- Airfoil design and redesign by interactive modification of surface speed distributions in two methods: full-inverse method and mixed-inverse method;
- Airfoil redesign by interactive modification of geometric parameters such as max thickness and camber, highpoint position, LE radius, TE thickness, camber line via geometry specification, camber line via loading change specification, flap deflection, explicit contour geometry;
- Blending of airfoils;
- Writing and reading of airfoil coordinates and polar save files
- Plotting of geometry, pressure distributions and multiple polars.

XFOIL is released under the GNU General Public License (GPL) [15] and it can be copied, modified and redistributed freely under the terms of the GPL. XFOIL uses a potential flow panel method, which makes faster and more efficient the analysis of an airfoil compared to a CFD simulation; this characteristic is a great advantage and makes it a suitable toolbox for the integration in an optimization loop.

In the presented analysis of the thesis, XFOIL has been mainly used for the evaluation of the polars ( $C_L$ ,  $C_D$  and  $C_M$ ) of the parametrized airfoils. Inputs of XFOIL are mainly represented by the point coordinates of an aerodynamic profile, the flow conditions such as Reynolds number and the range of angles of attack that have to be analysed. The code iterates until it converges on an airfoil surface and it computes the airfoil characteristics: aerodynamic polars, boundary layer characteristics and the pressure distribution.

## 2.6 RFOIL

RFOIL is a code based on XFOIL, which has been modified by a consortium of ECN [22], NLR and TU Delft [23]. Later, ECN has acquired the RFOIL code and, after 1996, maintained and improved the tool.



**Figure 2.5:** The logo of ECN.

The code shows better correlation with experimental results, particularly around stall; for this reason, it has been chosen to use RFOIL over XFOIL for the presented analysis, where the stall behaviour has a non-negligible effect in the overall performance of the considered turbine.

The original XFOIL code is not able to predict the airfoil performances over a large range of angles of attack in the stall zone and it usually breaks down in the post stall region. RFOIL introduced improvements of the numerical stability of the code using adjustments of some closure relations for the turbulent boundary layer formulations, as reported in [24]. This leads to an improved prediction for the maximum lift coefficient and to the inclusion of a method for predicting the effect of rotation on the airfoil characteristics, allowing the phenomenon of stall delay to be incorporated into its output. The numerical stability improvements in the maximum lift calculation were obtained by using the

Schlichting velocity profiles [25] for the turbulent boundary layer, instead of Swafford’s velocity profiles incorporated in XFOIL. The last version of XFOIL and RFOIL codes includes also an improved formulation of drag estimation for thick airfoils. A comparison between the codes with experimental data and results from commercial CFD methods is presented in [26]: the improved version of RFOIL demonstrates a good agreement with experimental data. The advantages in using RFOIL are the same of XFOIL (panel codes have an high-order accuracy and they faster than any CFD tool), in addition, it better predict the airfoil performances when stall phenomena occurs.

## 2.7 Dakota

Dakota (Figure 2.6) is an open source toolkit developed by SANDIA and it contains algorithms for the design exploration and the simulation credibility. As reported in the official website [27], Dakota provides an interface between external analysis code and the iterative systems analysis methods.

The most important algorithms concern:

- Optimization with gradient and non-gradient-based methods;
- Uncertainty quantification with sampling, reliability, stochastic expansion, and epistemic methods;
- Parameter estimation with non-linear least squares methods;
- Sensitivity and variance analysis with design of experiments and parameter study methods.

The capabilities may be used on their own or as components within advanced strategies such as hybrid optimization, surrogate-based optimization, mixed integer non-linear programming, or optimization under uncertainty.



**Figure 2.6:** The logo of Dakota.

Dakota is particular suitable to lead an optimization with computational methods developed in structural mechanics, heat transfer, fluid mechanics, shock physics and many other fields of engineering. Written in C++, the Dakota tool kit is intended as a flexible, extensible interface between simulation codes and a variety of iterative systems analysis methods, including optimization, uncertainty quantification, non-linear least squares methods and sensitivity-variance analysis.



Dakota tool-kit is available under a GNU Lesser General Public License (LGPL) [18] since the version 5.0; versions 3.0 through 4.2+ are available under a GNU General Public License (GPL)[15] .

The advantages in using Dakota, compared to other commercial optimization tools, are represented by the capabilities in building blocks within more sophisticated strategies such as hybrid optimization, surrogate-based optimization, mixed integer nonlinear programming, or optimization under uncertainty. Dakota can be easily coupled with any engineering tool and in-house code (it support all the most important programming language).

### 2.7.1 MOGA Algorithm

MOGA (Multi-Objective Genetic Algorithm) represents the evolutionary algorithm included in Dakota for the multi-objective optimization analysis. MOGA is one of the two global optimization methods included in the JEGA library [28]: it performs Pareto optimization and it supports general constraints and a mixture of real and discrete variables. The basic steps of MOGA algorithm are represented by the common procedures of the genetic algorithms, as reported in the Dakota Reference Manual [29]:

1. Initialize the population;
2. Evaluate the population;
3. Loop until converged or stopping criteria reached:
  - (a) Perform crossover;
  - (b) Perform mutation;
  - (c) Evaluate the new population;
  - (d) Assess the fitness of each member in the population;
  - (e) Replace the population with members selected to continue in the next generation;
  - (f) Apply niche pressure to the population;
  - (g) Test for convergence.
4. Perform post processing.

Further information on how to set an optimization with MOGA algorithm are given in Appendix D.

## 2.8 OpenFOAM

OpenFOAM (acronym for Open Field Operation and Manipulation) represents the most important open source CFD code, based on the Finite Volume Method (FVM). The first OpenFOAM version (1.0) has been released in December 2004 by OpenCFD Ltd. In the year 2011 OpenCFD has been acquired by the Silicon Graphics International (SGI) and the OpenFOAM Foundation was created. In 2012 OpenCFD became a part of the ESI Group and, from 2016, OpenCFD has released OpenFOAM directly once again, since from the release of OpenFOAM v3.0+.



**Figure 2.7:** The logo of OpenFOAM.

The sources of OpenFOAM are freely available at the official web site [30] under the GNU General Public License (see Section 2.2). OpenCFD has chosen to distribute OpenFOAM under GPL license mainly for the following reasons:

- To create a wide user community in order to quickly identify and correct the bugs in the code, to improve the efficiency and the validation of the numerical results and to complete the documentation and the test-case database;
- To facilitate the development of the code: the experiences and the new functionalities implemented by the single users can be shared to the community and extended to a great number of applications.

OpenFOAM is developed in C++ and, in order to maximize the computational efficiency, several parts of the code and the basic libraries are continuously tested and updated with the new features of the C++ language. In addition, in order to manage the architecture of the code in a flexible way, a `wmake` routine is implemented as a bash script. OpenFOAM is actually composed by a series of solvers for the numerical solution of the several cases, libraries for the common operations, utilities for the incidental operations and a choice of numerical schemes. Furthermore, OpenFOAM includes two meshing tools (BlockMesh and SnappyHexMesh) and a post-processing environment (ParaFOAM). The main structure of OpenFOAM is shown in Figure 2.9.

OpenFOAM is organized as a set of different folders and files where the setting of the desired analysis has to be specified, as shown in Figure 2.8. The main folders of a typical OpenFOAM case are:

- **system:** in this folder, the files *controlDict* (definitions of the temporal options, iteration number, output values), *fvSchemes* (definition of the numerical schemes to be used) and *fvSolution* (definition of numerical solver for the system of equations) are defined. Other dictionary files could be also specified in order to run a specific analysis (*decomposeParDict*, *fvOptions*, etc...);
- **constant:** the folder contains the mesh files (inside the *polyMesh* sub-folder), the specifications of the thermodynamic and transport properties of the fluid and the turbulence model to be used;
- **0:** the folder contains the initial condition for the variables to be used in the analysis (U, p, T, k, omega, epsilon, ..);
- **1,2,3..:** other folders with the same structure of the 0 folder are automatic created during the analysis: they contain the results of the simulation at the specified iteration/timestep.



Figure 2.8: OpenFOAM folder structure

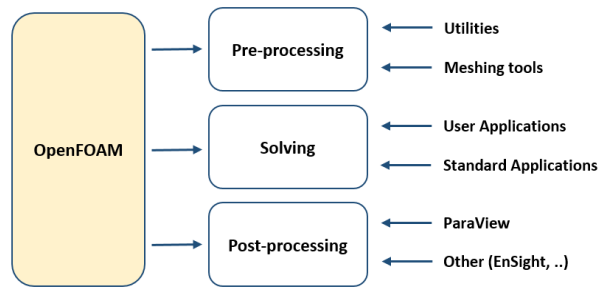


Figure 2.9: Overview of the OpenFOAM structure

### 2.8.1 OpenFOAM Solvers

In the topics covered by the thesis, several OpenFOAM solvers have been tested. In the present section, the main features of the used solver are summarized:

- **rhoSimplecFoam:** *Steady-state SIMPLE solver for laminar or turbulent RANS flow of compressible fluids.*

This solver is included in OpenFOAM since the version 1.7 and some controls have been added in order to increase the convergence of the solution (e.g. the definition of  $\rho_{Min}$  and  $\rho_{Max}$ ). The required files have to be defined in the folder *0* (the variables  $p$ ,  $U$ ,  $T$ ), in the folder *constant* (turbulence parameters in the files *RASProperties*, *thermophysicalProperties*, *transportProperties* and *turbulenceProperties*) and in the folder *system* (the *controlDict*, *fvSchemes*, *fvSolution* and *decomposeParDict* files). The *fvOptions* file is also defined to deactivate the energy equation for the first iterations in order to improve the stability of the solution.

- **simplecFoam:** *Steady-state solver for incompressible, turbulent flow, using the SIMPLE algorithm.*

This solver is one of the most common in OpenFOAM; it has been tested in combination with the *fvOption* file specification in order to simulate a rotating machine in a Multiple Reference Frame (MRF) analysis. In *fvOption*, the rotating zone of the fluid is indicated by specifying the rotational velocity, the rotational axis and the origin of the rotational system.

- **pimpleDyMFoam:** *Transient solver for incompressible, turbulent flow of Newtonian fluids on a moving mesh.*

The solver is used for the unsteady analysis with a moving mesh technique in OpenFOAM; the *dynamicMeshDict* file has to be specified in the constant folder: it contains the specification of the rotational zones, the centre, axis and speed of rotation. The *createPatchDict* files is required inside the system folder in order to couple the interfaces between the moving stationary meshes.

The advantages in using OpenFOAM, compared to the other commercial CFD software, are firstly represented by the open-access code: its C++ language is easy to modify and every feature can be customised according to analysed problems. Furthermore, OpenFOAM presents good unstructured polyhedral grid capabilities and the automatic parallelization of applications. Finally, the code is provided with a wide range of applications and models ready to use and, most important, it has not license costs.

## 2.9 SALOME

SALOME represents one of the most important open source CAE platforms and it is released under the LGPL license, Section 2.3, from the official web site [31]. SALOME provides a complete environment for the pre and post-processing for numerical simulations.



**Figure 2.10:** The logo of SALOME.

SALOME has been created from the integration and collaboration of 9 industrial software developed by high technology French engineering companies:

- OPEN CASCADE
- CEA
- EDF
- EADS
- Bureau Veritas
- Principia
- Cedrat
- LIP6
- LEG

The most important features of SALOME are the support of the interoperability between CAD modelling and computation software, the possibility of integrate new components on heterogeneous

systems for numerical computation and the multi-physics coupling between computation software. Furthermore, the user-friendly graphical interface helps to reduce the costs and delays of carrying out the studies and the training time for learning the software solution, which has been based on the platform. Finally, the functionalities are accessible through the programmatic integrated Python console; this allows to set up the CAD generation and the meshing phase using appropriate shell scripts and to integrate SALOME in the proposed optimization environment. In the current thesis SALOME has been adopted in Chapter 9 as open source tool for both the parametric CAD definition (OPEN CASCADE Libraries) and the generation of the meshes through the its meshing tools.

As explained, SALOME has a great potential and it provides all the geometrical tools needed to generate a simple solid model and to mesh an object. SALOME has mainly be chosen for the possibility to script every operation using an high level programming language; this characteristic made SALOME suitable for the integration in an optimization loop. However, in the opinion of the author of the thesis, SALOME is still not a mature product. Many routines are unstable (e.g. the creation of a loft through many splines, the boundary layer generation) and it do not still provide all the useful geometric features of a commercial CAD software.

## 2.10 ParaView

ParaView is a multiple-platform application for interactive, scientific visualization and it can be downloaded from the official web site [32]. It represents one of the most popular open source tools for the pre and post-processing analysis; it uses a permissive BSD license 2.4 that enables the broadest possible audience, including commercial organizations, to use the software, royalty free for most purposes. The ParaView project started in 2000 with the collaboration between Kitware, Inc. and Los Alamos National Laboratory; the first version was released in October 2002. In January 2016 the version 5 of ParaView has been released and it includes a new rendering back-end.



**Figure 2.11:** The logo of ParaView.

ParaView is an application based on the Visualization Toolkit (VTK) libraries [33]. It is designed for data parallelism on shared-memory or distributed-memory multicomputers and clusters; however it can also be run as a single-computer application.

The goals of the ParaView team can be summarized in:

- Develop an open-source, multi-platform visualization application;
- Support distributed computation models to process large data sets;
- Create an open, flexible, and intuitive user interface;
- Develop an extensible architecture based on open standards;

The components of the ParaView code are designed in order to be reused to quickly develop vertical applications; this flexibility allows ParaView developers to quickly develop applications that have specific functionality for a specific problem domain. ParaView is fully scriptable using the Python language and it can be run as a batch application using the Python interface. Furthermore, Python Programmable Filters with NumPy and SciPy can be implemented. The filters can be defined in an easy manner. Furthermore, ParaView works reliably also in parallel mode.

All these features represent a great advantage in using ParaView compared to other post-processing tools and they make ParaView particularly well suited for the post-processing operations of the proposed open source optimization environment.

## Chapter 3

# Validation of a compressible CFD model for an external aerodynamic analysis

In the present Chapter, an external aerodynamic analysis is presented in order to reproduce the performances of a tiltrotor, in wind tunnel conditions. The case study, represented by the ERICA tilt rotor, has been tested in wind tunnel during the WP2 of the DREAM-tilt project, task 2.2 *Blind test assessment via CFD simulations of both the baseline and optimized tiltrotor geometry in wind tunnel flow conditions*, [4].

Specifically, the work aims to validate the numerical model of the ERICA tiltrotor fuselage using the open-source CFD code OpenFOAM. The results of the analysis are compared with both experimental and numerical data coming out from the fluid dynamic simulations, performed using the commercial software ANSYS Fluent and reported in [34]. The results are presented in terms of global aerodynamic coefficients, flow distortion, total pressure losses and flow separation. The calculated velocity and vorticity fields are also illustrated for both ANSYS Fluent and OpenFOAM analysis and compared with the PIV experimental data.



### 3.1 Reference Values and Moment Center

In order to calculate the performances of the tiltrotor, the adopted aerodynamic coefficients formulation is:

- Lift coefficient, positive upwards

$$C_L = \frac{L}{1/2\rho V_\infty^2 A} \quad (3.1)$$

- Drag coefficient, positive rearwards

$$C_D = \frac{D}{1/2\rho V_\infty^2 A} \quad (3.2)$$

- Pitching moment coefficient, positive nose up

$$C_M = \frac{M_Y}{1/2\rho V_\infty^2 A c} \quad (3.3)$$

where  $L$  is the lift force,  $D$  is the Drag force,  $M_Y$  represents the pitching moment and  $V_\infty$  is the freestream velocity speed of the tiltrotor.

In the formulation the wing surface  $A$  and the wing aerodynamic mean chord  $c$  are used to normalize the values of forces and moments from the calculations. Furthermore, the intersection point between the fuselage symmetry plane and the rotation axis of the wings and nacelles determines the pitching moment centre (Figure 3.5). For the 1/8 scaled model of the ERICA tiltrotor, the values reported in Table 3.1 are used.

Parameter	Value
Area $A$	0.5780 $m^2$
Chord $c$	0.3034 $m$
x-coordinate moment centre	1.100 $m$
y-coordinate moment centre	0 $m$
z-coordinate moment centre	0.562 $m$

**Table 3.1:** Geometric reference values and pitching moment centre coordinates

## 3.2 Geometric Model

Seven main components determine the geometry of ERICA tiltrotor model, specifically the nose, the wing-fuselage junction, the wings and nacelles, the fuselage, the tail, the empennage and the sponsons. Figure 3.1 shows an isometric view of the different zones on which the surface is divided.

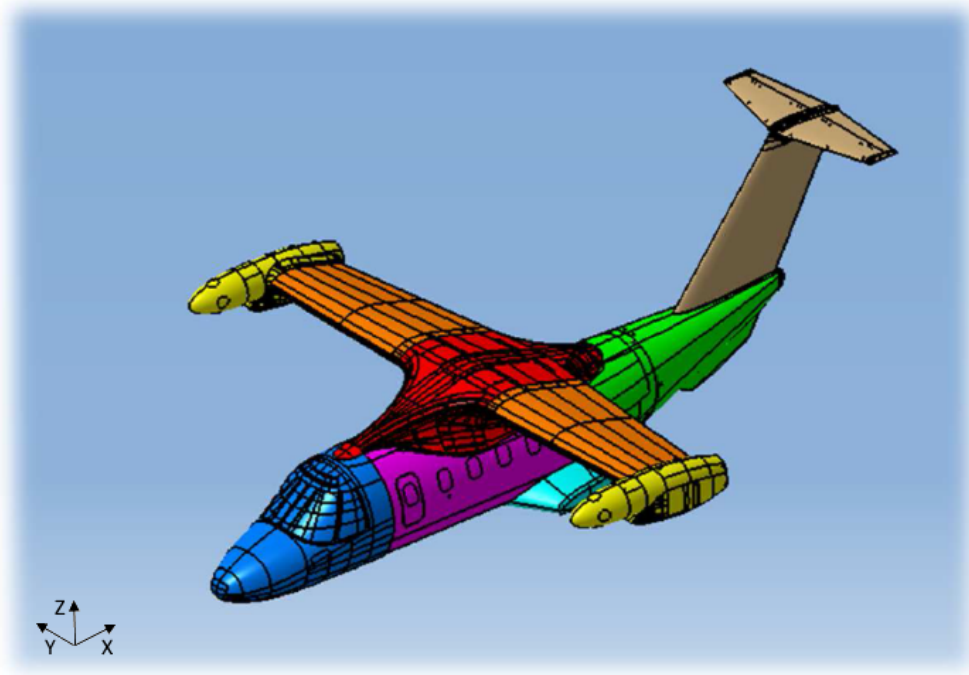


**Figure 3.1:** Subdivision of the tiltrotor surface in patches: nose (blue), fuselage (violet), wing-fuselage junction (red), wing and nacelle (orange and yellow), sponsons (cyan), tail (green), empennages (brown)

The symmetric geometry of the tiltrotor has allowed to compute only half of the aircraft model in the CFD simulation. The symmetry plane at a null sideslip angle has been used to considerably reduce the number of mesh elements and hence the total analysis time.

The wind tunnel model reproduces the cross-section shape and size provided by RUAG. The dimensions suggested by previous similar analysis have been adopted in the longitudinal direction: the fluid domain has been extended for 3 times aircraft length upstream and 6 times the aircraft length downstream the fuselage. Figure 3.2 shows an overall view of the wind tunnel model.

In order to obtain a more accurate analysis, the pylon for the support of the scaled aircraft in the wind tunnel has also been modelled. The support system constrains the tiltrotor model through a ventral connection: the pylon is connected at the bottom side of the fuselage. Figure 3.3 shows the CAD model provided by RUAG. However, some details of the original geometry have been simplified: several small surfaces and the wiring (green components of Figure 3.3) have been suppressed. Two

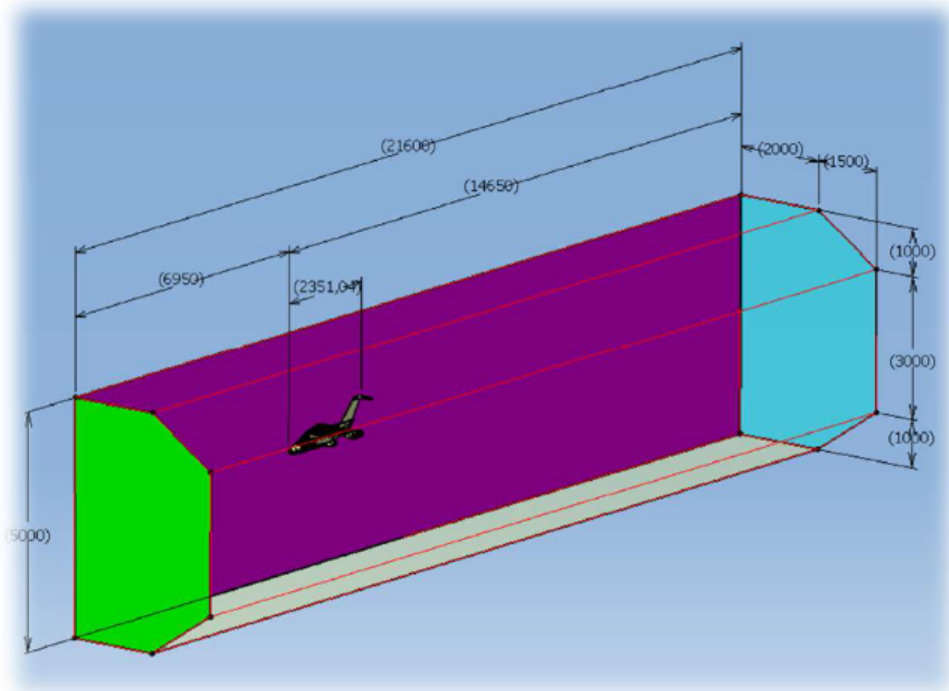


**Figure 3.2:** The bounding box represents the fluid domain of the wind tunnel. Surface subdivision: inlet (green), outlet (cyan), symmetry plane (violet), symmetry (yellow and missing surfaces)

main components determine the adopted model, the fixed pylon (coloured in cyan) connected to the tunnel ceiling and the movable portion of the pylon (coloured in red), that is directly connected to the aircraft through the main balance. The movable portion of the pylon can rotate through a hinge and the attitude of the tiltrotor can be varied in order to run different configurations.

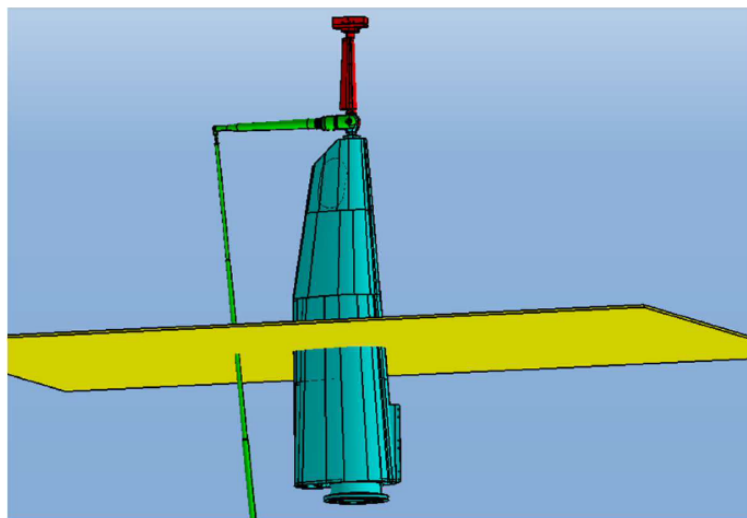


**Figure 3.3:** CAD model of the support system of the tiltrotor. Fixed pylon (cyan), rotating pylon (red), wiring (green) and tunnel floor (yellow)

To generate a better mesh, the surfaces of the junction connecting the fixed pylon to the rotating one have also been modified, as shown in Figure 3.4. All the existing gaps, holes and unnecessary features have been removed; the simplification has allowed to obtain a smoother junction.

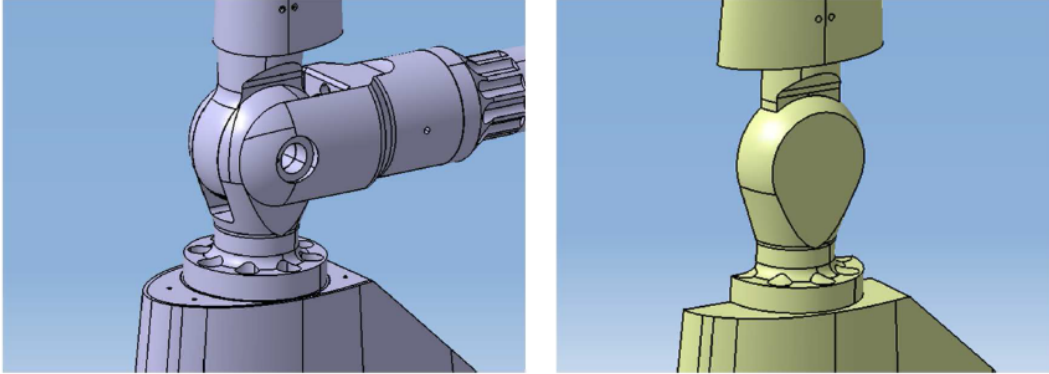


**Figure 3.4:** Comparison between the junction geometry provided by RUAG (on the left) and the simplified geometry for the meshing operations (on the right)

The most important characteristic points of the fuselage and sporting system are shown in Figure 3.5. The centre of the main balance with respect to the fuselage is represented by the point  $A$ , while the pitching moment centre  $C$  is located at the intersection of the wing rotation axis with the aircraft longitudinal symmetry plane.

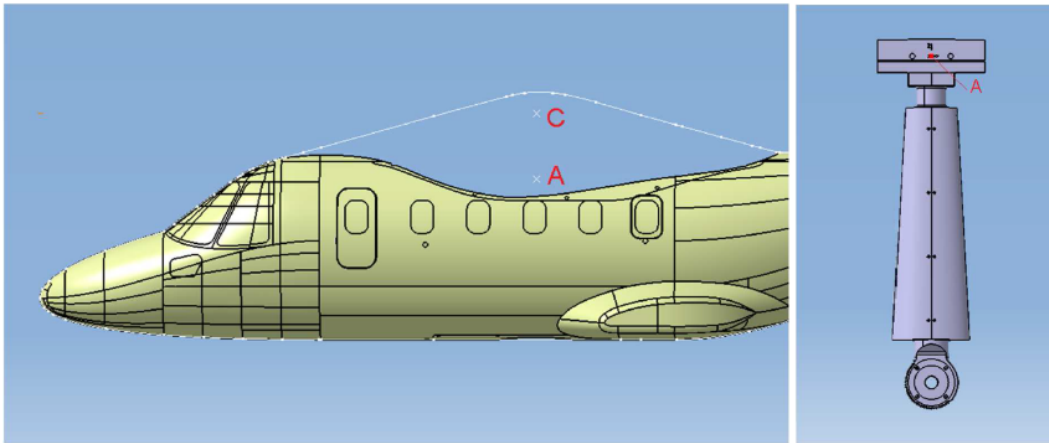


**Figure 3.5:** Characteristic points on the fuselage and support: main balance center ( $A$ ) and wing rotation axis centre ( $C$ )

In Figure 3.6 the whole geometry with the characteristic points is shown and the pitch attitude variation obtained through the hinge is displayed. The main balance centre (point  $A$ ) is located in the middle of the wind tunnel cross section (tunnel height is 5 m) when the incidence angle is null.

The non-incidence angle configurations are obtained by rotating the fuselage and only the moving portion of the pylon around the  $y$ -axis through the point  $R$  (Figure 3.6). The fixed portion of the

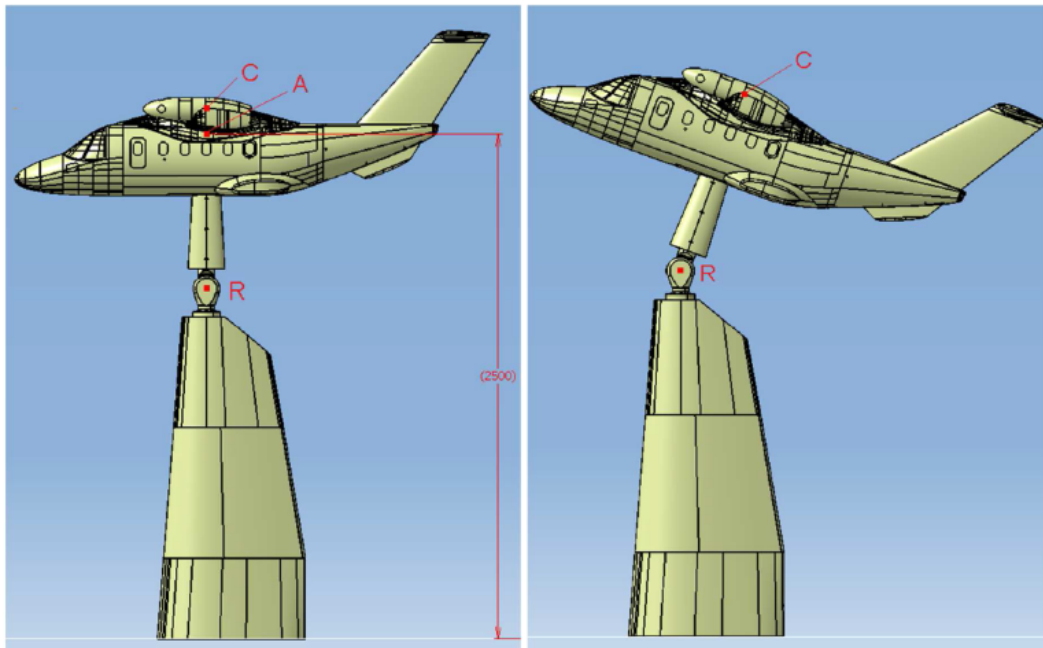


**Figure 3.6:** The whole geometry is composed by fuselage and ventral pylon. The configuration is shown at null pitch angle (on the left) and with non-null incidence angle (on the right)

pylon is connected to the ceiling in order to minimize interference effects. This structure hence allows to precisely reproduce the behaviour of the physical model in the real wind tunnel.

### 3.3 Mesh Setting

In the current section, the settings adopted to generate, first a 2D mesh on the tiltrotor surface and then the volume mesh, are described. The meshing software used in the present analysis is Altair Hypermesh V12.

#### 3.3.1 Surface Mesh Generation

In the work accomplished in [35], the superficial mesh over the fuselage was generated using the Advanced Meshing Tool (AMT) within CATIA. In the present work, however, the software used to carry out the mesh is Altair Hypermesh V12. After importing the CATIA CAD model in Hypermesh a further cleaning procedure on the geometry has been necessary in order to close all gaps and suppress unnecessary edges (Figure 3.7).

A tolerance equal to 0.1 mm has been used while gaps larger than tolerance have been already fixed in the geometry CAD model, as explained above. In order to facilitate and speed up the surface mesh generation some edges have been retained to subdivide each patch in more surfaces. The superficial mesh generated is similar to the mesh created in [35]; the used elements are first order triangle based of the linear type. Regarding the mesh evaluation, the adopted quality indicators are the cell aspect ratio and skewness; Table 3.2 specifies the recommended values for a satisfactory mesh quality.

	Optimal interval	Poor interval	Bad interval
<b>Skewness</b>	0 - 0.45	0.45 - 0.6	0.6 - 1
<b>Aspect Ratio</b>	1 - 2.5	2.5 - 5	5 +

**Table 3.2:** Quality parameters limits specified for ERICA surface mesh

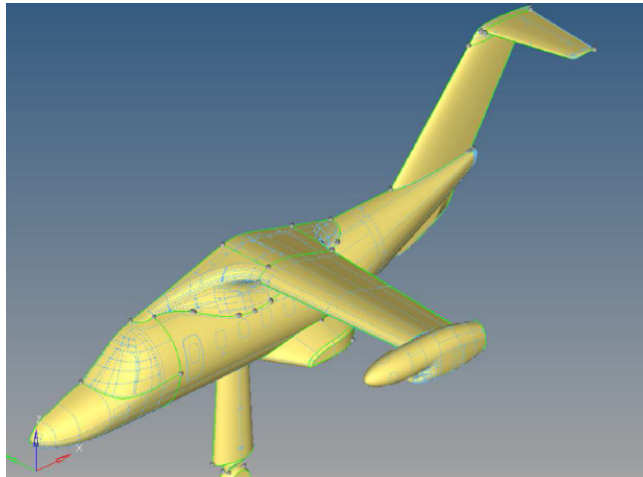


**Figure 3.7:** Imported and cleaned geometry of ERICA tiltrotor model. Active edges (green), and suppressed edges (blue, dashed)

As mentioned above, the supporting pylon has been also considered in the analysis and, therefore, a surface mesh has been created. A refined mesh has been adopted in the portion of pylon closer to the fuselage, insofar is expected that only this part would have some aerodynamic effects on the aircraft model. In order to limit the number of mesh elements not necessary for the simulations, the mesh grid gradually become coarse starting from the fuselage towards the wind tunnel ceiling. In this way, a better refinement has been possible around the aircraft. The surface was generated using the *surface deviation subpanel* present in the 2D automesh panel of Hypermesh. The values of the imposed parameters are summarized in Table 3.3, where all the surfaces are listed in order of surface mesh generation.

patch	el. size	growth rate	min el. size	max deviat.	max feature ang	mesh type
refinement surface 1-tail	0.7	1.10	0.7	0.1	10	trias-1st
refinement surface 2-tail	1	1.10	1	0.1	10	trias-1st
tail	1	1.10	1	0.1	10	trias-1st
wing-nacelle	5.5	1.10	1	0.04	10	trias-1st
w-f junction	5	1.10	1	0.08	10	trias-1st
empennage trailing edge	1	1.10	1	0.1	10	trias-1st
empennage	4	1.10	1	0.1	10	trias-1st
nose	5	1.10	1	0.1	10	trias-1st
fuselage	6	1.10	1	0.1	10	trias-1st
sponson	5	1.10	1	0.1	10	trias-1st
rot. pylon	10	1.23	8	0.1	10	trias-1st
fix. pylon	30	1.05	15	0.4	30	trias-1st
inner sym. plane	50	1.10	1	0.1	10	trias-1st
pylon shell	30	1.08	30	0.1	10	trias-1st
aircraft shell	50	1.05	30	1	40	trias-1st
inner ceiling	30	1.10	30	0.1	10	trias-1st
outer sym. plane	500	1.10	10	0.1	10	trias-1st
outer ceiling	500	1.10	10	0.1	10	trias-1st
outer wind tunnel surf.	500	1.10	10	0.1	10	trias-1st

**Table 3.3:** 2D automeshing settings for the parches of ERICA tiltrotor model

The worst elements, created through the surface mesh generation procedure, are located in the

trailing edge of the vertical empennage zone, as shown in Figure 3.8. However, the number of bad elements is very limited with respect to the total number of elements and their quality is not so poor, so they were considered not to significantly affect the reliability of the numerical model. Overall the quality of the superficial mesh is very satisfactory, as can be seen in the statistics of generated mesh, reported in Table 3.4.

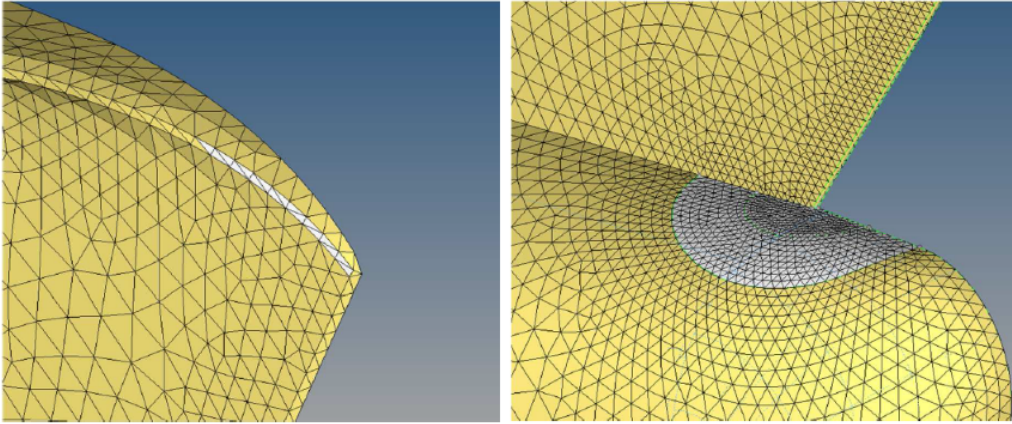


**Figure 3.8:** View of the surface mesh over the supporting pylon (on the left) and over the aircraft nacelle (on the right)

	<b>Total el.</b>	<b>Poor el.</b>	<b>Bad el.</b>	<b>Worst el.</b>	<b>% bad el.</b>
<b>Skewness</b>	483747	990	251	0.66	0.06%
<b>Aspect Ratio</b>	483747	242	0	3.19	0%

**Table 3.4:** Quality statistic of the superficial mesh on the baseline tiltrotor configuration

Further details of the surface mesh of supporting pylon and aircraft nacelle are shown in Figure 3.9.



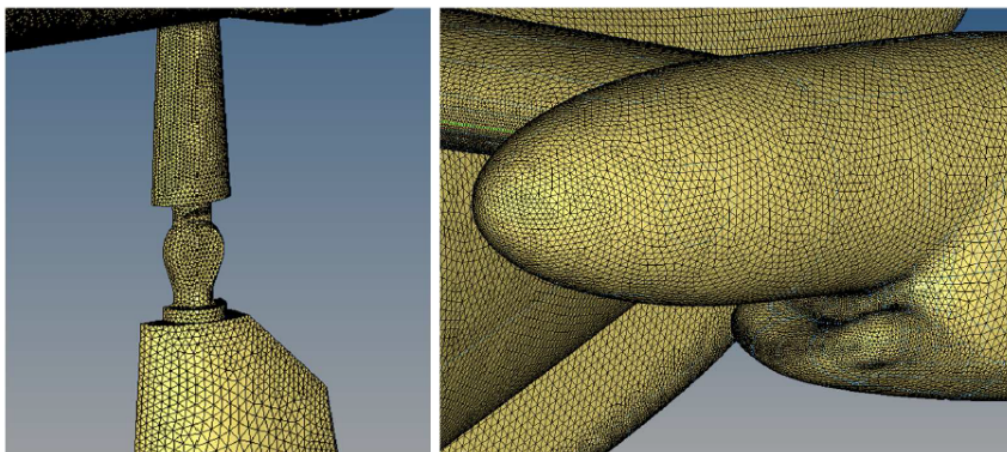


**Figure 3.9:** Detail of the empennage trailing edge worst surface elements (on the left) and closeup of the mesh refinement around the empennage-fuselage junction (on the right)

### 3.3.2 Volume Mesh Generation

The volume mesh has been generated starting from the surface mesh using Hypermesh V12. The CFD tetramesh subpanel allows to create the two types of elements needed for the simulation. The physic boundary layer around the wall surfaces of the aircraft and the pylon have been reproduced using structured elements (triangular based prismatic elements) while unstructured elements have been used in the rest of the fluid domain (tetrahedral elements).

The main parameters involved in the boundary layer structure are the the *growth rate*, the *total number of layers* and the *first cell height*. These parameters have been chosen based on the specifications in [35]. The first cell height has been fixed in order to obtain a  $y+$  value around 1 on the aircraft surface, ensuring an accurate resolution of the boundary layer. The only modification, compared to the mesh specified in [35], is the adopted number of layers: the software used for volume mesh did not easily handle a configuration where two different surfaces with boundary layer are facing, as it is the case for vertical tail and fuselage. The tool *BL reduction in automatic mode*, available in Hypermesh, was used to properly reduce the boundary layer thickness in the critical areas, avoiding cross-intersection of the structured volume mesh elements, as illustrated in Figure 3.10.

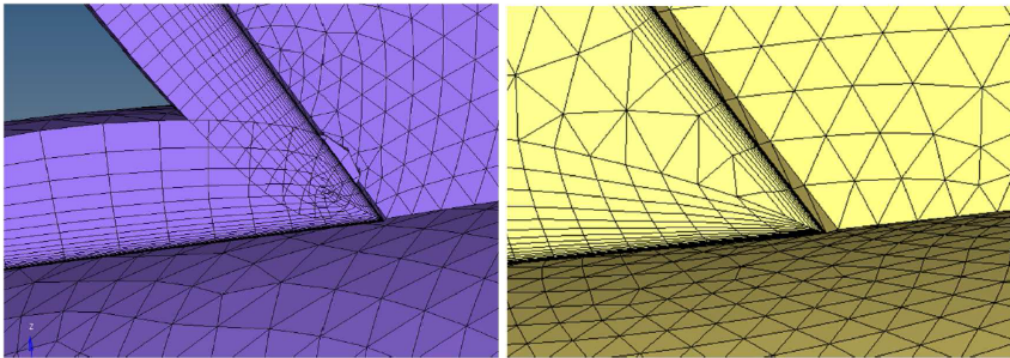


**Figure 3.10:** Prismatic mesh over the empennage-fuselage junction without BL correction (on the left) and after application of BL automatic reduction (on the right)

The fluid domain has been divided into two different zones: the first one is represented by a shell surrounding the tiltrotor fuselage while the volume of the outer space represents the second one. In order to ensure the continuity of the discretion, the two volumes have been meshed subsequently, keeping fixed the surface mesh of the shell. Different values for tetrahedral mesh growth rate inside the two regions have been adopted, allowing a better control of the tetrahedral mesh size around the aircraft. The elements were prevented to become too large near the fuselage by using a target size value for the inner volume. In a previous configuration an unique fluid volume was used, however the adoption of the two volumes has allowed a lower growth rate of the volumetric elements size and

limited the mesh size in the inner volume. In this way, it is possible to impose a growth rate in the box in addition to the target mesh size. From Figure 3.11 to Figure 3.14 a comparison between the volumetric mesh obtained in the two cases is shown, highlighting the beneficial effects of the refinement shell around the aircraft. Figure 3.11 shows a detail of the mesh near the horizontal tailplane, Figure 3.12 presents the wing mid-section region, while two comprehensive longitudinal sections of the mesh are depicted in Figures 3.13 and 3.14.

In particular, the volume mesh without shell presents a growth rate equal to 1.08, while that with the shell adopts an inner growth rate equal to 1.04 and a target mesh size equal to 50 mm. The values of those parameters were selected after several trials.

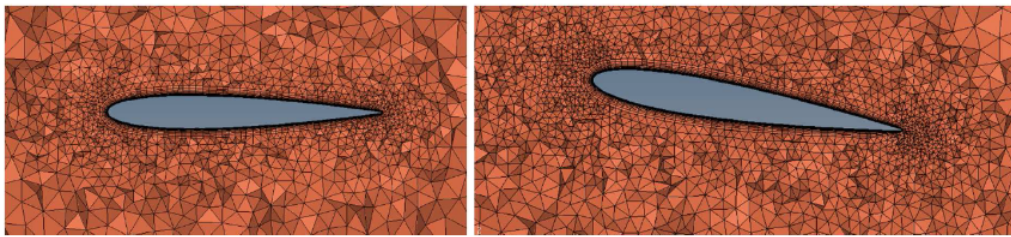


**Figure 3.11:** Close-up of the volume mesh near the horizontal tailplane: comparison of mesh obtained without (on the left) and with (on the right) the refinement shell

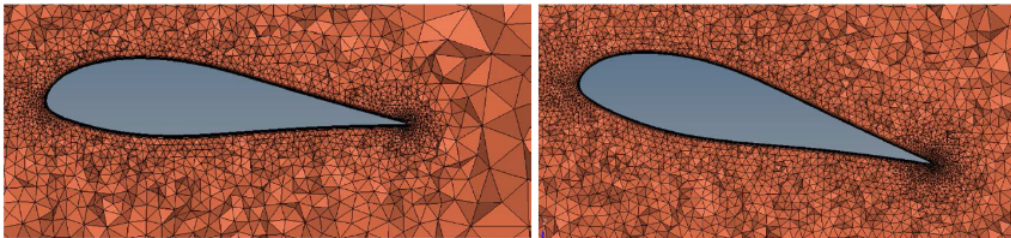


**Figure 3.12:** Close-up of the volume mesh near the mid wing: comparison of mesh obtained without (on the left) and with (on the right) the refinement shell

The adoption of the refinement shell to divide the fluid volume clearly increases the quality of the volumetric mesh and the found parameters for mesh control have been chosen for the final setting. Tables 3.5 and 3.6 list the final setting parameters, for both the inner and outer volume, used to generate the definite volume mesh. Two other parameters for the mesh generation have been left at their default values. The resulting mesh is composed by 16.2 M elements on half aircraft (6.1 M prismatic elements and 10.1 M tetrahedral elements). Finally, the model has been exported using the instructions for the specific CFD solver employed (ANSYS Fluent and OpenFoam), merging all fluid volumes in one single named fluid and renaming surfaces according to their boundary types (wall or symmetry).

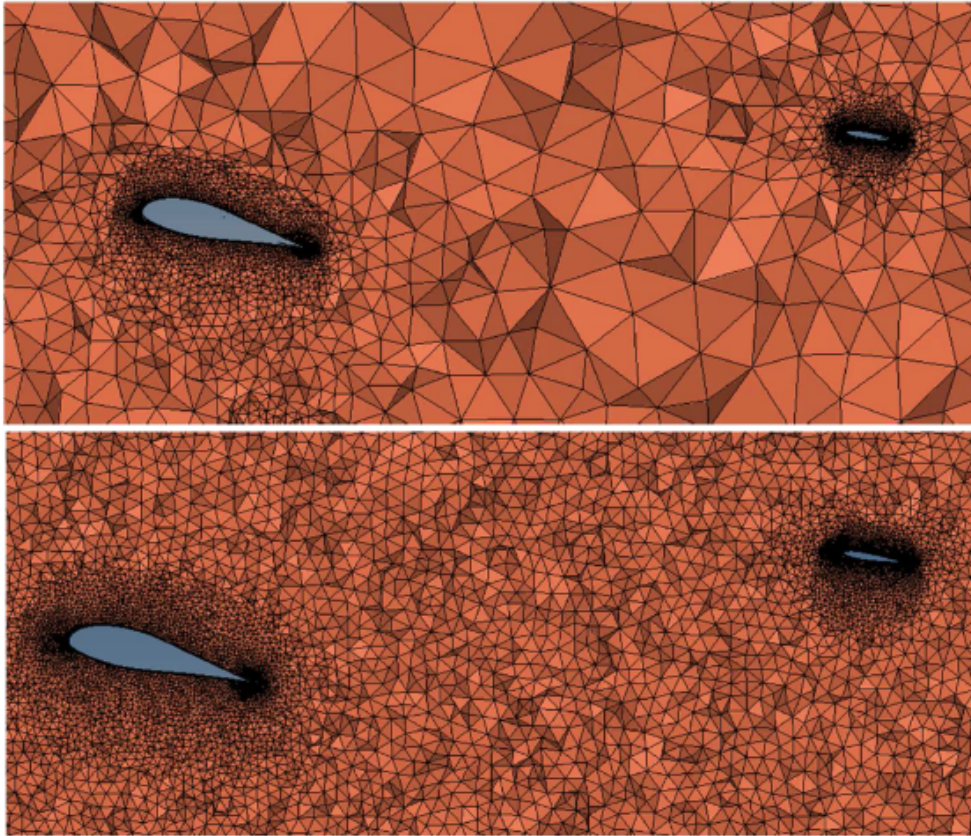


**Figure 3.13:** Longitudinal section of the volume mesh: comparison of mesh obtained without (on top) and with (on bottom) the refinement shell

<b>Boundary selection</b>	With BL (fixed)	fuselage, nose, sponson, junction, tail, wing-nacelle, empennage, pylons
	Without BL (float)	inner symmetry plane, inner ceiling, shell
<b>Boundary layer parameters</b>	Number of layers	18
	First layer thickness	0.01 mm
	BL growth rate	1.3
	Minimum thickness ratio	2
	BL thickness at corners	0.45
<b>Tetra mesh parameters</b>	Max tetra size	50 mm
	Optimized mesh quality	activated
	Uniform layers	1
	Growth rate	1.04
	Smooth BL	activated

**Table 3.5:** Mesh parameters for the inner volume

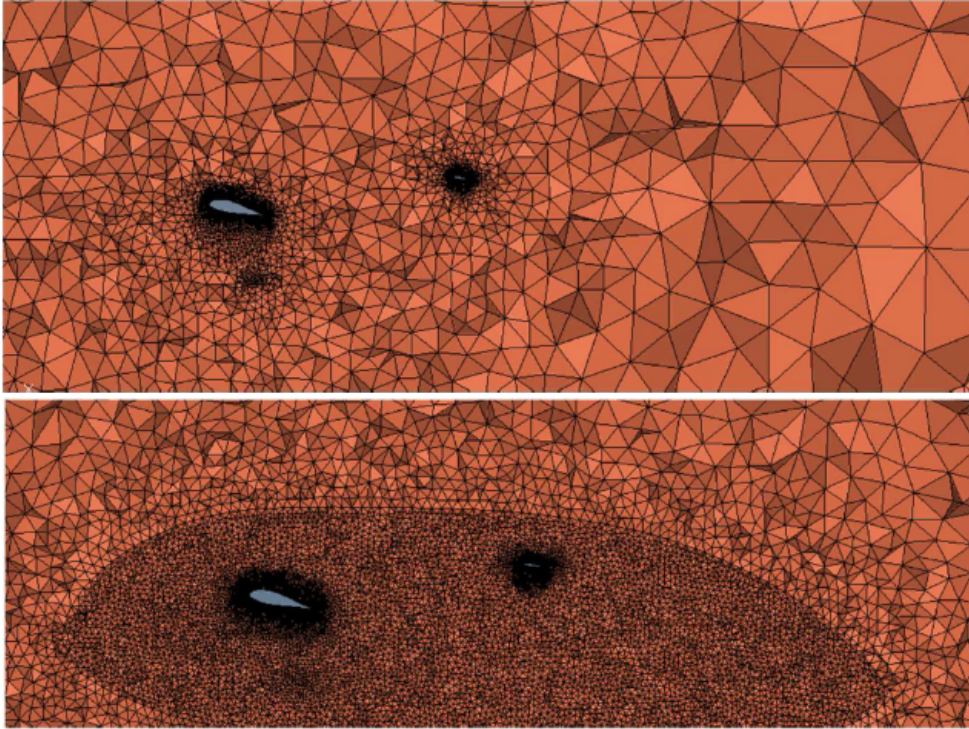


**Figure 3.14:** Overall longitudinal section of the volume mesh: comparison of mesh obtained without (on top) and with (on bottom) the refinement shell

<b>Boundary selection</b>	With BL (fixed)	-
	Without BL (float)	inlet, outlet, outer symmetry plane, outer ceiling, others wind tunnel walls (symmetry)
	Without BL (fixed)	shell
<b>Tetra mesh parameters</b>	Max tetra size	not activated
	Optimized mesh quality	activated
	Uniform layers	1
	Growth rate	1.08

**Table 3.6:** Mesh parameters for the outer volume

### 3.4 Boundary Conditions Setup

In the present section, the settings adopted for the tiltrotor CFD simulations are presented and compared. In the first analysis the commercial code ANSYS Fluent V14 is used, the second analysis is carried with the open source code OpenFOAM 2.3.0.

Table 3.7 summarizes the adopted boundary conditions in accordance with the operating test condition derived from the test case TN47 in [6].

$V_\infty[m/s]$	$\rho[kg/m^3]$	$p[Pa]$	$T[K]$	$M[-]$	$p_0[Pa]$	$T_0[K]$
44.85	1.16	97956	294.18	0.13	99127.7	295.176

**Table 3.7:** Flow conditions for the test case TN47 over 1/8 scaled tiltrotor [6]

#### 3.4.1 ANSYS Fluent Boundary Conditions

A first campaign of simulations has been carried out using ANSYS Fluent V14. A pressure based solver type has been chosen and an absolute velocity formulation with steady approach has been used for the analysis. The adopted turbulence model is the  $k - \omega SST$ ; this model gives a satisfactory correlation against experimental data, as found in [6]. The air has been treated as an ideal gas having constant specific heat; the default parameter values for constant pressure specific heat coefficient and thermal conductivity have been used. The Sutherland law with default values of the three coefficients controlled the viscosity.

At the inlet, the total pressure and the total temperature conditions have been imposed while, at the outlet, the static pressure has been set. The values of total pressure and total temperature have been calculated using the static pressure, static temperature and freestream velocity ( $V_\infty$ ). In ANSYS Fluent the turbulence quantities have also to be specified at inlet and outlet; the adopted uniform specification method required to specify a hydraulic diameter (equal to the total aircraft length, 2.1 m) and the turbulence intensity (equal to 0.3%), as described in [36]. In fact, the specification method used in [35] (turbulence intensity and viscosity ratio), causes an unwanted drop of turbulence intensity throughout the fluid domain upstream of the aircraft fuselage. The aircraft surfaces have been modelled as no-slip and adiabatic walls, while a symmetry condition has been used for the lateral surfaces of the wind tunnel. The adopted set of boundary conditions are summarized in Table 3.8.

<b>Viscous model</b>	$k - \omega - SST$	
<b>Energy equation</b>	activated	
<b>Fluid</b>	Air	Density: ideal gas
		$c_p = \text{constant} = 1006.43 \text{ [J/kgK]}$
		$\lambda = \text{constant} = 0.242 \text{ [W/mK]}$
		Viscosity: three coefficients Sutherland law
<b>Boundary conditions</b>	Pressure Inlet	Gauge Total Pressure = 99127.7 [Pa]
		Total Temperature = 295.176 [K]
	Pressure Outlet	Gauge pressure = 97956 [Pa]
		Backflow Total Temperature = 295.176 [K]
	Symmetry	All later wind tunnel surfaces
Wall	No-slip, adiabatic	
<b>Operating conditions</b>	Pressure	0 [Pa]
	Gravity	deactivated

**Table 3.8:** Adopted set of boundary conditions for ANSYS Fluent simulations of ERICA scaled model

### 3.4.2 OpenFOAM Boundary Conditions

The second campaign of CFD simulation has been carried using OpenFOAM v. 2.3.0 and the solver *rhoSimplecFoam*; the solver has been first included in the OpenFOAM v. 2.0 and it is a steady-state SIMPLEC solver for laminar or turbulent RANS flow of compressible fluids. The SIMPLE-Corrected algorithm improves the SIMPLE one using a different cell and velocity correction [37]. Specifically, it is a segregated, pressure-based and compressible solver with steady approach. In order to simulate the viscous effects, the  $k - \omega$  SST has been chosen as turbulence model:  $k$  and  $\omega$  parameters have been estimated using the *turbulence intensity and eddy viscosity ratio* formulation.

- Turbulent kinetic energy:

$$k = \frac{3}{2}(u_{avg}I)^2 \quad (3.4)$$

- Specific turbulence dissipation:

$$\omega = \rho \frac{k}{\mu} \left( \frac{\mu_t}{\mu} \right)^{-1} \quad (3.5)$$

In the formulation,  $u_{avg}$  represents the mean flow velocity,  $I$  is the turbulence intensity equal to 0.3%, the value of density  $\rho$  used is  $1.16 \text{ kg/m}^3$ , the dynamic viscosity  $\mu$  is equal to  $1.5e^{-5} \text{ m}^3/\text{s}$  and the eddy viscosity ratio (the ratio of the turbulent viscosity  $\mu_t$  and the molecular dynamic viscosity  $\mu$ ) has been set to 10. A further formulation based on turbulence intensity and length scale has also been

tested, however, the adopted formulation has produced best results compared to wind tunnel test. The operative fluid is the air, treated as an ideal gas with specific constant heat; the viscosity has been expressed using the two coefficients Sutherland law:

$$\mu = \frac{C_1 T^{3/2}}{T + C_2} \quad (3.6)$$

where  $\mu$  is the viscosity (in kg/ms),  $T$  is the static temperature in K and  $C_1$  and  $C_2$  are constant coefficients.

The boundary conditions have been calculated based on the flow conditions for the test cases on the 1/8 scaled model tiltrotor reported in Table 3.7.

The freestream velocity value has not been imposed at inlet. It has been used with static pressure and static temperature in order to calculate the total pressure and the total temperature values to be specified at the inlet of the flowfield. The static pressure has been assigned on the wind tunnel outlet using the *pressureInletOutletVelocity* option. The condition represents a combination of the *pressureInletVelocity* option (when  $p$  is known at inlet,  $U$  is evaluated from the flux, normal to the patch) and the *inletOutlet* option (that switches  $U$  and  $p$  between *fixedValue* and *zeroGradient* depending on direction of  $U$ ). The fuselage surfaces have been treated as hydraulically smooth and adiabatic walls, while a symmetry condition has been used for the lateral surfaces of the wind tunnel box.

To ensure a better convergence, the flowfield has been initialized at 5 m/s in the flow direction (positive x-axis direction).

The adopted boundary conditions for Inlet and Outlet are summarized in Table 3.9.

Variable	Inlet B.C.	Outlet B.C.
<b>U</b>	PressureInletVelocity	pressureInletOutletVelocity
<b>p</b>	totalPressure	fixedValue
<b>T</b>	totalTemperature	inletOutletTotalTemperature
<b>k</b>	turbulentIntensityKineticEnergyInlet	inletOutlet
$\omega$	fixedValue	inletOutlet

**Table 3.9:** Setup of boundary conditions at wind tunnel inlet and outlet surfaces



## 3.5 Solution Strategies

In the present section, the adopted solution strategies for the analysis with the commercial software ANSYS Fluent and with the open source code OpenFOAM are illustrated. For both the analysis, the used mesh is the same, as explained in the previous sections.

### 3.5.1 ANSYS Fluent Solution Strategy

The chosen algorithm to run the analysis is represented by the pressure-velocity coupled solver. For the spatial discretization, the least squares method has been used for gradient calculation, a second order scheme for pressure and the third-order MUSCL for the other scalars.

To control and improve the solution convergence, the flow Courant number has been set to 40 while the relaxation factors for momentum pressure and the other quantities have been left at their default values. Regarding the initialization of the flowfield, the inlet values have been assigned to the whole flow domain, however the velocity value has been initialized at 5 m/s in the positive x direction in order to start from a reasonable value and speed up the convergence. During the first 50 iterations the energy equation has been deactivated in order to improve solution convergence. The iterative process stops when the convergence criteria, based on the residual values, is reached. The solution has been considered reached when RMS residuals values were less than  $10^{-5}$  (except for the  $k$  residual for which  $10^{-3}$  was considered acceptable) and the lift, drag and pitching moment reached an asymptotic trend. Finally, the aerodynamic coefficients have been averaged over a whole of 600 iterations, due to the intrinsic instabilities of the physic phenomena involved.

Tables 3.10 and 3.11 list the main settings used in ANSYS Fluent for the simulations of the 1/8 scaled.

<b>Solver</b>	pressure based	
	steady	
	absolute velocity formulation	
<b>Solution scheme</b>	pressure velocity coupled	
<b>Spatial discretization</b>	gradient	least squares method
	pressure	second order
	density	third-order MUSCL
	momentum	third-order MUSCL
	$k, \omega$	third-order MUSCL
	energy	third-order MUSCL

**Table 3.10:** ANSYS Fluent solver setting and discretization used for CFD simulations

<b>Solution initialization</b>	method	standard
	values computed from	inlet
	x-velocity	5 m/s
	y-velocity	0 m/s
	z-velocity	0 m/s
<b>Running calculation strategy</b>	energy equation deactivated	first 50 iterations
	energy equation activated	after 50 <sup>th</sup> iteration

**Table 3.11:** ANSYS Fluent solution strategy adopted for the CFD simulations

### 3.5.2 OpenFOAM Solution Strategy

The solver used in OpenFOAM to run the analysis is represented by the *rhoSimplecFOAM*, a steady-state SIMPLEC solver for laminar or turbulent RANS flow of compressible fluids. The solution and discretization schemes used in OpenFOAM have to be set respectively in the files *fvSchemes* and *fvSolution*, inside the system folder.

In order to correct the instability due to the non-orthogonality of some elements of the adopted mesh, the *nonOrthogonalCorrectors* option of the chosen solver has been needed. This option re-iterates a specified number of times the calculation of the pressure field for the current iteration.

The solution strategy is structured in three different steps, where different schemes and relaxation factors have been used.

- In the first phase of simulation (about 100 iterations), the energy equation has been deactivated in order to stabilize the iterative process and to obtain an initial approximation of the correct flow field; this has been possible by imposing the *temperatureLimitConstraint* option for the static temperature value, in the *fvOption* file. Furthermore, 4 non-orthogonal correctors are set.

A set of first order schemes have been used to initialize the simulation runs as specified in Table 3.12. The under-relaxation factors are decreased with respect to the default values (0.25 for  $p$ , 0.07 for  $\rho$  and 0.5 for  $U$ ) in order to improve the convergence for the first order solution.

- During the second phase of simulation, the energy equation has been activated by removing the temperature constraints, while the number of non-orthogonal-correctors is decreased to 2.

The discretization schemes and the under-relaxation factors remain the same as the previous phase. The present setting is maintained until the convergence reaches the  $< 1e^{-4}$  target for all the residuals (between about the 2500-3000 iterations).

- The third phase of simulation starts when the convergence is reached for the first order scheme

setting. A second-like order scheme is used; a *Gauss linearUpwind* scheme for the divergence and a *Gauss linear* scheme for the gradient are set as reported in Table 3.12. The under-relaxation factors are bring back to their default value (0.3 for  $p$ , 0.1 for  $\rho$  and 0.7 for  $U$ ) and the *nonOrthogonalCorrectors* option is not used. The solution is considered converged when the residual reaches the  $< 1e^{-5}$  target. Furthermore, the aerodynamic coefficients are monitored in order to ensure the achievement of a stabilized value at the end of simulations.

Scheme	First order	Second-like order
<b>Gradient</b>	Gauss Linear	-cellLimited Gauss Linear 1 -cellMDLimited Gauss Linear 1 (velocity term)
<b>Divergence</b>	-bounded Gauss Upwind -Gauss linear (viscosity term)	-bounded Gauss linearUpwind cel- lLimited Gauss Linear 1 -bounded Gauss linearUpwindV cellMDLimited Gauss Linear 1 (velocity term) -Gauss linear (viscosity term)
<b>Laplacian</b>	Gauss linear corrected	Gauss linear corrected
<b>Interpolation</b>	linear	linear

**Table 3.12:** OpenFOAM numerical discretization schemes

### 3.6 Discussion of Results

In the present section the results of simulations over the tiltrotor scaled model carried out with ANSYS Fluent and OpenFOAM are presented and compared to the wind tunnel experimental data [6].

The experimental results are reported in Table 3.13.

$\alpha$ [°]	Wind tunnel		
	$C_L$	$C_D$	$C_M$
-18,259	-0,9747	0,22	0,1068
-15,234	-0,9523	0,1354	0,3733
-12,16	-0,7155	0,0958	0,3062
-9,08	-0,4436	0,0681	0,2314
-6	-0,1463	0,0527	0,1556
-3,94	0,0564	0,0501	0,1047
-1,89	0,2605	0,0533	0,0545
0,17	0,4599	0,0617	0,0106
2,224	0,6544	0,0745	-0,0314
4,267	0,8421	0,093	-0,0733
6,324	1,0135	0,1152	-0,1183
9,34	1,1779	0,1661	-0,2206
12,38	1,2780	0,2236	-0,3176
15,41	1,3615	0,2941	-0,372
18,393	1,4169	0,3782	-0,4115

**Table 3.13:** Results of the wind tunnel test over 1/8 scaled tiltrotor model

#### 3.6.1 Lift, Drag and Pitching Moment Polars Comparison

Tables 3.14 and 3.15 report the numerical aerodynamic coefficients of the baseline 1/8 scaled tiltrotor model (in terms of lift, drag and pitching moment) of CFD analysis carried out with ANSYS Fluent 14.5 and OpenFOAM 2.3.0. The deviations from the experimental results are presented in both cases. The resulting polars are shown in Figures 3.15 and 3.16.

Regarding the ANSYS Fluent simulations, an excellent correlation between experimental and numerical data has been found at low and medium angle of attack ( $\alpha$  in range  $[-12^\circ, +12^\circ]$ ), while at an absolute higher angle of attack ( $\alpha < -12^\circ$  and  $\alpha > 12^\circ$ ) the discrepancy is slightly higher. The lift coefficient values are very similar to the experimental results in the whole range of analysed angles (minimum deviation of about 3.5% with respect the wind tunnel data) except for the angles of incidence higher than  $12^\circ$ . The numerical results seem to anticipate the stall with respect to the experiment. The drag coefficient prediction is in good accordance with experimental data in the range  $[-18^\circ, +6^\circ]$ , however, for  $\alpha > 4^\circ$  the numerical calculations underestimate the drag with respect to experimental data (with

a deviation higher than 10%). At an angle near the cruise attitude ( $\alpha = -2^\circ$ ) the correlation of the aerodynamic coefficients found in ANSYS Fluent is satisfactory, hence the model is reliable for a further optimization of the geometry. Regarding the pitching moment coefficient, the numerical results present higher values of deviations than the previous coefficient, however the correlation found in the range  $[-12^\circ, +12^\circ]$  is acceptable; the slope of the linear portion of the curve is very well captured, with some discordances at higher and lower angles of incidence.

$\alpha [^\circ]$	Wind tunnel			Ansys Fluent			Deviation		
	$C_L$	$C_D$	$C_M$	$C_L$	$C_D$	$C_M$	$C_L$	$C_D$	$C_M$
-18,259	-0,9747	0,22	0,1068	-1,0078	0,2096	0,2575	3,40%	-4,73%	141,10%
-15,234	-0,9523	0,1354	0,3733	-0,9695	0,1456	0,3184	1,81%	7,53%	-14,71%
-12,16	-0,7155	0,0958	0,3062	-0,7246	0,1055	0,3029	1,27%	10,13%	-1,08%
-9,08	-0,4436	0,0681	0,2314	-0,4454	0,0761	0,2507	0,41%	11,75%	8,34%
-6	-0,1463	0,0527	0,1556	-0,1436	0,0582	0,1708	-1,85%	10,44%	9,77%
-3,94	0,0564	0,0501	0,1047	0,0584	0,0525	0,118	3,55%	4,79%	12,70%
-1,89	0,2605	0,0533	0,0545	0,2586	0,0526	0,071	-0,73%	-1,31%	30,28%
0,17	0,4599	0,0617	0,0106	0,4558	0,0576	0,027	-0,89%	-6,65%	154,72%
2,224	0,6544	0,0745	-0,0314	0,6459	0,0668	-0,0165	-1,30%	-10,34%	-47,45%
4,267	0,8421	0,093	-0,0733	0,8298	0,081	-0,0524	-1,46%	-12,90%	-28,51%
6,324	1,0135	0,1152	-0,1183	1,0043	0,1003	-0,0884	-0,91%	-12,93%	-25,27%
9,34	1,1779	0,1661	-0,2206	1,1628	0,1438	-0,1871	-1,28%	-13,43%	-15,19%
12,38	1,2780	0,2236	-0,3176	1,2448	0,1931	-0,3323	-2,60%	-13,64%	4,63%
15,41	1,3615	0,2941	-0,372	1,2533	0,2598	-0,4208	-7,95%	-11,66%	13,12%
18,393	1,4169	0,3782	-0,4115	1,1175	0,3186	-0,3212	-21,13%	-15,76%	-21,94%

**Table 3.14:** Results of ANSYS Fluent CFD simulations

The analysis carried with OpenFOAM present similar good results and they are in accordance with the experimental data. The lift coefficient values present a deviation of about [5%-10%] in the whole simulated range of angle of incidence, except for the cases with  $\alpha$  higher than  $18^\circ$  or lower than  $-18^\circ$ . The numerical results seem to over-predict the absolute value of the lift coefficient. The prediction of the lift coefficient seems to be less accurate in OpenFOAM than in ANSYS Fluent. The drag coefficient values are in a better accordance with the experimental results in OpenFOAM than in Ansys Fluent; the deviations assume a lower value for almost the whole range of angles of incidence. Regarding the pitching moment coefficients, the OpenFOAM results are similar than the ANSYS Fluent analysis with lower deviations at the positive angles of incidence. Also in this case, the correlation found in the range  $[-12^\circ, +12^\circ]$  is acceptable showing a linear trend in the central part of the curve (Figure 3.16a), according to experimental results.

Table 3.16 summarizes and compares the different deviations values found with the ANSYS Fluent and OpenFOAM numerical analysis.

$\alpha$ [°]	Wind tunnel			OpenFOAM			Deviation		
	$C_L$	$C_D$	$C_M$	$C_L$	$C_D$	$C_M$	$C_L$	$C_D$	$C_M$
-18,259	-0,9747	0,22	0,1068	-1,2704	0,1997	0,2392	30,33%	-9,22%	123,97%
-15,234	-0,9523	0,1354	0,3733	-1,0257	0,1456	0,2351	7,70%	7,54%	-37,01%
-12,16	-0,7155	0,0958	0,3062	-0,7882	0,1021	0,3387	10,15%	6,58%	10,63%
-9,08	-0,4436	0,0681	0,2314	-0,4688	0,0728	0,2548	5,69%	6,93%	10,12%
-6	-0,1463	0,0527	0,1556	-0,1552	0,0563	0,1710	6,09%	6,83%	9,89%
-3,94	0,0564	0,0501	0,1047	0,0593	0,0515	0,1182	5,18%	2,84%	12,86%
-1,89	0,2605	0,0533	0,0545	0,2710	0,0528	0,0630	4,03%	-0,94%	15,60%
0,17	0,4599	0,0617	0,0106	0,4844	0,0565	0,0123	5,33%	-8,47%	16,20%
2,224	0,6544	0,0745	-0,0314	0,6902	0,0674	-0,0327	5,47%	-9,54%	4,27%
4,267	0,8421	0,093	-0,0733	0,8872	0,0829	-0,0705	5,36%	-10,90%	-3,84%
6,324	1,0135	0,1152	-0,1183	1,0942	0,1046	-0,1120	7,97%	-9,18%	-5,30%
9,34	1,1779	0,1661	-0,2206	1,2771	0,1467	-0,1606	8,42%	-11,65%	-27,22%
12,38	1,2780	0,2236	-0,3176	1,3765	0,2067	-0,2039	7,71%	-7,58%	-35,79%
15,41	1,3615	0,2941	-0,372	1,3429	0,2784	-0,3813	-1,37%	-5,35%	2,50%
18,393	1,4169	0,3782	-0,4115	1,2311	0,3756	-0,4567	-13,11%	-0,69%	10,99%

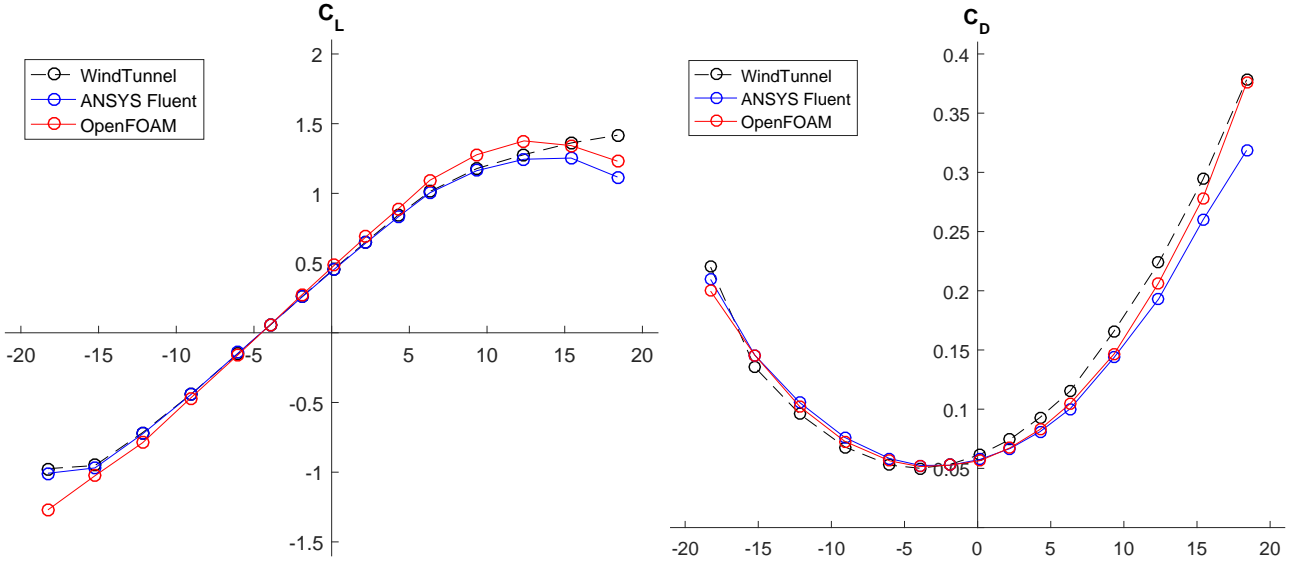
Table 3.15: Results of OpenFOAM CFD simulations

$\alpha$ [°]	ANSYS Fluent vs exp.			OpenFOAM vs exp.		
	$C_L$	$C_D$	$C_M$	$C_L$	$C_D$	$C_M$
-18,259	3,40%	-4,73%	141,10%	30,33%	-9,22%	123,97%
-15,234	1,81%	7,53%	-14,71%	7,70%	7,54%	-37,01%
-12,16	1,27%	10,13%	-1,08%	10,15%	6,58%	10,63%
-9,08	0,41%	11,75%	8,34%	5,69%	6,93%	10,12%
-6	-1,85%	10,44%	9,77%	6,09%	6,83%	9,89%
-3,94	3,55%	4,79%	12,70%	5,18%	2,84%	12,86%
-1,89	-0,73%	-1,31%	30,28%	4,03%	-0,94%	15,60%
0,17	-0,89%	-6,65%	154,72%	5,33%	-8,47%	16,20%
2,224	-1,30%	-10,34%	-47,45%	5,47%	-9,54%	4,27%
4,267	-1,46%	-12,90%	-28,51%	5,36%	-10,90%	-3,84%
6,324	-0,91%	-12,93%	-25,27%	7,97%	-9,18%	-5,30%
9,34	-1,28%	-13,43%	-15,19%	8,42%	-11,65%	-27,22%
12,38	-2,60%	-13,64%	4,63%	7,71%	-7,58%	-35,79%
15,41	-7,95%	-11,66%	13,12%	-1,37%	-5,35%	2,50%
18,393	-21,13%	-15,76%	-21,94%	-13,11%	-0,69%	10,99%

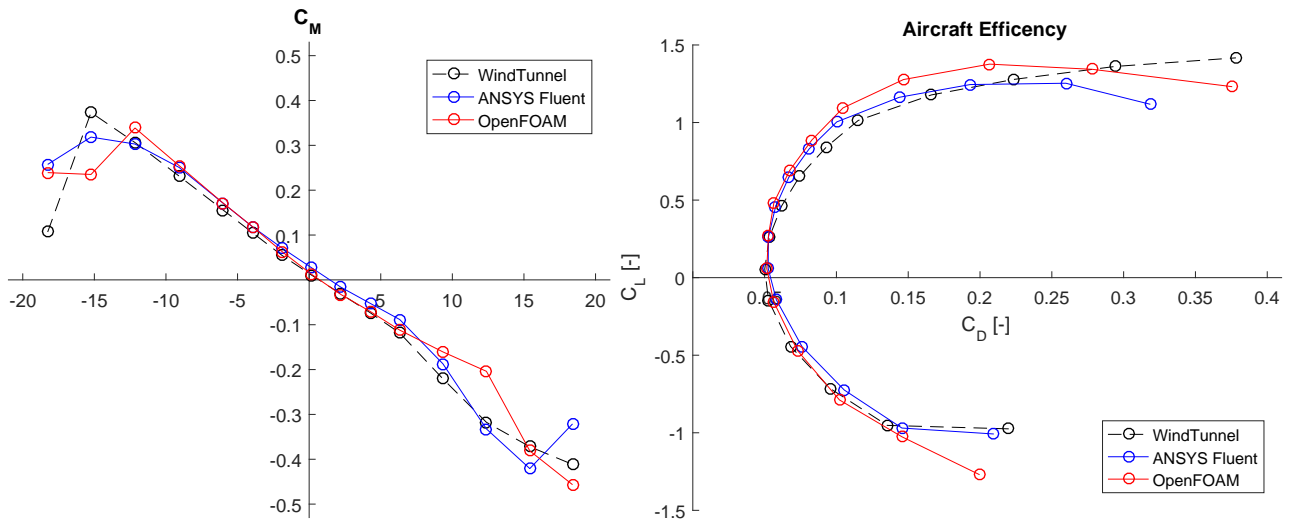
Table 3.16: Deviation (%) comparison between OpenFOAM and ANSYS Fluent against experimental data

Figure 3.16b illustrates the aerodynamic efficiency trend of the tiltrotor; a good correlation with experimental data is found for both the ANSYS Fluent and OpenFOAM analysis, however the OpenFOAM results product a wider curve. The efficiency maximum value can be located around  $\alpha = 5^\circ$ . Finally, it is useful to remark that the CFD models also include the supporting pylon of LWTE wind

tunnel, contrary to the experimental results coming from *Politecnico di Milano*, corrected for pylon interference. It can be deduced that the supporting system has a negligible influence on aerodynamic coefficients of the baseline tiltrotor.



**Figure 3.15:** Lift and drag coefficients comparison of OpenFOAM simulations against ANSYS Fluent results and wind tunnel data



**Figure 3.16:** Pitching moment polar and aircraft aerodynamic efficiency: comparison of OpenFOAM simulations against ANSYS Fluent results and wind tunnel data

### 3.6.2 Static Pressure Coefficient Comparison

A comparison of the pressure coefficient distribution on the surface of the tiltrotor is presented from Figure 3.17 to Figure 3.20 for several angles of attack in front and back view. The  $C_P$  is calculated as follows:

- Pressure coefficient

$$C_P = \frac{p - p_\infty}{1/2\rho_\infty V_\infty^2} \quad (3.7)$$

assuming  $p_{Ref}$  as 97956 Pa.

The distribution of the pressure coefficient, calculated from ANSYS Fluent and OpenFOAM simulation, is quite identical in the central range of the analysed angles of incidence; at the highest angles of attack ( $\alpha > 12^\circ$ ) slightly differences are registered regarding the flow separation over the wing.



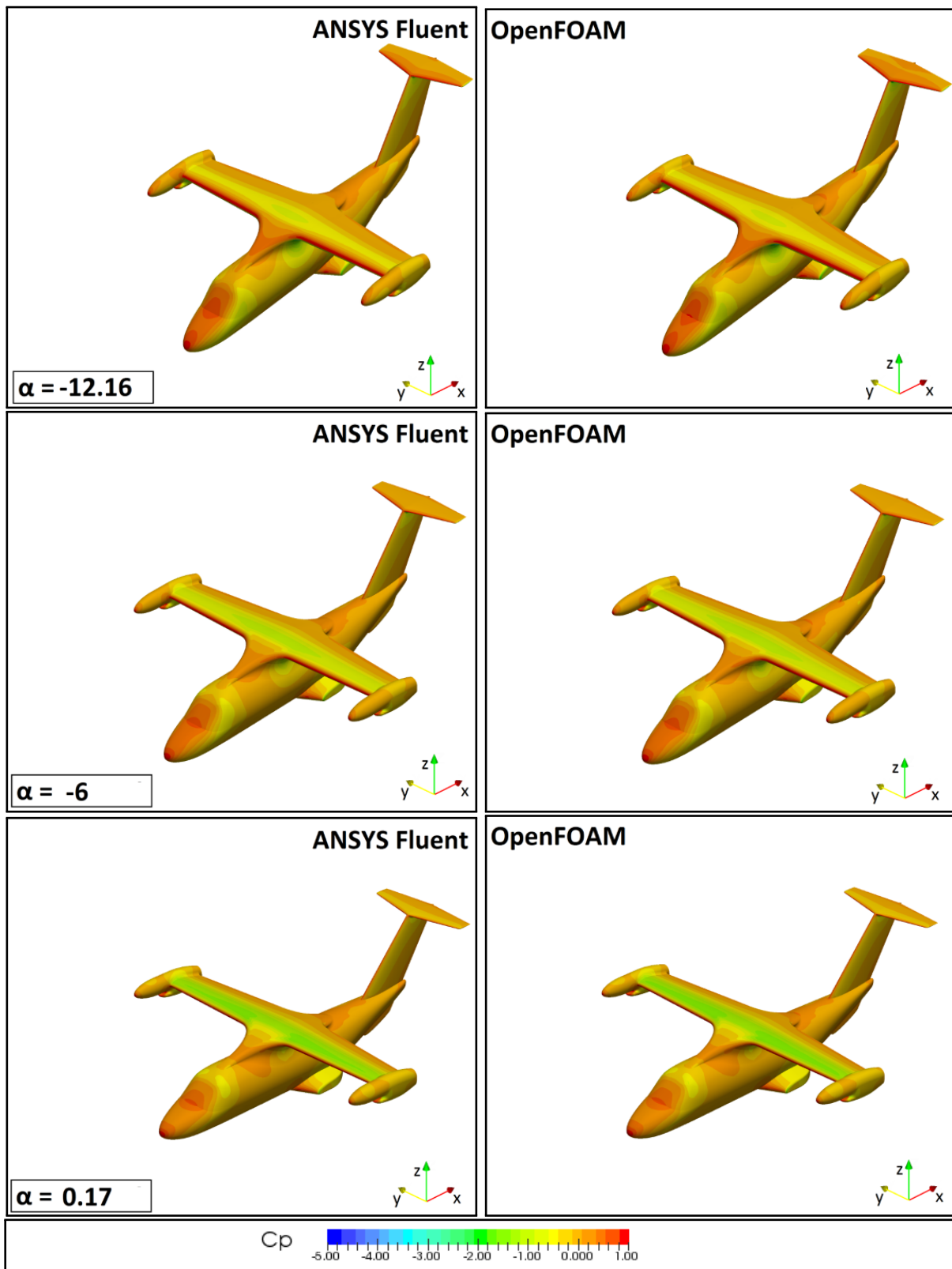


**Figure 3.17:** Contour plots of the static pressure coefficient  $C_p$  over the full scale tiltrotor model at various incidences (front view): comparison of the Fluent (on the left), OpenFOAM (on the right) results

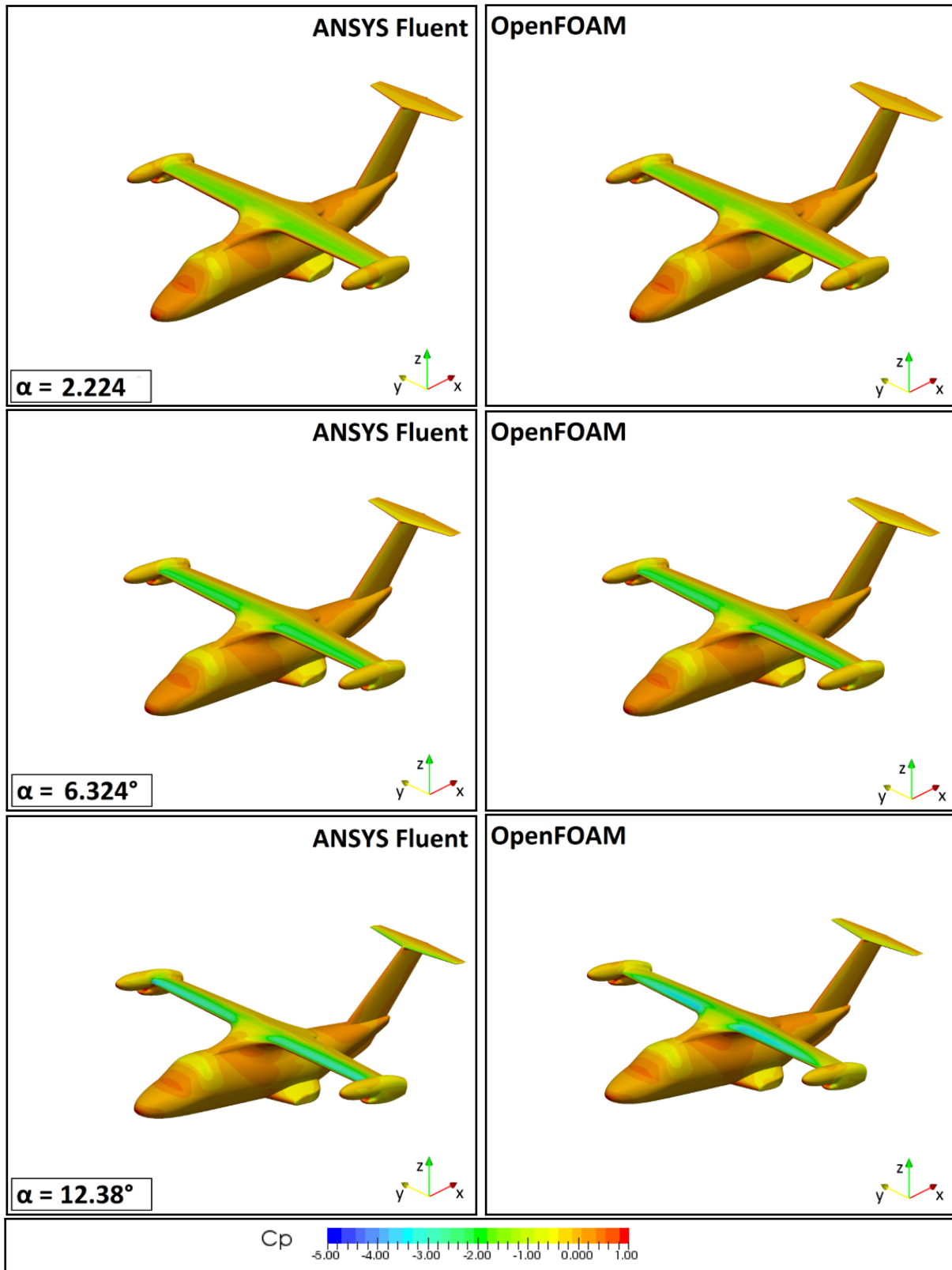


**Figure 3.18:** Contour plots of the static pressure coefficient  $C_p$  over the full scale tiltrotor model at various incidences (front view); comparison of the Fluent (on the left), OpenFOAM (on the right) results

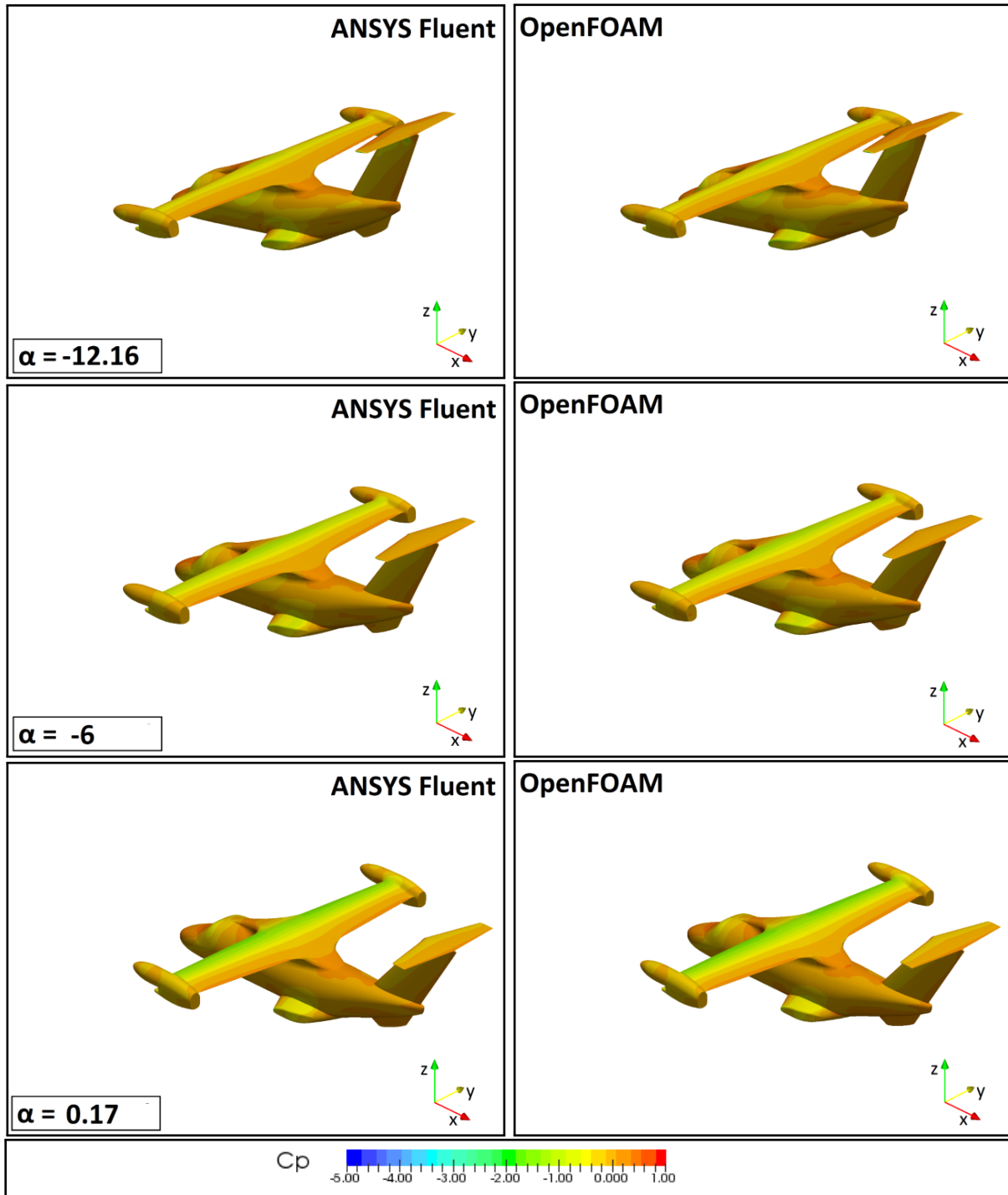


**Figure 3.19:** Contour plots of the static pressure coefficient  $C_P$  over the full scale tiltrotor model at various incidences (front view): comparison of the Fluent (on the left), OpenFOAM (on the right) results

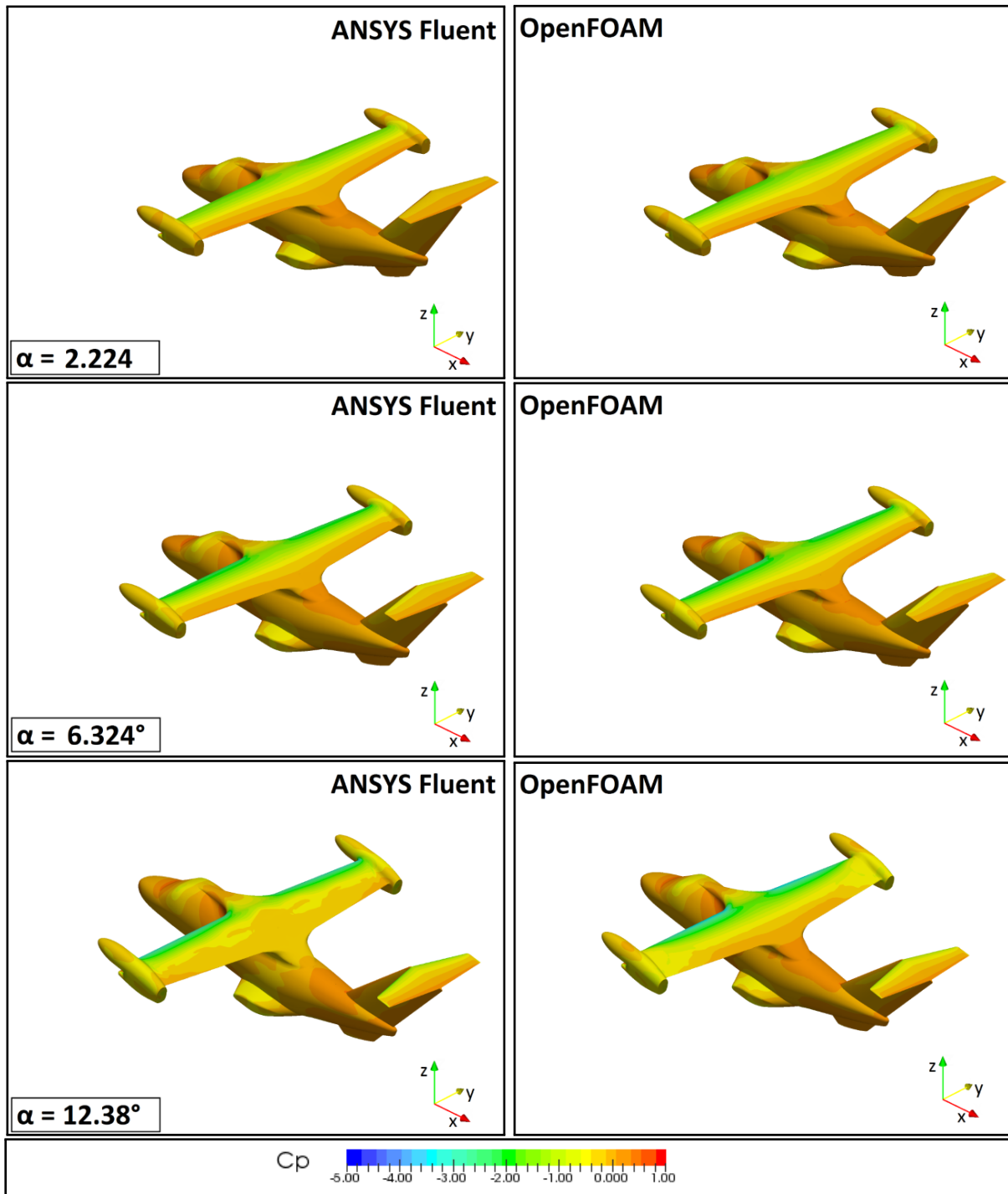


**Figure 3.20:** Contour plots of the static pressure coefficient  $C_P$  over the full scale tiltrotor model at various incidences (front view): comparison of the Fluent (on the left), OpenFOAM (on the right) results

### 3.6.3 Total Pressure Losses Comparison

From Figure 3.21 to Figure 3.24 the total pressure contours on the tiltrotor surface are presented in both front and back views for various angles of incidence. The parameter considered for the total pressure is the *total pressure coefficient*  $C_{P\_tot}$ , evaluated as follows:

- Total pressure coefficient

$$C_{P\_tot} = \frac{p_{0\infty} - p_0}{p_{0\infty} - p_\infty} \quad (3.8)$$

In order to show the distribution of the  $C_{P\_tot}$  in the rear section of the tiltrotor, 7 different slices have been created in the YZ plane. The slices start near the nacelle and are spaced of 0.25 m. The post-processing contours have been created with the open source ParaView software.

The *total pressure coefficient* contour distributions present a similar behaviour in ANSYS Fluent and in OpenFOAM, for all the considered angles of incidence. At low incidences, pressure losses from both the rear ramp and the tail fin are less intense than those calculated with ANSYS Fluent. The sources of the losses are mainly represented by the nacelles and the rear ramp. At cruise conditions, for both ANSYS Fluent and OpenFOAM, the losses are still caused by the nacelles and the rear ramp. The main wing drag seems to be acceptable since it does not present any separation. At positive attitude the nacelles still represent one of the main sources of losses, however the rear ramp influence decrease. For the high incidence angles ( $\alpha > 12^\circ$ ) the discrepancies in the drag coefficient between ANSYS Fluent and OpenFOAM analysis are more marked and it can be shown in the total loses comparison. The results of ANSYS Fluent simulations highlight the formation of a stall in the central part of the main wing, contributing to a separation of the flow in the upper part of the rear fuselage which propagates downstream. In OpenFOAM analysis, the losses seem to be related to a flow separation that originates in the external part of the wings, near the nacelle, that is propagated downstream.

It is worth noting that, at low and moderate incidences, the OpenFOAM analysis seems to produce a slightly less intense total pressure loses from both the nacelles and the rear ramp than ANSYS Fluent analysis. The fact is consistent with the lower drag polars (Table 3.15), closer to experimental data, found using OpenFOAM.

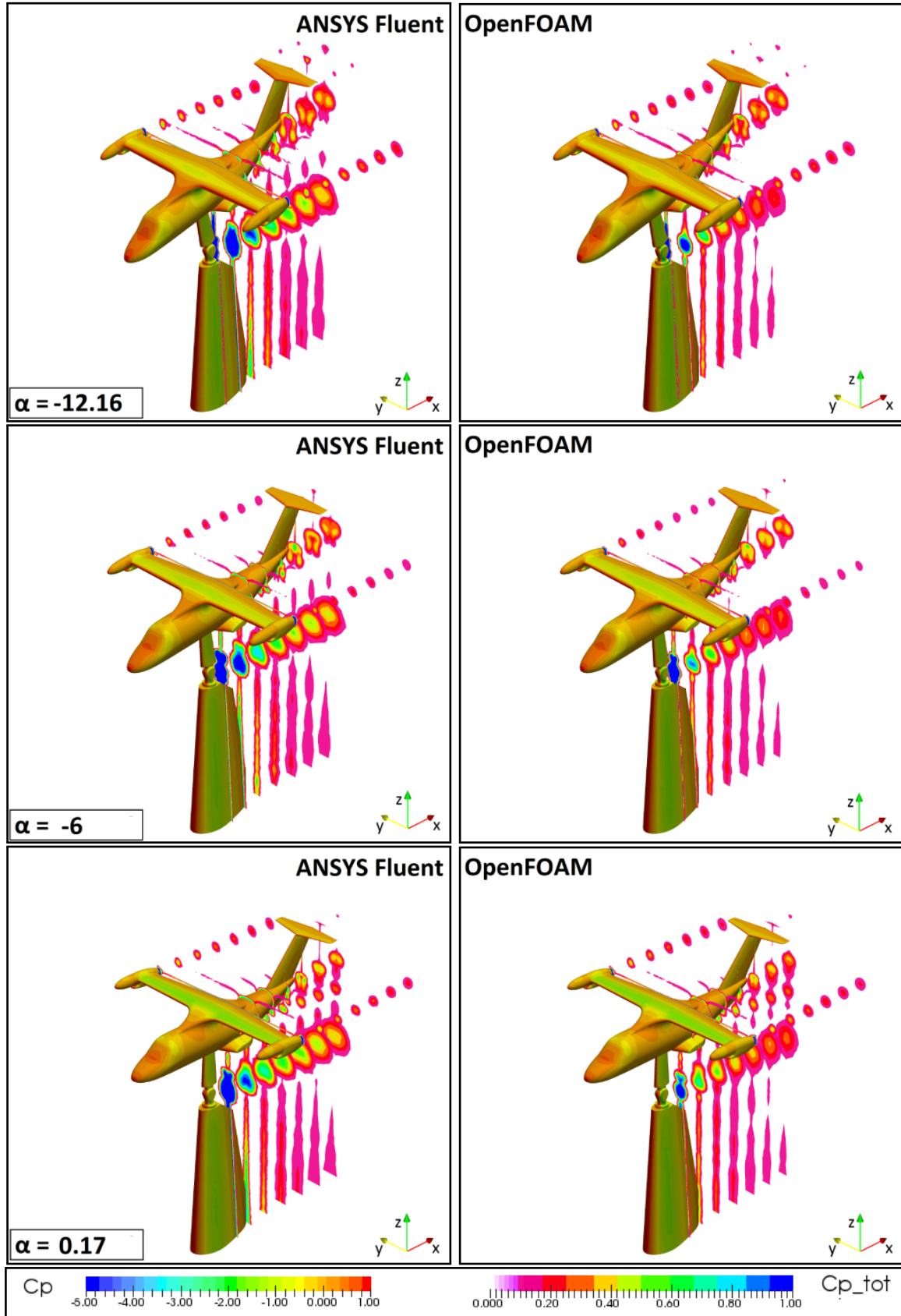


**Figure 3.21:** Total pressure losses visualization of the full scale tiltrotor with null deflection of the control surfaces at various incidences: comparison of OpenFOAM (on the right) and Fluent (on the left) results

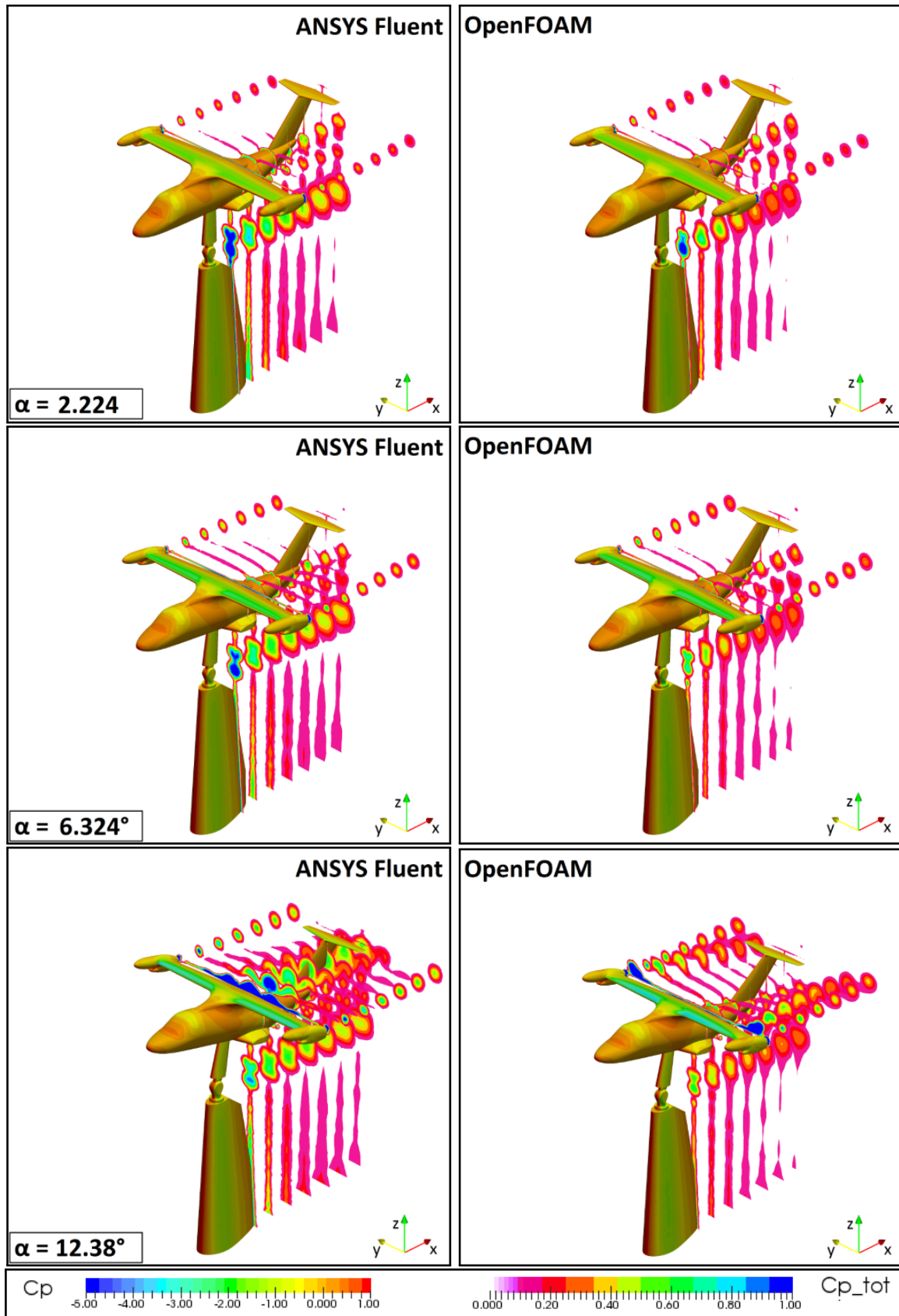


**Figure 3.22:** Total pressure losses visualization of the full scale tiltrotor with null deflection of the control surfaces at various incidences: comparison of OpenFOAM (on the right) and Fluent (on the left) results

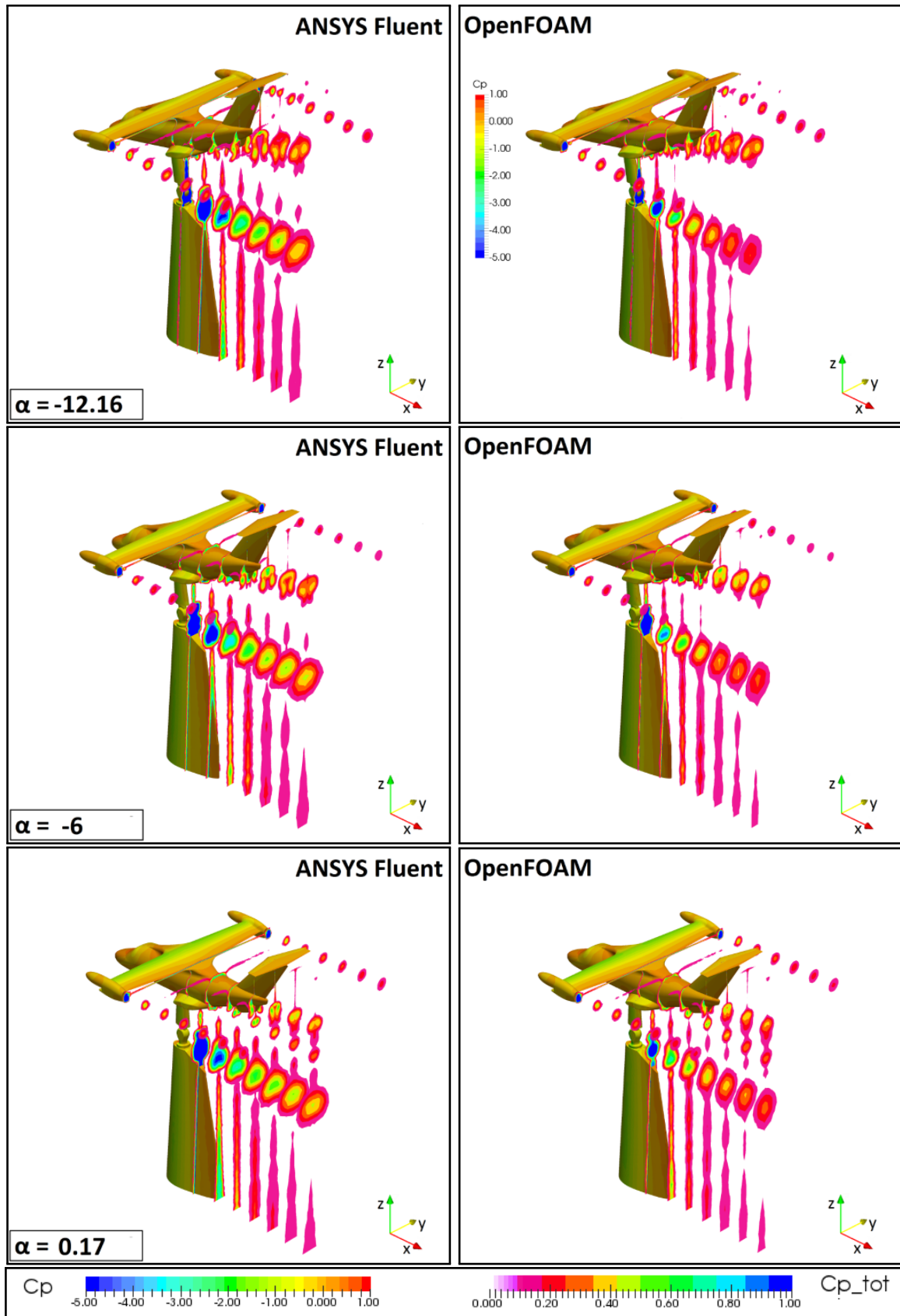


**Figure 3.23:** Total pressure losses visualization of the full scale tiltrotor with null deflection of the control surfaces at various incidences: comparison of OpenFOAM (on the right) and Fluent (on the left) results



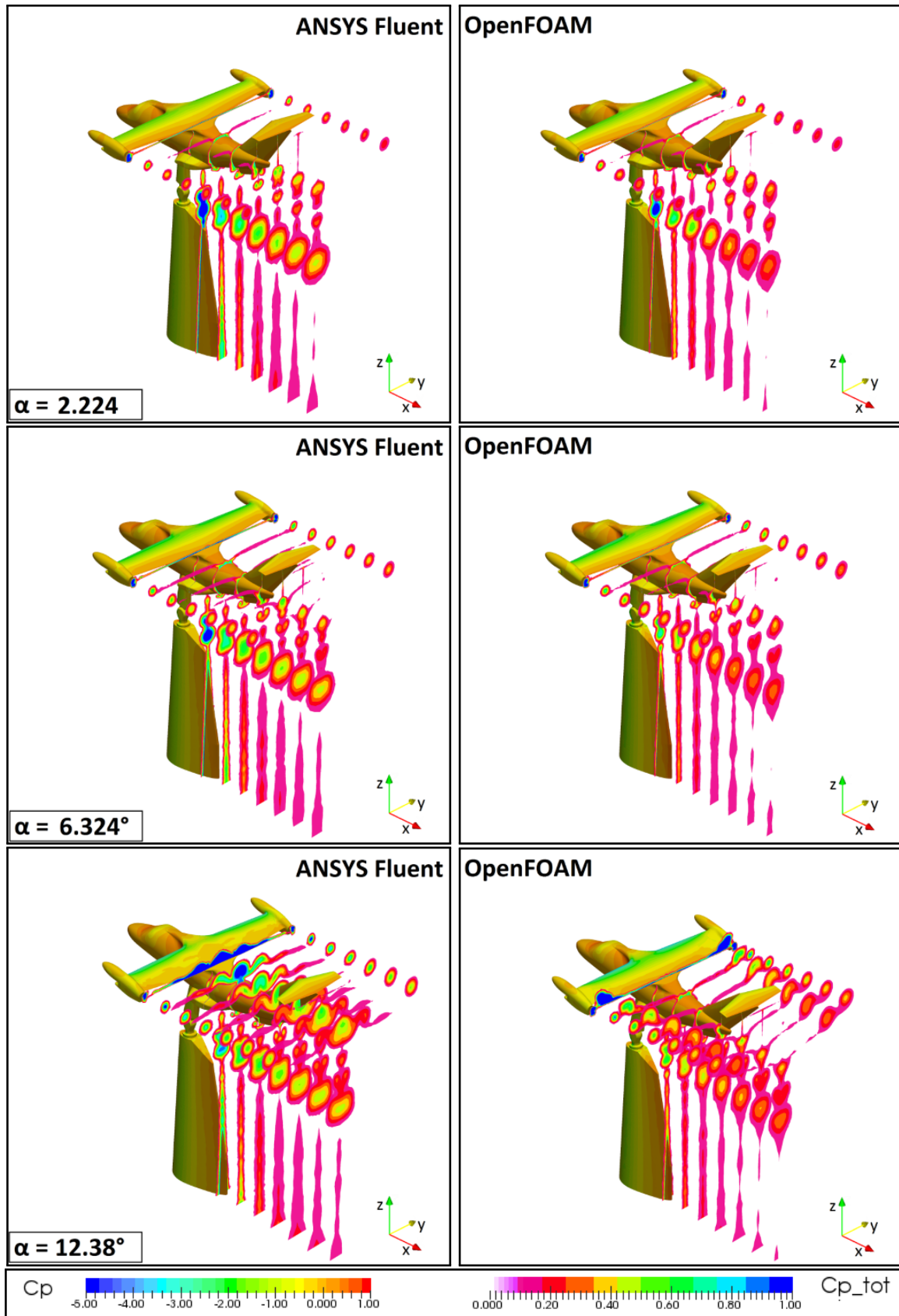


**Figure 3.24:** Total pressure losses visualization of the full scale tiltrotor with null deflection of the control surfaces at various incidences: comparison of OpenFOAM (on the right) and Fluent (on the left) results

### 3.6.4 Friction Lines

In order to understand how the flow develops around the most fuselage components, the friction lines distribution on the surface of the tiltrotor is presented for both the CFD codes, ANSYS Fluent and OpenFOAM. The friction lines are represented by a vector on a wall surface; they are auto-calculated in Fluent while, in OpenFOAM, they are determined using the function *wallShearStess*.

In the zone of the nose, an uniform behaviour of the flow is registered as expected, for both ANSYS Fluent and OpenFOAM analysis. No negative effects referring to the flow separation are registered and the results from the both codes are in a good agreement. Regarding the wing-fuselage junction, the friction lines analysis confirms the declaration of the previous analysis. As can be observed, a regular distribution of the friction lines is present on the wing suction side for the incidence angles  $\alpha < 6^\circ$  and so near the cruise condition. However, a separated flow pattern is visible at the higher angles of incidence in the rear part of the wing suction side; at these angles of incidence the distribution of the friction lines is different, as shown in detail in Figure 3.29. The fact is consistent with the difference in total pressure losses reported in the previous section.

In the connection zone between wing suction side and fuselage, no clear interference is noticeable at the normal attitude, however, the presence of flow distortion is noticed at higher attitudes: the flow is diverted downstream and forced to join the upcoming flow from the fuselage. Both the ANSYS Fluent and OpenFOAM predictions are in excellent agreement as can be seen in Figure 3.30.

The rear part of the fuselage and the sponsons present the most evident non-uniform flow-path. In cruise condition both the presence of the inclined ramp and the wing downwash are responsible for an evident descending diversion of the flow coming from the wing. The phenomena is predicted by both ANSYS Fluent and OpenFOAM and the presence of the sponsons compress the friction lines, coming from opposite directions, to join together to form an attachment line which leads to a vortex formation propagating downstream and negatively affecting the aircraft drag. The phenomena also leads to the total pressure defect presented in the previous section. At the highest attitudes the rear ramp contribution to the drag increase is much lower, however, a significantly stronger effect is caused by the upper wing-fuselage junction. Furthermore, the sponsons provoke a more much severe influence, generating a very strong flow distortion and the appearance of an evident tip vortex which probably leads to a remarkable induced drag.

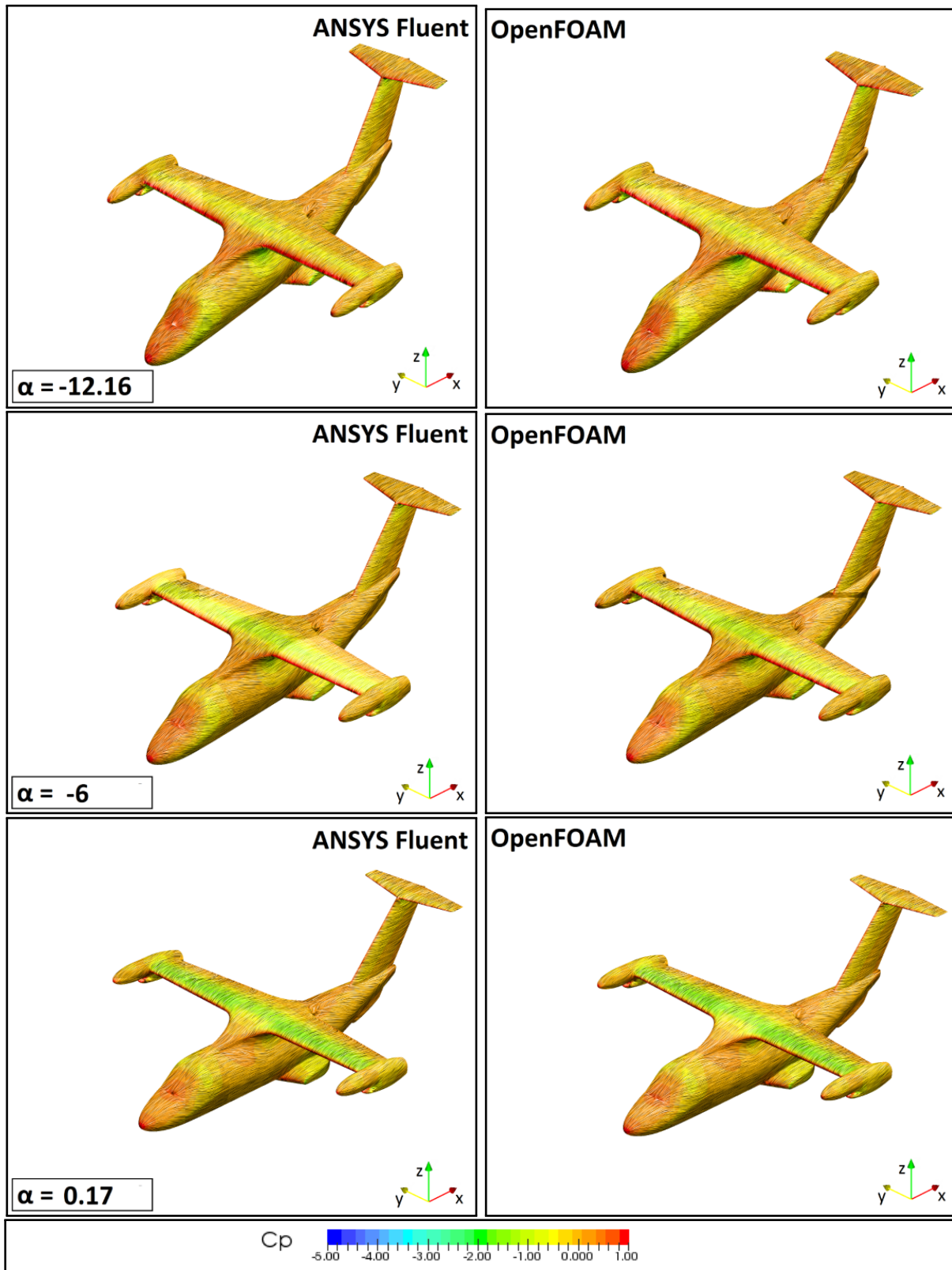


**Figure 3.25:** Friction lines over the tiltrotor model at various angle of incidence (front view): comparison of OpenFOAM (on the right) and Fluent (on the left) results

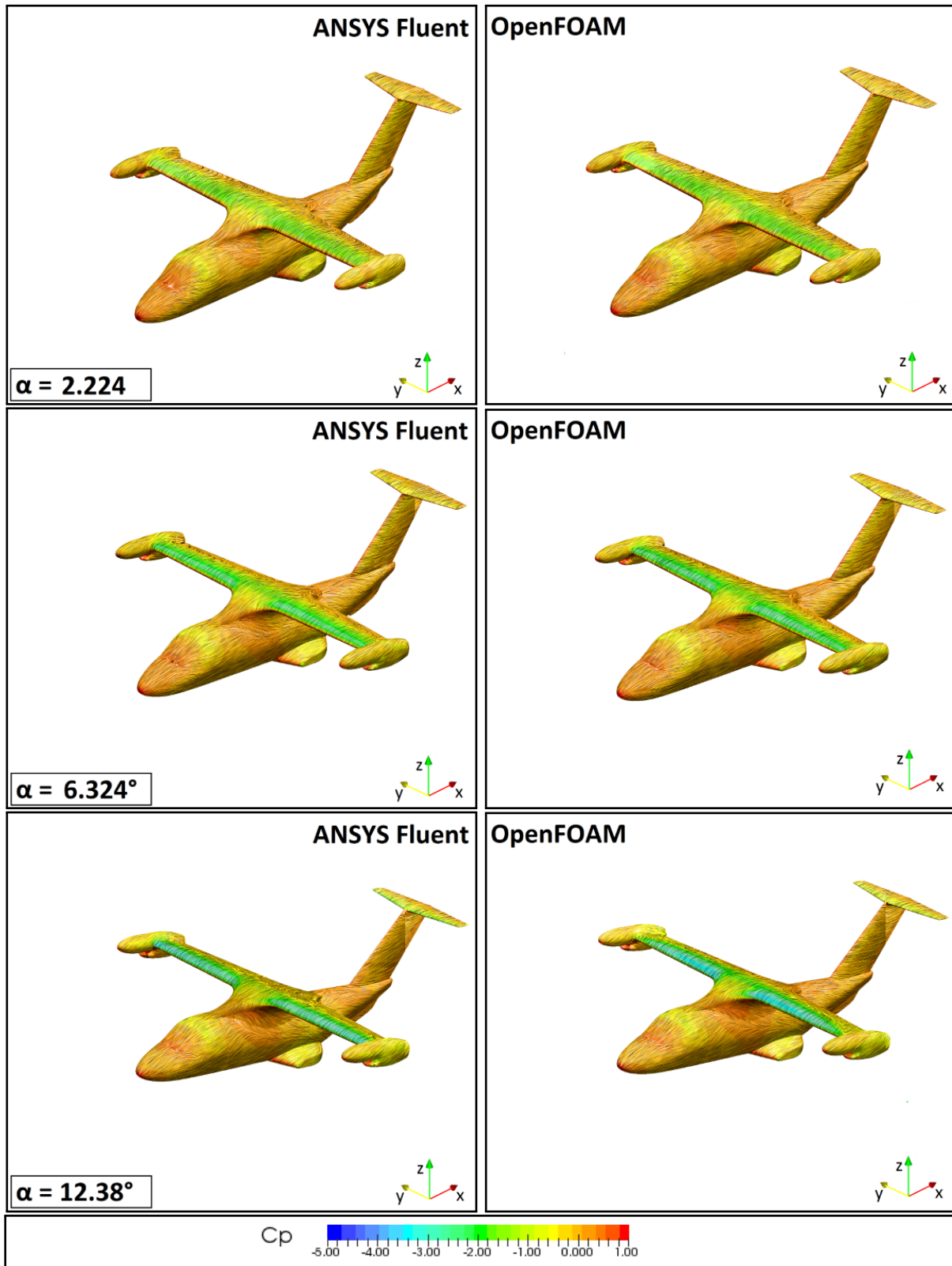


Figure 3.26: Friction lines over the tiltrotor model at various angle of incidence (front view): comparison of OpenFOAM (on the right) and Fluent (on the left) results

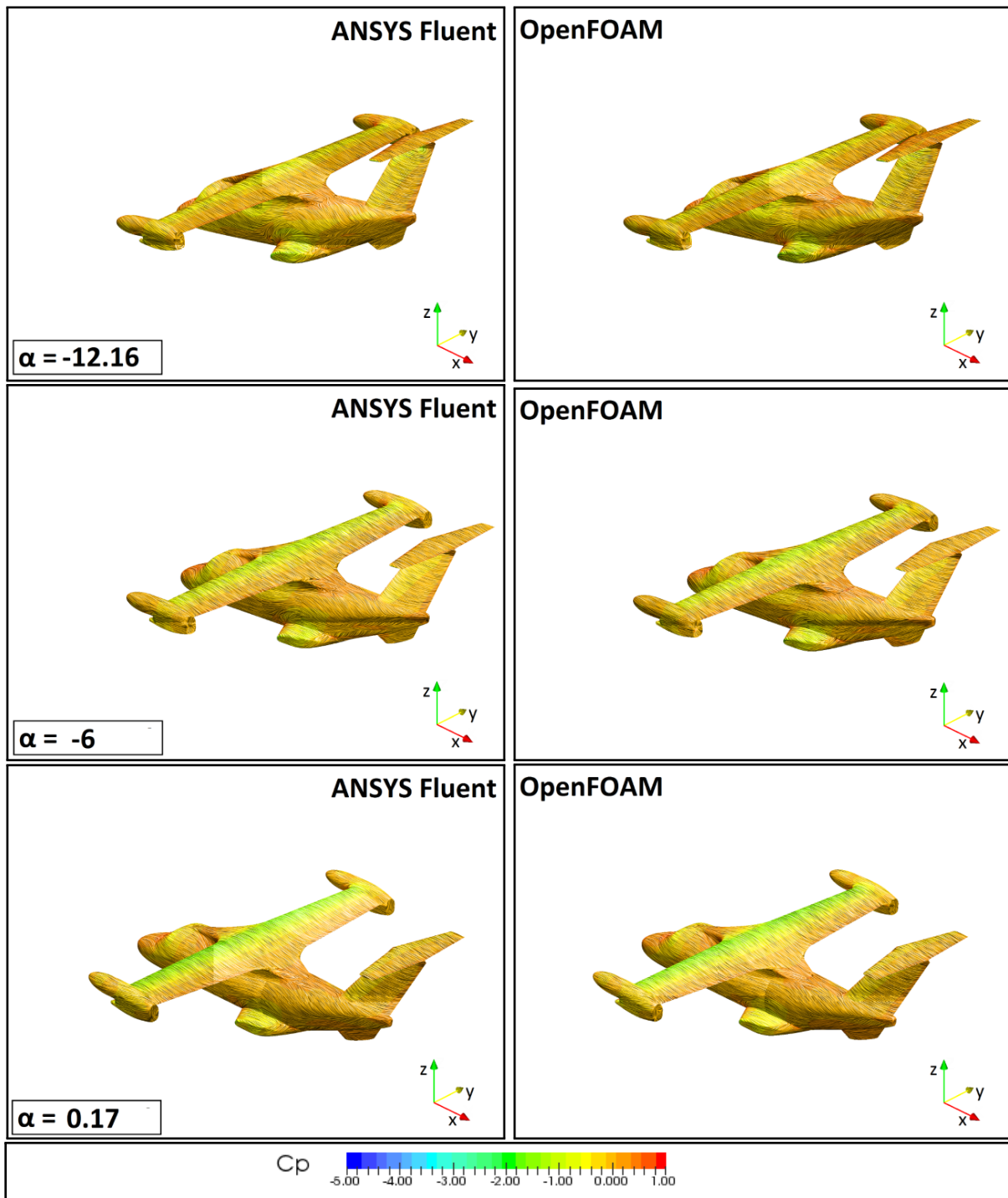
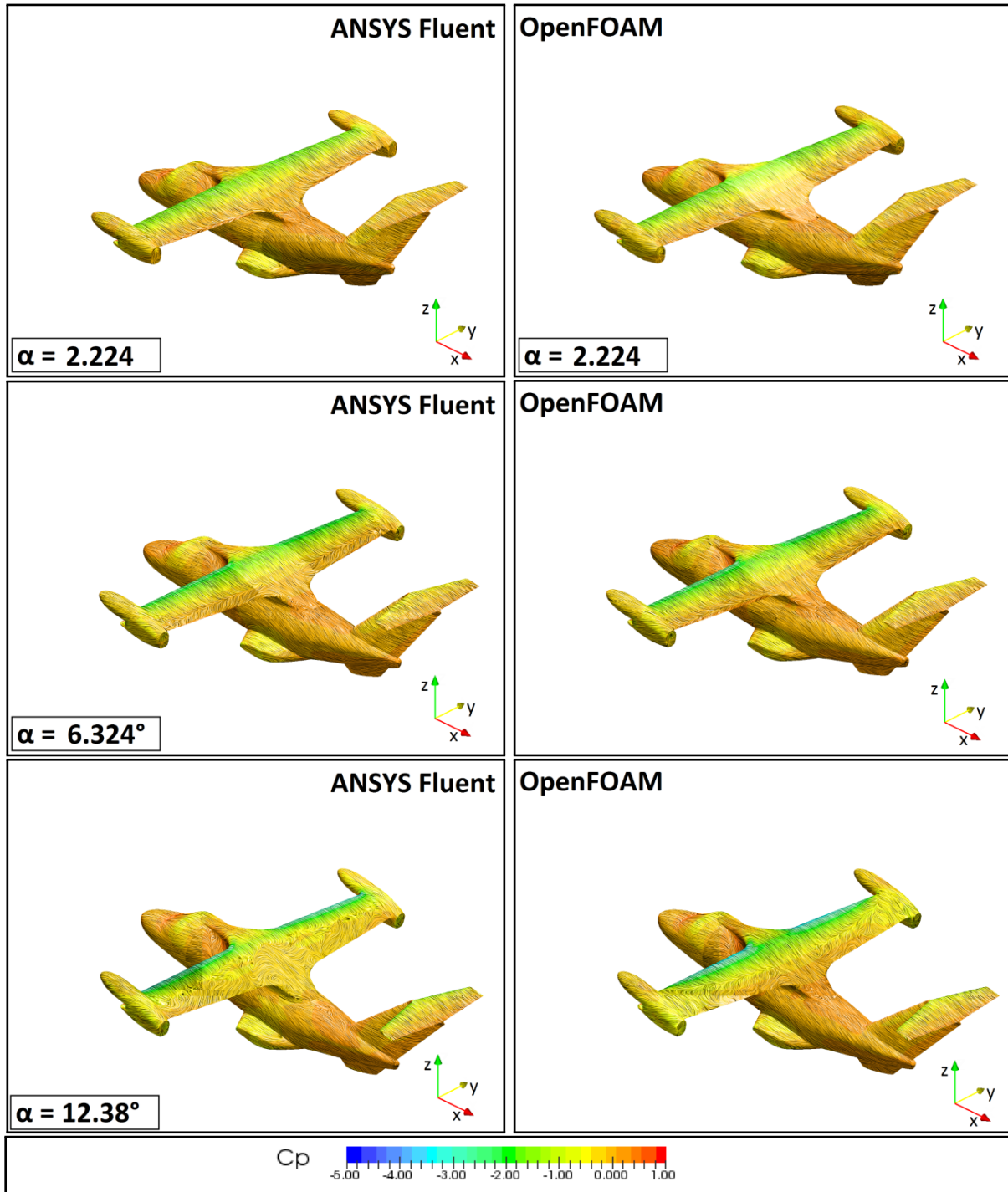
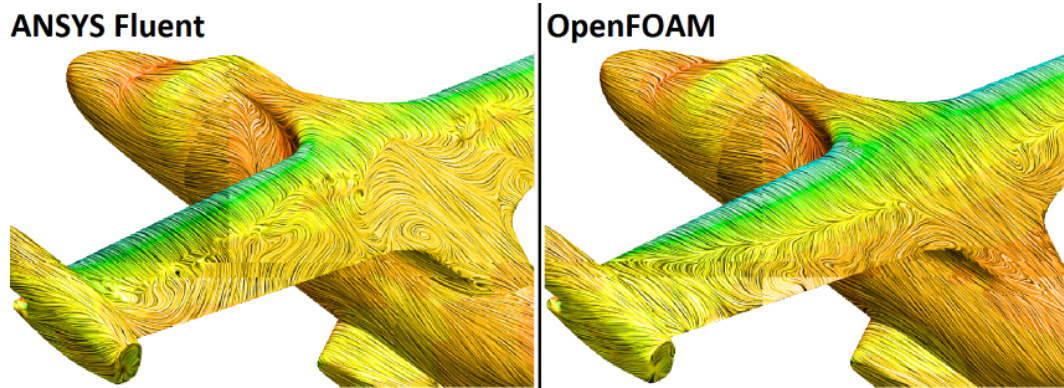


Figure 3.27: Friction lines over the tiltrotor model at various angle of incidence (rear view): comparison of OpenFOAM (on the right) and Fluent (on the left) results



**Figure 3.28:** Friction lines over the tiltrotor model at various angle of incidence (rear view): comparison of OpenFOAM (on the right) and Fluent (on the left) results



**Figure 3.29:** Detail of the friction lines in the wing-fuselage connection zone at  $\alpha = 12.38^\circ$

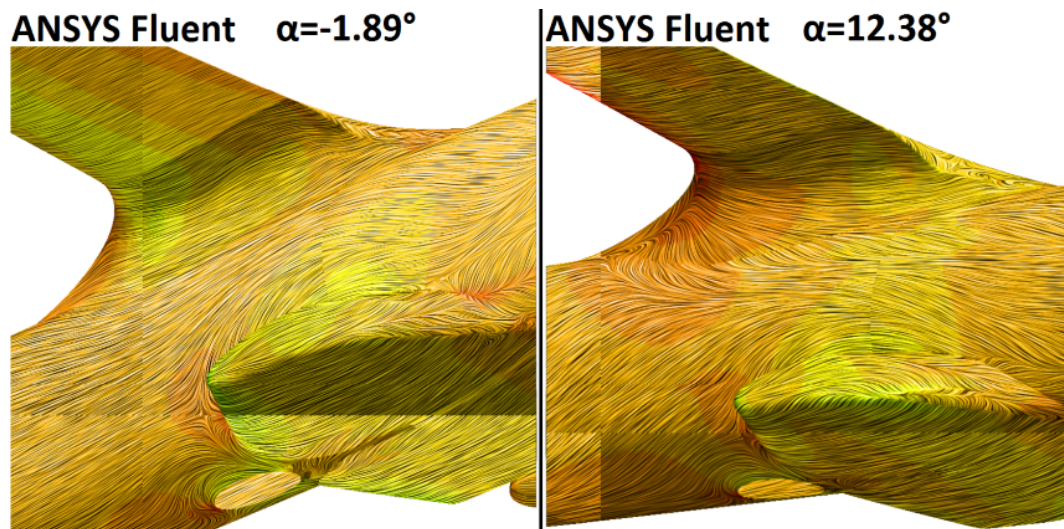


**Figure 3.30:** Detailed comparison of the friction lines (from Fluent analysis) in the rear part of the fuselage at  $\alpha = -1.89^\circ$  and  $\alpha = 12.38^\circ$

### 3.7 PIV Analysis

During the presented test campaign the aerodynamic loads have been measured, also considering the boundary layer transition and some flow visualization [38]. A further test campaign has been planned in order to investigate the characteristics of the wake released behind the fuselage model and the influence of the optimised sponsons with respect to the original ERICA configuration [39]. The wake characterization has been carried out at RUAG LWTE immediately after the DREAM-TILT project on a limited number of test conditions. The flow field measurements have been performed by Stereo PIV measurements on several cross-planes for different model attitudes conditions [40].

The results obtained by the numerical analysis, using ANSYS Fluent and OpenFOAM are quite similar; on the other hand, they are not totally consistent with the wind tunnel experimental PIV data. The experimental results have been conducted by the RUAG and consider flowfield measurements at several distances from the fuselage. Figure 3.31 illustrates the considered planes for the PIV analysis.

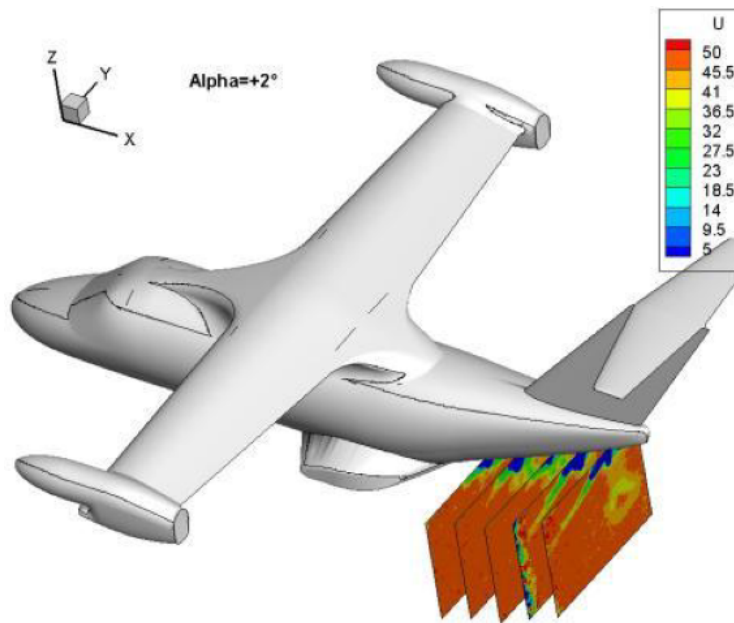


**Figure 3.31:** Graphical illustration of the considered planes for the PIV analysis

The contour plots of the velocity field for the considered planes have been illustrated from Figure 3.32 to Figure 3.34.

The first case study has discussed the results for the angle of incidence  $\alpha = +2^\circ$ . Both ANSYS Fluent and OpenFOAM have shown a good agreement in the determination of the wake behind tiltrotor shape, while an expansion discrepancy between numerical models and experimental PIV data occurred in z and y directions. In z-direction, the wake predicted by the CFD codes is more extended than the PIV results, on the other hand, in y-direction it is slightly underestimated.



In the second case study the incidence angle  $\alpha = 0^\circ$  has been investigated. The predicted shape by the numerical models is different compared to the experimental data. However, in z-direction the wake was well captured while in y-direction again the PIV experimental data has a wider extension.

The last case represents the cruise attitude at  $\alpha = -2^\circ$ ; the numerical codes show again a similar behaviour in the wake's shape prediction. However, in this particular case, OpenFOAM has shown a better agreement with experimental data in both z and y directions of wake expansion, while ANSYS Fluent seemed to slightly overestimate the wake dimension in z-direction and underestimate it in y-direction. Nevertheless, the development of the wake, evaluated by the numerical codes, had similar overall behaviour to the PIV experimental data in the x-direction of the flow: in the last planes (1850 mm and 1950 mm) is clearly shown the same pattern of wake separation with a drop shape. The pattern is slightly different; in ANSYS Fluent, the shape of the wake appears more stretched in the z-direction, while OpenFOAM shows a good agreement with the PIV data in the determination of the extension of the wake.

In general, the ANSYS Fluent model appears to be more dissipative than OPENFOAM, especially in the z-direction, while OpenFOAM is better in predicting the intensity of the wake in the zone adjacent to the tiltrotor. The comparison of the development of the wake evaluated by the numerical solvers is furthermore presented from Figure 3.35 to Figure 3.36. Both the codes show a good agreement in the prediction of the shape of the wake, however a slightly lower intensity is found in the OpenFOAM analysis. In the OpenFOAM analysis the pressure gradient  $\frac{dp}{dx}$  presents a global lower intensity and the changes in the develop of the wake appear to be slightly delayed compared to the ANSYS Fluent model. This delay is consistent with the cross extension of the wake of the PIV results. Furthermore, the intensity of the velocity field in the wake, resulting from ANSYS Fluent, anticipates the intensity values found in PIV analysis while OpenFOAM appears to be more consistent with the experimental results. The effect is an extension of the total length of the wake in the flow direction resulting from the ANSYS Fluent analysis.

Finally, Figure 3.37 shows the analysis of the x-component (the flow direction) of the Vorticity flowfield for the cruise attitude case ( $\alpha = -2^\circ$ ). The contours derived from OpenFOAM present a slightly lower intensity in the vorticity parameter compared to the ANSYS Fluent, however both the numerical analysis are not totally consistent with the PIV data, as found in the velocity flowfield analysis presented in Figure 3.32. The vorticity contours of the numerical data underline the presence of two counter-rotating vortex below the fuselage of the tiltrotor as found in the PIV analysis. The numerical codes overestimate the extension in z-direction of the vortex: OpenFOAM is more consistent with the PIV results, however the intensity of the x-component of the vorticity appears to have a less intensity

compared to Ansys FLUENT analysis and PIV data. In the zone far from the fuselage the numerical codes show a good agreement with the PIV data in the determination of the presence of the two vortices. On the other hand, in the proximity of the tiltrotor the PIV results present a lack of data, therefore the accuracy in this zone can not be considered optimal and a comparison with numerical data could not be considered reliable.

It is important to underline the consistency of the lift and drag coefficients resulting from the numerical analysis with the coefficients calculated from the experimental results. The discrepancies of the ANSYS Fluent analysis are in the range of 3% for the lift and the 14% for the drag, whereas OpenFOAM analysis shows deviation of about 8% in the Lift and about 11% in the Drag estimation. The deviations of the used model in the entire range of analysed angles of attack can be found in Table 3.16.

The PIV test campaign has also investigated the shape of the wake for the optimized configuration of the tiltrotor; the same conclusions discussed above can be drawn for the second configuration. Appendix A reports the results of the PIV analysis.

Finally, the analysis of the Vorticity flowfield is presented in Figure 3.37 for the cruise attitude case ( $\alpha = -2^\circ$ ). The contours derived from OpenFOAM present a less intensity of the vorticity parameter compared to the ANSYS Fluent; however, both the numerical analysis are not consistent with the PIV data, as found in the velocity flowfield analysis presented in Figure 3.32.

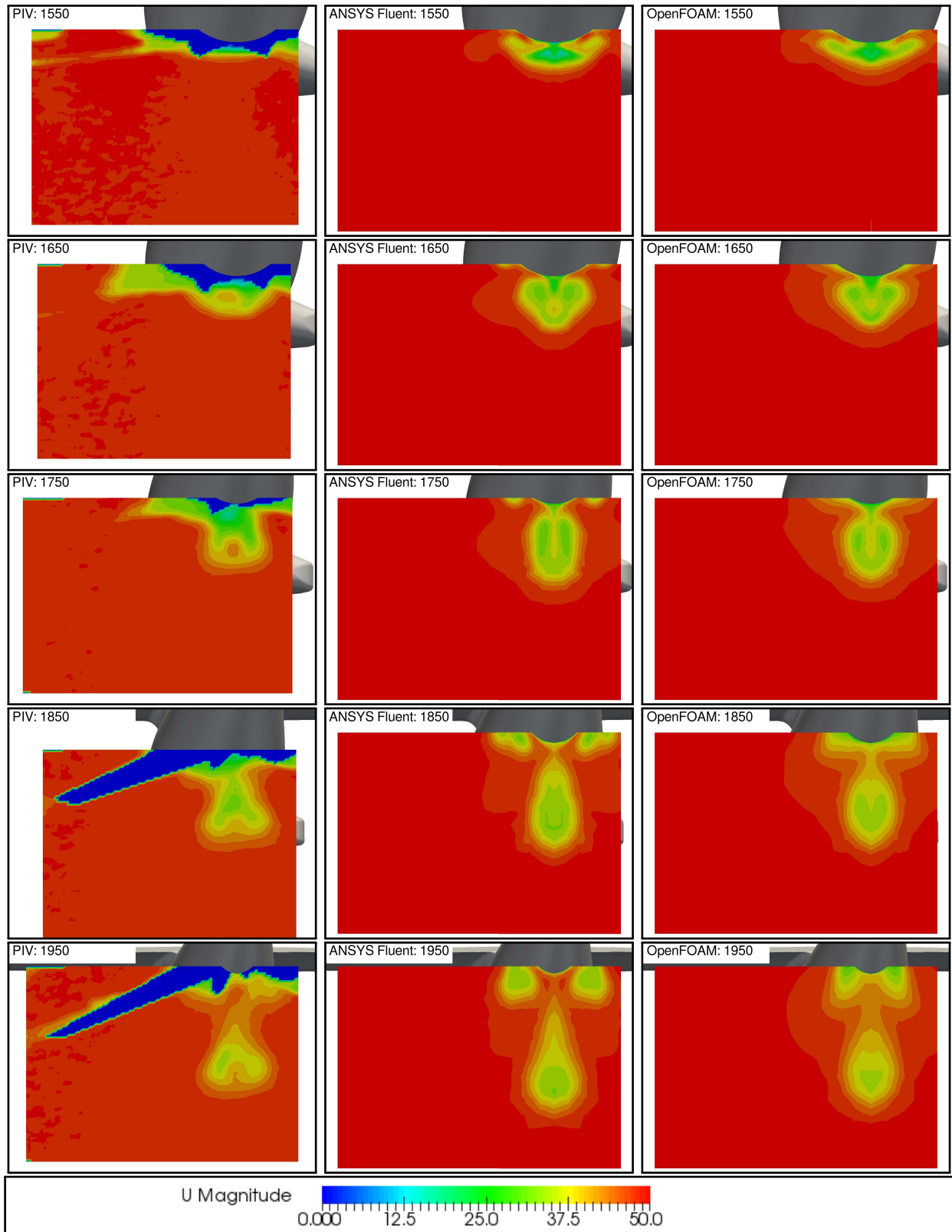


**Figure 3.32:** Velocity contours in the wake of the baseline model, case  $\alpha = -2^\circ$ : the comparison among PIV data, ANSYS Fluent and OpenFOAM analysis is illustrated for the considered planes.

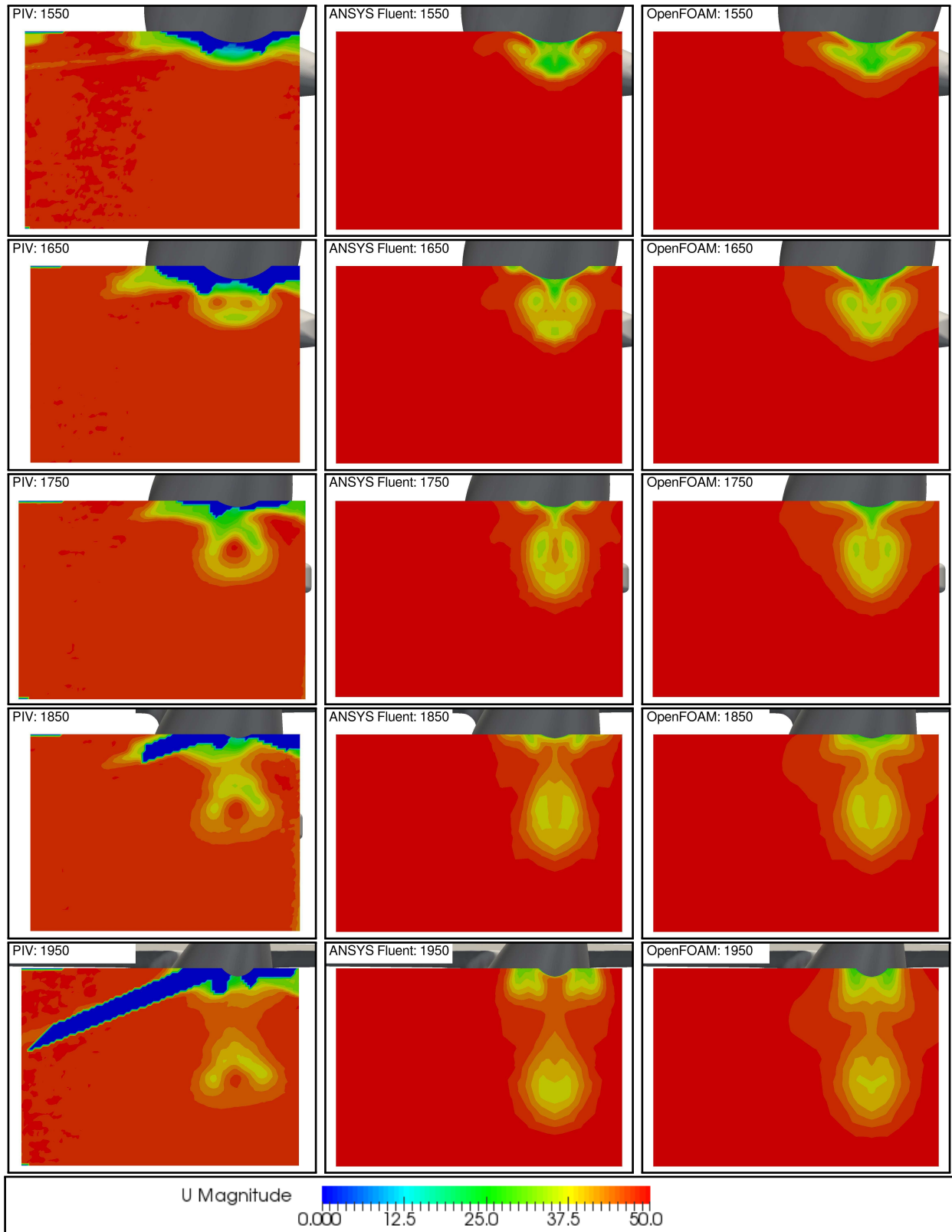


**Figure 3.33:** Velocity contours in the wake of the baseline model, case  $\alpha = 0^\circ$ : the comparison among PIV data, ANSYS Fluent and OpenFOAM analysis is illustrated for the considered planes

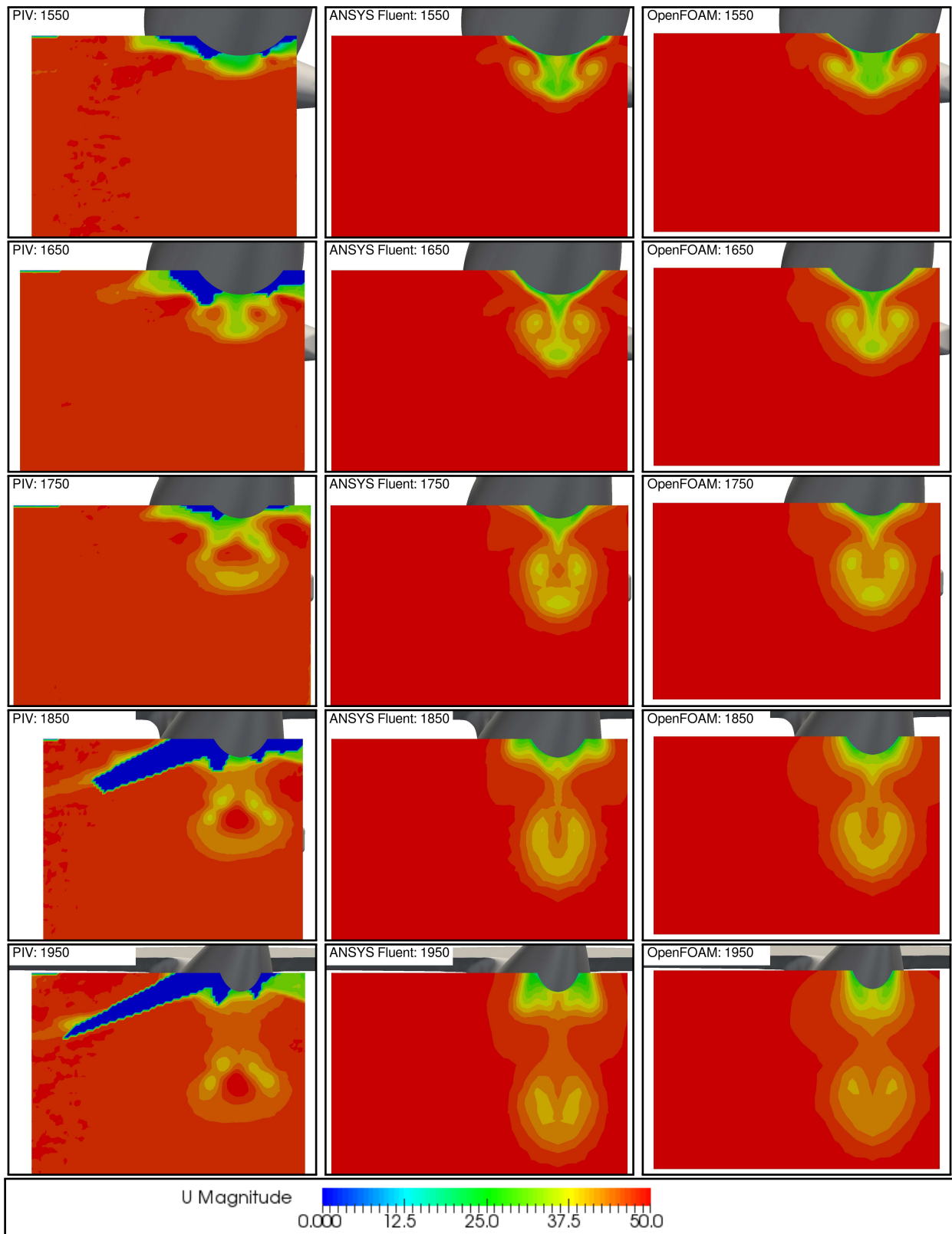


**Figure 3.34:** Velocity contours in the wake of the baseline model, case  $\alpha = +2^\circ$ : the comparison among PIV data, ANSYS Fluent and OpenFOAM analysis is illustrated for the considered planes

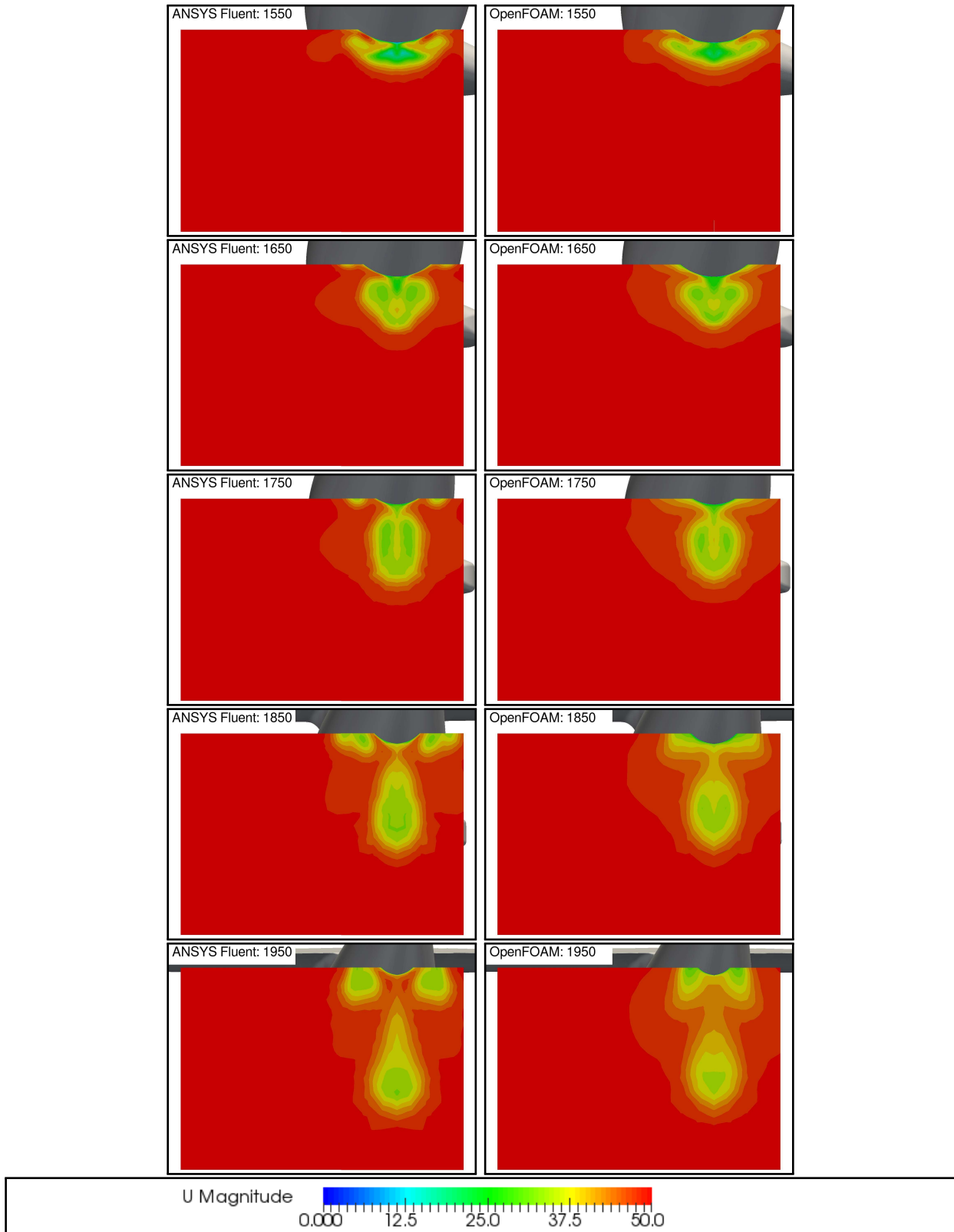


**Figure 3.35:** Velocity contours in the wake of the baseline model, case  $\alpha = -2^\circ$ : the comparison among ANSYS Fluent and OpenFOAM analysis is illustrated for the considered planes

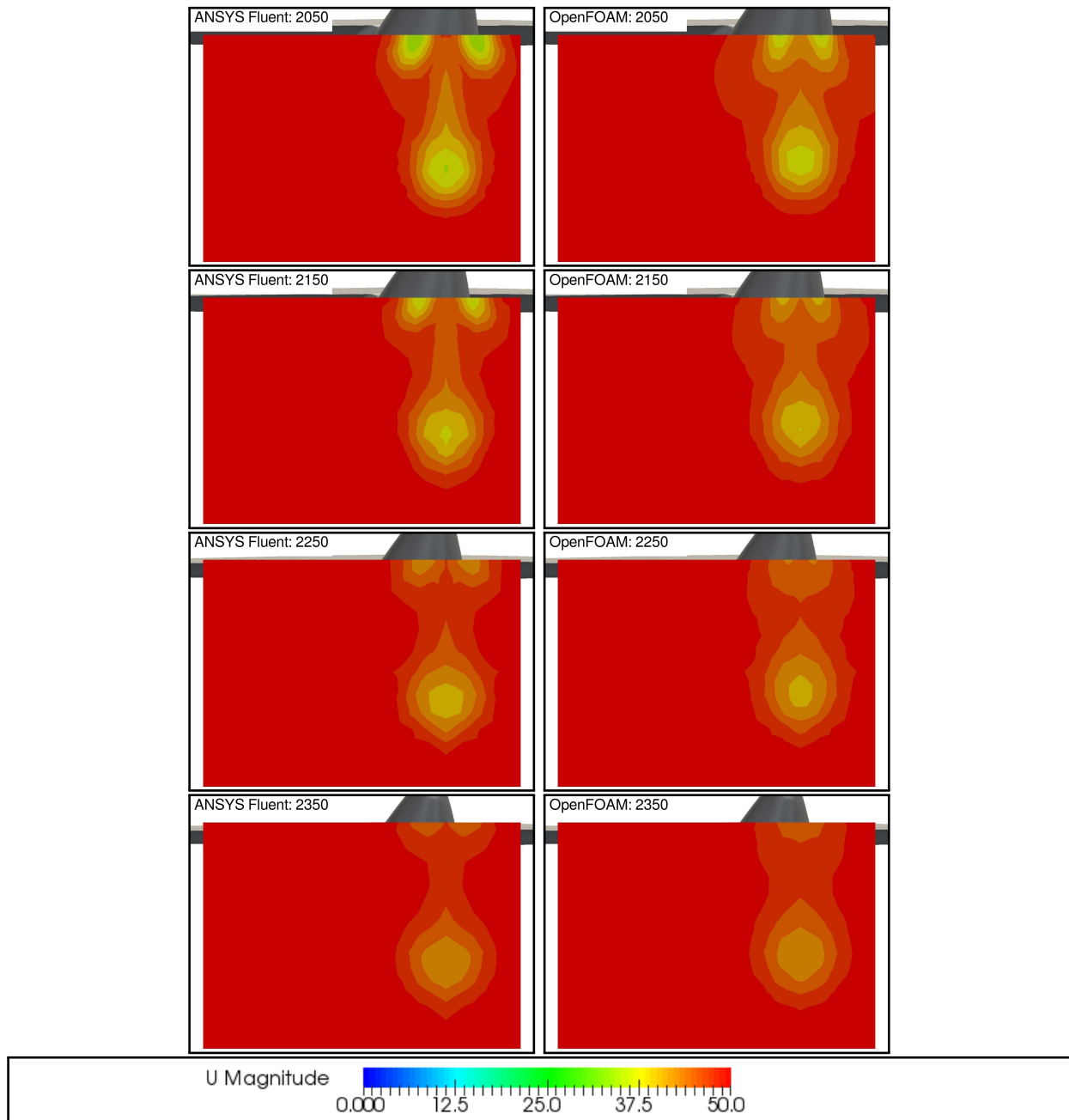


**Figure 3.36:** Velocity contours in the wake of the baseline model, case  $\alpha = -2^\circ$ : the comparison among ANSYS Fluent and OpenFOAM analysis is illustrated for further planes (2050mm, 2150mm, 2250mm 2350mm)

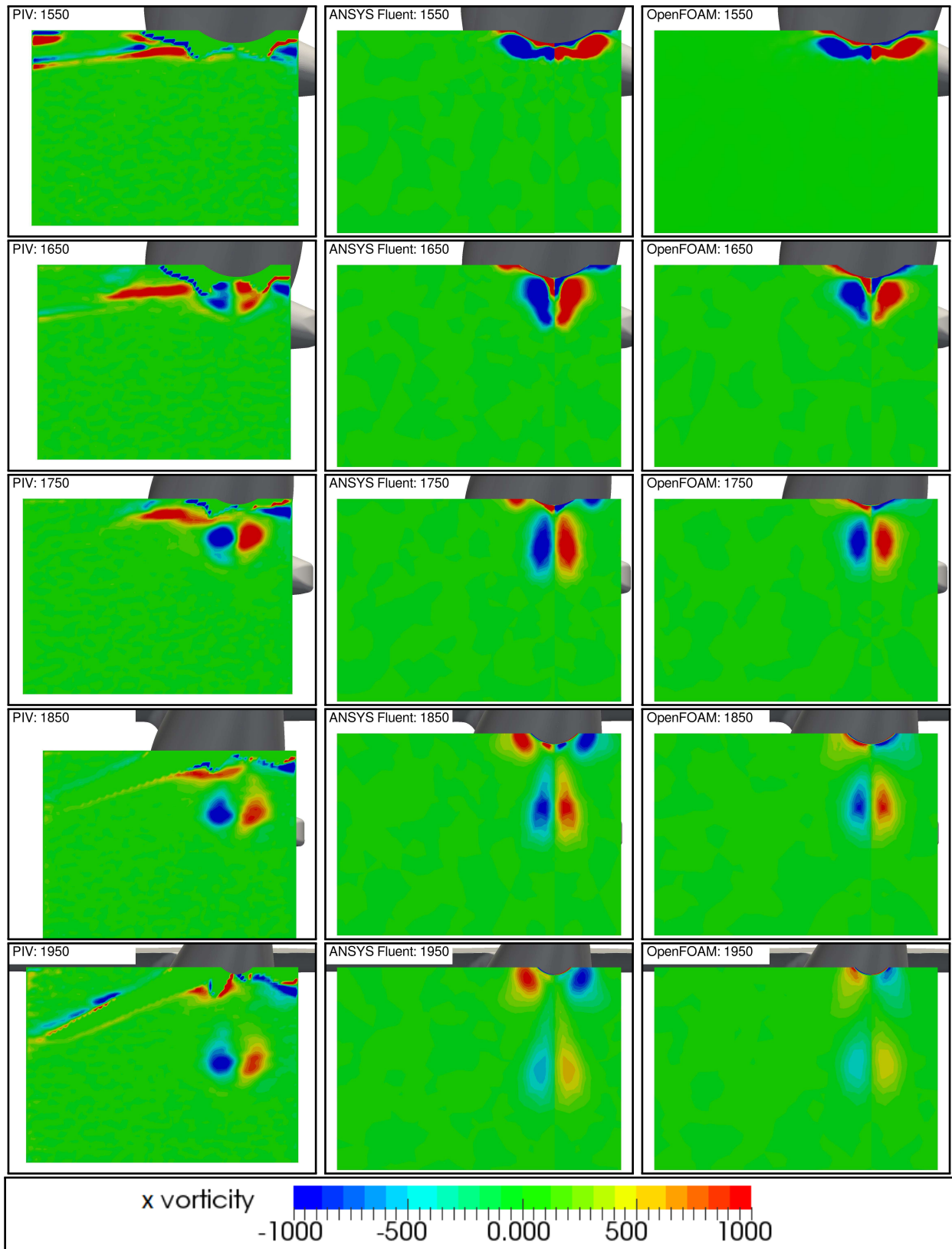


**Figure 3.37:** Contours of the x-component of the vorticity in the baseline model, case  $\alpha = -2^\circ$ : the comparison among PIV data, ANSYS Fluent and OpenFOAM analysis is illustrated for the considered planes





# Conclusions

In Chapter 3, the performances of the baseline configuration of ERICA tiltrotor have been analysed through two CFD software: the commercial ANSYS Fluent and the open source OpenFOAM.

Firstly, the procedure to clean and simplify the geometric model is explained and the parameters adopted to generate the 2D and 3D mesh are illustrated. The quality of the mesh is also presented in terms of skewness and aspect ratio. Both the analysis use a compressible solver and the same boundary conditions set (the total pressure is specify at the inlet and the static pressure at the outlet). In order to stabilize the analysis, both the adopted solution strategies disable the energy equation for the first 50 iterations. The numerical results are presented in terms of global aerodynamic coefficients, flow distortion, total pressure losses and flow separation phenomena.

In the ANSYS Fluent, an excellent correlation between experimental and numerical data has been found at low and medium angles of attack. The lift coefficient calculation is very accurate, with a maximum discrepancy of 3.55%. The drag polar is in a good accordance with the experimental results, however for  $\alpha > 4^\circ$  the numerical calculations underestimate the drag with respect to experimental data. In OpenFOAM analysis, the lift coefficient values present a deviation of about [5-10%], slightly higher than ANSYS Fluent, however the drag coefficient calculations are in a better accordance with the experimental results; the deviations assume a lower value for almost the whole range of angles of incidence.

The further analysis regarded the pressure coefficient distribution on the surface of the tiltrotor. The  $C_P$  values have revealed to be quite similar between the two codes; slightly differences are registered only for the highest angles of attack.

The total pressure losses analysis revealed again a similar behaviour between ANSYS Fluent and OpenFOAM. Some differences are found at high incidence angles : ANSYS Fluent shows the formation of a stall in central part of the main wing that causes the separation of the flow downstream. On the other hand, in OpenFOAM analysis the losses seem to be related to a flow separation that originates in the external part of the wings, near the nacelle.

Finally, the numerical results have been compared with the PIV experimental data. The results obtained by both the codes are quite similar, however, they are not totally consistent with the wind tunnel experimental PIV data. The numerical analysis show a wake more extended in z-direction and slightly underestimated in y-direction than the PIV results. OpenFOAM revealed to be more consistent with PIV results, however the developed wake seems to have a less intensity compared to ANSYS Fluent and experimental data.

In conclusion, OpenFOAM revealed to be an excellent open source alternative to the commercial software, for the considered fluid dynamic analysis. The calculations are consistent with both experimental data and ANSYS Fluent analysis. It confirmed to be very accurate, especially in the prediction of the drag coefficients in the entire range of angles of incidence. Also the determination of the intensity of the wake seems to be slightly better predicted in OpenFOAM than in ANSYS Fluent.

## Nomenclature Part I

$A$ [ $m^2$ ]	Wing surface
$c$ [ $J/kg/k$ ]	Specific heat
$c$ [ $m$ ]	Wing aerodynamic mean chord
$C_D$ [-]	Drag coefficient
$C_L$ [-]	Lift coefficient
$C_M$ [-]	Pitching moment coefficient
$C_P$ [-]	Static pressure coefficient
$C_{P\_tot}$ [-]	Total pressure coefficient
$D$ [ $N$ ]	Drag Force
$E$ [ $J/kg$ ]	Specific energy
$k$ [ $J/kg$ ]	Turbulent kinetic energy
$h_0$ [ $J$ ]	Total entalpy
$i$ [ $J/kg$ ]	Internal energy
$I$ [-]	Turbulence intensity
$k$ [ $W/m/k$ ]	Thermal conductivity
$L$ [ $N$ ]	Lift Force
$M$ [-]	Mach Number
$M_Y$ [ $Nm$ ]	Pitching moment
$n$ [-]	Vector normal component to the surface
$p$ [ $Pa$ ]	Static pressure
$p_0$ [ $Pa$ ]	Total pressure
$p_{0\infty}$ [ $Pa$ ]	Total freestream pressure
$p_{Ref}$ [ $Pa$ ]	Reference pressure
$p_\infty$ [ $Pa$ ]	Freestream Pressure
$\bar{q}$ [ $W$ ]	Heat flux vector
$\vec{r}$ [ $m$ ]	Position of a rotating point
$s_{i,j}$ [ $s^{-1}$ ]	Rate of linear deformation
$S_E$ [ $J/kg$ ]	Source term of internal energy equation
$S_E$ [ $kg * m/s$ ]	Source term of energy equation
$S_{M_x}$ [ $kg * m/s$ ]	Source term of x-component of momentum
$S_{M_y}$ [ $kg * m/s$ ]	Source term of y-component of momentum

$S_{Mz}$ [ $kg * m/s$ ]	Source term of z-component of momentum
$t$ [ $s$ ]	Time
$T$ [ $k$ ]	Temperature
$T_0$ [ $k$ ]	Total temperature
$u$ [ $m/s$ ]	X-component of the velocity vector
$u_{avg}$ [ $m/s$ ]	Average velocity
$\bar{u}$ [ $m/s$ ]	Velocity vector
$\vec{u}_r$ [ $m/s$ ]	Whirl velocity
$v$ [ $m/s$ ]	Y-component of the velocity vector
$\vec{v}$ [ $m/s$ ]	Absolute velocity
$\vec{v}_r$ [ $m/s$ ]	Relative velocity
$V$ [ $m^3$ ]	Volume
$V_\infty$ [ $m/s$ ]	Freestream velocity
$w$ [ $m/s$ ]	Z-component of the velocity vector
$\Gamma$ [ $m^2/s$ ]	Diffusion coefficient
$\lambda$ [ $Pa * s$ ]	Bulk viscosity
$\mu$ [ $kg/m^3$ ]	Dynamic viscosity
$\mu_T$ [ $kg/m^3$ ]	Turbulent viscosity
$\omega$ [ $s^{-1}$ ]	Specific rate of turbulence dissipation
$\omega$ [ $rad/s$ ]	Rotational Velocity
$\vec{\omega}$ [ $-$ ]	Rotational Axis
$\phi$ [ $-$ ]	Generic property of the fluid
$\Phi$ [ $N/s$ ]	Dissipation function
$\rho$ [ $kg/m^3$ ]	Fluid density
$\tau_{i,j}$ [ $Pa$ ]	Viscous stress

## Part II

# Development of an Optimization Environment for the Horizontal Axis Wind Turbine Design



# Introduction and Background

The Horizontal Axis Wind Turbine (HAWT) represents the most common architecture among existing wind energy conversion systems, with thousands of MWs of new capacity worldwide installed each year. Its design process, largely accepted by manufacturers as well as by academic institutions, is generally separated in two consecutive stages [45]:

- the external geometry of the blade (in terms of both chord and twist angle distribution along the blade span, rotor size and other factors, often empirical, related to the cost of energy) is first determined using a Blade Element Momentum (BEM) based algorithm;
- a proper layout of both blade skin and reinforcements is determined by means of a structural analysis based on the finite element method (FEM), considering both the aerodynamic and inertial loads acting on the blade.

Both stages have been widely investigated by several authors. Liu and Janajreh [46] proposed an improved BEM model for the analysis of HAWT performance, considering both the tip loss effect and the rotational one, with the aim of extending its application to the turbulent wake regime. Refan and Hangan [47] investigated the aerodynamic performance of a 2.2 m diameter three-bladed HAWT in order to assess the applicability of the BEM Theory for the modelling of small scale rotors. ElQuatary and Elhadidi [48] compared BEM and Computational Fluid Dynamics (CFD) simulations for two HAWTs characterized by different blade thickness, registering a marked agreement especially for the thicker blade configuration. Kong et al. [49] proposed a structural design of a medium scale composite HAWT blade made of E-glass/epoxy. Several design load cases (such as aerodynamic forces, those due to ice accumulation, hygro-thermal and mechanical loads) were considered and the most dominant design parameters were included in a FEM analysis, also estimating the fatigue life of the blade. Among numerical optimization methods, particular relevance is nowadays assumed by evolutionary algorithms, whose solutions are generated on the basis of techniques inspired by natural evolution. As observed by Mendez and Greiner [50], genetic algorithms are global optimizers that have a wide trade-off between exploration and exploitation of the space problem: among their advantages, a global search capability



---

is to be recognized, due to the management of a population of candidate solutions instead of only one. Moreover, their only requirement is the knowledge of the fitness function, without any other consideration such as its derivability or continuity. A great number of engineering problems can be dealt with genetic algorithms [51]: Benini and Toffolo [52] performed a multi-objective optimization for the design of stall-regulated HAWTs, coupling the BEM Theory and a multi-objective evolutionary algorithm, with the scope of achieving the best trade-off between annual energy production per square meter and cost of energy. Cai et al. [53] developed a structural optimization of an HAWT blade using a particle swarm optimization algorithm based on FEM calculations, proving a great potential improvement on overall structural blade performance. Dal Monte et al. [54] improved the structural response of the AOC 15/50 Sandia blade using the S.O.C.R.A.TE. (Structural Optimization for Composite Rotor Air TurbinE) algorithm: both the choice of the employed materials and their placement in the layout of the blade skin were considered as design variables for the optimization, obtaining a marked reduction in the mass of the blade and a corresponding increment of its flapwise rigidity. An optimization procedure for a HAWT blade based upon an ultimate limit state analysis was proposed by Hu et al. [55]. In order to minimize the blade cost and its total mass, two different composite materials, such as glass fiber reinforced plastic (GFRP) and carbon fibre reinforced plastic (CFRP) were considered, being the design variables of the blade skin the input parameters for a combined FEM and evolutionary algorithm analyses. Several tools for the multi-disciplinary wind turbine optimization have been proposed in the open literature in the last years; Pourrajabian et al. [56] proposed a procedure for the aero-structural design of a small wind turbine blade based on a BEM code and on a simple structural model. Bottaso et al. [57] described a procedure for the multidisciplinary optimization of wind turbines with a parametric high fidelity aero-servo-elastic model, considering the Annual Energy Production and the Weight of the blade as cost functions. Ashuri et al. [58] also developed a multidisciplinary optimization for the design of offshore wind turbines; the considered objective functions is represented by the levelized cost of energy and it included design constraints as stresses, deflections modal frequencies and fatigue limits. Grujicic et al. [59] proposed a multidisciplinary design optimization procedure for the development of the cost effective composite layout of an HAWT using the Cost of Energy (COE) as single fitness function. In the cited tools, the multi-objective design is not formulated as a Pareto optimal problem but using a combined cost (AEP divided by total weight), a levelized cost of energy or the Cost Of Energy only. Even though aerodynamic and structural optimizations of HAWT blades have been widely proposed by several authors, in reviewing the literature, the potential of an evolutionary algorithm based on the coupling of an aerodynamic model (based upon the BEM Theory) and a structural one (based on a FEM analysis) have been not often investigated; Zhu et al. [60] proposes

---

an aerodynamic and structural integrated optimization for the HAWT Blades design, Wang et al. [61] developed an aerodynamic and structural integrated design optimization method for a composite wind turbine blade based on multidisciplinary design optimization (MDO). Gradient-based optimizers have also proved their capabilities in aerospace optimization. They have played and continue to play a key role during the aero-structural design of the aircraft. Ghommem et al. [62] implemented a shape optimization of flapping wings in forward flight, combining a gradient-based optimizer (GCMMA) with the unsteady vortex lattice method (UVLM). Gillebart et al. [63] presented a two-dimensional low-fidelity aero-elastic analysis of an airfoil and a gradient based optimization (GCMMA) consisting of a coupled potential flow model and curved Timoshenko beam model combined with a boundary layer model. A great advantage of the gradient-based optimizer is to handle a large number of design variables and constraints; furthermore they result faster and less computational expensive compared to genetic algorithms, however a potential weakness is the relative intolerant of difficulties such as noisy objective function spaces and topology optimization; additionally they find a local rather than a global minimum [64]. The characteristics of the analysed problem potentially involve several local minimum, furthermore the evaluation of both aerodynamic and structural function is not expensive in terms of time. For such reason the genetic algorithm formulation has been chosen as optimization method over the gradient based formulation.

The proposed optimizations are based on a genetic algorithm. The first analysis (Chapter 5) considers at the same time both BEM and FEM genes, in order to determine an aerodynamic fitness function and a structural one. The purpose is therefore to increase both the power production and the flapwise rigidity of the blade, using an iterative BEM-FEM analysis. A further development of the optimization environment allows to also implement several definition of the Cost Of Energy as objective functions, to use an extended version of the BEM algorithm and to specify the characteristics of installation site of the wind turbine. In the analysis proposed in Chapter 6, the AOC 15/50 Sandia wind turbine is hence also optimized for the Annual Energy Production density, to be maximized, and for the Levelized cost of Energy to be minimized. Finally, a numerical validation of the performances of the AOC 15/50 wind turbine is also presented in Chapter 7.



## Chapter 4

# BEM Theory for Horizontal Axis Wind Turbine

### 4.1 1D Momentum Theory for an Ideal Wind Turbine

A wind turbine is a machine that intercepts the wind and converts its kinetic energy first to mechanical energy and, finally, to electric energy. The used method to predict the performances of an Horizontal Axis Wind Turbine is described in Hansen [41]. A first hypothesis made in the 1D model consists in considering the rotor as an ideal permeable disc, without friction and rotational components of the wake. The rotor disc can be assimilated to a drag device that slows the wind speed from the undisturbed velocity  $V_0$ , first to the  $u$  value in the rotor plane, then to  $u_1$  value in the wake. A consequence is the divergence of the streamlines, as shown in Figure 4.1. The pressure drop in the rotor plane originates the drag force; the pressure slightly increases its value close upstream the rotor from the atmospheric level  $p_0$  to  $p$ , drop of  $\Delta p$  in the rotor plane and, downstream, it recovers to the undisturbed level. The axial velocity decreases continuously from  $V_0$  to  $u_1$ .

It is possible to derive a simple relationship between the velocities, the thrust  $T$  and the absorbed shaft Power  $P$ . The thrust is caused by the pressure drop and reduces the velocity value from  $V_0$  to  $u_1$ .

$$T = \Delta p A$$

where  $A = \pi R^2$  is the area of the rotor.

Applying the Bernulli Equation (hypothesis of stationary, incompressible, frictionless flow without external forces acting on it) in the fluid domain, upstream and downstream the rotor, results:

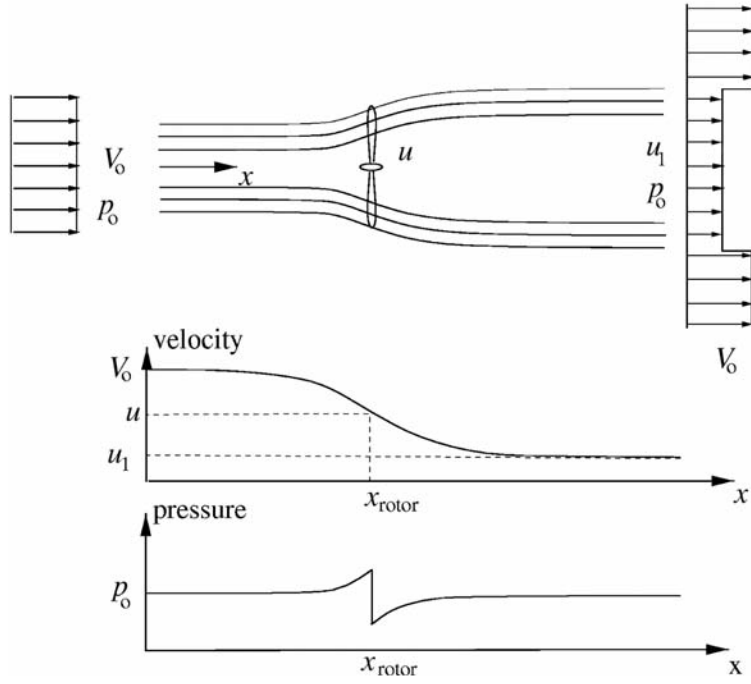


**Figure 4.1:** Streamlines distribution in the considered 1D model; velocity and pressure distributions upstream and downstream

$$p_0 + \frac{1}{2}\rho V_0^2 = p + \frac{1}{2}\rho u^2$$

$$p - \Delta p + \frac{1}{2}\rho u^2 = p_0 + \frac{1}{2}\rho u_1^2$$

Combining the two equations, the pressure drop is:

$$\Delta p = \frac{1}{2}\rho(V_0^2 - u_1^2)$$

Once a circular control volume with sectional area  $A_{cv}$  is defined around the wind turbine, (Figure 4.2) **the axial momentum equation**, in its integral form, can be applied:

$$\frac{\delta}{\delta t} \int \int \int_{cv} \rho u(x, y, z) dx dy dz + \int \int_{cs} u(x, y, z) \rho V \cdot dA = F_{ext} + F_{pres*}$$

where  $dA$  it is the vector normal to an infinitesimal area on the control surface and  $F_{pres}$  is the axial component of the pressure forces acting on the control volume. The first and the last terms are null for the hypothesis of stationary flow and atmospheric pressure acting on an equal area. Furthermore, the pressure on the lateral boundary control has no axial component.

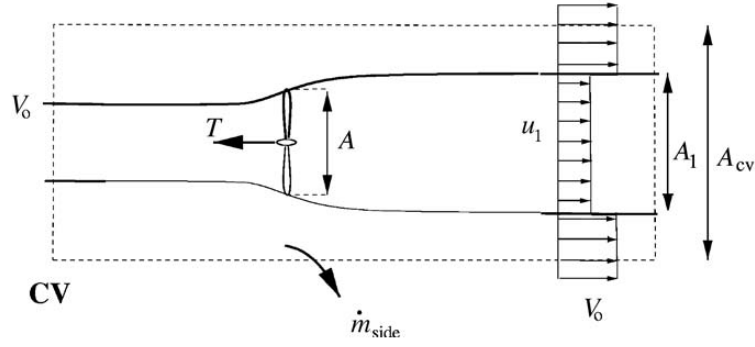


**Figure 4.2:** Circular control volume around the wind turbine

Using the simplified assumption, the equation yields:

$$\rho u_1^2 A_1 + \rho V_0^2 (A_{cv} - A_1) + \dot{m}_{side} V_0 - \rho V_0^2 A_{cv} = -T$$

The conservation of mass equation allows to calculate  $\dot{m}_{side}$ :

$$\rho A_1 u_1 + \rho (A_{cv} - A_1) V_0 + \dot{m}_{side} = \rho A_{cv} V_0$$

$$\dot{m}_{side} = \rho A_1 (V_0 - u_1)$$

Using the conservation of mass, it is also possible to relate  $A$  and  $A_1$  :

$$\dot{m} = \rho u A = \rho u_1 A_1$$

By combining the equations, it is possible to calculate the Trust:

$$T = \rho u A (V_0 - u_1) = \dot{m} (V_0 - u_1)$$

Using the trust formulation with the pressure drop  $\Delta p$ , it can be observed that the velocity in the rotor plane is the mean between the undisturbed wind speed  $V_0$  and the final value in the wake  $u_1$ :

$$u = \frac{1}{2} (V_0 - u_1) \quad (4.1)$$

An alternative control volume, contained among the streamlines, is introduced as shown in Figure 4.3.

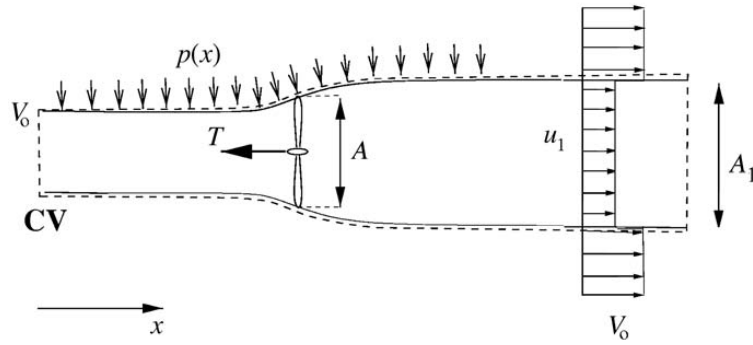


**Figure 4.3:** Alternative volume around the wind turbine

The net pressure distribution  $F_{pres*}$  and the resulting forces from pressure distribution on the lateral surface  $F_{lat}$  are unknown. In this case, there is no lateral mass flow and the **axial momentum equation** becomes:

$$T = \rho u A (V_0 - u_1) + F_{pres*} \quad (4.2)$$

Comparing the torque equations of the two cases, the net pressure force  $F_{pres*}$  on the alternative control volume results zero.

The integral energy equation can be applied on the control volume of Figure 4.3 in order to evaluate the shaft power  $P$ . The flow is indeed assumed to be frictionless and there is no change in the internal energy, from inlet to outlet.

$$P = \dot{m} \left( \frac{1}{2} V_0^2 + \frac{p_0}{\rho} - \frac{1}{2} u_1^2 - \frac{p_0}{\rho} \right) \quad (4.3)$$

Substituting  $\dot{m} = \rho u A$ :

$$P = \frac{1}{2} \rho u A (V_0^2 - u_1^2) \quad (4.4)$$

The **axial induction factor**  $a$  is defined from:

$$u = (1 - a) V_0 \quad (4.5)$$

The velocity  $u_1$  can be written using the axial induction factor:

$$u_1 = (1 - 2a) V_0 \quad (4.6)$$

The power  $P$  and the trust  $T$  can be calculated as functions of the axial induction factor:

$$P = 2\rho V_0^3 a(1-a)^2 A \quad (4.7)$$

$$T = 2\rho V_0^2 a(1-a) A \quad (4.8)$$

The available power in a cross section corresponding to the swept area  $A$  of the rotor is:

$$P = \frac{1}{2} \rho A V_0^3 \quad (4.9)$$

The power coefficient  $C_p$  is used in order to non-dimensionalize the power  $P$  with respect  $P_{avail}$ :

$$C_p = \frac{P}{\frac{1}{2} \rho A V_0^3} \quad (4.10)$$

The trust coefficient  $C_T$  is defined as:

$$C_T = \frac{T}{\frac{1}{2} \rho A V_0^2} \quad (4.11)$$

The power and trust coefficients can be evaluated using the axial induction factor:

$$C_P = 4a(1-a)^2 \quad (4.12)$$

$$C_T = 4a(1-a) \quad (4.13)$$

Differentiating  $C_P$  with respect to  $a$  leads to:

$$\frac{dC_P}{da} = 4(1-a)(1-3a) \quad (4.14)$$

The graph of the Equation 4.14 is shown in Figure 4.4: the theoretical maximum of the power coefficient is  $16/27$  when  $a=1/3$ , this is known as the *Betz Limit*.

Experimental results have found that the equation 4.13 is valid for an axial induction factor  $a$  of less 0.4 because of the assumption of an ideal wind turbine. Increasing  $C_T$  the expansion of the wake increases and, therefore, the velocity jump from  $V_0$  to  $u_1$ , as shown in Figure 4.5.

The continuity equation can be used to calculate the ratio between the areas  $A_0$  and  $A_1$ .

$$\frac{A_0}{A_1} = 1 - 2a \quad (4.15)$$



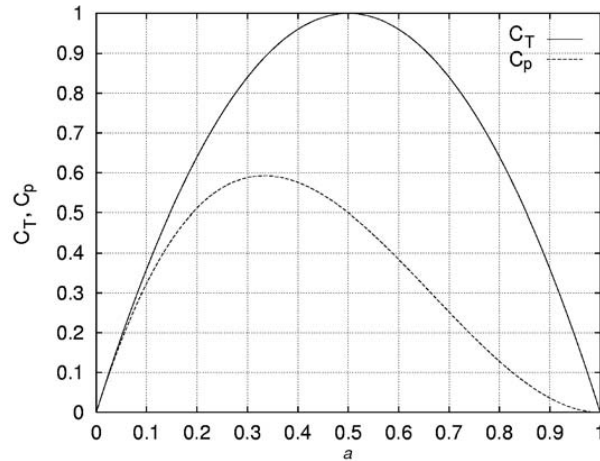


**Figure 4.4:** Power and trust coefficients  $C_P$  and  $C_T$  as function of the axial induction factor  $a$

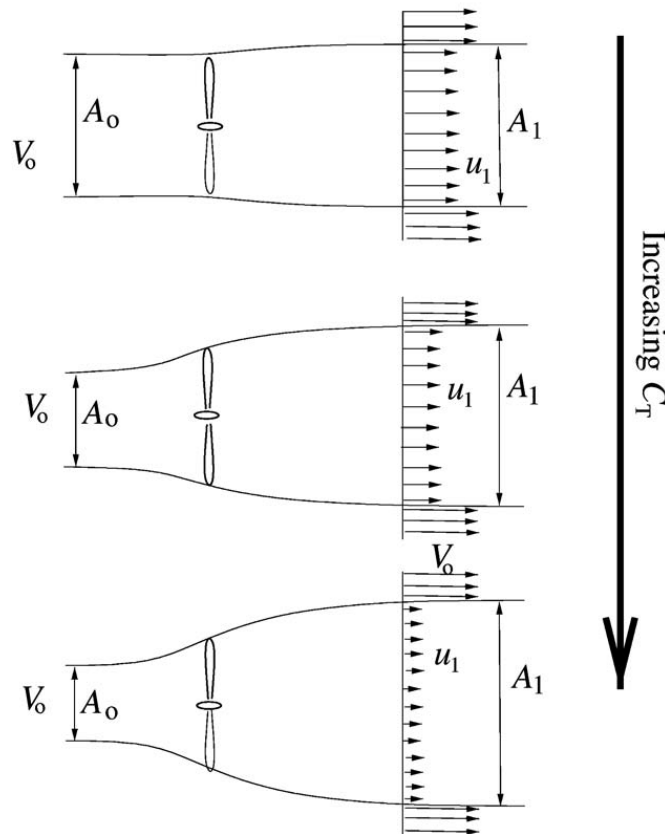


**Figure 4.5:** Expansion of the wake and velocity jump for the 1D ideal wind turbine model

For low wind speed, both high trust coefficient  $C_T$  and axial induction factor  $a$  are present. The momentum theory is not valid for  $a$  greater than 0.4: when the velocity jump becomes too high, eddies transport momentum from the outer flow into the wake that becomes unstable (turbulent-wake state), as can be observed in Figure 4.6.

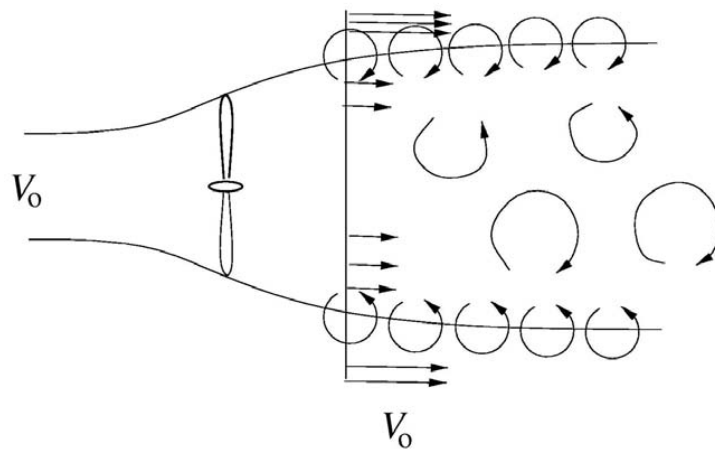


**Figure 4.6:** The turbulent-wake state induced by the unstable shear flow at the edge of the wake

## 4.2 Effects of Rotation

In an ideal rotor there is no rotation in the wake, hence the **Tangential Induction Factor**  $a'$  is 0. Considering an infinitesimal control volume of thickness  $dr$ , as shown in Figure 4.7, the power can be computed as:

$$dP = \dot{m}r\omega C_\theta = 2\pi r^2 \rho u \omega C_\theta dr \quad (4.16)$$

where  $C_\theta$  is the azimuthal component of the absolute velocity and  $u$  the axial velocity through the rotor.

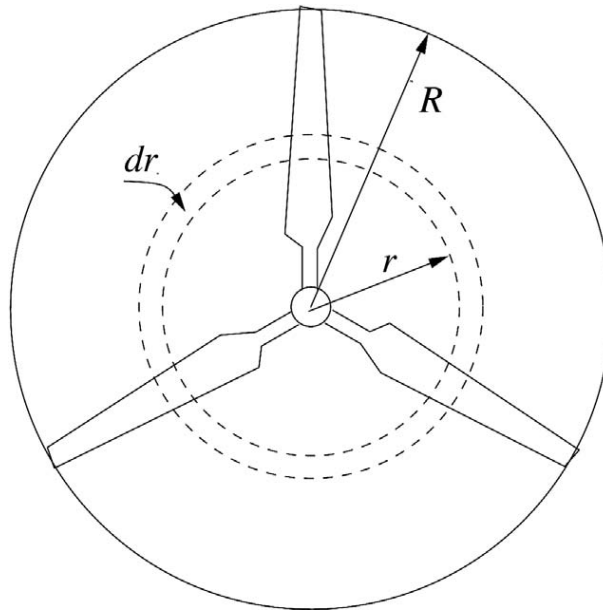


**Figure 4.7:** Schema of a 3 blade rotor

Figure 4.8 illustrates the component of the velocities for a section of the rotor. The relative velocity upstream of the blade  $V_{rel,1}$  is composed by the axial velocity  $u$  and the rotational velocity  $V_{rot}$ . For moderate angles of attack, the downstream relative velocity  $V_{rel,2}$  follows the trailing edge. The conservation of the mass imposes the equivalence between the axial components  $u$  and  $C_a$ . The velocity triangle downstream is now fixed, as shown in Figure 4.8: the absolute velocity  $C$  has a tangential component  $C_\theta$  in the opposite direction of the blade.

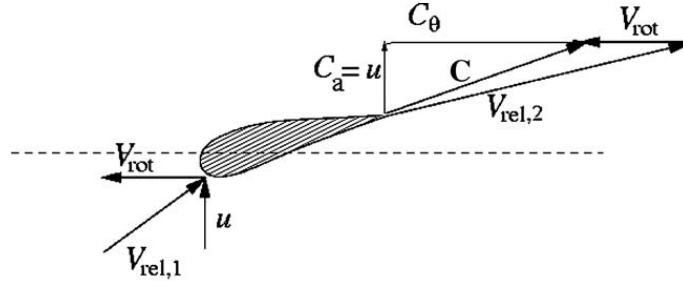


**Figure 4.8:** Triangles of velocities in a section of the blade

From 4.16 can be observed that for a given power  $P$ ,  $C_\theta$  decreases increasing the rotational speed  $\omega$ . The loss of kinetic energy contained in the rotational wake in the wake is minimized with high rotational speeds. The rotational speed can be written as function of  $a'$ :

$$C_\theta = 2a'\omega r \quad (4.17)$$

The power can be written as:

$$dP = 4\pi\rho\omega^2 V_0 a'(1-a)r^3 dr \quad (4.18)$$

The total power  $P$  is calculated integrating  $dP$  from 0 to  $R$ :

$$P = 4\pi\rho\omega^2 V_0 \int_0^R a'(1-a)r^3 dr \quad (4.19)$$

The power coefficient  $C_P$  is written in non-dimensional form as:

$$C_P = \frac{8}{\lambda^2} \int_0^\lambda a'(1-a)x^3 dx \quad (4.20)$$

where the tip speed ratio is  $\lambda = \omega R/V_0$  and  $x = \omega r/V_0$  is the local rotational speed at the radius  $r$ , non-dimensionalized with respect the wind speed  $V_0$ .

The power can be optimized maximizing the expression:

$$f(a, a') = a'(1 - a) \quad (4.21)$$

If the local angles of attack are below stall, the reacting force  $L$  is perpendicular to the local velocity  $V_{Rel}$ , seen by blade, as illustrated in Figure 4.9.

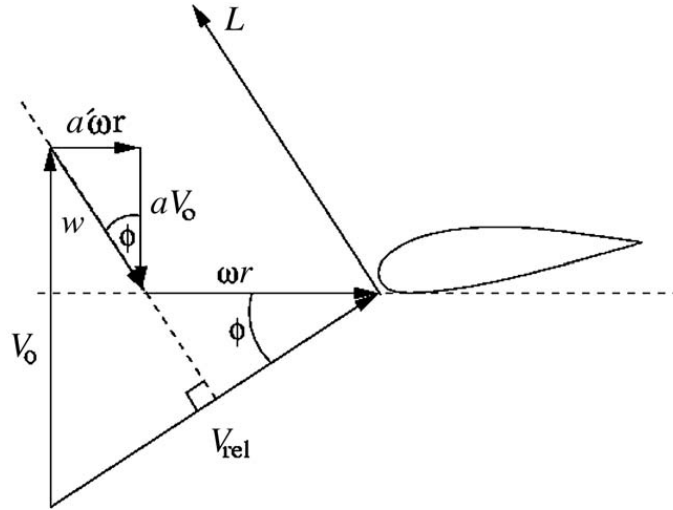


**Figure 4.9:** Triangle of velocities with induced velocities for a section of the blade

The total induced velocity  $w$  must be in the same direction of the force and perpendicular to the local velocity. Using the trigonometric,  $a$  and  $a'$  can be correlated by the following relationship:

$$x^2 a'(1 + a') = a(1 - a) \quad (4.22)$$

Differentiating 4.21 and 4.22 with respect  $a$  and combining them with 4.22, the optimum relationship between  $a$  and  $a'$  is found;

$$a' = \frac{1 - 3a}{4a - 1} \quad (4.23)$$

When  $\omega$  and hence  $x = \omega r/V_0$  are increased, the optimum value for  $a$  tends to  $1/3$ , as predicted by the simple momentum theory for an ideal rotor.

### 4.3 The Classical Blade Element Momentum Method

The classical Blade Element Momentum method has been developed by Glauert in the 1935 [42]. The model allows to calculate steady loads, thrust and power for different setting of wind speeds, rotational speeds and pitch angles. In the presented previous model, the geometry of the rotor was not considered. The BEM method couples the moment theory with the local events in the proximity of the blades. The model discretizes the stream-tube in  $N$  annular elements of height  $dr$ , as shown in Figure 4.10: there is no flow across the boundary of the elements since they are formed by the streamlines.

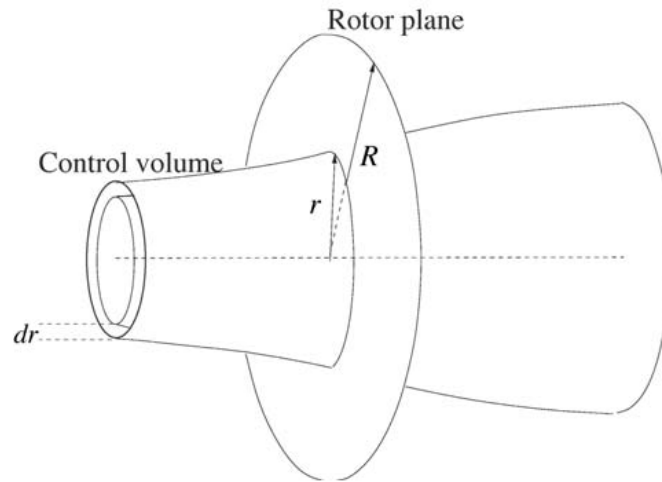


**Figure 4.10:** Control volume adopted for the 3D model analysis

The considered hypothesis are:

- No radial dependency between the elements;
- Constant force from the blades on the flow for each annular element (i.e. infinite number of blades);
- No axial component of the forces along the streamlines enclosing the annular control volume.

The trust and the torque can be calculated as:

$$dT = (V_0 - u_1)d\dot{m} = 2\pi r \rho u (V_0 - u_1) dr \quad (4.24)$$

$$dM = r C_\theta d\dot{m} = 2\pi r^2 \rho u C_\theta dr \quad (4.25)$$

If the axial velocity in the wake  $u_1$  is expressed as function of the induction factors,  $a$  and  $a'$  are inserted in the previous equations. Thrust and torque of the annular element can be expressed as:

$$dT = 4\pi r \rho V_0^2 a(1-a) dr \quad (4.26)$$

$$dM = 4\pi r^3 \rho V_0 \omega(1-a)a' dr \quad (4.27)$$

The relative velocity  $V_{rel}$ , seen by a section of the blade, is a combination of the axial velocity  $(1-a)V_0$  and the tangential velocity  $(1+a')\omega r$ , as shown in Figure 4.11:

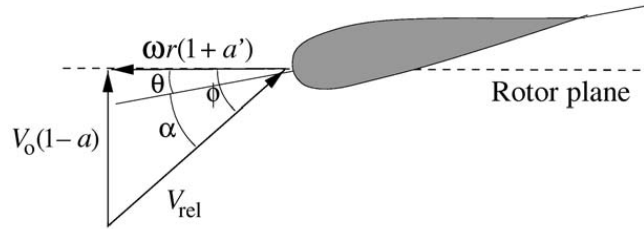


**Figure 4.11:** Velocities at the rotor plane

In Figure 4.11,  $\theta$  is the twist of the blade (between chord and plane of rotation) and it is calculated as  $\theta = \theta_P + \theta_T$ , where  $\theta_P$  is the pitch angle and  $\theta_T$  represents the local twist angle of the blade. The pitch angle  $\theta_P$  is the angle between the tip chord and the rotor plane and the twist  $\theta_T$  is measured relative to the tip chord.  $\psi$  is the angle between the plane of rotation and the relative velocity  $V_{rel}$ . The local angle of attack  $\alpha$  is given by:

$$\alpha = \phi - \theta \quad (4.28)$$

and:

$$\tan \phi = \frac{(1-a)V_0}{(1+a')\omega r} \quad (4.29)$$

In order to calculate the lift (perpendicular to the velocity seen by the airfoil by definition) and the drag (parallel to the same velocity) forces, the relative velocity  $V_{rel}$ , the lift and drag coefficients  $C_L$  and  $C_D$  are required:

$$L = \frac{1}{2} \rho V_{rel}^2 c C_L \quad (4.30)$$

$$D = \frac{1}{2}\rho V_{rel}^2 c C_D \quad (4.31)$$

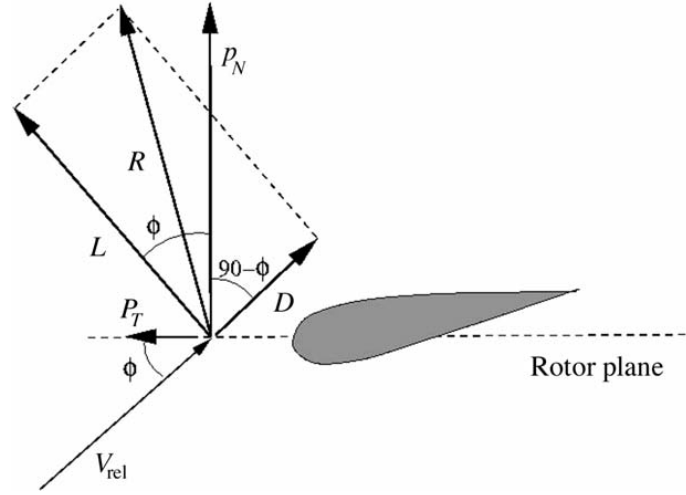


**Figure 4.12:** Loads on the blade

In order to calculate the force normal and tangential to the rotor plane, the Lift and Drag forces have to be projected on these directions, as shown in Figure 4.12.

$$p_N = L \cos \phi + D \sin \phi \quad (4.32)$$

$$p_T = L \sin \phi + D \cos \phi \quad (4.33)$$

and:

$$C_N = C_L \cos \phi + C_D \sin \phi \quad (4.34)$$

$$C_T = C_L \sin \phi + C_D \cos \phi \quad (4.35)$$

where the normal and the trust coefficients  $C_N$  and  $C_T$  are:

$$C_N = \frac{p_N}{\frac{1}{2}\rho V_{rel}^2 c} \quad (4.36)$$

$$C_T = \frac{p_T}{\frac{1}{2}\rho V_{rel}^2 c} \quad (4.37)$$

From the geometry (Figure 4.12) the following relations are determined:

$$V_{rel}\sin\phi = V_0(1 - a) \quad (4.38)$$

$$V_{rel}\cos\phi = \omega r(1 + a') \quad (4.39)$$

The solidity  $\sigma$  can be defined as the fraction of the annular area covered by the volume:

$$\sigma(r) = \frac{c(r)B}{2\pi r} \quad (4.40)$$

where  $B$  is the number of blades,  $c(r)$  is the local chord and  $r$  is the radial position on the control volume. The normal force and torque on a control volume of thickness  $dr$  are computed as:

$$dT = Bp_N dr \quad (4.41)$$

$$dM = rBp_T dr \quad (4.42)$$

Using 4.36 for  $p_N$  and 4.38 for  $V_{rel}$ ,  $dT$  becomes:

$$dT = \frac{1}{2}\rho B \frac{V_0^2(1 - a)^2}{\sin^2\phi} cC_N dr \quad (4.43)$$

Similarly 4.37 for  $p_T$  and 4.38 and 4.39 for  $V_{rel}$ ,  $dM$  becomes:

$$dM = \frac{1}{2}\rho B \frac{V_0(1 - a)\omega r(1 + a')}{\sin\phi\cos\phi} cC_T r dr \quad (4.44)$$

Finally an expression for the axial induction factor  $a$  can be found by equalizing the equations 4.26 and 4.43 for  $dT$  and using the definition of solidity  $\sigma$ :

$$a = \frac{1}{\frac{4\sin^2\phi}{\sigma C_N} + 1} \quad (4.45)$$

and the tangential induction factor is found by equalizing equations 4.27 and 4.44 for  $dM$ :

$$a' = \frac{1}{\frac{4\sin\phi\cos\phi}{\sigma C_T} - 1} \quad (4.46)$$



## 4.4 BEM Method Algorithm

The algorithm of the BEM method can be summarized by the following steps:

1. initialize  $a$  and  $a'$  to 0;
2. compute the flow angle  $\phi$  using equation 4.29;
3. compute the local angle of attack  $\alpha$  using equation 4.28;
4. read  $C_L(\alpha)$  and  $C_D(\alpha)$  from the tables;
5. compute  $C_N$  and  $C_T$  using equation 4.34 and 4.35;
6. calculate  $a$  and  $a'$  from equation 4.45 and 4.46;
7. if  $a$  and  $a'$  have changed more than a tolerance go to (2), else finish;
8. compute the local loads on the segment of the blade.

In order to get good results, it is necessary to apply two corrections, as will be further explained. After the iterative process that calculates the local loads in all the control volumes, it is possible to compute the mechanical power, thrust and root bending moment. When integrating the tangential loads to obtain the shaft torque, a linear variation of the tangential force per length ( $p_T$ ) between  $r_i$  and  $r_{i+1}$  is assumed as shown in Figure 4.13.

The tangential force  $p_T$  is:

$$p_T = A_i r + B_i \quad (4.47)$$

where:

$$A = \frac{p_{T,i+1} - p_{T,i}}{r_{i+1} - r_i} \quad (4.48)$$

$$B = \frac{p_{T,i} r_{i+1} - p_{T,i+1} r_i}{r_{i+1} - r_i} \quad (4.49)$$

The torque for an infinitesimal part of the blade  $dr$  is:

$$dM = r p_T dr = (A_i r^2 + B_i r) dr \quad (4.50)$$

The contribution  $M_{i,i+1}$  to the total shaft torque from the linear tangential loads variation between  $r_i$  and  $r_{i+1}$  is:

$$M_{i,i+1} = \left[ \frac{1}{3}A_i r^3 + \frac{1}{2}B_i r^2 \right]_{r_i}^{r_{i+1}} = \frac{1}{3}A_i (r_{i+1}^3 - r_i^3) + \frac{1}{2}B_i (r_{i+1}^2 - r_i^2) \quad (4.51)$$

and finally the total shaft torque is computed as the sum of all the  $M_{i,i+1}$  contributes:

$$M_{tot} = B \sum_{i=1}^{N-1} M_{i,i+1} \quad (4.52)$$

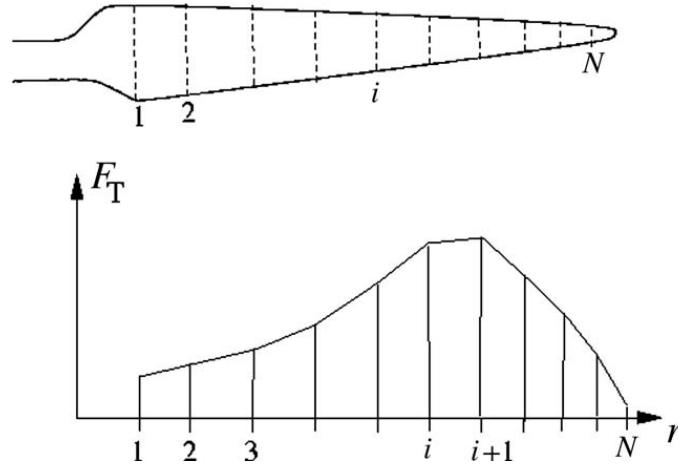


**Figure 4.13:** Linear variation of the loads with the radius

## 4.5 Corrections to the Classical Blade Element Momentum Method

In order to increase the accuracy of the BEM code, two corrections have to be applied.

The **Prandtl's tip loss factor** corrects the assumption of an infinite number of blades; for a rotor with a finite number of blades, the vortex system in the wake is different from the vortex predicted by the classical BEM model. Therefore, a correction factor  $F$  is introduced in equations 4.26 and 4.27:

$$dT = 4\pi r \rho V_0^2 a(1-a)F dr \quad (4.53)$$

$$dM = 4\pi r^3 \rho V_0 \omega (1-a)a' F dr \quad (4.54)$$

where:

$$F = \frac{2}{\pi} \cos^{-1}(e^{-f}) \quad (4.55)$$

$$f = \frac{B R - r}{2 r \sin \phi} \quad (4.56)$$

$B$  is the number of blades,  $R$  is the total radius of the rotor,  $r$  is the local radius  $\phi$  is the flow angle.  $a$  and  $a'$  can now be computed as:

$$a = \frac{1}{\frac{4F \sin^2 \phi}{\sigma C_N} + 1} \quad (4.57)$$

$$a' = \frac{1}{\frac{4F \sin \phi \cos \phi}{\sigma C_T} - 1} \quad (4.58)$$

The **Glauert correction** considers the field of validity of the simple moment theory; the developed model is indeed valid for the axial induction factor lower than 0.4. Spera [43] proposed an empirical relation between  $C_T$  and  $a$  to fit the measurements:

$$C_T = \begin{cases} 4a(1-a)F & a \leq a_c \\ 4a(a_c^2 + (1-2a_c)a)F & a > a_c \end{cases} \quad (4.59)$$

where  $a_c$  is 0.2 and  $F$  is Prandtl's loss factor. Figure 4.14 compares two empirical expressions for  $C_T(a)$  with the simple momentum theory.

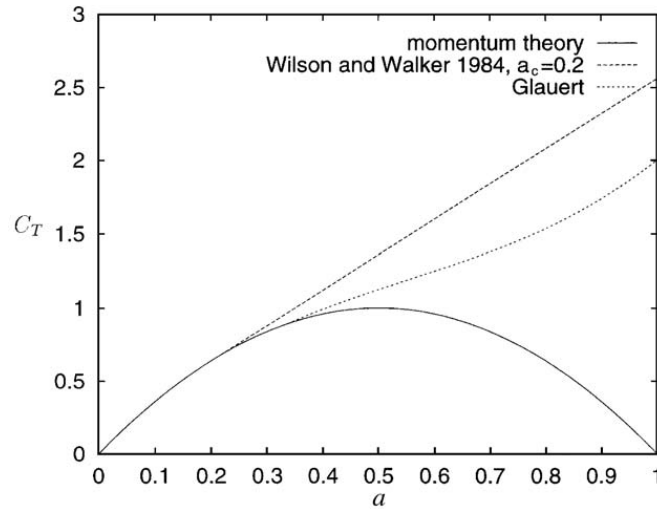


**Figure 4.14:** Expressions for  $C_T$  versus the axial induction factor  $a$

The trust coefficient  $C_T$  is by definition:

$$C_T = \frac{d_T}{\frac{1}{2} \rho V_0^2 2\pi r dr} \quad (4.60)$$

using equation 4.43 for  $dT$ :

$$C_T = \frac{(1-a)^2 \sigma C_N}{\sin^2 \phi} \quad (4.61)$$

Comparing equations 4.61 and 4.59 for  $a < a_c$ :

$$4a(1-a)F = \frac{(1-a)^2 \sigma C_N}{\sin^2 \phi} \quad (4.62)$$

the equation 4.57 is found:

$$a = \frac{1}{\frac{4F \sin^2 \phi}{\sigma C_N} + 1} \quad (4.63)$$

if  $a > a_c$ :

$$4(a_c^2 + (1-2a_c)a)F = \frac{(1-a)^2 \sigma C_N}{\sin^2 \phi} \quad (4.64)$$

$$a = \frac{1}{2} [2 + K(1-2a_c) - \sqrt{K(1-2a_c) + 2)^2 + 4(Ka_c^2 - 1)}] \quad (4.65)$$

where:

$$K = \frac{4F \sin^2 \phi}{\sigma C_N} \quad (4.66)$$

Equation 4.65 and 4.63 replaces 4.57 from the simple momentum theory in order to correctly compute the induced velocities for small wind speed.

## 4.6 Annual Energy Production

Once the power curve is computed as a function of wind speed  $V_0$  it is necessary to combine it with a probability density function for the wind speed in order to obtain the annual energy production. To calculate the energy annual production, the steps reported below have to be followed:

- compute the power curve with BEM;
- compute the probability density function for the wind  $f(V_i < V_0 < V_{i+1})$ ;
- multiply with the total number of hour per year;
- multiply by the power (in kW) produced by the wind turbine when wind speed is in the range  $V_i < V_0 < V_{i+1}$ ;

- correct the production for losses in gearbox and generator.

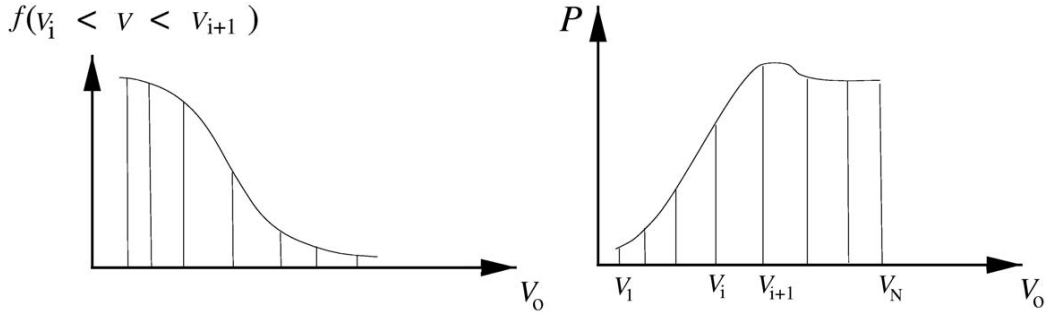


**Figure 4.15:** Probability of wind speed and power curve

The wind speed distribution is discretized in  $N$  intervals, as shown in Figure 4.15. The probability density function can be given by Rayleigh or Weibull distribution. For example, using Weibull distribution, the scaling factor  $A$  and the shape parameter  $k$  consider corrections for landscapes, obstacles and vegetation:

$$h_W(V_0) = \frac{k}{A} \left( \frac{V_0}{A} \right)^{k-1} \exp\left(-\left(\frac{V_0}{A}\right)^k\right) \quad (4.67)$$

$A$  and  $k$  can be obtained for the European Wind Atlas [44]. The probability density function can be calculated from Weibull distribution:

$$f(V_i < V_0 < V_{i+1}) = \exp\left(-\left(\frac{V_i}{A}\right)^k\right) - \exp\left(-\left(\frac{V_{i+1}}{A}\right)^k\right) \quad (4.68)$$

The total annual energy production  $AEP$  is finally computed as:

$$AEP = \sum_{i=1}^{N-1} \frac{1}{2} (P(V_{i+1}) + (P(V_i)) * f(V_i < V_0 < V_{i+1}) * 8760 \quad (4.69)$$

In order to compare turbines of different sizes, the annual energy production can also be normalized with the radius of the rotor. The AEP density,  $AEP_d$  is:

$$AEP_d = \frac{AEP}{R^2} \quad (4.70)$$

## Chapter 5

# Proposal for a Coupled Aerodynamic-Structural Wind Turbine Blade Optimization

### 5.1 The Case Study

The AOC 15/50 wind turbine was selected as case study for the present optimization as it represents the validate test case for the S.O.C.R.A.TE. software. The turbine is one of the few examples with both openly available structural data (with the complete description of the composite layout of the blade) and experimental results (experimental power curve resulting from a test campaign). Using this example of wind turbine is possible to validate both the models (structural and aerodynamic) on the same geometry. The main characteristics of the AOC 15/50 are reported in the NREL Test Report [65] and summarized in Table 5.1.

<b>Number of blades</b>	3
<b>Rated power</b>	50 kW
<b>Cut-in wind speed</b>	4.9 m/s
<b>Cut-out wind speed</b>	22.3 m/s
<b>Rated wind speed</b>	12 m/s
<b>Rotor diameter</b>	15 m
<b>Online rotational speed</b>	65 rpm
<b>Control type</b>	Constant speed - Fixed pitch
<b>Pitch setting</b>	1.54°
<b>Power regulation</b>	Stall regulation
<b>Tower height</b>	24.4 m

Table 5.1: AOC 15/50 Wind Turbine characteristics

The AOC 15/50 HAWT blade was initially designed by the Sandia National Laboratories [66]: starting at 0.279 m from the rotational axis and extending up to 7.490 m, the blade was based on the S821, S819 and S820 airfoils (from root to tip). An improved version of the AOC 15/50 blade [67] [68] is based on the S814, S812 and S813 airfoils (from root to tip, placed at 7.2 m from the rotational axis): such configuration is adopted in the hereby proposed analysis.

Table 5.2 summarizes the main geometrical features of the blade model, while the layup schedule of the adopted composite materials is reported in Table 5.3: the layer number increases from the tip to the root. As can be observed from Figure 5.2, several reinforcements are added to the blade skin. Furthermore, in order to increase the overall blade rigidity, both a Spar Flange and a Spar Web are adopted in the central sections (from the spanwise coordinate 1.092 m to 7.061 m), as can be seen from Figure 5.1. It can also be observed that the blade is subdivided in 9 main zones in the spanwise direction and in 5 chordwise areas.

Distance from the rotational axis [m]	Blade profile	c [m]	$\theta$ [°]
0.279	S814	0.4570	8.10
0.775	S814	0.5303	8.10
0.88	S814	0.5462	7.60
1.092	S814	0.5745	6.72
1.702	S814	0.6568	6.24
2.311	S814	0.7173	5.94
3.124	S814	0.7400	5.53
3.937	S814	0.6920	4.86
4.750	S812	0.6258	4.10
5.563	S812	0.5572	3.28
6.603	S813	0.4780	2.37
7.059	S813	0.4410	1.95
7.490	S813	0.4060	1.54

**Table 5.2:** Aerodynamic profiles characterizing the external geometry of the AOC 15/50 blade

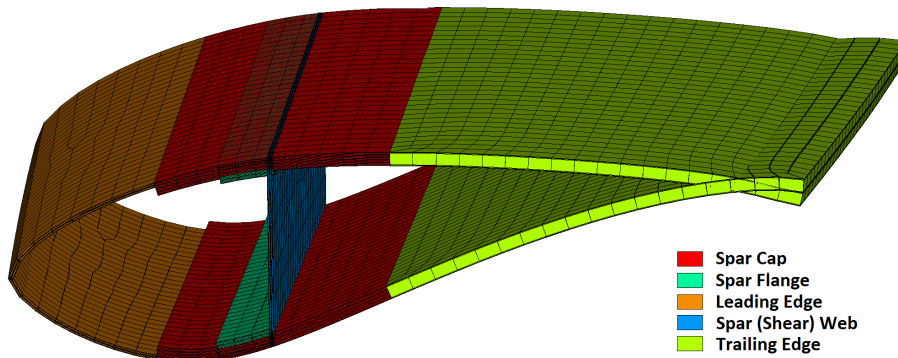


**Figure 5.1:** Scheme of the subdivision of the blade layout in the chordwise direction

Component	Location [mm]	Layup schedule	Thickness [mm]	Layup n. [-]
Root	279 to 775	$[\pm 45/0_6/\pm 45/0_6/+45]_S$	15.7	1
	775 to 889	$[\pm 45/0_5/\pm 45/0_5/+45]_S$	13.5	2
	889 to 1092	$[\pm 45/0_4/\pm 45/0_4/+45]_S$	11.2	3
Spar cap	1092 to 2311	$[\pm 45/0_4/\pm 45/0_4/+45]_S$	11.2	3
	2311 to 3937	$[\pm 45/0_3/\pm 45/0_3/+45]_S$	8.9	4
	3397 to 5563	$[\pm 45/0_2/\pm 45/0_2/+45]_S$	6.6	5
	5563 to 7493	$[\pm 45/0/\pm 45/0/+45]_S$	4.3	6
Leading edge	1092 to 2311	$[\pm 45/0_2/\pm 45]_S$	3.9	7
	2311 to 7493	$[\pm 45/0/\pm 45]_S$	2.8	8
Trailing edge	1092 to 6604	$[\pm 45/0/\text{balsa}/0/\pm 45]$	11.5	9
	6004 to 7493	$[\pm 45/0]_S$	2.0	10
Spar flange	1092 to 7493	$[\pm 45/0_2/\pm 45]_S$	3.9	11
Spar web	1092 to 7061	$[\pm 45/0_2/\pm 45]_S$	3.9	12

Table 5.3: Layup schedule of the analyzed rotor blade

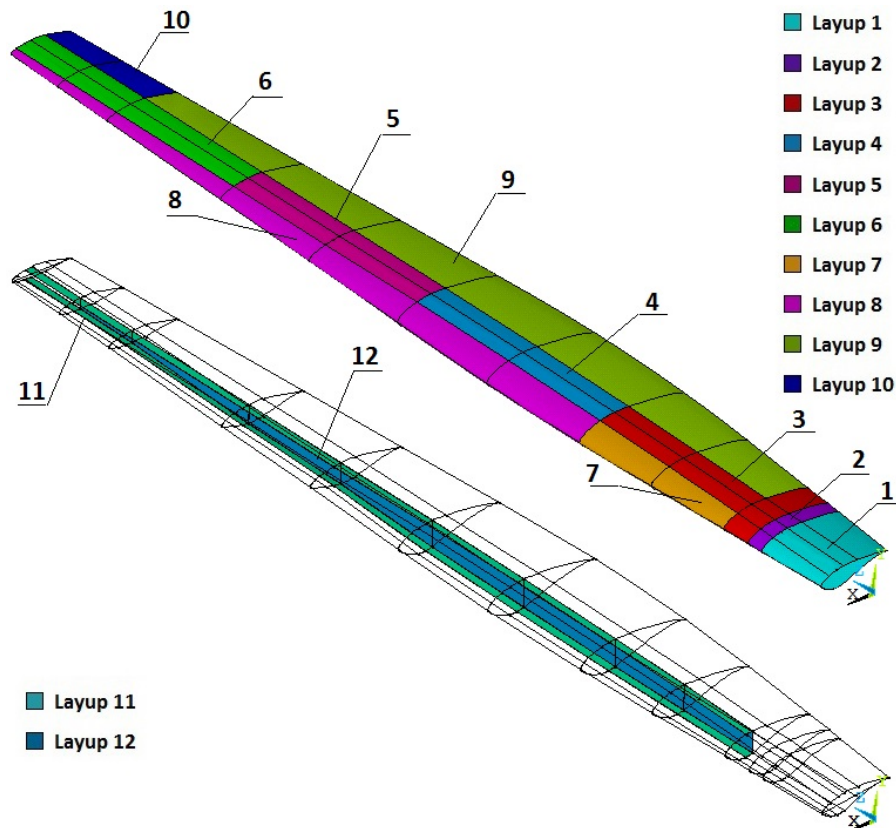


Figure 5.2: Exploded drawing of the analyzed rotor blade geometry, showing the subdivision in 9 areas spanwise and 8 zones chordwise



## 5.2 Description of the BEM Code

The proposed BEM code has been developed and validated by the researchers of the University of Padova (as the S.O.C.R.A.TE. software) and it is based on the well-known theory presented by Martin O.L.Hansen [41]. The intent is to further develop the internal codes in order to archive a complete multidisciplinary analysis of a horizontal wind turbine. The BEM Theory, whose equations are far too known to be reported here again, is commonly used by wind turbine designers for the prediction of rotor aerodynamic performance. It combines two independent approaches: the *Momentum Theory* and the *Blade Element Theory*. The former concerns the computation of both thrust and torque by applying the conservation of the linear momentum and of the angular one to a control volume, the latter refers to the analysis of aerodynamic forces acting at each blade section, as a function of blade geometry [69]. Following the BEM method, the rotor is subdivided into a finite number of control volumes, each independent from the others, and according to the classical theory, the force exerted from the blades on the flow is considered constant in each annular element. This corresponds to an assumption of a rotor characterized by an infinite blade number [41], which, of course, has a vortex system in the wake that is different from that of an actual rotor with a finite number of blades. In order to simulate a rotor with a finite blade number, the classical Prandtl's tip loss correction [42] is hereby considered. A detailed description of the process with an extensive explanation of its fundamental equations can be found in [41]. Among the advantages of such approach with respect to more advanced tools (like Computational Fluid Dynamics), its high computational speed and ease of implementation can be recalled [70] [71] [72]. However, unlike more advanced calculation methods, the accuracy of the results is not always ensured and is heavily influenced by the precision of the airfoil polars characterizing each blade station. Moreover, experimental polars are often not available, requiring the adoption of numerical codes based on panel methods, such as XFOIL [73], for the prediction of airfoil characteristics. In this work the RFOIL code [74], an improved version of XFOIL, is used due to its better correlation with experimental results, especially in the stall region. The AOC 15/50 wind turbine is stall regulated and, even using the RFOIL code, the stall condition could not be well captured. However, this doesn't represent an issue for the proposed optimization; the validation of the code shows a good prediction even in the stall zone of the power curve. Furthermore, the aerodynamic objective function refers to the power production in a single point (10 m/s), quite far from the stall conditions as shown in Figure 5.3.

Another weakness of BEM codes is that aerodynamic data are often available only for a limited range of angles of attack, requiring the extension of both lift and drag coefficients up to  $90^\circ$ . This is particularly critical for stall controlled wind turbines to accurately capture the behaviour of the rotor

subjected to high wind speeds. The authors observe that a good agreement with measured data can be obtained following the extension method proposed by Lindenburg [75]. In addition, in order to obtain accurate rotor sectional lift characteristics, and hence accurate power prediction (in particular in the stalled region), bi-dimensional airfoil data need to be corrected for the three-dimensional inboard stall delay effects [76]. In fact, due to rotation, the boundary layer is subjected to Coriolis and centrifugal forces which alter the bi-dimensional airfoil characteristics [77]. Accordingly, the boundary layer is less thick and more stable compared to the non-rotational state [75], enhancing the performance of the blades, particularly in their innermost portion. To take into account these effects, the correction on the lift and drag coefficients proposed by Lindenburg [75] is hereby considered.

### 5.2.1 BEM Code Validation

The adopted BEM code is validated against experimental data of the AOC 15/50 wind turbine installed at NREL's National Wind Technology Center (NWTC) in Colorado [65]. All the numerical simulations are conducted considering a constant rotor angular speed of 65 rpm for a range of wind velocities between 5 m/s and 20 m/s. Air density is set to  $1.225 \text{ kg/m}^3$  and the dynamic viscosity to  $1.78 \text{ Pa}\cdot\text{s}$ . The polar curves for the S814, S812 and S813 airfoils are obtained using RFOIL for a constant Reynolds number of  $10^6$  and extended up to  $90^\circ$  using the Lindenburg method [75]. The generator efficiency is assumed constant and equal to 89.4% (from: [68]). Figure 5.3 shows a comparison between the power curve at sea level air density and the numerical simulations. The numerical power curve at low velocities presents an overestimation of the wind turbine performances. This is probably caused by the inertia of the wind turbine in the start-up phase; the cut-in speed is indeed 4.8 m/s and the inertia of the blades (that are starting to moving) could influence the experimental measurement at low velocities. A remarkable agreement can be observed up to a wind velocity of 18 m/s, where a deep stall condition is experienced by the blades. However, this portion of the power curve can be neglected for the scope of the present analysis and the accuracy of the prediction can be therefore considered acceptable.

## 5.3 Description of the Structural Model

The FEM model adopted for the present optimization is built using SHELL 181 elements to simulate the composite skin of the blade; such element can reproduce the behaviour of the layered structures by specifying the sequence of layers, the thickness and the orientation of each single lamina and the adopted material.

As shown in Figure 5.4, each element is composed of 4 nodes and has 6 degrees of freedom at each

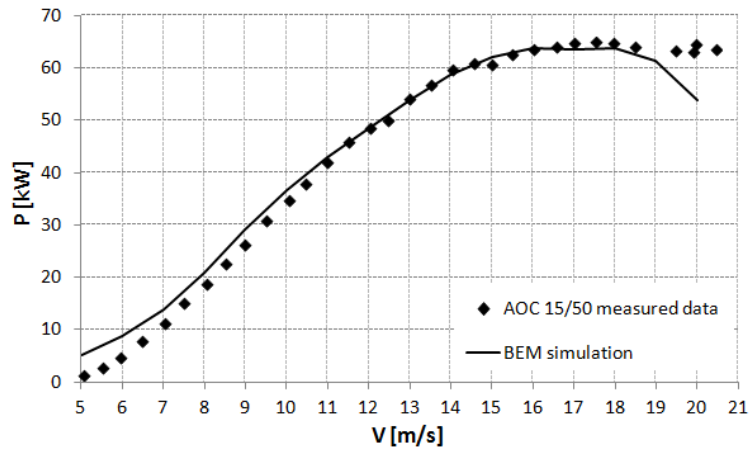


**Figure 5.3:** Experimental and numerical power production as a function of the wind speed for the AOC 15/50 wind turbine

node: translations in the nodal  $x$ ,  $y$  and  $z$  directions and rotations about the nodal  $x$ ,  $y$  and  $z$  axes. A free mesh topology and a quad shape of the elements are adopted to discretize each surface of the model. A medium dimension of the surface elements of 20 mm is imposed; a representation of the mesh in the root area is shown in Figure 5.5.

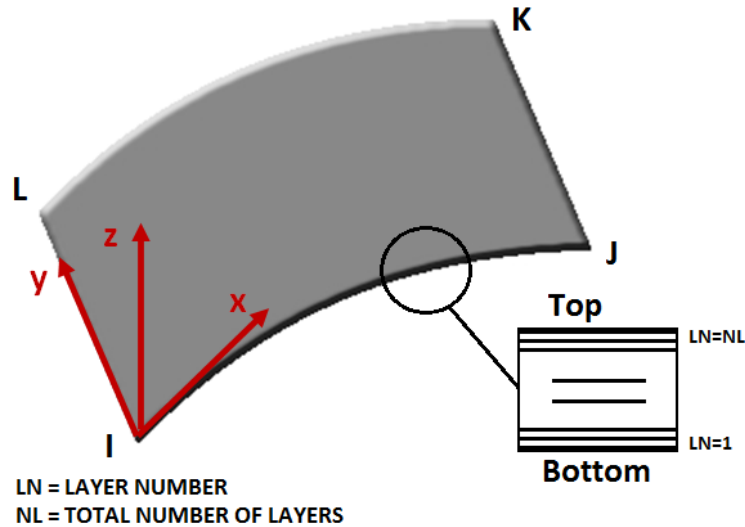


**Figure 5.4:** Shell 181 configuration

The layup schedule of the model blade is assumed by the Sandia report [66] and summarized in Table 5.3. A *Layup number* is assigned to every area of the blade where the layup changes. The graphic representation of the different layup distribution along the blade is shown in Figure 5.2. Number 11 represents the spar flange layers, overlapped to the central ones from 3 to 6 and number 12 represents the Spar Web.

The adopted materials are some varieties of Glass Reinforced Polyester (GRP): all the lamina are

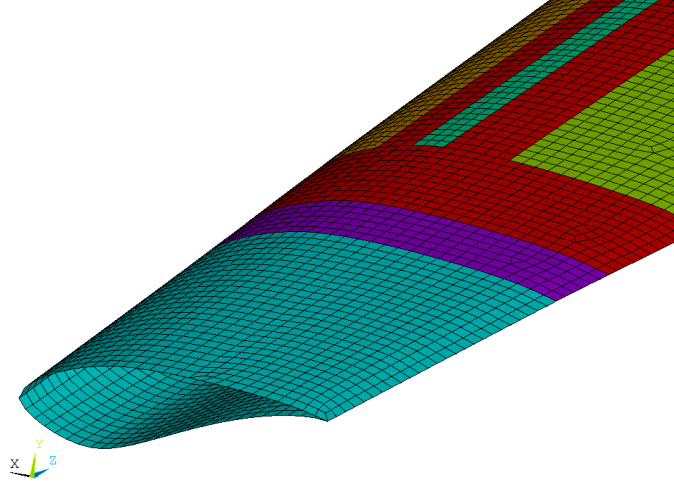


**Figure 5.5:** A detail of the adopted in mesh in the root area

	<b>A130 (0°)</b>	<b>DB120 (±45°)</b>	<b>Balsa Wood</b>
$E_L=E_X$ [MPa]	31700	26200	187
$E_T=E_Y$ [MPa]	7580	6550	61
$E_Z=E_Z$ [MPa]	7580	6550	4070
$\nu_{LT} = \nu_{XY}$ [-]	0.32	0.39	0.67
$\nu_{TZ} = \nu_{YZ}$ [-]	0.32	0.35	0.01
$\nu_{LZ} = \nu_{XZ}$ [-]	0.32	0.32	0.02
$G_{LT}=G_{XY}$ [MPa]	3450	4140	20.3
$G_{TZ}=G_{YZ}$ [MPa]	3100	3720	150
$G_{LZ}=G_{XZ}$ [MPa]	3100	3720	220
$\rho$ [kg/m <sup>3</sup> ]	1714	1714	153
t [mm]	0.571	0.203	9.530

**Table 5.4:** Structural properties of the materials adopted in the AOC 15/50 blade

composed by E-glass fibres embedded in a polymer matrix. The layup is modelled as orthotropic in a given layer with two of the principal material axes in the plane of the shell, as can be seen from the material parameters listed in Table 5.4. Different materials are adopted for the layers with different orientations of the fibres. The 0° layups are made by A130, while DB120 is used for the ±45° ply layups. In order to minimize the probability of buckling, the balsa wood is adopted as a filler in the sandwich layup of the trailing edge (zone 9).

A rigid constraint is applied to the root area of the blade: the three spatial displacements and the three rotations are fixed for the nodes belonging to the surface. The mechanical loads for the structural model are obtained by an interpolation of the aerodynamic forces computed from the BEM model.

The validation of the structural model is obtained by comparing the results of a FEM analysis to the same results provided in the AOC 15/50 Sandia report [66]. The flapwise, edgewise and torsional

rigidities of the blade (treated as a cantilever beam) with a fixed load applied at its tip are computed and compared with experimental results. The detailed description of the validation procedure is provided in [54] and is not reported here again for brevity's sake.

## 5.4 Design Variables

The design variables of the optimization problem are composed by both BEM and FEM parameters:

1. BEM: the y-coordinates of 5 points of a Bezier curve representing the distribution of the chord length in the spanwise direction (Figure 5.6);
2. BEM: the y-coordinates of 5 points of a Bezier curve representing the distribution of the twist angle in the spanwise direction (Figure 5.7);
3. FEM: the thickness of each lamina composing the blade reinforcements.

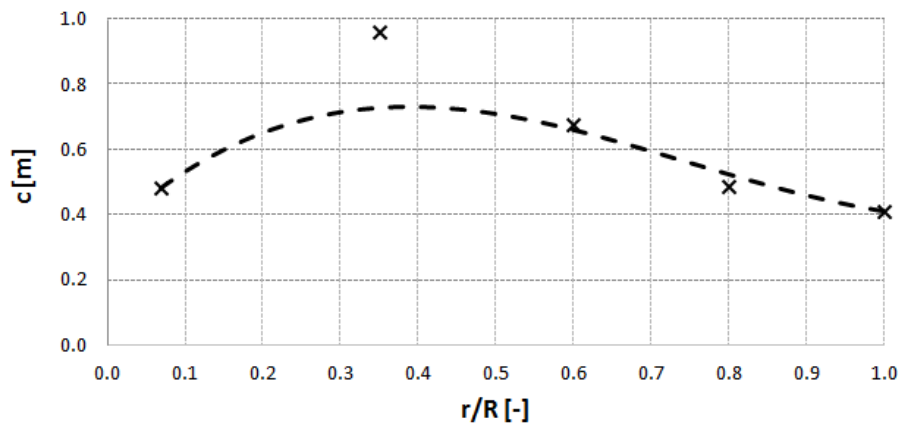


**Figure 5.6:** Representation of the Bezier points and of the corresponding curve for the chord spanwise distribution of the AOC 15/50 blade

The adoption of continuous functions to describe chord and twist distribution is a common and established practice in the aero-structural parametrization of the wind turbine blades. Examples of this parametrization can be found in [52], [79] and [80]. Twist and chord distribution are two of the factors that mainly influence the power production and the structural behaviour of the blade. Furthermore, the manufacturing costs result to be not greatly affected by choice of the adopted continuous functions with the relative constraints, considering the blade built using the common prepreg moulding technique.

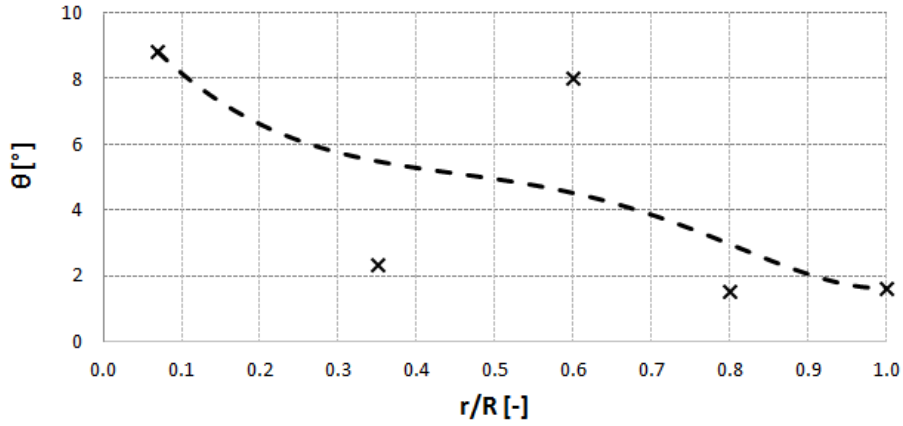


**Figure 5.7:** Representation of the Bezier points and of the corresponding curve for the twist spanwise distribution of the AOC 15/50 blade

## 5.5 Formulation of the Optimization Problem

The multi-objective optimization problem concerns the minimization of two functions. The first fitness function  $f_P$  considered for the optimization process is the result of the BEM analysis. It is represented by the ratio between the power  $P_0$  of the original Sandia blade and the power  $P$  generated by the candidate blade configuration. A second fitness function  $f_d$  is the result of the structural analysis. The total deformation (deriving from the combination of the flapwise deformation, the edgewise one and the axial one) of the candidate blade  $d$  is compared to the deformation of the original Sandia model  $d_0$ . High displacements could change the aerodynamic performances so the displacement function has been considered preferable to limit the displacements at the tip of the blade. Alternative structural functions could be represented by stress and strain values on the root area, however these values resulted limited and admissible for an HAWT composite blade, which geometry does not change much from the original one, during the optimization process.

The choice of using two contrasting functions belonging to two different fields of analysis instead of a combined index such as the Cost Of Energy (already investigated for an HAWT optimization in [52]) guarantee the identification of a Pareto Front and the possibility to identify different solutions which favour the structural or the aero-dynamical behaviour of the blade.

The optimization problem is formulated as follow:

$$\min f_P(x) = \frac{P_0}{P(x)} * i_A(x) * i_P(x) \quad (5.1)$$

$$\min f_d(x) = \frac{d(x)}{d_0} * i_m(x) \quad (5.2)$$

subject to:

$$f_P(x) < 3 \quad (5.3)$$

$$f_d(x) < 1.2 \quad (5.4)$$

$$i_m(x) = \begin{cases} 1 & f_m(x) \leq 1.20 \\ (1 + f_m(x) - 1.20)^2 & f_m(x) > 1.20 \end{cases} \quad (5.5)$$

$$i_A(x) = \begin{cases} 1 & f_A(x) \leq 1.05 \\ (1 + (A - A_0))^2 & f_A(x) > 1.05 \end{cases} \quad (5.6)$$

$$i_P(x) = \begin{cases} 1 & \frac{P_0}{P(x)} \leq 1.25 \\ (1 + f_P - 1.25) & \frac{P_0}{P(x)} > 1.25 \end{cases} \quad (5.7)$$

where  $f_m$  is the ratio between the mass of the considered blade  $m$  and that of the original one  $m_0$  and  $f_A$  is the ratio between the area of the considered blade  $A$  and that of the original one  $A_0$ :

$$f_m = \frac{m(x)}{m_0} \quad (5.8)$$

$$f_A = \frac{A(x)}{A_0} \quad (5.9)$$

The upper bounds of the power fitness function  $f_P$  and the deformation fitness function  $f_d$  are respectively set to 3 and 1.2.

The deformation fitness function  $f_d$  is related to the mass of the considered solution. A penalty function  $i_m$  is applied to  $f_d$  when the mass of the considered blade exceeds by 20% the mass of the original one. In order to avoid an excessive increase in the area of the blade and hence an unfair increment of the generated power, a penalty function  $i_A$  is also applied to the value of the power fitness function  $f_P$  when the calculated area  $A$  exceeds by 5% the original one  $A_0$ .

Finally, In order to deeply explore the zone characterized by a power fitness function  $f_P$  close to 1, a second analysis is performed using a more restrictive upper bound: the power fitness function is limited to a value of 1.5 and a penalty function  $i_P$  is applied when such value exceeds 1.25.

A summary of the main features of the optimization problem is reported in Table 5.5.

<b>Variables</b>	1) y-coordinates of Bezier points for the chord distribution 2) y-coordinates of Bezier points for the twist distribution 3) Layout of blade skin reinforcements
<b>Fitness functions</b>	1) Power fitness function $f_P$ 2) Deformation fitness function $f_d$
<b>Constraints</b>	Upper bound on $f_d$ Upper bound on $f_P$ Penalty function $i_m$ on $f_d$ Penalty function $i_A$ on $f_P$ Penalty function $i_P$ on $f_P$

**Table 5.5:** Summary of the main optimization settings

The constraints adopted for the optimization problem have been found through a trial and error test campaign on the code. The optimization parameters have been proper set after several test: the penalty function have been introduced to avoid unacceptable increases of mass, area and to avoid the g.a. to do evolve solution with low power production. Furthermore an alternative approach has also already been partially tested; the minimization of the mass of the blade has been considered as objective in a previous optimization of the AOC 15/50 [54]. In the presented optimization, objective functions of different field of analysis, as power production and tip displacement (which affects power), are considered.

## 5.6 The Multi-Objective Genetic Algorithm

The adoption of a multi-objective genetic algorithm represents a powerful strategy in order to improve both the aerodynamic performances and the structural behaviour of a rotor blade. The original version of the S.O.C.R.A.T.E.(Structural Optimization for Composite Rotor Air TurbinE) algorithm [54] is here modified and adapted in order to consider the results of a BEM analysis as the input for the following computations. In the present formulation, both chord and twist distributions are initially computed from the y-coordinates of two Bezier series of 5 points; the coordinates of the blade profiles are successively calculated. Such variables are used as input parameters for the BEM analysis, in order to evaluate the aerodynamic power  $P$  produced by the blade.

The S.O.C.R.A.T.E. algorithm uses the input geometry and the output parameters of the BEM analysis (i.e. the aerodynamic force distribution on the blade surface) to generate an appropriate series of APDL (Ansys Parametric Design Language) commands. The ANSYS software rebuilds the blade using the coordinates of 13 profiles and applies the aerodynamic forces resulting from the BEM



analysis (interpolated on these profiles) to the structural model. A further input for the FEM analysis is represented by the layout of the blade skin; the thicknesses of the reinforcement laminas are the structural design variables of the FEM step of the optimization process.

Figure 5.8 shows the position of the 14 reinforcements (letters from A to P) inside the original AOC 15/50 blade. In order to compute the new thicknesses of the laminas, the algorithm assigns an entire value (from 0 to 3) to the 14 thickness factors  $T_f$ : if the value of  $T_f$  is 0, the lamina is deleted in the new configuration; if  $T_f$  is 1, the lamina and its thickness are maintained; if  $T_f$  is 2 or 3, the lamina is duplicated or tripled. Each blade configuration is encoded through 24 parameters and the complete genetic pool of an individual is represented in Figure 5.9: the BEM genes for the chord variation are coloured in purple, the BEM genes for the twist variation are coloured in blue and the FEM genes for the thickness variation of the reinforcements are coloured in orange.

Zone	Blade													
	A	B	C	D	E	F	G	H	I	L	M	N	O	P
	45°	-45°	0°	0°	0°	0°	0°	0°	0°	0°	0°	0°	0°	0°
1	x	x	x	x	x	x	x	x	x	x	x	x	x	x
2	x	x	x	x	x	x	x	x	x	x	x	x		
3	x	x	x	x	x	x	x	x	x	x				
4	x	x	x	x	x	x	x	x						
5	x	x	x	x	x	x								
6	x	x	x	x										
7	x	x			x									
8	x	x												

**Figure 5.8:** Location of the reinforcements (all zones with the exception of 9 and 10, the Spar Web and the Spar Flange) inside the original AOC 15/50 blade (from Table 5.3)

C1	C2	C3	C4	C5									
0.482	0.961	0.675	0.489	0.410									
T1	T2	T3	T4	T5									
8.839	2.332	8.029	1.542	1.634									
A	B	C	D	E	F	G	H	I	L	M	N	O	P
1	1	1	1	1	1	1	1	1	1	1	1	1	1

**Figure 5.9:** Genetic pool of the original AOC 15/50 blade

An initial blade population is entirely evaluated first in the BEM model and then in ANSYS, opened by Dos commands in batch mode. For every blade configuration, Matlab generates a series of profiles for the BEM code and an APDL file, allowing ANSYS to create the corresponding geometry. In order to evaluate the mechanical behaviour of the blade, a mass computation and a static analysis are successively run.

After evaluating the power and the deformation fitness functions, all the individuals of the population are sorted using the Pareto ranking. According to the default Matlab Pareto Ranking option, a fraction of 0.35% of individuals is kept on the first Pareto front, while the solver selects individuals from higher fronts.

The best individuals of the population are selected and combined in accordance to the criteria of natural selection implemented in the *gamultiobj* function of Matlab. In order to sort the 160 individuals of a generation, the Pareto Ranking method is used: the individuals with highest fitness functions have an highest probability to be chosen for the creation process. Using the Stochastic Uniform method, the algorithm creates a line adding some segments proportional to the fitness values of the individuals. The algorithm moves along the resulting line and chooses the individuals referred to the segment it stops.

In order to mix the genetic pools of the chosen individuals, the Crossover function (scattered option) exchanges some genes between the individuals using a random binary vector. In the generated vector, the 1 values represent a gene from the first individual and the 0 values represent a gene from the second one. The child is generated according to the scheme of Table 5.6:

Crossover scheme	
parent 1	a b c d e f g h
parent 2	1 2 3 4 5 6 7 8
binary vector	1 1 0 0 1 0 0 0
resulting child	a b 3 4 e 6 7 8

**Table 5.6:** Scheme of the Crossover function

The genetic diversity is furthermore safeguarded by a Mutation function. The option allows to explore different zones of the space of variables by introducing small random variations in a certain number of genes of some individuals.

A certain number of the best individuals in every population is expected to be preserved through the generations: this option of Elitism (Elitecount option) improves the effectiveness of the algorithm.

A peculiarity of the S.O.C.R.A.T.E. algorithm is to force the creation and mutation functions of the Matlab *gamultiobj* to assume integer values for some genes of the genetic pool. Indeed, the genes referred to the structural features of the blade (genes from 11 to 24) represent an integer factor for the thickness of the laminas in the blade skin.

A schematic representation of the current version of the S.O.C.R.A.T.E. algorithm is shown in Figure 5.10. For further details about the S.O.C.R.A.T.E. algorithm, see [54].

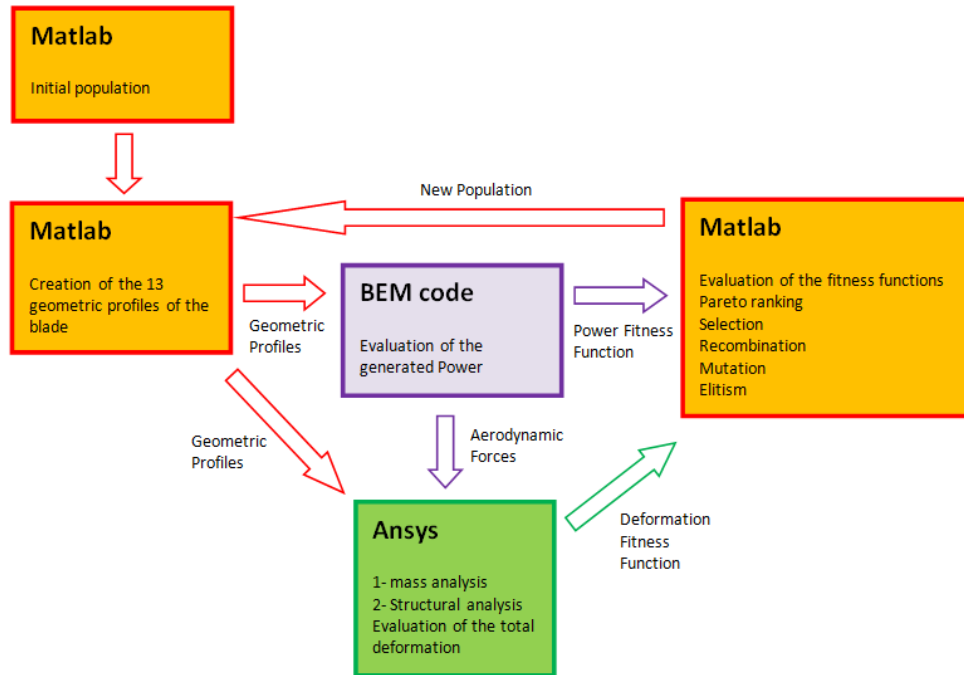


**Figure 5.10:** Functional diagram of the S.O.C.R.A.T.E. optimization process; the algorithm is based upon the coupling of the commercial code Ansys, an in-house made BEM code and the commercial code Matlab

The whole evolutionary process is represented by the following flowchart:

- $q=0$ ;
- initialization of the parent's population;
- while  $q=q_{max}$ ;
- evaluation of the fitness functions;
- Pareto Ranking (35% of individuals from the first front);
- selection (*Stochastic uniform*);
- recombination (*Crossover Scattered*);
- mutation;
- elitism (*Elitecount*);
- new population;
- $q=q+1$ ;

## 5.7 Description of the Optimization Process

The optimization process looks for the ideal distribution of both the chord lengths and the twist angles along the blade span and, simultaneously, for the optimal internal layer distribution. The initial population is the result of the combination of two different set of individuals. A first set is composed by individuals whose genes include limited variation compared to the baseline blade genes. The second set is random initialized through a specific function within the boundless of the parameters range. In this way is possible to explore the whole range of feasible solutions and not exclusively the most promising individual; in addition, the effect of the variation from the baseline configuration are immediately computed.

The BEM section of the genetic pool is elaborated by Matlab in order to generate chord and twist distributions from the y-coordinates of the Bezier points. The outputs of the BEM analysis are represented by the generated power (from which the first fitness function is computed) and by the values of the aerodynamic forces acting on the blade. The geometry, the constrains and the loads are imported in ANSYS and both a mass analysis and a structural one are run. In order to compare the performance of different blade configurations, the total deformation is estimated on a reference point located at the tip of the blade (at 30% of the chord length).

For each optimization, the Pareto optimal front is built (using the Non-Dominated Sorting Method) considering the set of non-dominated solutions: thus, if a solution results not to be dominated, at least in one of the two objective functions, it belongs to the Pareto frontier.

The reference values for the model representing the AOC 15/50 Sandia blade are evaluated in a preliminary structural analysis: the total deformation at the reference point results  $d_0 = 219.46$  mm and the blade total mass is  $m_0 = 85.78$  kg. The BEM analysis of the original model indicates a generated power  $P_0$  of 36.72 kW for an unperturbed wind speed of 10 m/s, here assumed as the reference value for the optimization process.

## 5.8 First Optimization: Settings and Results

The main features of the first genetic optimization are summarized in Table 5.7.

The trend of the Pareto Front is shown in Figure 5.11. As can be observed, the solutions identify a clear Pareto Front from the 10<sup>th</sup> generation; subsequent improvements are minimal.

The genetic pool of Figure 5.12 is referred to one of the optimal individuals (the 135<sup>th</sup> of the 27<sup>th</sup> generation) of the first optimization. The corresponding values of the fitness functions are:  $f_P = 0.9592$  and  $f_d = 0.6938$ . The total measured deformation of 152.26 mm for the reference point shows a great

First Optimization	
Genes	24
Population size	160
Generations	30
$f_P$ upper bound	3
$f_d$ upper bound	1.20
$i_m$ penalty on $f_d$	Quadratic over the 20%
$i_A$ penalty on $f_P$	Quadratic over the 5%

**Table 5.7:** Settings of the first optimization process

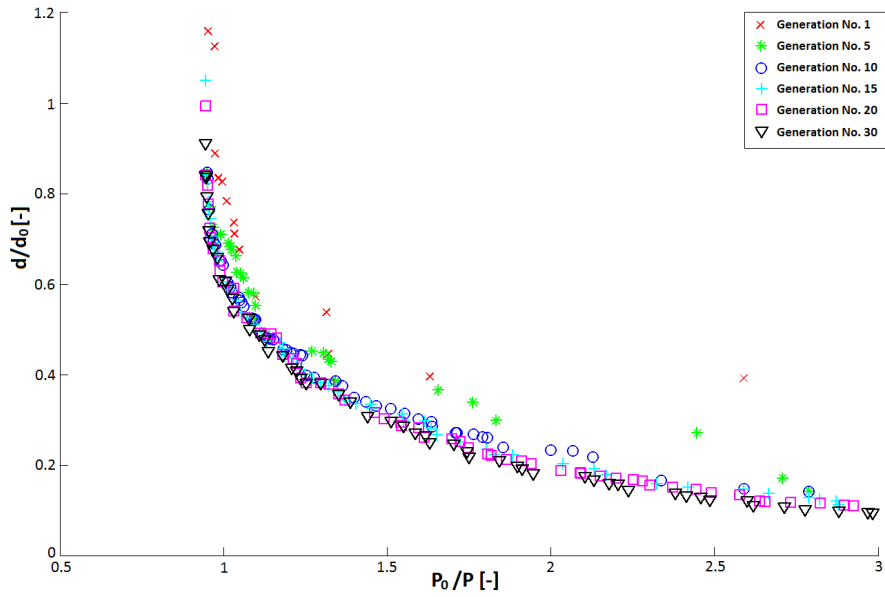


**Figure 5.11:** Evolution of the Pareto front for the first optimization process

increase in the structural performances (-30.62% deformation), while the generated power results of 38.28 kW (+4.25%) at 10 m/s.

C1	C2	C3	C4	C5									
0.531	1.017	0.689	0.522	0.387									
T1	T2	T3	T4	T5									
23.213	7.733	7.392	2.767	3.256									
A	B	C	D	E	F	G	H	I	L	M	N	O	P
1	1	1	2	1	2	1	1	2	2	1	1	1	1

**Figure 5.12:** Genetic pool of the 135<sup>th</sup> individual of the 27<sup>th</sup> generation (first optimization)

## 5.9 Second Optimization: Settings and Results

In order to focus the optimization on the left side of the Pareto Front, a more restrictive upper bound (1.5) is set for the Power fitness function  $f_P$ . Furthermore, an additional linear penalty function

is introduced, in order to correct  $f_P$  when its value exceeds 1.25. The last generation of the first optimization is adopted as the initial generation of the current optimization process. The main features of the second genetic optimization are summarized in Table 5.8.

Second Optimization	
Genes	24
Population size	160
Generations	30
$f_P$ upper bound	1.5
$f_d$ upper bound	1.20
$i_m$ penalty on $f_d$	Quadratic over 20%
$i_A$ penalty on $f_P$	Quadratic over 5%
$f_P$ penalty on $f_P$	Linear over 20%

**Table 5.8:** Settings of the second optimization process

The Pareto front for generations No. 1, 5, 10, 15, 20 and 30 is shown in Figure 5.13. The improvements are less marked than those obtained from the previous optimization, however the general trend of the front can be clearly observed. As can be seen, the more restrictive bounds on  $f_P$  force the solutions to assume higher values of generated power.

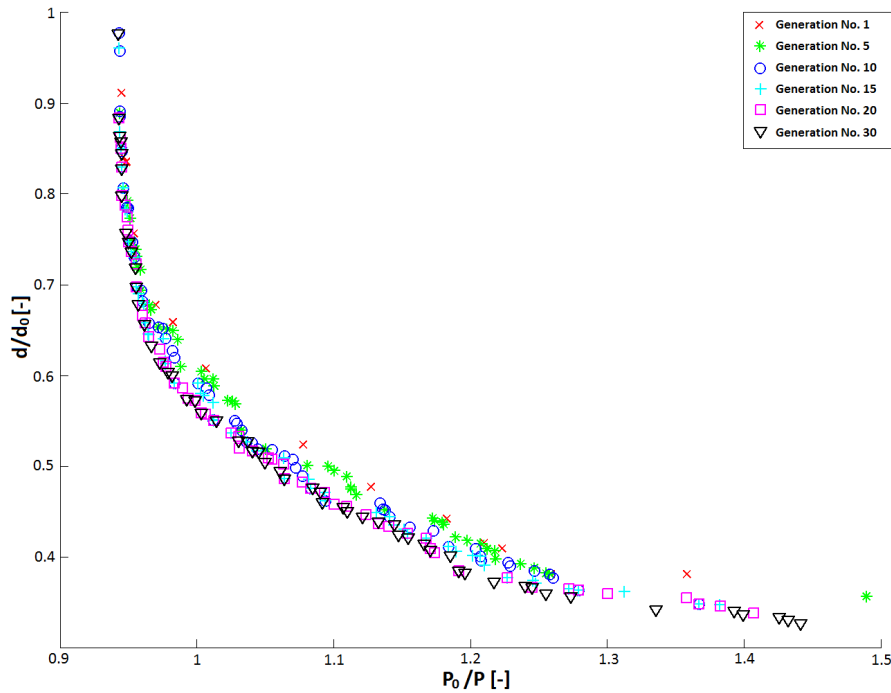


**Figure 5.13:** Evolution of the Pareto front for the second optimization process

Figure 5.14 summarizes the genetic pool of the selected solution (corresponding to the 146<sup>th</sup> individual of the 24<sup>th</sup> generation) for the second optimization. The fitness functions assume the values  $f_d=0.6785$  and  $f_P=0.9574$ . The resulting displacement of the reference point is 148.90 mm (-32.15%)

and the generated power is 38.35 kW (+4.44%).

C1	C2	C3	C4	C5									
0.518	1.026	0.692	0.525	0.385									
T1	T2	T3	T4	T5									
21.883	8.026	7.859	3.101	2.291									
A	B	C	D	E	F	G	H	I	L	M	N	O	P
0	1	1	1	1	2	2	1	2	2	1	1	1	1

**Figure 5.14:** Genetic pool of the 146<sup>th</sup> individual of the 24<sup>th</sup> generation (second optimization)

## 5.10 Discussion of the Optimization Results

The main geometric features and aerodynamic loads of the original blade and of the (second) optimized one are presented in Tables 5.9 and 5.10.

$r$ [m]	$c$ [m]	$\theta$ [°]	$\alpha$ [°]	$F$ [N]
0.279	0.4570	8.10°	-	0
0.775	0.5303	8.10	39.60	19
0.889	0.5462	7.60	36.90	11
1.092	0.5745	6.72	33.86	43
1.702	0.6568	6.24	26.10	38
2.311	0.7173	5.94	19.66	135
3.124	0.7400	5.53	13.39	236
3.937	0.6920	4.86	9.39	301
4.750	0.6258	4.10	8.69	376
5.563	0.5572	3.28	7.55	435
6.603	0.4780	2.37	6.67	366
7.059	0.4410	1.95	5.56	224
7.490	0.4060	1.54	-	109

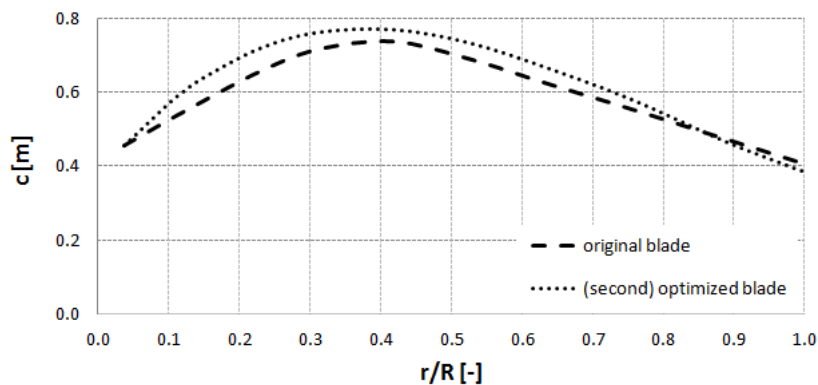
**Table 5.9:** Geometric features and load conditions of the original AOC 15/50 blade; no angle of attack is computed for the root section (being characterized by a junction between an airfoil and an oval section) and for the tip one (due to Prandtl’s tip loss factor, see [41])

Figure 5.15 shows the evolution of the chord distribution for both the original model and the (second) optimized one: chord values are increased along the whole blade span, up to the maximum value allowed from the constraint imposed on the blade surface. As a consequence, the blade results to be more loaded in almost every section (see Tables 5.9 and 5.10 and Figure 5.18): the global amount of aerodynamic forces is 2293 N in the original blade and increases to 2418 N in the (second) optimized one. Moreover, as shown in Figure 5.16, the generalized increment in the twist angle  $\theta$  determines a corresponding decrease in the angle of attack  $\alpha$  for all the considered sections (the trend is shown in Figure 5.17). In the second part of the optimized blade, the values of  $\alpha$  result to be closer to the angle that determines the highest aerodynamic efficiency of the adopted airfoils (6° for the S812 and

$r$ [m]	$c$ [m]	$\theta$ [°]	$\alpha$ [°]	$F$ [N]
0.279	0.4570	20.24	-	0
0.775	0.5766	20.24	28.69	18
0.889	0.5994	19.57	27.56	11
1.092	0.6361	18.41	25.49	40
1.702	0.7179	15.38	19.12	82
2.311	0.7616	12.89	14.23	142
3.124	0.7700	10.24	9.60	249
3.937	0.7338	8.14	7.39	296
4.750	0.6669	6.39	6.46	403
5.563	0.5834	4.85	6.31	466
6.603	0.4723	3.18	6.04	380
7.059	0.4263	2.63	5.27	227
7.490	0.3851	2.29	-	104

**Table 5.10:** Geometric features and load conditions of the (second) optimized AOC 15/50 blade; no angle of attack is computed for the root section (being characterized by a junction between an airfoil and an oval section) and for the tip one (due to Prandtl’s tip loss factor, see [41])

5° for the S813). The twist distribution of AOC 15/50 reveals to be not optimized for the nominal wind velocity. The blade root has small influence on aerodynamic performance as shown in Figure 5.18, however the non-optimized twist of the baseline AOC 15/50 probably causes detachments of the boundary layer and a diffuse stall in the sections near the root. Adopting a higher twist in the root zone helps to reduce these issues, however it does not greatly affect the overall performances, due to the small influence the root zone on the power production.



**Figure 5.15:** Comparison between the chord distributions for both the original AOC 15/50 blade and the (second) optimized one

The composite skin layout of the (second) optimized blade is changed by the genetic algorithm. The +45° lamina (gene A), that covered the entire blade span in the baseline configuration, is removed and replaced by the duplication of the more resistant 0° laminas (Genes F, G, I and L). A great



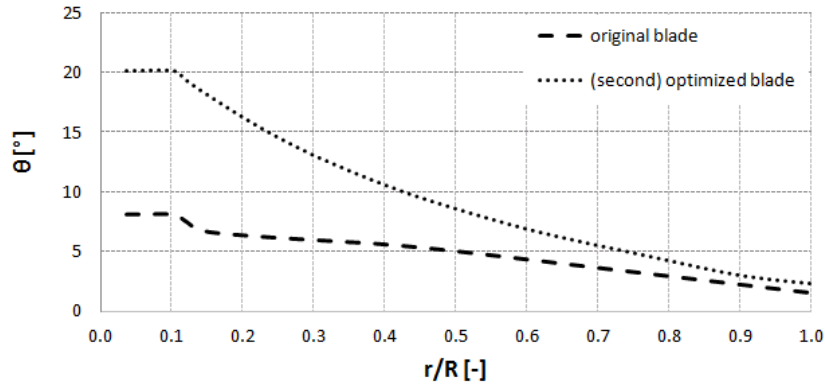


**Figure 5.16:** Comparison between the twist distributions for both the original AOC 15/50 blade and the (second) optimized one

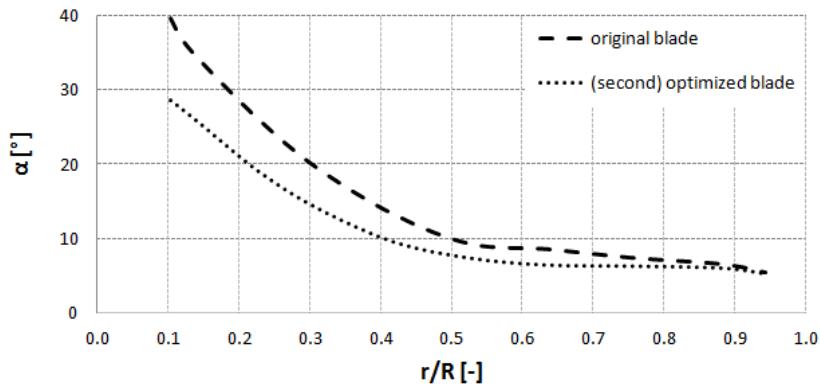


**Figure 5.17:** Comparison between the angle of attack distributions for both the original AOC 15/50 blade and the (second) optimized one

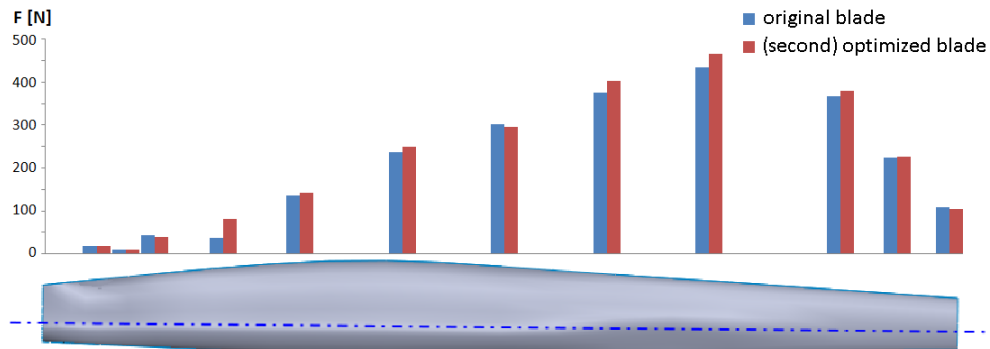


**Figure 5.18:** Comparison between the aerodynamic force distributions evaluated in 12 blade sections for both the original AOC 15/50 blade and the (second) optimized one

improvement in the structural characteristics is obtained, passing from a 219.46 mm deformation of the original blade to the 148.90 mm of the (second) optimized one (-32.15%).

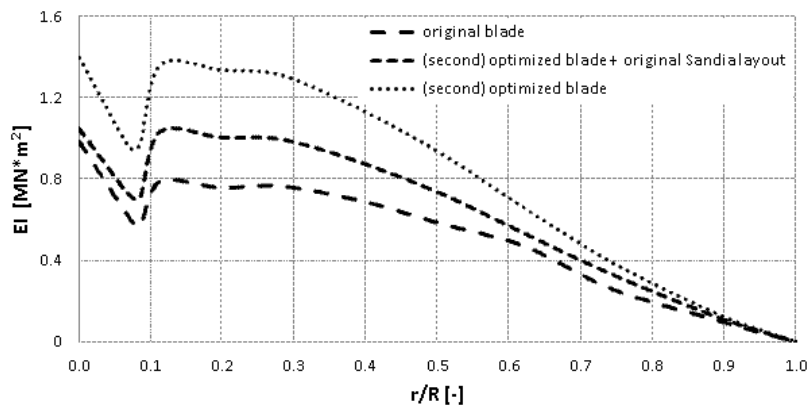
In order to better understand the influence of blade geometry on its structural behaviour, a further investigation is hereby proposed: the (second) optimized blade is analysed using the original Sandia

layout. A total deformation of 187.99 mm is registered (-14.34%), confirming that a structural improvement can also be achieved by means of a proper twist distribution. It is just the case of reminding that the solution of extending the twisted portion of the blade up to its root can be found in all commercial Enercon models [78]: as is clearly proved in this work, such architecture, besides increasing the aerodynamic efficiency of the blade portion close to the nacelle, presents also a not negligible structural benefit.

The present findings prove that the registered enhancement in the (second) optimized blade are to be ascribed to two contributions:

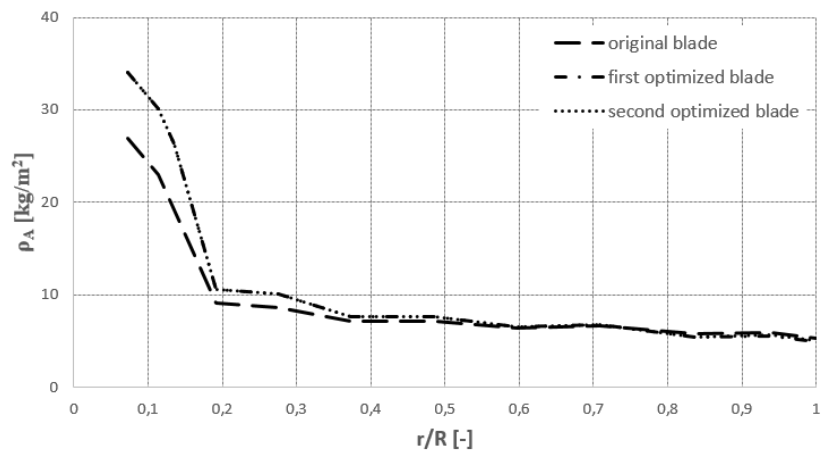
- a blade stiffening due to the higher values of both chord and twist angles along the blade span, responsible for a 14.34% reduction in the blade deformation;
- a more efficient layer distribution, responsible for a 17.81% reduction in the blade deformation.

Figure 5.19 shows the evolution of the flexural rigidity  $EI$  along the blade span, computed as the ratio between the moment  $M$  acting on a given cross section and the rate of rotation  $d\Theta/dz$  of the section itself (see [54] [66]) for the original AOC 15/50 blade, the (second) optimized one and the (second) optimized geometry coupled with the original Sandia layout. A marked improvement can be observed over the whole blade span, particularly in the central blade portion.



**Figure 5.19:** Comparison of the flexural rigidity distribution for the original AOC 15/50 blade, the (second) optimized one and the (second) optimized geometry coupled with the original Sandia layout

The surface density distribution along the blade is also presented in Figure 5.20. The overall mass of the blade has been increased, particularly in the root zone. The two optimized solutions present a similar trend of the surface density. The results show improvements in the power generation reducing the blade deformation, however the mass of the blade is increased: a further deeper analysis should take into account also the Cost Of Energy, not considered in the present optimization.



**Figure 5.20:** Comparison between the surface density distribution for the original AOC 15/50 blade and the optimized solutions

## Chapter 6

# Parametric Aero-Structural Optimization of a Small Wind Turbine

### 6.1 Description of Wind Turbine

The AOC 15/50 is a well-known Horizontal Axis Wind Turbine and it represents one of the most complete examples of a full description of wind turbine that can be found in literature: the available data take into account the geometrical data, the structural aspects and the aerodynamics performances of the turbine.

The full characterization of the composite layout which constitutes the blades and the results of the mechanical tests are described in a Sandia technical report [66]. The experimental power curve has been measured through a test campaign conducted at south of Boulder site (Colorado, USA) by the National Wind Technology Center (NWTC) and the National Renewable Energy Laboratory in the year 2003 [65]. The main characteristics of the AOC 15/50 are summarized in Table 6.1.

<b>Number of blades</b>	3
<b>Rated power</b>	50 kW
<b>Cut-in wind speed</b>	4.9 m/s
<b>Cut-out wind speed</b>	22.3 m/s
<b>Rated wind speed</b>	12 m/s
<b>Rotor diameter</b>	15 m
<b>Online rotational speed</b>	65 rpm
<b>Control type</b>	Constant speed - Fixed pitch
<b>Pitch setting</b>	1.54°
<b>Power regulation</b>	Stall regulation
<b>Tower height</b>	24.4 m

**Table 6.1:** AOC 15/50 wind turbine characteristics

The wind turbine blades measure 7.49 m and they are composed by a sequence of three aerodynamic profiles, as described in [66]. The S814 is used from the root to a distance of 4.49 m, the central section of the blade presents the S812 airfoil (from 4.49 m to 5.99 m) and, in the tip section, the S813 is adopted (5.59 m to 7.49 m). The chord and twist distributions of the AOC 15/50 are reported in Table 6.2.

Section [m]	0.515	1.124	1.874	2.624	3.374	4.120	4.870	5.620	6.370	7.120	7.490
Chord [m]	0.494	0.579	0.68	0.744	0.738	0.677	0.616	0.558	0.497	0.436	0.406
Twist [°]	7.69	5.04	4.6	4.26	3.85	3.15	2.45	1.75	1.05	0.35	0

**Table 6.2:** AOC 15/50 chord and twist distributions

The optimization procedure is described in the following sections and it is illustrated in Figure 6.1. The genetic pool of the individual is used inside the parametrization function to generate a file containing the normalized coordinates of the considered profile (*points.dat*). The coordinates file represents the RFOIL input file for the evaluation of the polars of the airfoil; being the range of angles of attack  $\alpha$  of a Horizontal Axis Wind Turbine quite large, the polars are extended through a proper function. The extended polars are later used by the BEM code in order to calculate the power curve of the wind turbine. By coupling the power curve with a Weibull distribution, first the Annual Energy Production (*AEP*), then the Annual Energy Production density (*AEP<sub>d</sub>*) values can be evaluated; the normalized *AEP<sub>d</sub>* represents the first fitness function of the proposed optimization. The coordinates file is also used in the structural function in order to calculate the mass of the blade, the structural behaviour and, later, the cost functions (Cost Of Energy or Levelized Cost Of Energy) that represent, once normalized, the second fitness function of the optimization loop.

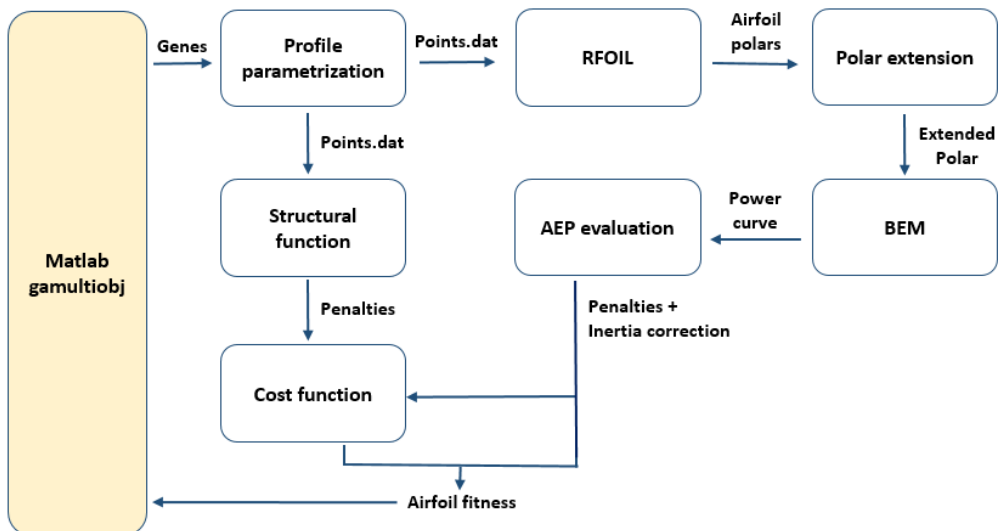


**Figure 6.1:** Scheme of the optimization algorithm for a Horizontal Axis Wind Turbine

## 6.2 Airfoil Parametrization

In order to reproduce the aerodynamic profiles sequence of the AOC 15/50 (airfoils S814, S812 and S813), the *Bezier curve discretization* has been adopted to generate the profiles. The suction side and the pressure side can be described using 7 Bezier control points: the first one (*Pt1*) represents the leading edge, the second point (*Pt2*) imposes the tangency between the suction and the pressure sides and the last one (*Pt7*) represents the trailing edge. On the whole, a profile is hence described by 12 Bezier control points. Table 6.3 reports the Bezier control points of the baseline profiles: they have been calculated through a minimization of the maximum distance between the true curve obtained from the profile points available in the airfoil tool [85] and the reproduced curve.

	<b>Pt1</b>	<b>Pt2</b>	<b>Pt3</b>	<b>Pt4</b>	<b>Pt5</b>	<b>Pt6</b>	<b>Pt7</b>
<b>S814 ps</b>	(0 0)	(0 -0.0203)	(0.2 -0.3195)	(0.4 -0.0695)	(0.6 -0.0202)	(0.8 0.0323)	(1 0)
<b>S814 ss</b>		(0 0.0461)	(0.2 0.1579)	(0.4 0.1535)	(0.6 0.0743)	(0.8 0.0825)	
<b>S812 ps</b>	(0 0)	(0 -0.0271)	(0.2 -0.0480)	(0.4 -0.2491)	(0.6 -0.0306)	(0.8 0.0096)	(1 0)
<b>S812 ss</b>		(0 0.0649)	(0.2 0.0494)	(0.4 0.2513)	(0.6 0.0334)	(0.8 0.0677)	
<b>S813 ps</b>	(0 0)	(0 -0.0390)	(0.2 -0.0634)	(0.4 -0.0765)	(0.6 -0.0771)	(0.8 0.0086)	(1 0)
<b>S813 ss</b>		(0 0.0494)	(0.2 0.0825)	(0.4 0.1453)	(0.6 0.1224)	(0.8 0.0379)	

**Table 6.3:** Bezier control points describing both the pressure and suction sides of the baseline profiles

From Figure 6.2 to Figure 6.4 the parametrization of the three profiles of the baseline configuration (S814, S812 and S813) is also illustrated and the respective polars are presented. The polars represent the trend of the lift coefficient  $C_L$  and the drag coefficient  $C_D$ , depending on the angle of attack  $\alpha$ . They have been calculated using RFOIL and extended with the *flat plate theory* method, as described in Section 6.4.1.

The Bezier curve reconstructions of the three profiles show a good agreement in fitting the baseline airfoil curves.

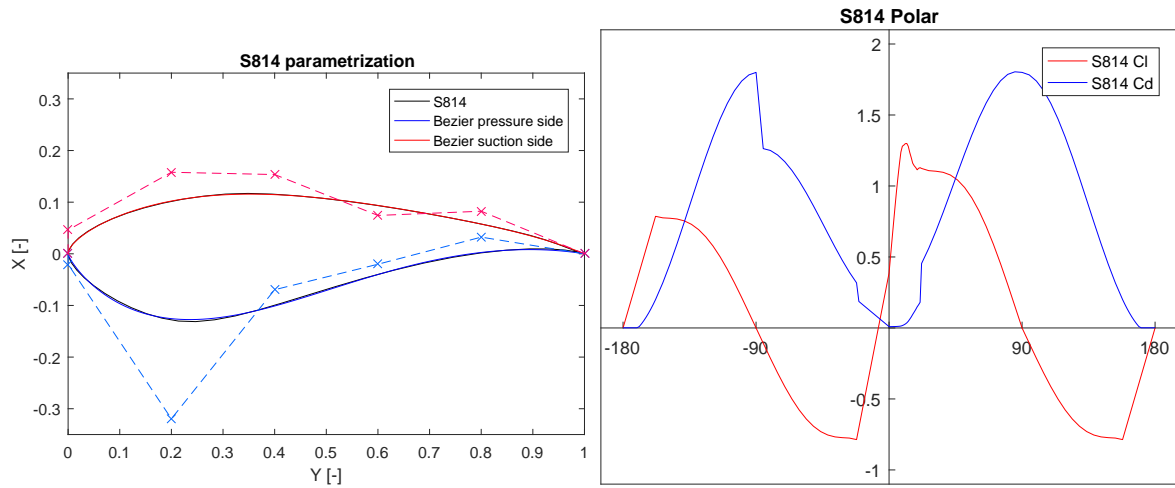


Figure 6.2: S814: Bezier parametrization and extended polar

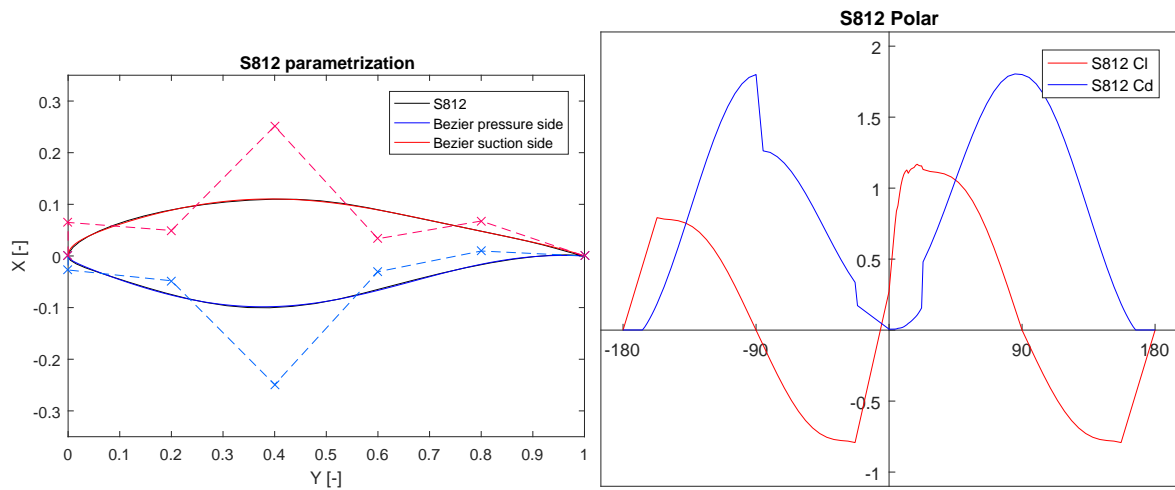


Figure 6.3: S812: Bezier parametrization and extended polar

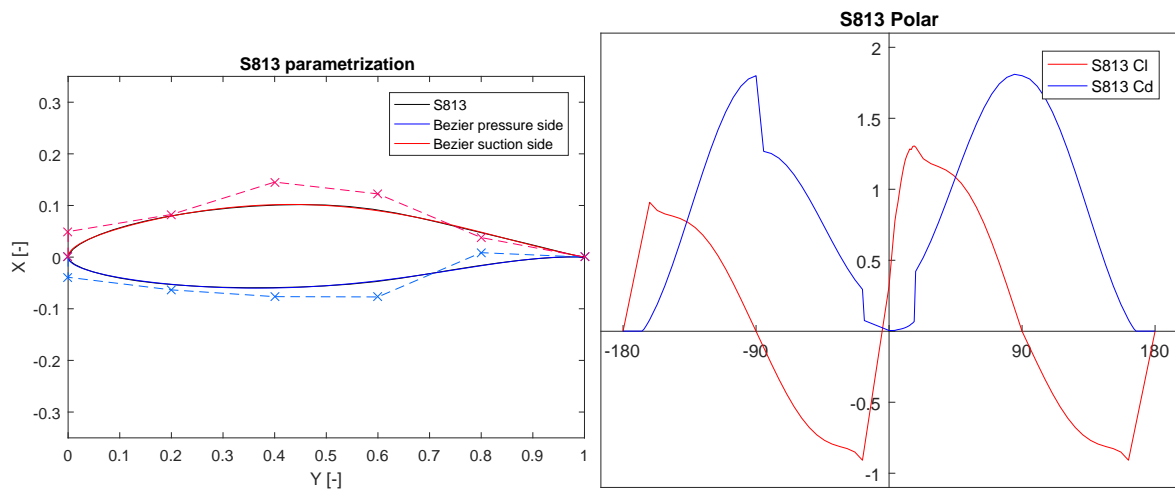


Figure 6.4: S813: Bezier parametrization and extended polar

## 6.3 Optimization Variables and Constraints

As already mentioned in Section 6.2, the airfoil is generated by composing the suction and pressure sides of a Bezier curve parametrization. In order to optimize the profile shapes, the control points, corresponding to leading and trailing edges, and all the x-coordinates, are considered fixed; the allowed displacements are represented by the y-coordinates of the 10 central points (from  $y_1$  to  $y_{10}$ ), as specified in Table 6.4.

	<b>Pt1</b>	<b>Pt2</b>	<b>Pt3</b>	<b>Pt4</b>	<b>Pt5</b>	<b>Pt6</b>	<b>Pt7</b>
<b>Profile ps</b>	(0 0)	(0 $y_1$ )	(0.2 $y_2$ )	(0.4 $y_3$ )	(0.6 $y_4$ )	(0.8 $y_5$ )	(1 0)
<b>Profile ss</b>		(0 $y_6$ )	(0.2 $y_7$ )	(0.4 $y_8$ )	(0.6 $y_9$ )	(0.8 $y_{10}$ )	

**Table 6.4:** Adopted variables for the pressure and suction sides discretization of the aerodynamic profiles

More specifically, the variables considered in the optimization (genes from  $G_1$  to  $G_{10}$ ) represent the values to be added to the y-coordinate of the baseline configuration (Table 6.3).

The control points for the profile generation are imposed to be bounded in the ranges reported in Table 6.5. The central points can be moved of a y-displacement of  $(-0.1 +0.1)$ ; the ranges of  $G_1$  and  $G_6$  (that impose the tangency at the leading edge),  $G_5$  and  $G_{10}$  (that impose the maximum available thickness at trailing edge) are constricted in a limited range. Furthermore, a check on the coordinates of the resulting curves, prevents the overlapping of the suction and pressure sides.

	<b>G1</b>	<b>G2</b>	<b>G3</b>	<b>G4</b>	<b>G5</b>	<b>G6</b>	<b>G7</b>	<b>G8</b>	<b>G9</b>	<b>G10</b>
<b>Lower bound</b>	-0.10	-0.10	-0.10	-0.10	-0.05	-0.015	-0.10	-0.10	-0.10	-0.050
<b>Upper bound</b>	+0.015	+0.10	+0.10	+0.10	+0.10	+0.05	+0.10	+0.10	+0.10	+0.05

**Table 6.5:** Constraints adopted for the proposed optimization

## 6.4 Objective Functions

Two conflicting fitness functions have been considered in order to take account of both the aerodynamic and the structural performances of the blades. Two further formulations of a cost function are also derived from the structural definition of the airfoils.

### 6.4.1 Aerodynamic Fitness Function

The aerodynamic performance of the blade is calculated through a BEM code, as described in Chapter 4 and more specifically in Section 4.4. The code has been validated against the experimental data, reported in [65].



The input of the BEM code is represented by the polar curves of the three considered airfoils: in order to calculate the  $C_L$  and  $C_D$  values for different angles of attack, both XFOIL and RFOIL panel codes have been tested. The best agreement with the experimental data has been found using RFOIL: it better predicts the experimental power curve at high wind speed, when stall phenomena occurs, as shown in Figure 6.5. In both the XFOIL and RFOIL settings, the performances of the three different airfoils of the blade have been calculated using the mean Reynolds Number  $Re$  of the baseline sections of the blade (1.0M, 1.5M and 1.5M respectively). The viscous analysis have been run using a total number of 200 panels along the airfoils and an angle of attack  $\alpha$  in the range  $[0^\circ - 40^\circ]$ . The aerodynamic codes calculate the performances of the profiles in terms of lift coefficient  $C_L$  and drag coefficient  $C_D$  until the stall occurs. In order to evaluate the performances in the entire range of angles of attack  $\alpha$ , the polars have been extended using both the *Viterna Method* ([87]) and the *Flat Plate Theory*: the second (using a maximum  $C_D$  limit of 1.8) has proved to be the most relevant. Figure 6.6 shows the comparison between the extension of the RFOIL polars using the two theories.

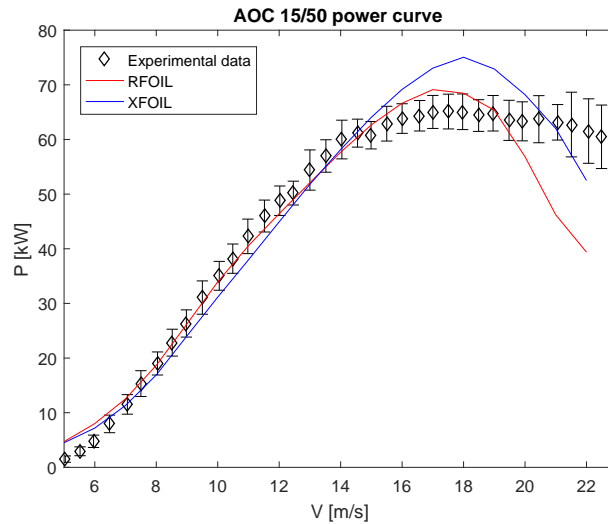


**Figure 6.5:** AOC 15/50 power curve: experimental data versus BEM results using XFOIL and RFOIL polars

After the evaluation of the power curve using the BEM code, the Annual Energy Production ( $AEP$ ) can be calculated as specified in Section 4.6, by multiplying the BEM power curve, the Weibull wind speed distribution curve and the total number of hours in a year (8760). Two different wind speed distributions, reported in Figures 6.7 and 6.8, have been examined in the present analysis: the adopted Weibull curves use a different velocity mean values (7.0 m/s and 7.5 m/s) and the same Rayleigh distribution ( $k = 2$ ). Since the cut-in wind speed of the AOC 15/50 wind turbine is 4.9 m/s the contribute to the power prediction are studied in the range from 5 m/s to 22 m/s (cut-out wind speed).

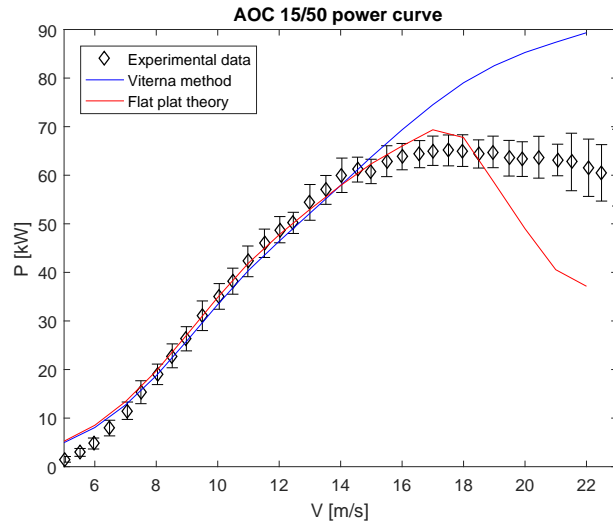


Figure 6.6: Experimental data versus *Flat plate theory* and *Viterna method*

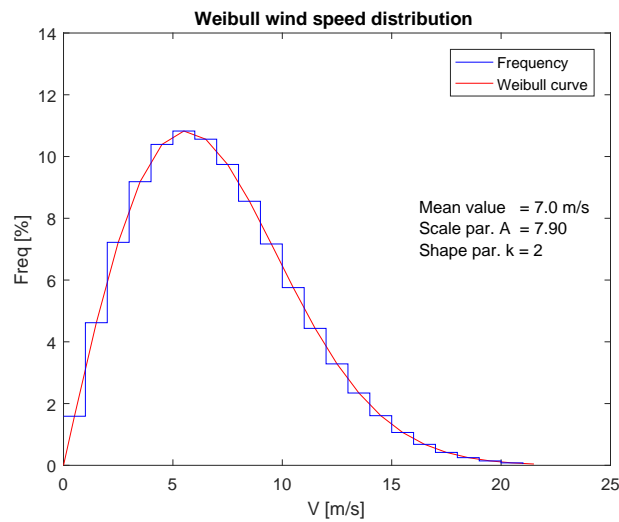


Figure 6.7: Weibull curve n.1 of the considered wind speed distribution ( $V_{ave} = 7.0$  m/s)

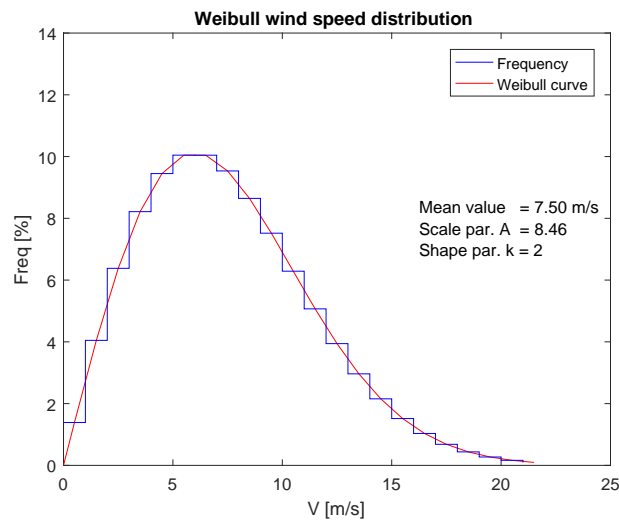


Figure 6.8: Weibull curve n.2 of the considered wind speed distribution ( $V_{ave} = 7.5$  m/s)

Since the number of turbines that can be installed in an area is inversely proportional to the square of turbine radius, the  $AEP$  value is normalized with the turbine rotor radius  $R$ . Therefore, the Annual Energy Production density is defined as:

$$AEPd = \frac{AEP}{R^2} \quad [kWh/y/m^2] \quad (6.1)$$

The aerodynamic fitness function  $f_{AEP}$ , to be minimized, is therefore represented by ratio between the  $AEPd_{bas}$  of the baseline configuration and the  $AEPd$  of the analysed individual.

$$f_{AEP} = \frac{AEPd_{bas}}{AEPd} \quad (6.2)$$

#### 6.4.2 Structural Fitness Function

In the previous work on AOC 15/50 of Dal Monte et al. [83], the mechanical behaviour of the wind turbine blade was the main topic of the analysis: a FEM model, using the software ANSYS Mechanical, has been set and validated, comparing the results to the structural test on the AOC 15/50 composite blade carried by SANDIA [66]. Two glass fibre reinforced plastic (GFRP), A130 and the DB120, represent the composite material adopted in the blade layout composition for  $0^\circ$  and  $\pm 45^\circ$  layers respectively, as specified in [66]. In the trailing edge zone (Layup n. 9) also balsa wood is used. For reasons of clarity, the materials properties and the AOC 15/50 composite layout visualization, reported in Section 5.1, are also described in the present Section. The structural properties of the adopted materials are described in Table 6.6. Table 6.7 reports the layup schedule and the thickness of the different blade sections in both the span-wise and chord-wise directions. A graphic illustration of the layout zones of the blade is presented in Figure 6.9.

	<b>A130 (<math>0^\circ</math>)</b>	<b>DB120 (<math>\pm 45^\circ</math>)</b>	<b>Balsa Wood</b>
$E_L=E_X$ [MPa]	31700	26200	187
$E_T=E_Y$ [MPa]	7580	6550	61
$E_Z=E_Z$ [MPa]	7580	6550	4070
$\nu_{LT} = \nu_{XY}$ [-]	0.32	0.39	0.67
$\nu_{TZ} = \nu_{YZ}$ [-]	0.32	0.35	0.01
$\nu_{LZ} = \nu_{XZ}$ [-]	0.32	0.32	0.02
$G_{LT}=G_{XY}$ [MPa]	3450	4140	20.3
$G_{TZ}=G_{YZ}$ [MPa]	3100	3720	150
$G_{LZ}=G_{XZ}$ [MPa]	3100	3720	220
$\rho$ [kg/m <sup>3</sup> ]	1714	1714	153
t [mm]	0.571	0.203	9.530

**Table 6.6:** Structural properties of the materials adopted in the AOC 15/50 blade

Component	Location [mm]	Layup schedule	Thickness [mm]	$\rho_{eq}$ [kg/m <sup>2</sup> ]	Layup n. [-]
Root	279 to 775	[±45/0 <sub>6</sub> /±45/0 <sub>6</sub> /+45] <sub>S</sub>	15.7	26.99	1
	775 to 889	[±45/0 <sub>5</sub> /±45/0 <sub>5</sub> /+45] <sub>S</sub>	13.5	23.07	2
	889 to 1092	[±45/0 <sub>4</sub> /±45/0 <sub>4</sub> /+45] <sub>S</sub>	11.2	19.16	3
Spar cap	1092 to 2311	[±45/0 <sub>4</sub> /±45/0 <sub>4</sub> /+45] <sub>S</sub>	11.2	19.16	3
	2311 to 3937	[±45/0 <sub>3</sub> /±45/0 <sub>3</sub> /+45] <sub>S</sub>	8.9	15.24	4
	3397 to 5563	[±45/0 <sub>2</sub> /±45/0 <sub>2</sub> /+45] <sub>S</sub>	6.6	11.32	5
	5563 to 7493	[±45/0/±45/0/+45] <sub>S</sub>	4.3	7.40	6
Leading edge	1092 to 2311	[±45/0 <sub>2</sub> /±45] <sub>S</sub>	3.9	6.70	7
	2311 to 7493	[±45/0/±45] <sub>S</sub>	2.8	4.75	8
Trailing edge	1092 to 6604	[±45/0/balsa/0/±45]	11.5	3.35	9
	6004 to 7493	[±45/0] <sub>S</sub>	2.0	3.35	10
Spar flange	1092 to 7493	[±45/0 <sub>2</sub> /±45] <sub>S</sub>	3.9	6.70	11
Spar web	1092 to 7061	[±45/0 <sub>2</sub> /±45] <sub>S</sub>	3.9	6.70	12

**Table 6.7:** Layup schedule of the analysed rotor blade

In the proposed analysis, the layout and the total length of the blade are not being modified, hence the mass of the blade has been evaluated through a simplified Matlab function. The 12 layup zones of Figure 6.9 are characterized by the value of  $\rho_{eq}$ , the *Equivalent Surface Density* in kg/m<sup>2</sup>, as reported in Table 6.7. The  $\rho_{eq}$  parameter has been calculated by summing the product of the thickness and the layer density of every section of the blade:

$$\rho_{eq} = \sum_{i=1}^N t_i * \rho_i \quad [kg/m^2] \quad (6.3)$$

In order to evaluate the total weight of the blade, the equivalent surface densities are later multiplied by the area of the sections (determined by the profile lengths, depending on the chosen control points) and summed. The mass of the considered baseline AOC 15/50 blade is 80.79kg.

The structural fitness function  $f_m$ , to be minimized, is therefore represented by ratio between the mass  $m$  of the considered individual and the mass  $m_0$  of the baseline blade individual.

$$f_m = \frac{m}{m_0} \quad (6.4)$$

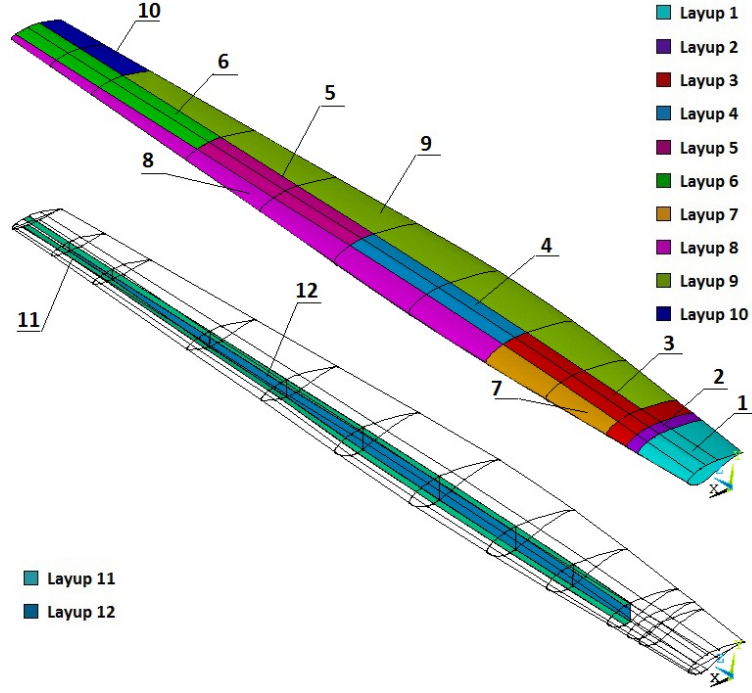


**Figure 6.9:** Exploded drawing of the analysed rotor blade geometry, showing the subdivision in 9 areas spanwise and 8 zones chordwise

### 6.4.3 Cost Fitness Function

An initial estimation of the cost function is done with the expression given by Giguere et al. [86] and used in Benini et al. [52]. The *Cost Of Energy* can be expressed as:

$$COE = \frac{(TC + BOS)}{AEP} * FCR + O\&M \quad (6.5)$$

The turbine cost  $TC$  is proportional to the blades weight, assuming that the blades, made in E-glass material, represent the 20% of the total cost of the turbine. The  $BOS$  cost (200\$/kW) represents the balance of the station, proportional to the turbine rate power. The considered fixed charge rate ( $FCR$ ) is 11%/y and the costs for Operation and Maintenance  $O\&M$  are estimated in 0.01\$/kWh. The cost model is based on the assumption that total turbine cost can be reconstructed on the basis of the wind turbine blade alone.

The cost fitness function  $f_{COE}$ , to be minimized, is represented by the ratio between the  $COE$  of the analysed individual and the  $COE_0$  of the baseline configuration, for the Weibull wind speed distribution considered. The  $COE$  of the AOC 15/50 baseline configuration results 0.0301 \$/kWh.

$$f_{COE} = \frac{COE}{COE_0} \quad (6.6)$$

The Cost Of Energy value results to be quite low compared to the current costs because of the adopted hypothesis in the formulation (the *COE* formulation was proposed in the year 1999). An updated formulation of the *Levelized Cost Of Energy (LCOE)* is also presented and used in a further optimization (Section 6.10).

## 6.5 Optimization Strategy

A preliminary global optimization (named as *Wb1Opt0*) of the wind turbine has run considering both the maximization of the AEP density ( $f_{AEP}$  to be maximized) and the minimization of the mass of the blade ( $f_m$ ); the results are reported in Appendix B. The strategy consisted in simultaneously modifying the control points of all the three airfoils of the blade.

The adopted strategy has revealed to be not suitable for the proposed analysis; the modification of a single point could improve the performances of a profile and, in the meanwhile, decrease the performances of the other two profiles. The analysis *Wb1Opt0*, indeed, converged to solution affected by the presence of semi-aerodynamic shapes in several zone along the blade. On the other hand, the simultaneous variation of 30 genes (i.e. the control points of the three aerodynamic profiles in span-wise direction) represents an excessive number of variables, which results in a larger population and an higher number of generation in order to reach a convergence of the Pareto front. Furthermore, the analysis of results (Figures from B.2 to B.4) shows the tendency to increase the angles of attack of the optimized profiles. This consideration suggested to perform a preliminary optimization on the twist of the blade. Since in the BEM code the different section of the bade are individually analysed and independent, an optimization on the airfoil shape has be performed in three separate and consecutive steps.

The final optimization strategy can be summarized as:

- *OptTw*: mono-objective twist angles distribution optimization
- *Opt1*: multi-objective shape optimization (root airfoil)
- *Opt2*: multi-objective shape optimization (primary airfoil)
- *Opt3*: multi-objective shape optimization (tip airfoil)

## 6.6 Twist Angles Distribution Optimization

The global optimization (*Wb1Opt0*), reported in Appendix B, has highlighted the possibility to increase the *AEP* by decreasing, at the same time, the overall mass of the blade. A deeper analysis of the optimized airfoils has underlined the tendency of bending the profiles in order to change the angle of attack  $\alpha$ . Because of that, a preliminary mono-objective optimization, concerning the twist angle distribution  $\theta$  (the sum between the pitch angle of the blade  $\theta_P$  and the local twist angle  $\theta_T$ ), has been necessary. The trend of twist angles  $\theta$  in the AOC 15/50 seems, indeed, to be not optimized for the nominal velocity, as found in [84]. The parameters of the analysis are represented by the y-coordinates of 6 Bezier points that determine the twist angle distribution  $\theta$  in the spanwise direction. Several mono-objective optimization analysis have been carried for different Weibull wind speed distribution targets, with mean values of velocity from 5.0 m/s to 7.5 m/s.

The optimization process consists in the maximization of the Annual Energy Production density (*AEPd*) of the wind turbine using the Weibull distribution of the considered cases: for every analysis, the Rayleigh distribution is assumed (shape parameter  $k$  equal to 2), while the scale parameters  $A$  changes depending on the considered mean wind speed, as reported in Table 6.8.

Case	Mean Wind Speed	A	k
<b>AEP50</b>	5.0 m/s	5.64	2
<b>AEP55</b>	5.5 m/s	6.21	2
<b>AEP60</b>	6.0 m/s	6.77	2
<b>AEP65</b>	6.5 m/s	7.33	2
<b>AEP70</b>	7.0 m/s	7.90	2
<b>AEP75</b>	7.5 m/s	8.46	2

**Table 6.8:** Cases considered for the optimization of the twist angle distribution

The adopted constraints of the optimization parameters are specified in Table 6.9. In order to guarantee a minimum value of the pitch angle  $\theta_P = 1^\circ$ , the lower bound of the last Bezier control point is imposed.

	Pt1	Pt2	Pt3	Pt4	Pt5	Pt6
<b>UpperBound</b>	45°	35°	25°	20°	15°	10°
<b>LowerBound</b>	12°	8°	5°	3°	2°	1°

**Table 6.9:** Upper and lower bounds of the Bezier points used in the twist optimization

$f_{AEP}$  represents the fitness function to be minimized, as defined in Section 6.4.1: the *AEPd* is normalized with respect the value of the baseline configuration. The initial population is random initialized and consists in 100 individuals. The maximum number of generations has been set to 100.

### 6.6.1 Results of the Twist Angle Analysis

From Figure 6.10 to Figure 6.12, the twist angle distribution of the AOC 15/50 baseline configuration is compared to the resulting distributions from the optimization processes. For all the considered cases, the twist angle values have been increased along the whole blade, especially in the root zone. The baseline twist angles have revealed to not be optimized for the nominal wind speed and this could causes detachments of the boundary layer and a diffuse stall in the root sections.

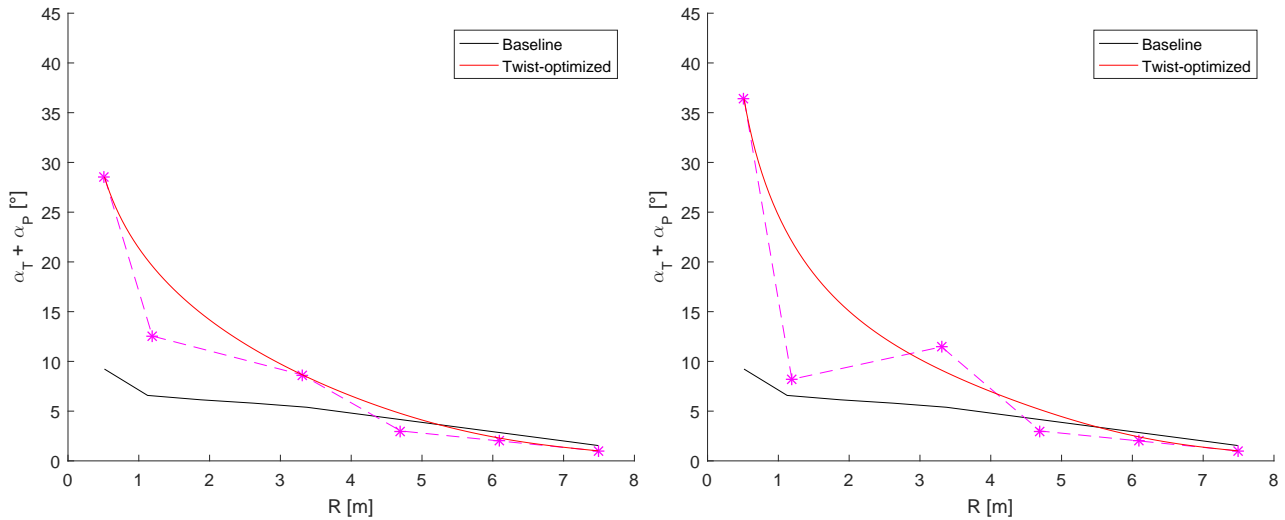


**Figure 6.10:** Twist angle distribution for a Weibull mean wind speed mean of 5.0 m/s (left) and 5.5 m/s (right)

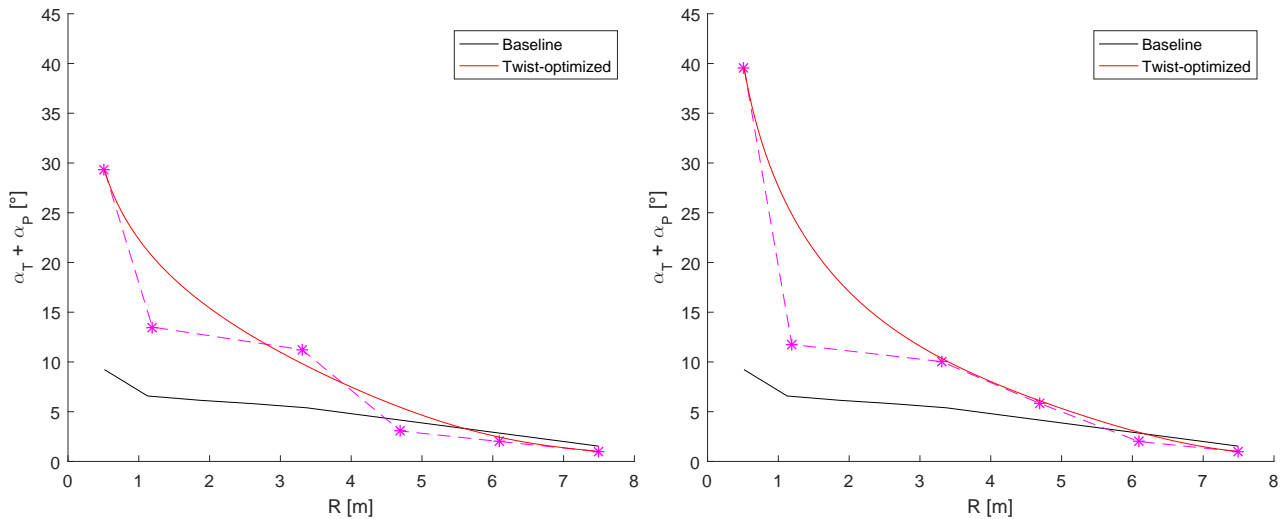


**Figure 6.11:** Twist angle distribution for a Weibull mean wind speed mean of 6.0 m/s (left) and 6.5 m/s (right)



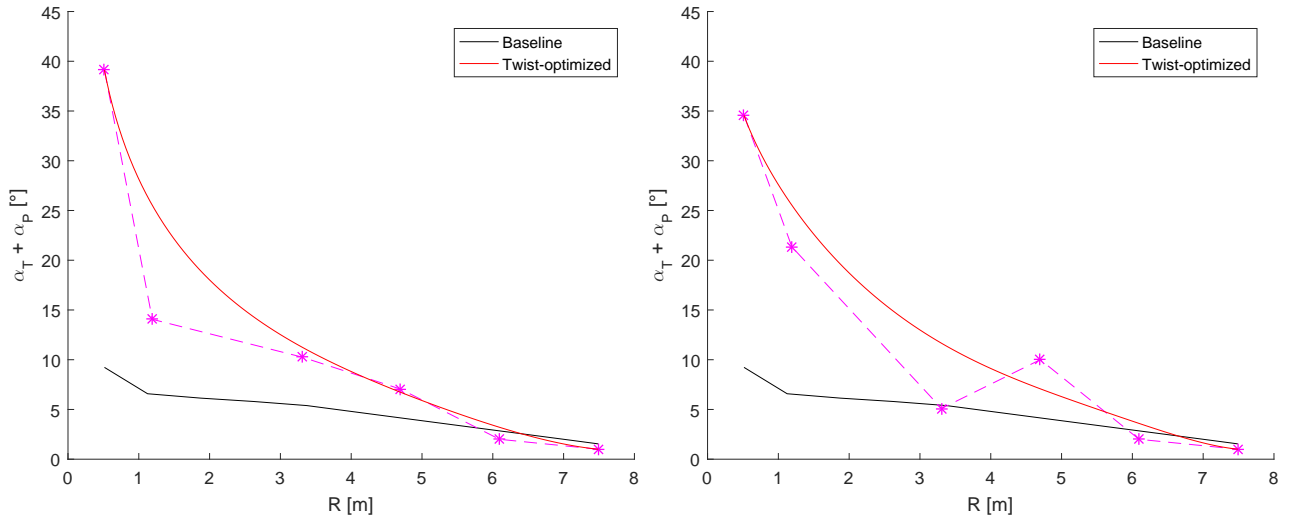


**Figure 6.12:** Twist angle distribution for a Weibull mean wind speed mean of 7.0 m/s (left) and 7.5 m/s (right)

For all the considered Weibull wind speed distributions, the optimal twist angle, evaluated at the root, results to be from three to four times the value assumed in the baseline profile ( $9.23^\circ$ ); at the same time, the pitch angle  $\theta_P$  at the tip of the blade has been slightly reduced from  $1.54^\circ$ , in the baseline configuration, to  $1.00^\circ$  for all the twist-optimized configurations (the value imposed by the lower bound constraint).

The Annual Energy Production density has been improved for all the twist-optimized configurations. In particular, for the *AEP70* condition, the optimized *AEPd* results  $2730.6 \text{ kWh/m}^2$  with an increment of 5.60% compared to the *AEPd* of the AOC 15/50 baseline configuration ( $2585.6 \text{ kWh/m}^2$ ). In the *AEP75* condition, the *AEPd* has been increased of 6.55% from the baseline value ( $2971.2 \text{ kWh/m}^2$ ) to the twist-optimized value ( $3165.7 \text{ kWh/m}^2$ ).

The *AEP70* and *AEP75* twist-optimized blades will represent the baseline configurations of the further analysis on the airfoil shapes.

## 6.7 Penalties and Corrections Adopted

The global optimization (*WpiOpt0*) has highlighted some issues in the robustness of the code, as reported in Appendix B. Furthermore, in order to avoid the generation of undesirable airfoils and to better fit the experimental power curve, the presented two corrections have been implemented.

### 6.7.1 Penalty for Thin Profiles

In order to avoid the generation of thin profiles with low structural proprieties (as found in *WpiOpt0*, Figure B.4), the bending stiffness in the flapwise direction has been monitored in three section along the blade, where each profile zone begins, at 15%, 60% and 75%. Figure 6.13 illustrates the different structural zones considered for the primary blade profile (S812).

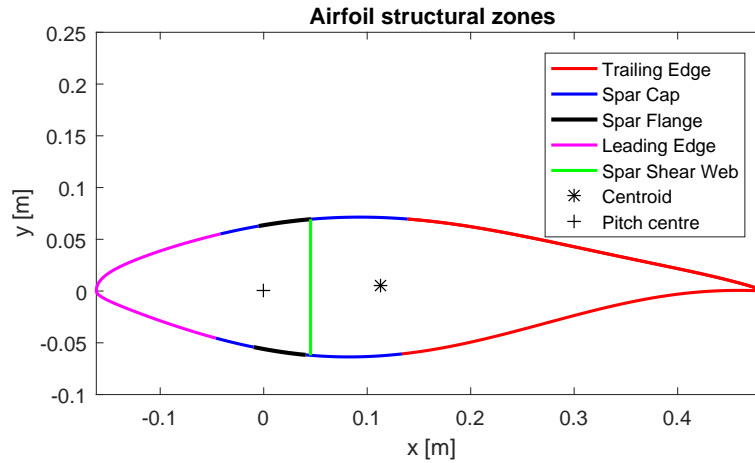


**Figure 6.13:** Structural zones of the blade profiles

A thin profile may generate structural issues during the lifetime of the wind turbine blade, hence a penalty factor has been applied in order to increase the resulting mass value of thin profiles. Thin profiles probably need to be reinforced in order to guarantee the structural requirements of the blade and these further reinforcements implicate an addition of mass in the blade structure.

The mass characteristics of the different sections and zones can be determined from Tables 6.6 and 6.7; the airfoil is divided in 200 segments and the *Equivalent Surface Density parameter*  $\rho_{eq}$  is used to calculate the mass of the single segment. Since the position of the segments  $(x_i, y_i)$  is known, the coordinates of the centroid of the profile can be calculated as:

$$x_{cm} = \sum_{i=1}^N m_i * x_i \quad y_{cm} = \sum_{i=1}^N m_i * y_i \quad (6.7)$$

The bending stiffness of the profile, with respect its centroid, is computed as:

$$I_{xx} = \sum_{i=1}^N m_i * y_{i,c}^2 \quad I_{yy} = \sum_{i=1}^N m_i * x_{i,c}^2 \quad (6.8)$$

where  $x_{i,c}$  and  $y_{i,c}$  represent the distance of the considered segment from the centroid.

A progressive penalty is applied to increase the mass of the airfoils with a low bending stiffness  $I_{xx}$  in the flapwise direction. The mass is increased by the penalty factor  $i_m$  if the bending stiffness is reduced between 40% and 55% compared to the bending stiffness of the baseline profile.  $I_{xx,rel}$  represents the ratio between the two bending stiffness.

$$i_m = \begin{cases} 1 & I_{xx,rel} > 0.6 \\ 1 + \frac{(0.6 - I_{xx,rel})}{2} & 0.45 \leq I_{xx,rel} \leq 0.6 \\ 1000 & I_{xx,rel} < 0.45 \end{cases} \quad (6.9)$$

The penalty is only applied to the zone of the blade where the considered airfoil is adopted, hence to the mass of the sector that is being optimized. As an example, Equation 6.10 calculates the resulting mass, when the penalty is applied to the zone-3 (tip airfoil):

$$m_{bla} = m_{pro,1} + m_{pro,2} + m_{pro,3} * i_m \quad (6.10)$$

being  $m_{pro,1}$ ,  $m_{pro,2}$ ,  $m_{pro,3}$  the components of the mass relative to the zone-1 (73.45% of the baseline mass), zone-2 (12.68% of the baseline mass) and zone-3 (13.87% of the baseline mass).

It is worth mentioning that the mass value of the blade is closely linked to the resulting cost of energy, since its formulations always take into account the cost of materials. The Cost Of Energy is therefore also affected by the penalty applied to the mass of the blade.

### 6.7.2 Correction for the Start-Up Inertia of the Wind Turbine

As reported in Figure 6.5, the BEM code, based on RFOIL estimation of the aerodynamic polars of the profiles, fits well the experimental data; the highest differences are found the in the first part of the curve (low wind speeds) and in the curve after stall. The cut-in velocity of the AOC 15/50 is 4.9 m/s, this means that the experimental results of the first part of the power curve could have been affected by the blade inertia to be moved from a condition of stillness. For a wind velocity of 5.0 m/s, indeed, the registered experimental power production is 1.51 kW, the one calculated using the BEM code results 4.71 kW. The difference greatly affects the global AEP value because the considered Weibull distribution of the wind has a mean velocity of 6.0 m/s. In order to take into account this behaviour, two penalty functions for the low wind speeds are proposed:

- Cubic penalty function

$$Y = 0.0061 * V^3 - 0.1827 * V^2 + 1.8259 * V - 5.1081$$

- Exponential penalty function

$$Y = -30e^{(2-e)V}$$

where  $V$  represents the wind speed in m/s and  $e$  is the Euler Number.

As can be seen in Figure 6.14, the use of both the proposed penalty functions fits well the experimental power curve at low velocities. The exponential penalty function has been chosen and applied in the wind speed range [5.0 - 11.0 m/s] for the further analysis.

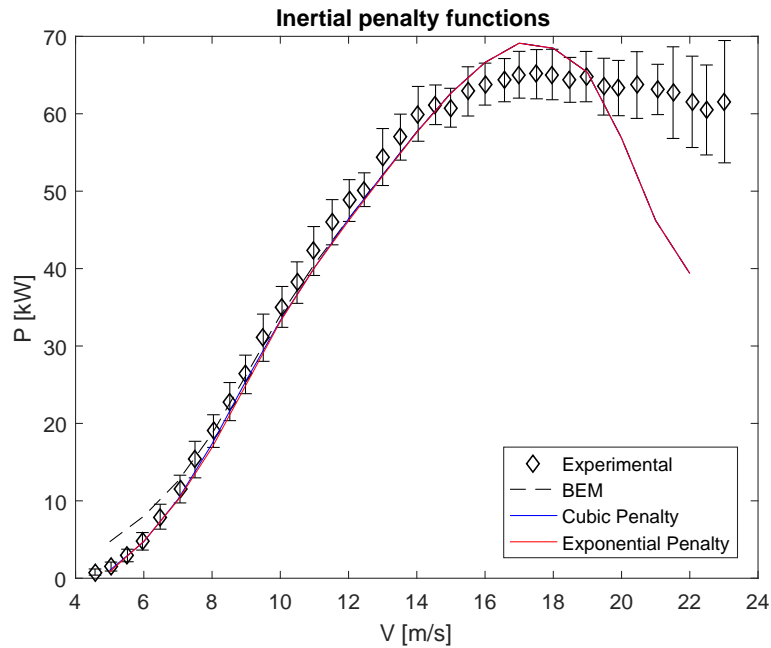


**Figure 6.14:** Effect of the proposed penalty functions on the power curve calculated by the BEM code

## 6.8 AEP70 - Shape Optimization of the Blade Airfoils

In optimization AEP70, the fitness function describing the Cost Of Energy  $f_{COE}$  has been considered in place of the structural function  $f_m$ , used in the global optimization analysis (*Wb1Opt0*). In order to avoid the generation of thin airfoils, a penalty related to the bending stiffness value is applied (further details in Section 6.7.1). In the presented calculation the twisted blade, optimized for a Weibull wind speed distribution of mean 7.0 m/s, represents the considered baseline, as found in Section 6.6.1.

### 6.8.1 AEP70-Opt1: Optimization of the Root Airfoil of the Blade

The first profile optimization (*AEP70 – Opt1*) concerns the shape of the root airfoil of the AOC 15/50 blade (S814 airfoil of the baseline configuration used from 0.515 m to 4.490 m in the span-wise direction). The optimization has been set using an initial population of 100 individuals and a total generation number of 50. Figure 6.15 illustrates the results of the optimization in terms of Pareto front convergence.

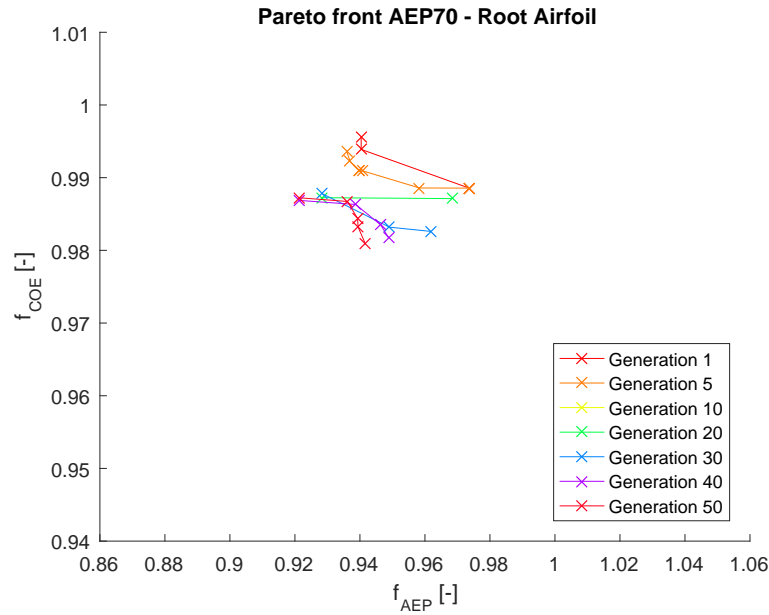


**Figure 6.15:** *AEP70 – Opt1*: Pareto front convergence for the root airfoil optimization

Three solutions belonging to the last the Pareto front have been analysed: the genetic pools are reported in Table 6.10.

	Genetic pool										Fitness	
<b>SolA</b>	-0.0623	0.0962	0.0998	0.0342	0.0438	0.0437	0.0636	-0.0403	-0.0227	0.0375	0.9212	0.9872
<b>SolB</b>	-0.0745	0.0906	0.0928	0.0922	0.0479	0.0455	0.0112	0.0442	0.0983	0.0409	0.9362	0.9867
<b>SolC</b>	-0.0394	0.0865	0.0959	0.0901	0.0466	0.0379	-0.0323	0.0381	0.0880	0.0387	0.9417	0.9809

**Table 6.10:** Genetic pool and fitness values of the considered points in Pareto front of *AEP70 – Opt1*

From Figure 6.16 to Figure 6.18 the resulting power curve and the shape of the chosen root airfoils are illustrates.

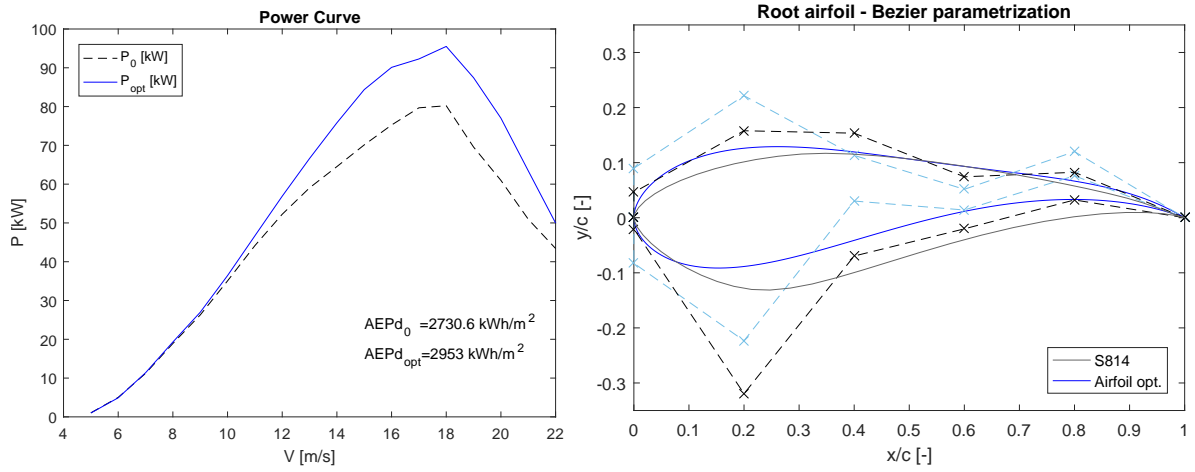


Figure 6.16: AEP70 – Opt1: Solution A power curve and airfoil parametrization

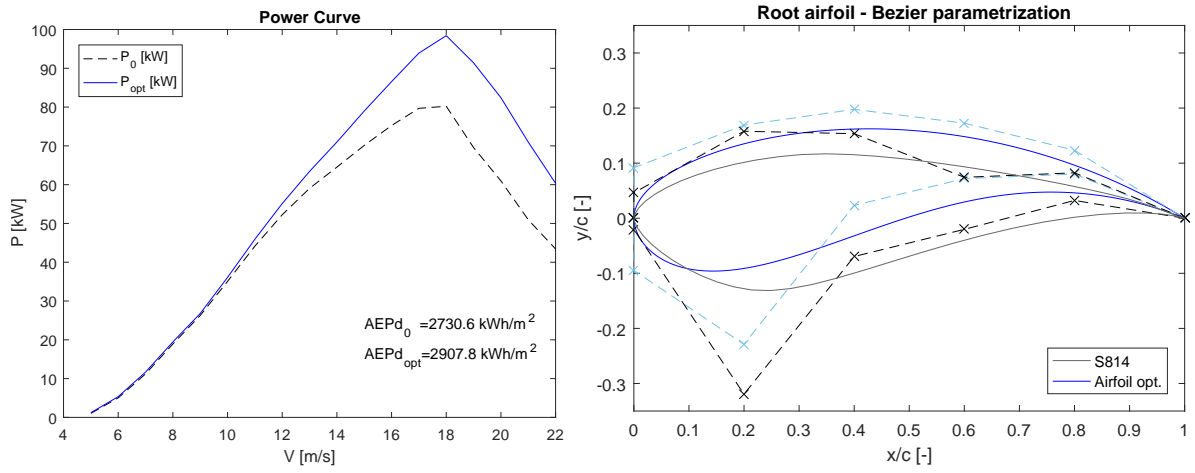


Figure 6.17: AEP70 – Opt1: Solution B power curve and airfoil parametrization

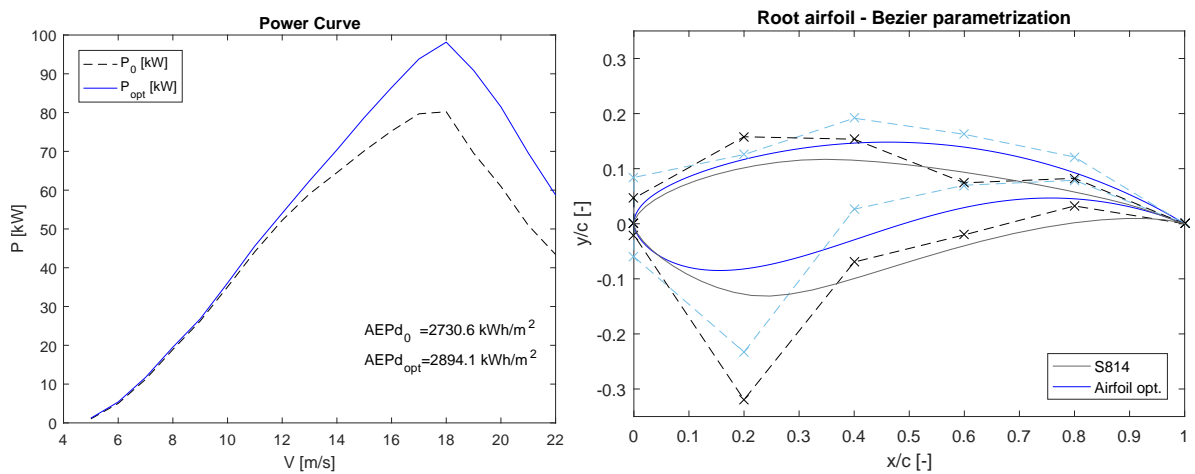
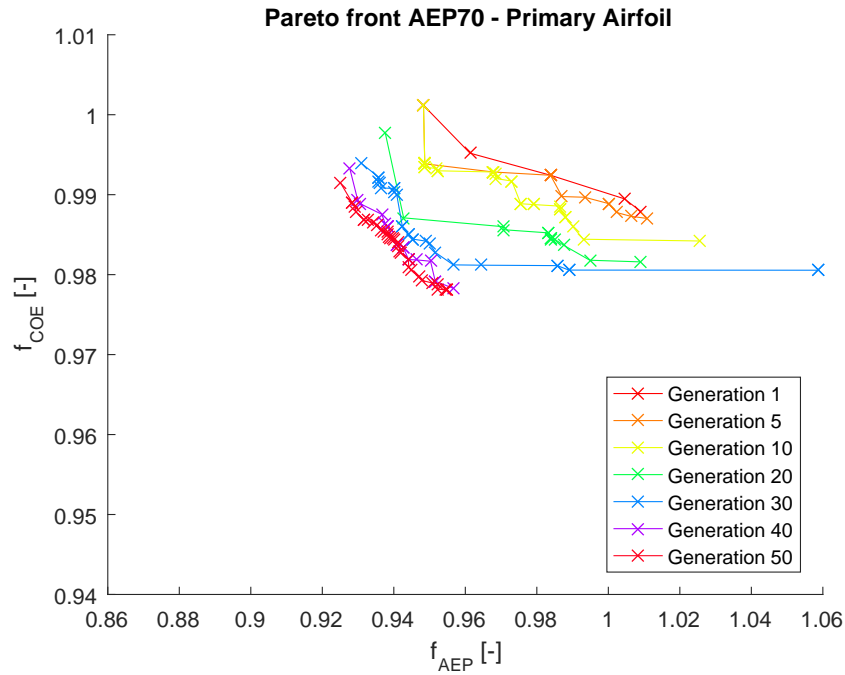


Figure 6.18: AEP70 – Opt1: Solution C power curve and airfoil parametrization

### 6.8.2 AEP70-Opt2: Optimization of the Primary Airfoil of the Blade

The second optimization (named *AEP70 – Opt2*) concerns the shape of the primary airfoil of the AOC 15/50 blade (S812 airfoil of the baseline configuration used from 4.490 m to 5.990 m in the span-wise direction). As the root profile optimization, an initial population of 100 individuals and a total generations number of 50 have been set.

Figure 6.19 illustrates the results of the optimization in terms of Pareto front convergence.



**Figure 6.19:** *AEP70 – Opt2*: Pareto front convergence for the primary airfoil optimization

As for the previous optimization, three solutions belonging to the last the Pareto front have been analysed: the genetic pools are reported in Table 6.11.

	Genetic pool										Fitness	
<b>Sol1</b>	-0.0425	0.0947	0.0807	0.0661	0.0421	0.0677	0.0711	0.0691	0.0673	0.0392	0.9251	0.9915
<b>Sol2</b>	-0.0479	0.0942	0.0817	0.0731	0.0445	0.0766	0.0175	0.0348	0.0707	0.0384	0.9399	0.9843
<b>Sol3</b>	-0.0555	0.0870	0.0798	0.0744	0.0424	0.0443	0.0040	0.0683	0.0761	0.0373	0.9548	0.9741

**Table 6.11:** Genetic pool and fitness values of the considered points in Pareto front of *AEP70 – Opt2*

Finally, Figures from 6.20 to 6.22 illustrate the resulting power curve and shape of the chosen optimized airfoils belonging to the Pareto front.

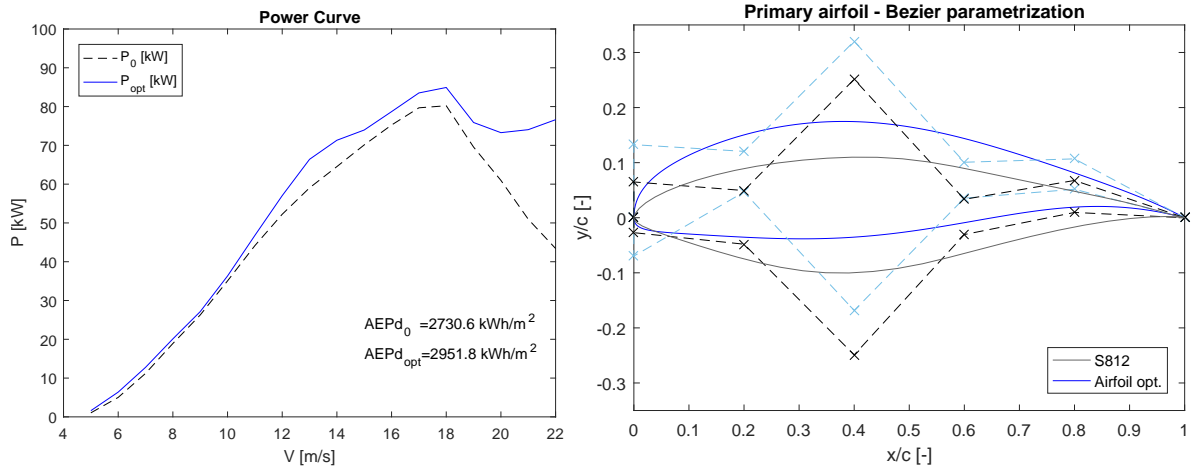


Figure 6.20: AEP70 – Opt2: Solution A power curve and airfoil parametrization

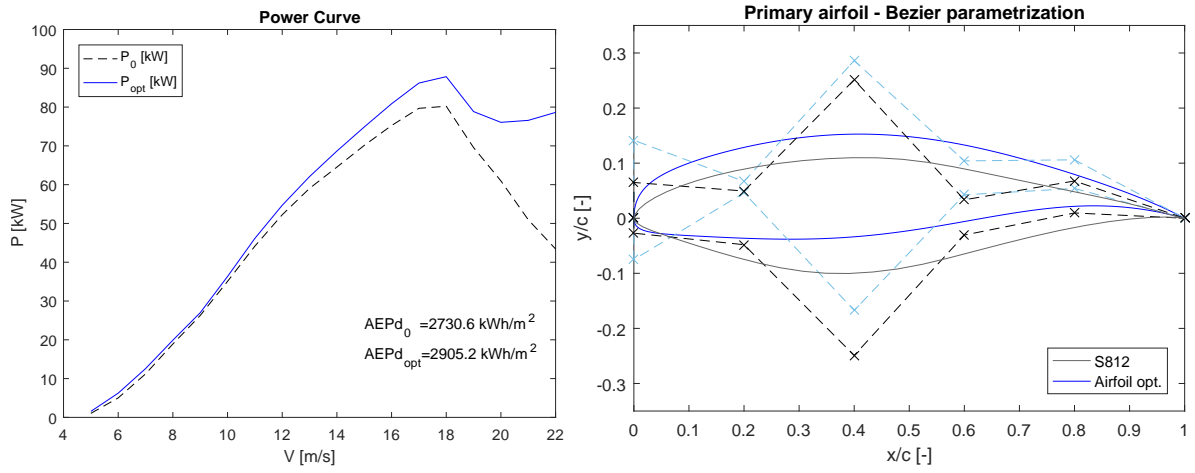


Figure 6.21: AEP70 – Opt2: Solution B power curve and airfoil parametrization

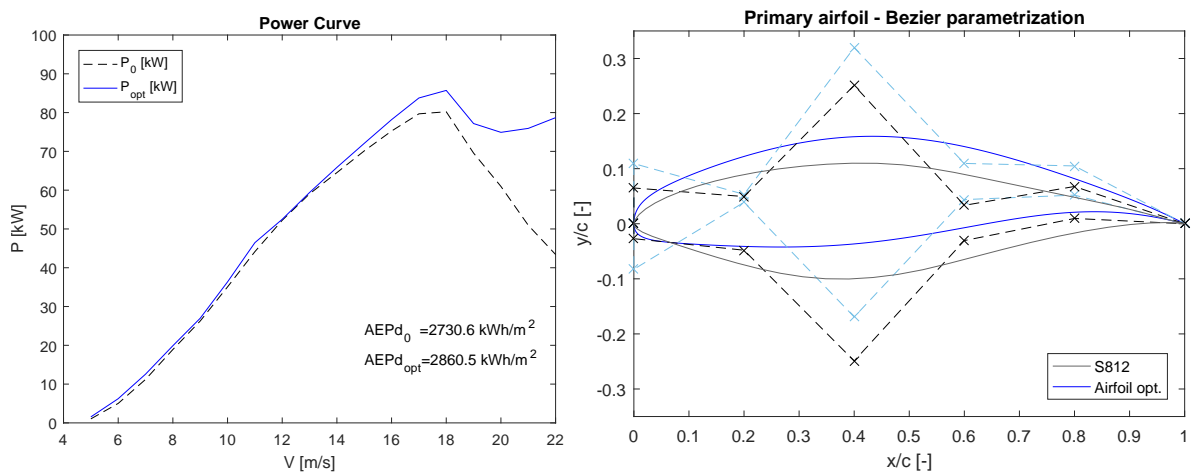
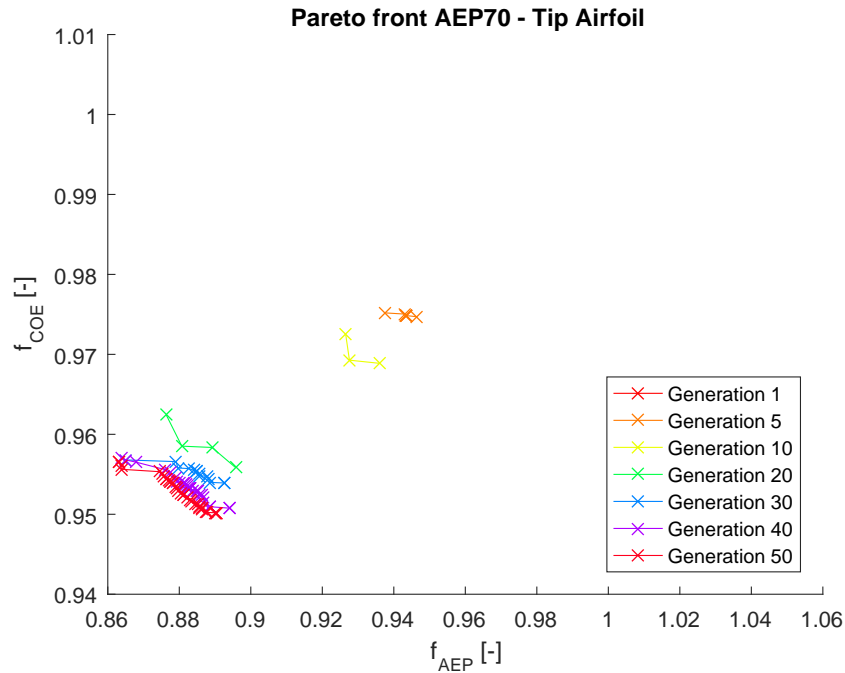


Figure 6.22: AEP70 – Opt2: Solution C power curve and airfoil parametrization



### 6.8.3 AEP70-Opt3: Optimization of the Tip Airfoil of the Blade

The third optimization (*AEP70 – Opt3*) concerns the shape of the tip airfoil of the AOC 15/50 blade (S813 airfoil of the baseline configuration used from 5.990 m to 7.490 m in the span-wise direction). The optimization has been set using an initial population of 100 individuals and a total generation number of 50. Figure 6.23 illustrates the results of the optimization in terms of Pareto front convergence.



**Figure 6.23:** *AEP70 – Opt3*: Pareto front convergence for the tip airfoil shape optimization

As for the previous optimizations, three solutions belonging to the last the Pareto front have been analysed: the genetic pools are reported in Table 6.12.

	Genetic pool										Fitness	
<b>SolA</b>	0.0049	0.0844	0.0967	0.0935	0.0496	0.0659	0.0872	0.0905	0.0962	0.0433	0.8632	0.9565
<b>SolB</b>	-0.0005	0.0886	0.0967	0.0957	0.0490	0.0837	0.0192	0.0848	0.0936	0.0460	0.8877	0.9502
<b>SolC</b>	0.0002	0.0863	0.0965	0.0936	0.0493	0.0803	0.0548	0.0735	0.0913	0.0461	0.9973	0.9371

**Table 6.12:** Genetic pool and fitness values of the considered points in Pareto front of *AEP70 – Opt3*

Finally, Figures from 6.24 to 6.26 illustrate the resulting power curve and shape of the chosen tip airfoils belonging to the Pareto front.

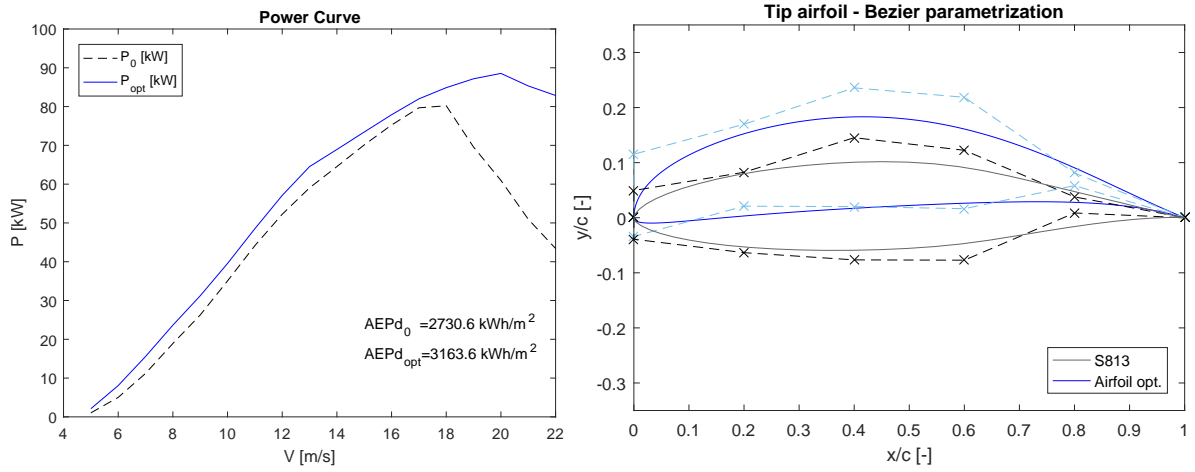


Figure 6.24: AEP70 – Opt3: Solution A power curve and airfoil parametrization

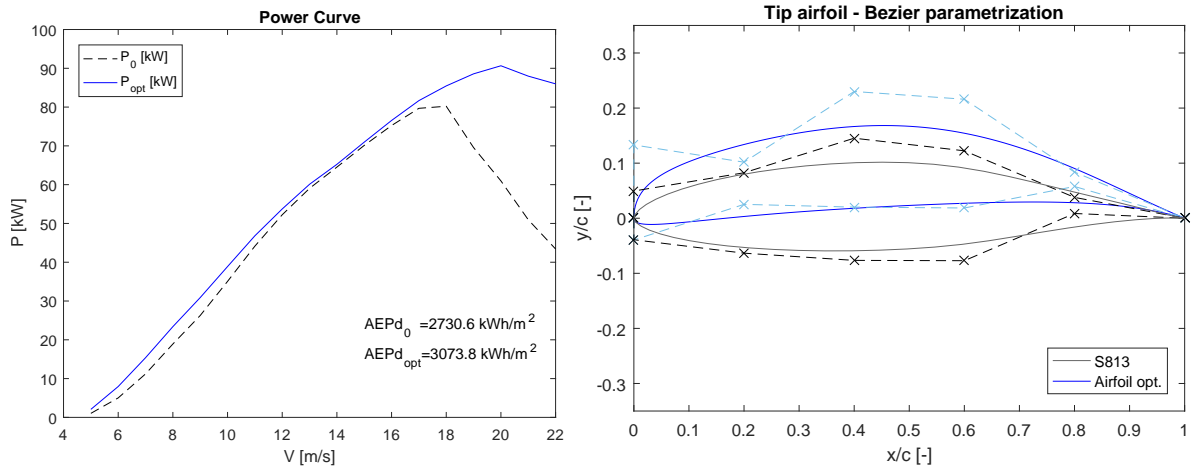


Figure 6.25: AEP70 – Opt3: Solution B power curve and airfoil parametrization

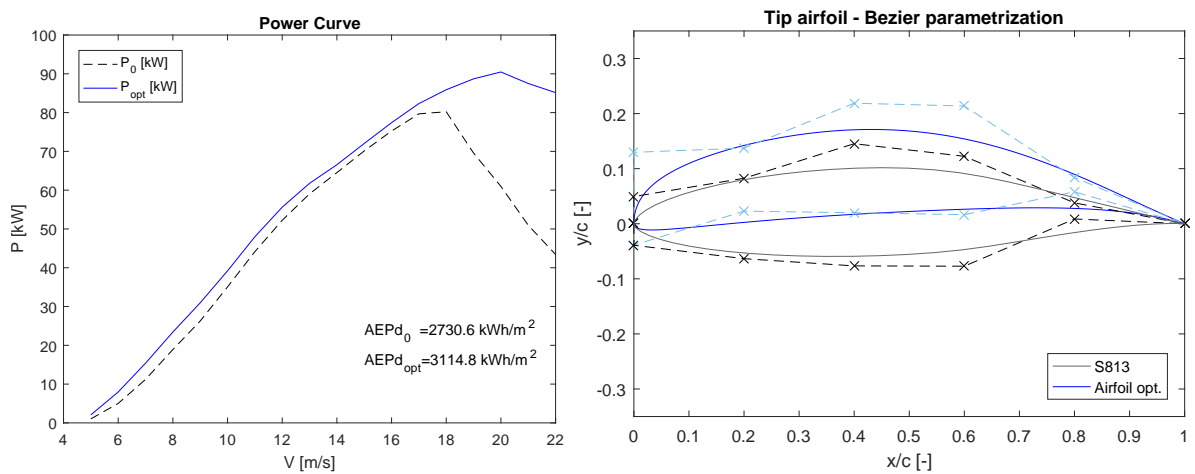


Figure 6.26: AEP70 – Opt3: Solution C power curve and airfoil parametrization

## 6.9 Results of the AEP70 Optimization

The AOC 15/50 wind turbine has been optimized in four different steps, according to the optimization strategy reported in Section 6.5.

First, the trend of the twist angles in spanwise direction has been optimized for a Weibull distribution with mean velocity of 7.0 m/s and Rayleigh distribution ( $k=2$ ). The mono-dimensional optimization identified a different distribution of the twist angles compared to the baseline configuration. The twist angles have been increased almost along the whole length of the blade: at the root section the optimized twist angle results more than three times the baseline value (Figure 6.12). The optimization of the twist results in a growth of the AEP, for the considered conditions, of the 5.60%.

The optimized blade has been later considered as the new baseline configuration of the further airfoil optimization analysis. The three consecutive analysis concerned a multi-dimensional optimization of the shape of the airfoils used along the blade. The optimizations take into account the maximization of the Annual Energy Production density,  $AEPd$  and the minimization of the Cost Of Energy,  $COE$ , as defined in Section 6.4.3.

The analysis produced three Pareto fronts and a database of optimized profiles to choose from the optimized configuration. As an example, the solutions B of the three multi-dimensional optimization could compose the airfoil sequence of the final optimized blade. In that case, Table 6.13 summarizes the improvements archived in terms of  $AEPd$ ,  $COE$  and weight of the blade during the steps of the analysis: the final optimized geometry presents an increase of the 32.3% of the Annual Energy Production density with a decrease of the Cost Of Energy of 11.89% compared to the AOC 15/50 baseline configuration.

	<b>AEPd</b> [kWh/m <sup>2</sup> ]	<b>Weight</b> [kg]	<b>COE</b> [\$/kWh]
<b>Baseline</b>	2585.6	80.79	0.0301
<b>Twist opt.</b>	2730.6 (+5.60%)	80.79 (-)	0.0297 (-1.41%)
<b>Airfoil opt.</b>	3222.9 (+32.38%)	81.95 (+1.44%)	0.0265 (-11.89%)

**Table 6.13:** Results of the optimization for a Weibull distribution of the wind speed with a mean velocity of 7.0 m/s and Rayleigh distribution

## 6.10 AEP75 - Shape Optimization with LCOE

In the current section, a second optimization is proposed using a different and more accurate formulation of the Cost Of Energy: the *Levelized Cost Of Energy (LCOE)*. The National Renewable Energy Laboratory occasionally publishes a *Cost of Wind Energy Review*, a report containing an average of the current share of costs for the development of a Horizontal Axis Wind Turbine. In the present analysis the used reference is the NREL cost review of the year 2014 [90].

The Weibull wind speed distribution for the current optimization assumes a mean of 7.5 m/s; this value has been chosen in order to consider an  $AEP_{NET}$  value close to the one considered in [90].

### 6.10.1 The Levelized Cost of Energy

The LCOE formulation proposed by NREL gets deeper in the specification of the costs of all the components which make up the wind turbine. The System Cost Breakdown Structure (SCBS) provides structured and consistent breakdowns of a wind project into smaller, more specific components, including both physical costs and financial costs. The SCBS deconstructs the total expenditures of a wind project down to six levels and includes more than 300 components. Figure 6.27 illustrates the first two levels of the decomposition.

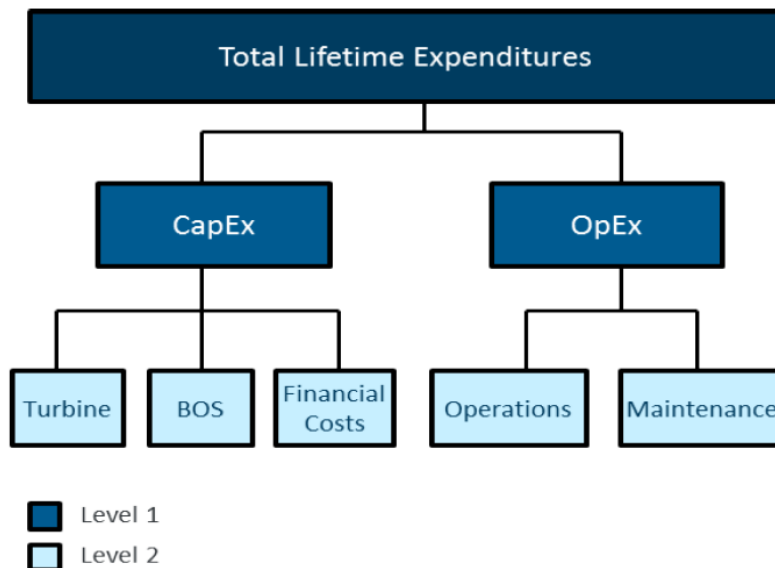


**Figure 6.27:** Levels 1 and 2 of the SCBS.

The *LCOE* is defined in [90] as:

$$LCOE = \frac{CapEx * FCR + OpEx}{(AEP_{NET}/1000)} \quad (6.11)$$

where  $CapEx$  represents the Capital Expenditures (in  $\$/kW$ ),  $FCR$  is the Fixed Charge Rate (assumed 10.3%),  $OpEx$  represents the Operational Expenditures (assumed  $51\$/kW$ ) and the  $AEP_{NET}$  is the Net Average Annual Energy Production (in  $MWh/MW/y$ ).

Figure 6.28 illustrates the Breakdown of  $CapEx$  for the NREL land-based reference project: the turbine capital costs are in green, blue represents the Balance Of System ( $BOS$ ) share of capital costs and the financial costs are highlighted in purple. The share of costs has been calculated from the land-based wind reference project consists of 103 1.94 MW wind turbines installed in the U.S. in the 2014.

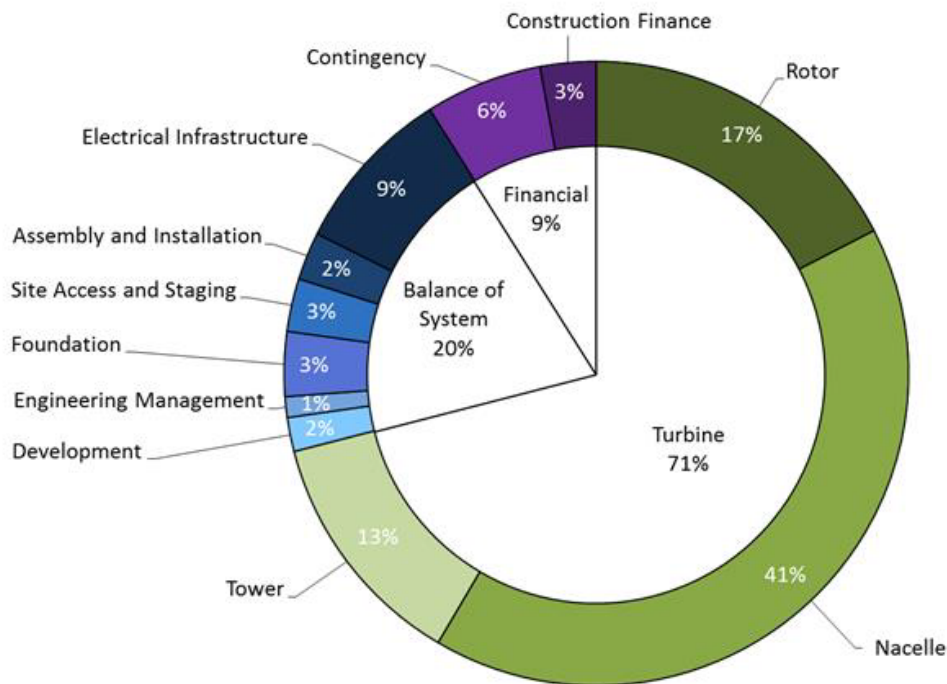


**Figure 6.28:** Capital Expenditures for the land-based wind reference project, NREL 2014.

Since the calculated cost-sharing of the NREL reference project refers to a sample of 1.94MW wind turbines, some assumptions have to be made in order to adjust the formulation to the considered small wind turbine. In the NREL cost share example, the blade cost component in the rotor module represents the 10.64% of the total Capital Expenditure cost. However, the AOC 15/50 nominal power (50kW) is considerably lower than the turbine of the example, therefore the impact of the materials and the labour costs have been considered as the 15.80% of the total Capital Expenditure formulation. This percentage is kept fixed and the  $CapEx$  value is calculated proportional to the cost of the blades.

In order to correctly calculate the cost of the blade, an estimate of a commercial GFRP material price has been requested to the *Compositex* company [89], specialized in the manufacturing of composite materials. The proposed price of DT120 material is  $10.25 \text{ €/m}^2$ , equivalent to  $27.23 \text{ \$/kg}$ .

Since the size of the wind turbine is not modified by the optimization loop (in terms radius of the rotor  $R$ ), the calculation of the *CapEx* cost has been considered as the sum of two components: a fixed component corresponding to the 84.20% of the cost sharing of the baseline AOC 15/50 and a variable component corresponding to the impact of the materials and labour costs (estimated in 12000\$ with the manual lay up production technique) of the blades. The proposed cost sharing is based on the experience and on the consultancy activity: the percentages are proportional to the cost of a private project concerning a Horizontal Axis Wind Turbine design of 60 kW and 9.0 m of rotor radius.

Finally, considering a Weibull wind speed distribution of 7.5 m/s mean value, the *LCOE* of the baseline AOC 15/50 results 0.0849 \$/kWh; in the twist-optimized configuration the value is slightly higher, 0.0863 \$/kWh.

The aerodynamic fitness function  $f_{LCOE}$ , to be minimized, is therefore represented by ratio between the *LCOE* of the analysed individual and the  $LCOE_0$  of the reference turbine (considered as the twist-optimized configuration).

$$f_{LCOE} = \frac{LCOE}{LCOE_0} \quad (6.12)$$

### 6.10.2 Optimization Strategy

In *APE70* optimization, the three airfoil shapes of the blade have been optimized separately. The aim was to identify the relative contributions on the overall performances and to create a database of airfoils to draw from, in order to chose the best suitable combinations for the blade design. Differently from *AEP70*, *AEP75* implements a sequential optimization strategy. The importance of an analysis that consists of consecutive steps, starting from the previous results, has been demonstrated by Benini et al. [88]. The sequential approach proposed by ONERA (*Le centre francais de recherche aérospatiale*) has obtained better results than the other illustrates strategies.

*AEP75* optimization starts from the twist-optimized configuration, found in Section 6.6.1, and sequentially optimizes the airfoil shapes, from the most influential profile to the lesser one:

- *OptTw*: Mono-objective twist angles distribution optimization
- *Opt1*: Multi-objective shape optimization (tip airfoil)
- *Opt2*: Multi-objective shape optimization (primary airfoil)
- *Opt3*: Multi-objective shape optimization (root airfoil)

The three multi-objective optimization have been set using an initial population of 100 individuals and a total generation number of 50. A summary of the shape optimizations setting is reported in Table 6.14.

<b>Optimization variables</b>	1) y-coordinate of Bezier points for the suction side 2) y-coordinate of Bezier points for the pressure side
<b>Objective functions</b>	1) <i>AEP</i> fitness function $f_{AEP}$ 2) <i>LCOE</i> fitness function $f_{LCOE}$
<b>Constraints adopted</b>	Upper and lower bounds on $f_{AEP}$ Upper and lower bounds on $f_{LCOE}$ Penalty functions as described in 6.9

**Table 6.14:** Summary of the main settings for *AEP75* optimization

Differently from *AEP70*, for the *AEP75* optimization, a set of larger constraints is adopted for the upper bounds of the parameters, as reported in Table 6.15.

	<b>G1</b>	<b>G2</b>	<b>G3</b>	<b>G4</b>	<b>G5</b>	<b>G6</b>	<b>G7</b>	<b>G8</b>	<b>G9</b>	<b>G10</b>
<b>Lower bound</b>	-0.10	-0.10	-0.10	-0.10	-0.05	-0.015	-0.10	-0.10	-0.10	-0.050
<b>Upper bound</b>	+0.015	+0.15	+0.15	+0.15	+0.50	+0.10	+0.15	+0.15	+0.15	+0.05

**Table 6.15:** Constraints adopted for the *AEP75* optimization

### 6.10.3 AEP75-Opt1: Optimization of the Tip Airfoil of the Blade

The first optimization (*AEP75 – Opt1*) concerns the shape of the tip airfoil of the AOC 15/50 blade (S813 airfoil of the baseline configuration used from 5.990 m to 7.490 m in the span-wise direction).

Figure 6.29 illustrates the results of the optimization in terms of Pareto front convergence. As for the analysis of *AEP70*, 3 solutions belonging to the last the Pareto front have been considered: the genetic pools are reported in Table 6.16, Figures from 6.30 to 6.32 illustrate the resulting power curve and shape of the optimized airfoils.

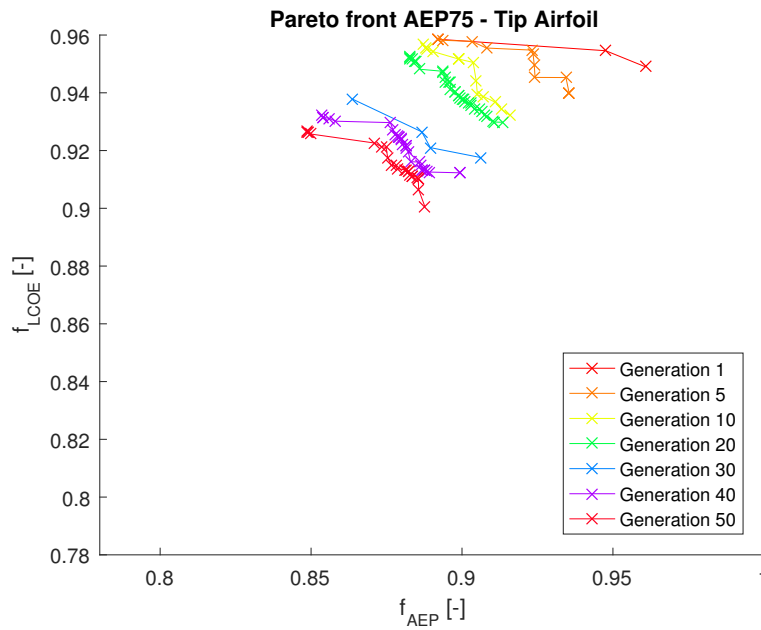


**Figure 6.29:** *AEP75 – Opt1*: Pareto front convergence of the tip airfoil shape optimization

	Genetic pool										Fitness	
<b>SolA</b>	-0.0278	0.1402	0.1005	0.1477	0.0486	0.0800	0.1118	0.1110	0.1265	0.0424	0.8487	0.9270
<b>SolB</b>	-0.0199	0.1104	0.1458	0.1461	0.0453	0.0991	0.0576	0.0528	0.1278	0.0422	0.8785	0.9138
<b>SolC</b>	-0.0147	0.1406	0.1178	0.1471	0.0480	0.0848	0.0077	0.0977	0.1356	0.0477	0.8877	0.9005

**Table 6.16:** Genetic pool and fitness values of the considered points in Pareto front of *AEP75 – Opt1*



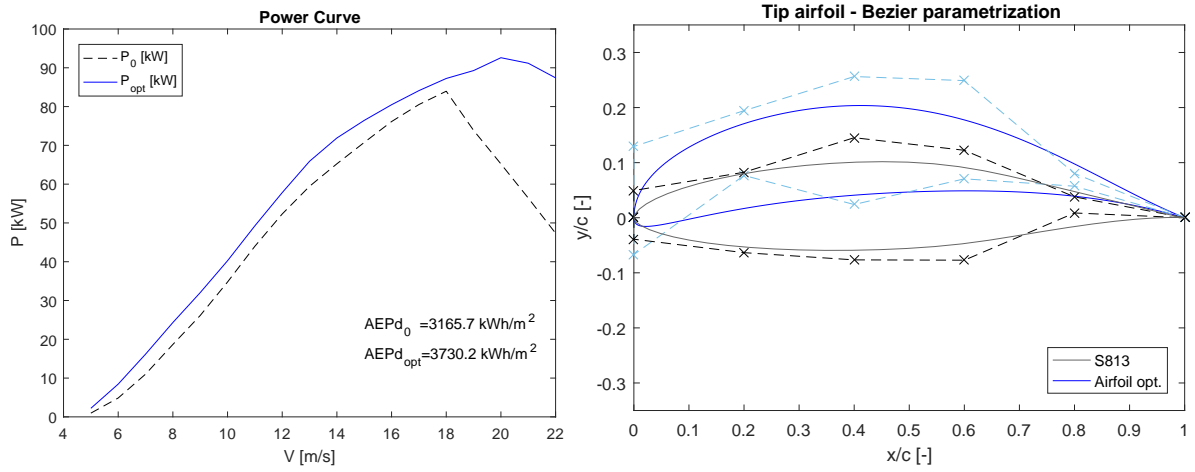


Figure 6.30: *AEP75 – Opt1*: Solution A power curve and airfoil parametrization

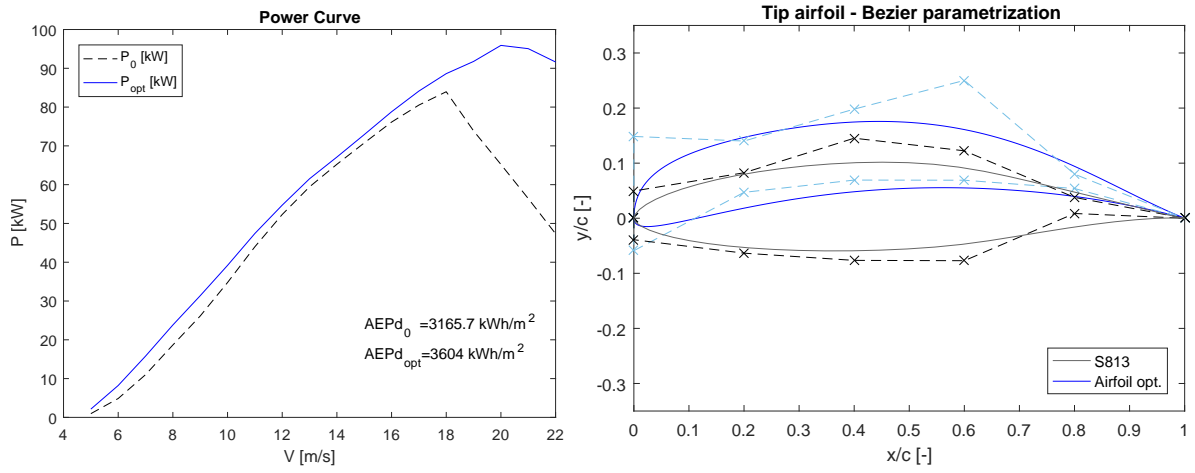


Figure 6.31: *AEP75 – Opt1*: Solution B power curve and airfoil parametrization

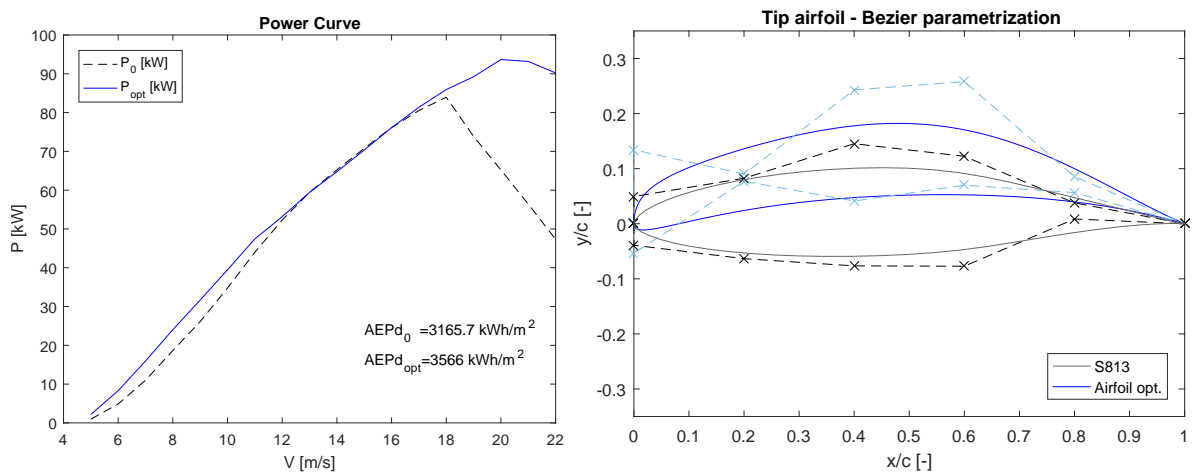
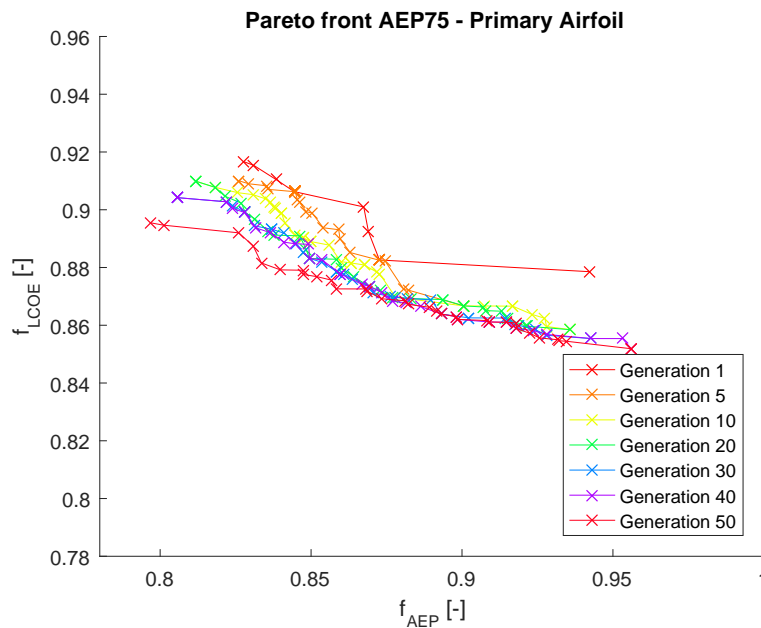


Figure 6.32: *AEP75 – Opt1*: Solution C power curve and airfoil parametrization

#### 6.10.4 AEP75-Opt2: Optimization of the Primary Airfoil of the Blade

The second optimization (*AEP75 – Opt2*) concerns the shape of the primary airfoil of the AOC 15/50 blade (S812 airfoil of the baseline configuration used from 4.490 m to 5.990 m in the span-wise direction). For the current optimization, the adopted tip airfoil is represented by the solution B of the *AEP75 – Opt1* analysis.

Figure 6.33 illustrates the results of the optimization in terms of Pareto front convergence. As for the previous analysis, 3 solutions belonging to the last the Pareto front have been considered: the genetic pools are reported in Table 6.17, Figures from 6.34 to 6.36 illustrate the resulting power curve and shape of the optimized airfoils.



**Figure 6.33:** *AEP75 – Opt2*: Pareto front convergence of the primary airfoil shape optimization

	Genetic pool										Fitness	
<b>SolA</b>	-0.0624	0.1247	0.1444	0.1053	0.0371	0.0540	0.1087	0.1185	0.0607	0.0353	0.7970	0.8954
<b>SolB</b>	-0.0573	0.1264	0.1016	0.1481	0.0269	0.0380	-0.0285	0.0434	0.1208	0.0398	0.8474	0.8776
<b>SolC</b>	-0.0625	0.0129	0.0952	0.0512	0.0228	0.0038	-0.0025	0.1156	0.1222	0.0324	0.8985	0.862

**Table 6.17:** Genetic pool and fitness values of the considered points in Pareto front of *AEP75 – Opt2*

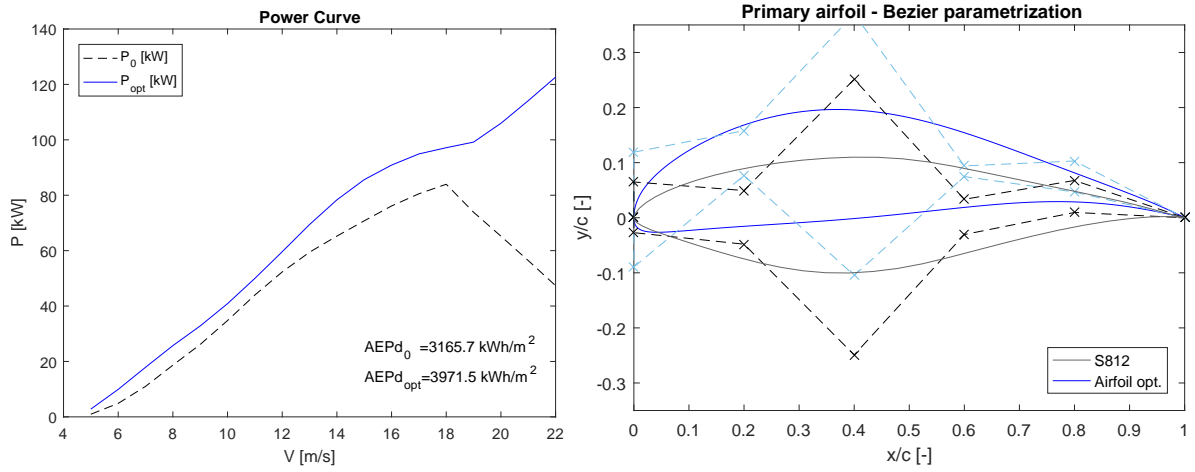


Figure 6.34: *AEP75 – Opt2*: Solution A power curve and airfoil parametrization

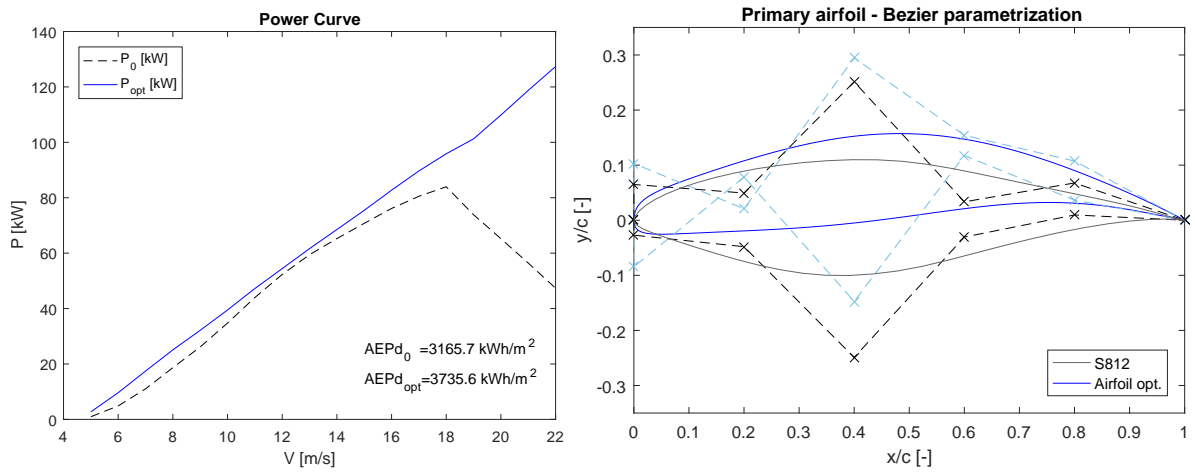


Figure 6.35: *AEP75 – Opt2*: Solution B power curve and airfoil parametrization

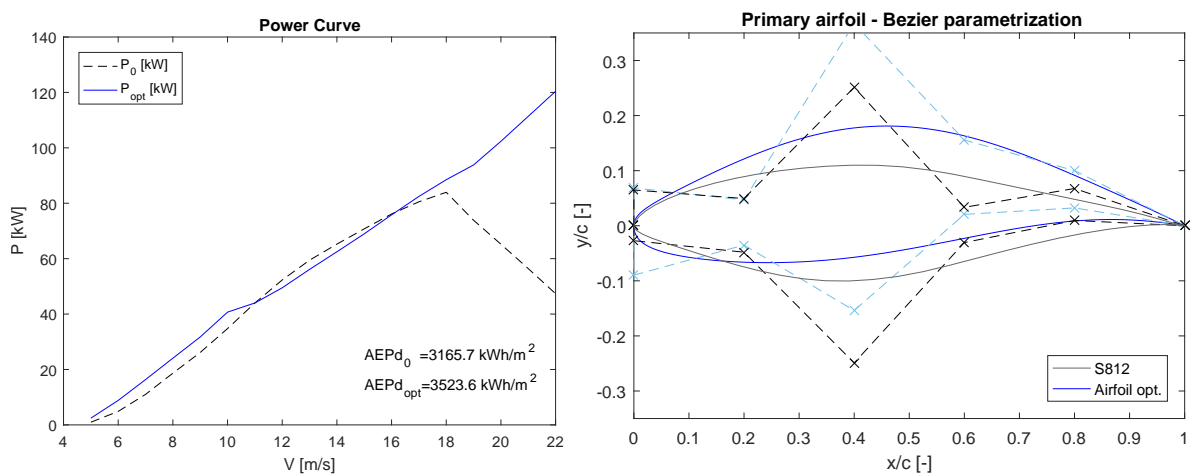
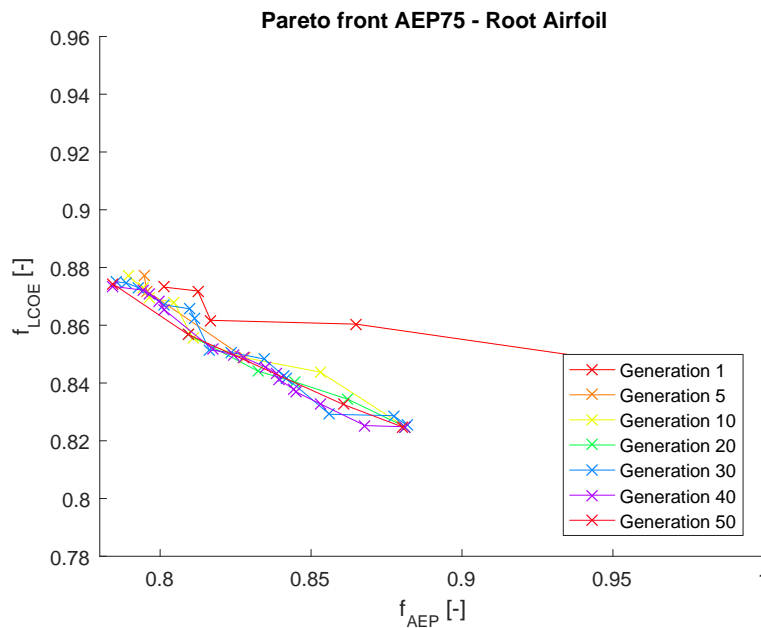


Figure 6.36: *AEP75 – Opt2*: Solution C power curve and airfoil parametrization

### 6.10.5 AEP75-Opt3: Optimization of the Root Airfoil of the Blade

The third optimization (*AEP75 – Opt3*) concerns the shape of the root airfoil of the AOC 15/50 blade (S814 airfoil of the baseline configuration used from 0.515 m to 4.490 m in the span-wise direction). For the current optimization, the adopted tip airfoil is represented by the solution B of the *AEP75 – Opt1* analysis, while the chosen primary airfoil is represented by the solution B of the *AEP75 – Opt2* analysis.

Figure 6.37 illustrates the results of the optimization in terms of Pareto front convergence. As for the previous analysis, 3 solutions belonging to the last the Pareto front have been considered: the genetic pools are reported in Table 6.18, Figures from 6.38 to 6.40 show the resulting power curve and shape of the optimized airfoils.



**Figure 6.37:** *AEP75 – Opt3*: Pareto front convergence of the primary airfoil shape optimization

	Genetic pool										Fitness	
<b>SolA</b>	-0.0520	0.0824	0.1015	0.1213	0.0169	0.0380	0.0460	-0.0558	-0.0089	0.0207	0.7841	0.8735
<b>SolB</b>	-0.0616	0.0342	0.0698	0.0436	0.0058	0.0365	-0.0470	0.0717	0.0906	0.0079	0.8243	0.8496
<b>SolC</b>	-0.0791	-0.0155	-0.0778	0.0314	-0.0152	0.0051	-0.0489	0.1260	0.0712	-0.0031	0.8804	0.8247

**Table 6.18:** Genetic pool and fitness values of the considered points in Pareto front of *AEP75 – Opt3*

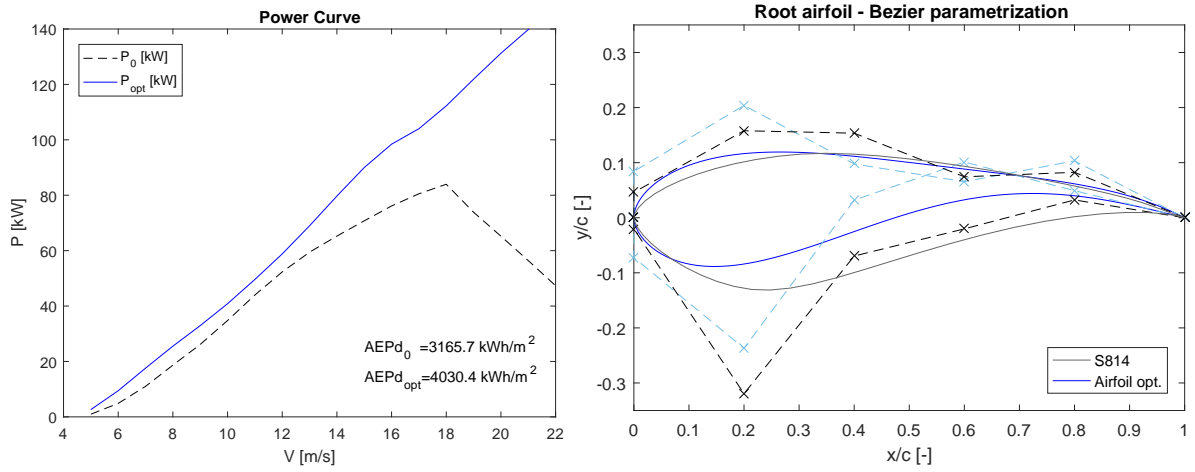


Figure 6.38: *AEP75 – Opt3*: Solution A power curve and airfoil parametrization

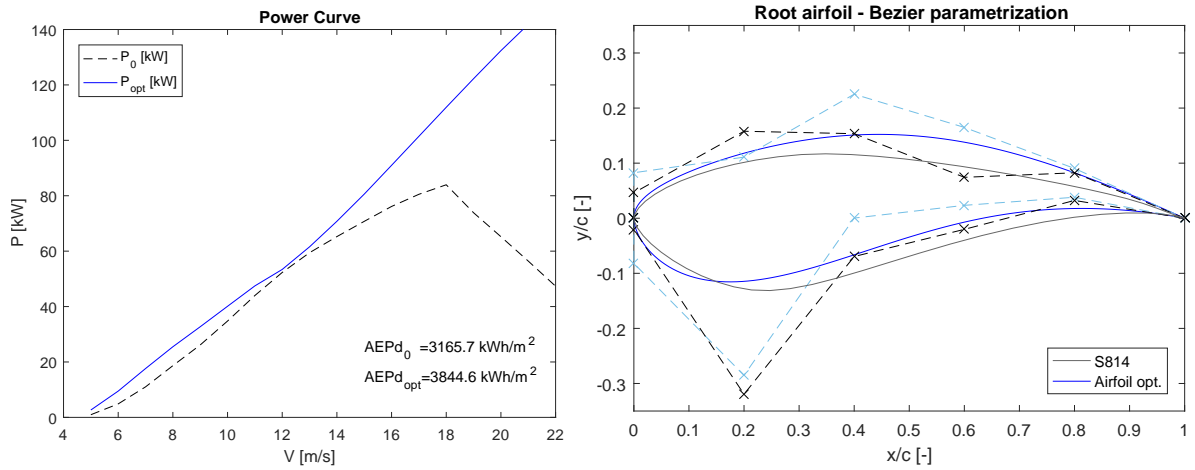


Figure 6.39: *AEP75 – Opt3*: Solution B power curve and airfoil parametrization

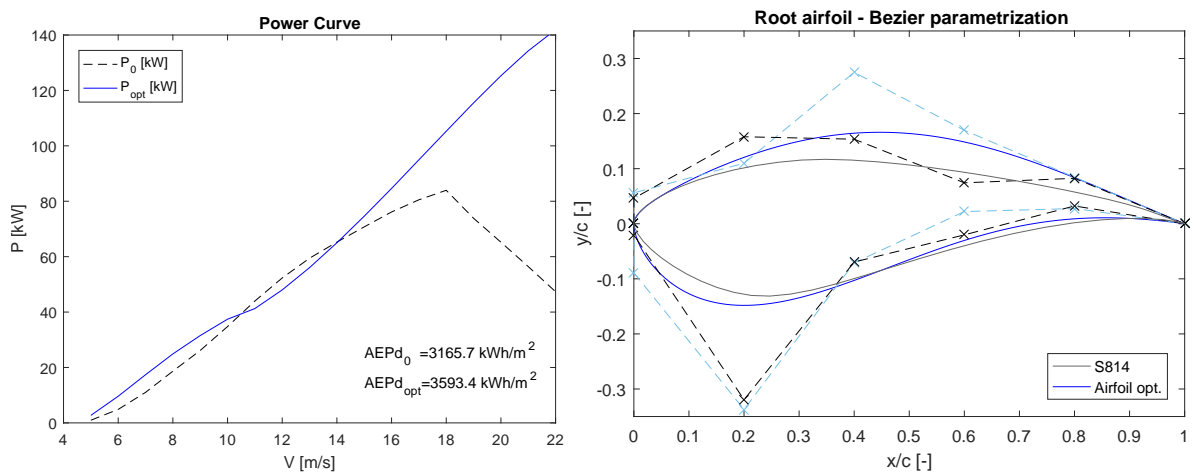


Figure 6.40: *AEP75 – Opt3*: Solution C power curve and airfoil parametrization

## 6.11 Results of the AEP75 Optimization

Differently from *AEP70*, *AEP75* represents an alternative optimization of the airfoil shapes for a HAWT. First, an updated cost of energy formulation has been used as objective function. The Levelized Cost Of Energy (*LCOE*) allows to compare the various method of producing energy by getting deeper in the specification of the costs of all the components; the final cost is expressed in  $\$/kWh$ . Secondly, the four steps of the optimization procedure have been implemented with a sequential strategy. After running the optimization of the twist angles distribution, the shape-optimizations are executed in a sequential way, using the result of the previous step as the starting point for the next analysis (see Section 6.10.2).

As found in *AEP70* optimization, the trend of the twist angles in spanwise direction of the baseline AOC 15/50 has revealed not to be optimized for the considered working conditions (Weibull wind speed distribution with mean velocity of 7.5 m/s and Rayleigh distribution). The twist-optimized blade has been later considered as the new baseline configuration for the further airfoil shape-optimizations. After that, the three sequential analysis, regard a multi-dimensional optimization of the shape of the airfoils used along the blade. The optimizations take into account the maximization of the Annual Energy Production density, *AEPd*, and the minimization of the Levelized Cost Of Energy, *LCOE*, as defined in Section 6.10.1.

Table 6.19 reports the results of the various step of the optimization strategy, with the improvements achieved.

	<b>AEPd</b> [kWh/m <sup>2</sup> ]	<b>Weight</b> [kg]	<b>LCOE</b> [\$/kWh]
<b>Baseline</b>	2961.2	80.79	0.0849
<b>Twist opt.</b>	3165.7 (+6.55%)	80.79 (-)	0.0863 (+1.63%)
<b>Tip airfoil opt.</b>	3604.0 (+13.84%)	80.72 (-0.09%)	0.0788 (-8.62%)
<b>Primary airfoil opt.</b>	3735.6 (+3.65%)	80.68 (-0.05%)	0.0757 (-3.96%)
<b>Root airfoil opt.</b>	3844.6 (+2.96%)	81.66 (+1.21%)	0.07323 (-3.25%)

**Table 6.19:** Results of the optimization for a Weibull distribution of the wind speed with a mean velocity of 7.5 m/s and Rayleigh distribution

The mono-dimensional optimization changed the twist angles distribution along the blade (Figure 6.12). The resulting trend is similar to the one found in *AEP70*: the twist angle of the blade in the root zone have been tripled ( $\theta = 34.95^\circ$ ) and the angle at the tip of the blade assumes the value of the imposed minimum angle of pitch,  $\theta_P = 1^\circ$ . The new distribution of twist angles improved the performances of the blade, in terms of Annual Energy Production density *AEPd*, of the 6.55%.

The first shape-optimization regarded the profile that most influenced the *APE70* optimization,

the tip airfoil. As can be noticed, all the solutions belonging to the Pareto front present a cambered tip airfoil, with thinner shapes when the *LCOE* assumes his lower value (Solution C, Figure 6.32). Solution B (Figure 6.31) represents a compromise between these solutions of best *LCOEd* and solutions with higher *AEPd* at the expense of *LCOE* (Solution A, Figure 6.30). Solution B has been chosen as the optimized tip airfoil; it allows to archive an increase in *AEPd* of 13.84% with a great decrease in *LCOE* of 8.62%.

The following shape-optimization concerned the second most influential profile, the primary airfoil. Even this analysis has led to the determination of cambered airfoils, however the resulting camber lines are less marked than the generated tips profiles. It is interesting to note how the primary airfoil optimization improved the performances in the stall conditions of the turbine, when the wind speed is higher than 18 m/s (Figures 6.34a to 6.36a); this effect, on a smaller scale, has been found also in the previous *AEP70* optimization. Again, a compromise solution has been chosen as the optimized primary airfoil (Solution B, Figures 6.35). High improvements are obtained for both *AEPd* (+3.65%) and *LCOE* (-3.96%) values, compared to the previous analysis.

The last analysis affected the shape of the root airfoil, the less influential profile in terms of *AEPd* improvements. As for the previous optimization steps, three solutions belonging to the Pareto front have been chosen. Solution B (Figures 6.39) represents the final configuration of the blade and it consists of the sequence of the three optimized airfoils. In this case, the root shape-optimization showed a lower influence on the Annual Energy Production density; it has been slightly increased of (+2.92%) compared to the second analysis; however, the Levelized Cost Of Energy has been reduced by the 3.25%.

The final wind turbine configuration presents a great improvement of the performances. Referring to the baseline AOC 15/50, the overall increase of *AEPd* is 29.39% (from 2961.2  $kWh/m^2$  to 3844.6  $kWh/m^2$ ) with a simultaneous reduction in the *LCOE* of 13.71% (from 0.0849  $$/kWh$  to 0.0732  $$/kWh$ ).

## Chapter 7

# Validation of a Numerical Model of a Horizontal Axis Wind Turbine with Experimental Data Using Two CFD Codes

A comparison between numerical models for the aero-dynamical evaluation of the performances of the AOC 15/50 using both open source and commercial software has been presented at the European Wind Energy Association (EWEA) conference in Bilbao, *Analysis of Operating Wind Farms 2016 – 3rd edition*, 14-15 April 2016 [81].

The aim of the work is the assessment of the numerical model of the AOC15/50 Horizontal Axis Wind Turbine using the open source CFD code OpenFOAM. The obtained results are compared with both experimental and numerical data obtained from the fluid-dynamic analysis performed using the commercial CFD Package ANSYS Fluent. The calculated power curve for the online rotational wind speed (65 rpm) and the contribution of the blade sections to the total torque in spanwise direction are presented. Also the comparison of the pressure distribution on the blade surface and the absolute velocity flow field are presented. The analysis show a good accordance in the power prediction for low velocities, however stall phenomena compromise the evaluation of the power curve for high velocities.



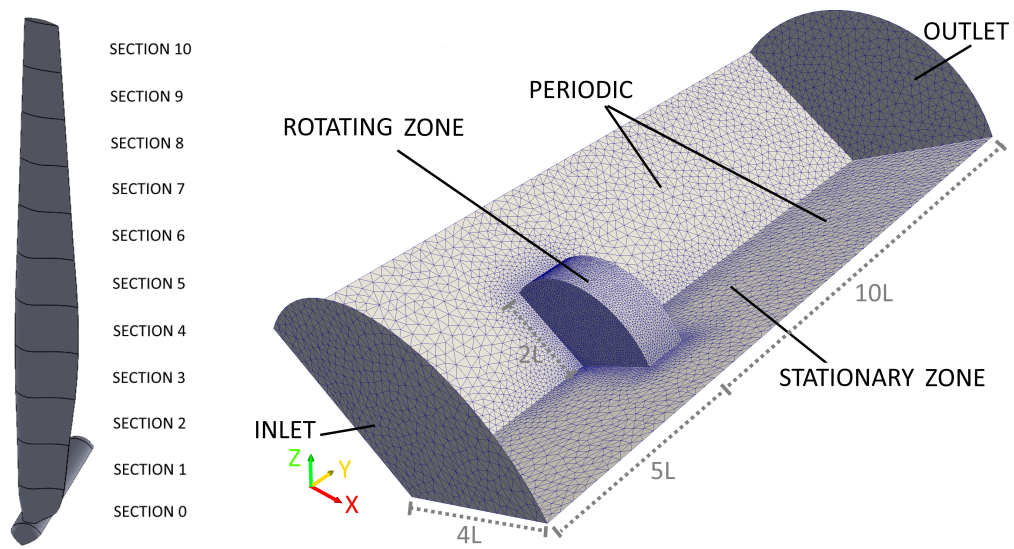
## 7.1 Objectives

The present work describes the numerical model for the analysis of a Horizontal Axis Wind Turbine and concerns the most suitable domain discretization, the choice of the turbulence model and the boundary condition set. The procedure is applied to two CFD codes, the commercial package ANSYS Fluent and the open source software OpenFOAM. The results are compared with the experimental data provided by the National Renewable Energy Laboratory [65]: the three blades turbine has been tested at south of Boulder (Colorado), leading to the definition of a power curve at different wind velocities, up to about 24 m/s.

## 7.2 Methods

In order to evaluate the performances of the AOC 15/50, a 3D model of the wind turbine has been reproduced through the geometrical information of a SANDIA National Laboratories report [66] and the numerical models have been validated with the experimental data acquired by NREL [65]. The main features of AOC1550 are: 7.2 m blade length, 15 m rotor diameter, 25 m hub height and a online rotational speed of 65 rpm. In order to calculate the contribution of the sections to the total torque, the blade surface has been divided into 11 slices as shown in Figure 7.1a. A structured mesh of quad elements has been created on the blade surface: the profiles have been divided in 200 elements imposing the size at the trailing edge and at leading edge (1 mm). A hexahedral boundary layer of 15 layers encloses the entire blade (2.1M cells, first cell height=0.02 mm, grow factor=1.15). The tetrahedral mesh of the internal zone (9M cells) has been created using a grow factor of 1.1 and a final size of 480 mm) and the external zone contains 395K cells. As shown in Figure 7.1b, two concentric zones have been created: the resulting bounding box is shaped as a cylinder of 108 m height and 28.8 m of radius.

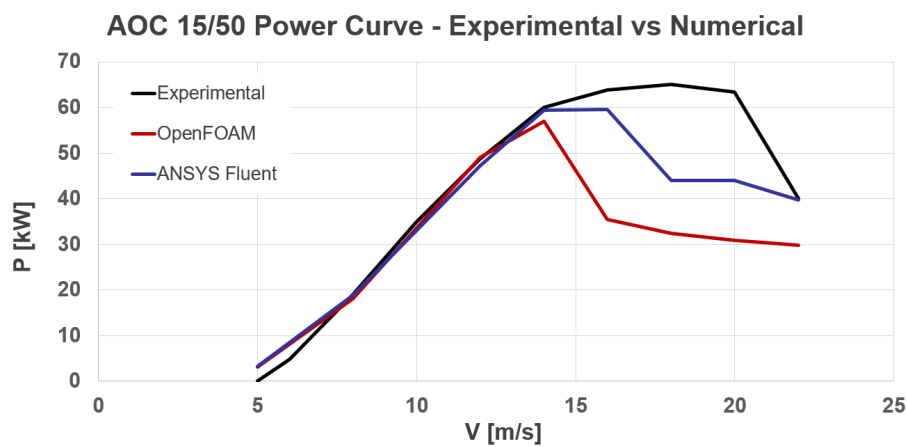
The numerical analysis have been set using the Multiple Reference Frame strategy, as described in Section 1.10: the internal zone rotates at a velocity of 6.81 rad/s while the external zone is in stationary frame. The symmetric property of the domain has allowed to simulate a single blade imposing periodic conditions. The boundary condition of velocity inlet has been varied to simulate the whole range of wind velocities and a pressure of 0 Pa (relative) has been set as outlet condition. In order to simulate the incompressible fluid domain, the SIMPLE algorithm has been chosen and the  $k - \omega - SST$  has been set as turbulence model.



**Figure 7.1:** AOC 15/50 3D model and adopted fluid domain with boundary conditions.

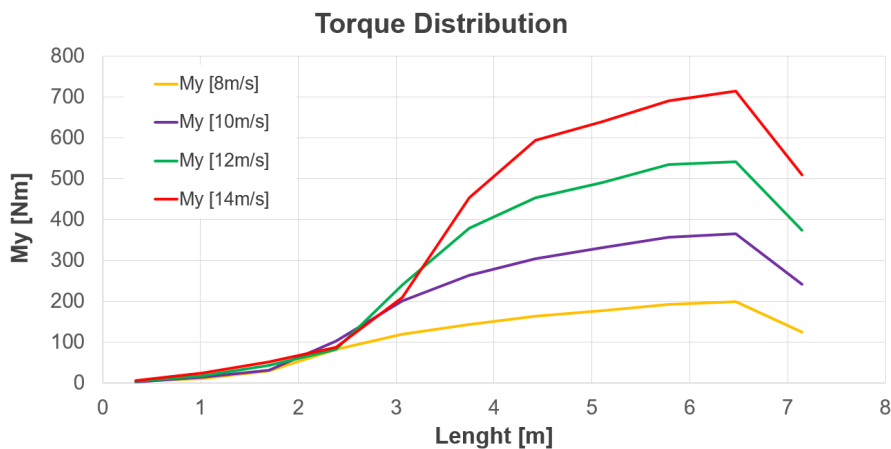
### 7.3 Results

The numerical power curve obtained with OpenFOAM is compared both with the numerical curve from ANSYS Fluent analysis and the experimental power curve of the AOC 15/50 wind turbine presented in [65]. Both the CFD codes, ANSYS Fluent and OpenFOAM, show a good accordance with the experimental data, especially in the first part of the power curve at low velocities (Figure 7.2). At high velocity, when stall occurs, RANS are not accurate in predicting the formation of strong vortices (due to separation at high speeds); this causes the differences between numerical curves and experimental data [82].



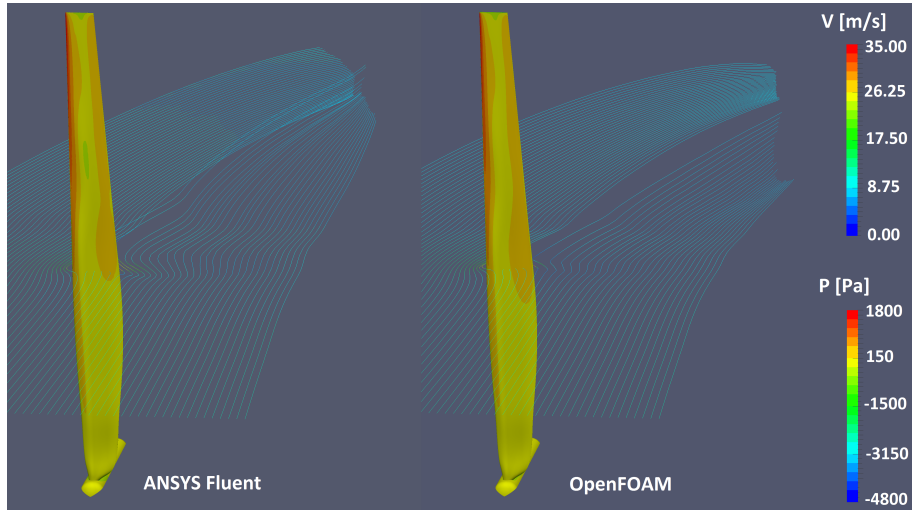
**Figure 7.2:** Power curve of AOC 15/50. Comparison between experimental and numerical data (OpenFOAM and Ansys FLUENT).

Figure 7.3 presents the contribution of the different sections of the blade to the total torque for 4 velocities, before stall. It can be observed how the contribution to the total torque, and therefore to the power production, increases with the radial position on the blade and decreases at the tip.



**Figure 7.3:** Contribution of the different sections of the blade to the total torque for different velocities (before stall).

In Figure 7.4 both the pressure distribution on the blade surface and the absolute velocity streamlines from the numerical analysis are compared for the Rated Wind Speed Case ( $V=12$  m/s). In the following images, it is shown that the flow field evolution is identical and the pressure distribution is in good accordance in both the codes.



**Figure 7.4:** Comparison of the pressure distribution on the blade surface and the velocity flow field between ANSYS Fluent (on the left) and OpenFOAM (on the right).



# Conclusion

The developed optimization environment for Horizontal Axis Wind Turbine has considered different aspects of the Sandia AOC 15/50; the turbine represents the baseline model for both the proposed analysis.

In Chapter 5, both the aerodynamic efficiency and the mechanical characteristics of the Sandia AOC 15/50 wind turbine blade have been improved using an evolved version of the S.O.C.R.A.TE. algorithm. For this purpose, the original S.O.C.R.A.TE. formulation has been modified and, in order to manage a coupled aerodynamic-structural optimization, a BEM code has been implemented in the algorithm: as a first step, the aerodynamic performance of the blade is evaluated by the BEM code and the aerodynamic forces acting on the blade are successively exported for the structural analysis with the commercial software ANSYS Mechanical APDL.

The algorithm has succeeded in increasing the power generation at 10 m/s of an interesting 4.44% by changing both chord and twist distributions along the blade span. The chord of the optimized blade has been increased in the most part of the sections, reaching the upper bound of the allowed blade surface. Also the optimal twist angle distribution has registered a marked increase, determining an angle of attack perceived by each blade section close to the one of maximum aerodynamic efficiency. The second part of the S.O.C.R.A.TE. algorithm has led to an optimized sequence of the laminas composing the blade layout, determining a marked decrease of the total deformation at blade tip. Nevertheless, the registered increase in the flexural rigidity of the blade has proved to be ascribed also to a blade stiffening due to the higher values of both chord and twist angles along the blade span.

The analysis proposed in Chapter 6, represents an improvement of the optimization environment for Horizontal Axis Wind Turbine by including further objective function, parametrization methods, working conditions and an extended version of the BEM code. Specifically, both the aerodynamic efficiency, in terms of Annual Energy Production density, and the Cost Of Energy of the Sandia AOC 15/50 wind turbine blade have been improved.

As for the previous optimization, the BEM code has been included in the algorithm: it allows to

calculate the Annual Energy Production starting with the sequence of airfoil adopted along the blade. The *AEP* value is successively used with the information about the total mass of the blade, in the cost of energy analysis. Two different optimization strategies have been proposed. In the sequential optimization *AEP75*, first a preliminary analysis on the twist angles distribution is considered, then three optimizations regarding the shape of the airfoils of the blade are carried. The shape-optimizations started with the most influential profile (tip airfoil) to the less one (root airfoil), in terms of *AEPd*. The optimization environment has succeeded in increasing the Annual Energy Production density, for a Weibull wind speed distribution of 7.5 m/s of mean value, of an interesting 28.27% by changing both the twist angles distribution and the shape of the airfoils along the blade span. At the same time the Levelized Cost Of Energy of the optimized blade has been reduced of 18.68% (from 0.0849 \$/kWh to 0.0690 \$/kWh) compared to the baseline AOC 15/50.

The optimized airfoils assume a cambered shape, especially in the tip zone of the blade. Furthermore, the twist angles distribution has been significantly changed in the optimized solution. The twist angles have been increased up to three times in the root zone of the blade: the baseline distribution has revealed to not be optimized for the nominal wind speed and this could causes detachments of the boundary layer and a diffuse stall in the root sections. On the other hand, in the tip zone, the optimized twist angle has been reduced to the minimum imposed value of pitch angle.

In Chapter 7 the fluid-dynamic analysis of the considered AOC 15/50 wind turbine is introduced. A comparison between two CFD analysis of the Sandia AOC 15/50 is presented; the analysis are carried with the commercial software ANSYS Fluent and the open source code OpenFOAM.

The software comparison reveals a good agreement for both the numerical analysis in relation to the experimental data provided by the National Renewable Energy Laboratory test campaign. The numerical results, illustrated in terms of power curve at different wind speed, reproduce quite well the linear portion of the power curve before the stall occurrence. Furthermore, the velocity flow field and pressure distribution on the blade, evaluated with the considered numerical codes, are in good agreement. Finally, the contribution of the different sections of the blade to the total torque, for several velocity, is also shown.

Further developments of the optimization environment for Horizontal Axis Wind Turbine should consider different fitness functions, such as various and more detailed formulations of the cost of energy. Furthermore, the implementation of a database containing different materials, like modern GFRPs or CFRPs, could also be considered. Additionally, a more accurate estimation of the blade structural performances could be obtained by replacing the simplified functions of Chapter 6 with an open source FEM solver (Code\_Aster). Finally, the calculation of the blade aerodynamic performance with a

CFD code (OpenFOAM) could allow to consider many aerodynamic phenomena as the stall. However, this can be possible only for a selected number of individuals because of the need of high computing resources.



## Nomenclature Part II

$a$ [-]	Axial induction factor
$a'$ [-]	Tangential induction factor
$A$ [ $m^2$ ]	Area of the rotor
$A$ [ $m^2$ ]	Blade surface
$A$ [-]	Scaling factor of Weibull distribution
$A_1$ [ $m^2$ ]	Area of the rotor wake
$A_{CV}$ [ $m^2$ ]	Area of the circular control volume
$AEP$ [ $kWh/y$ ]	Annual Energy Production
$AEP_{NET}$ [ $MWh/MW/y$ ]	Net Annual Energy Production
$AEP_d$ [ $kWh/y/m^2$ ]	Annual Energy Production density
$A_0$ [ $m^2$ ]	Original AOC 15/50 blade surface
$B$ [-]	Number of blades
$BOS$ [ $$/kW$ ]	Balance Of the Station
$c$ [ $m$ ]	Chord length
$C$ [ $m/s$ ]	Absolute velocity
$C_a$ [ $m/s$ ]	Axial component of the absolute velocity
$C_D$ [-]	Drag coefficient
$C_L$ [-]	Lift coefficient
$C_N$ [-]	Normal coefficient
$C_T$ [-]	Thrust coefficient
$C_\theta$ [ $m/s$ ]	Azimuthal component of the absolute velocity
$CapEx$ [ $$/kW$ ]	Capital Expenditures
$COE$ [ $$/kWh$ ]	Cost Of Energy
$COE_0$ [ $$/kWh$ ]	Cost Of Energy of the reference turbine
$d$ [ $mm$ ]	Total displacement at the tip
$d_0$ [ $mm$ ]	Total displacement at the tip of the original AOC 15/50 blade
$D$ [ $N$ ]	Drag force
$EI$ [ $MN \cdot m^2$ ]	Blade flexural rigidity
$E_L$ [ $MPa$ ]	Longitudinal elastic modulus
$E_T$ [ $MPa$ ]	Transversal elastic modulus
$E_Z$ [ $MPa$ ]	Out-of-plane elastic modulus

---

$f_A$ [-]	Ratio between blade surface area and that of the original AOC 15/50 blade
$f_{AEP}$ [-]	Objective function of Annual Energy Production density
$f_{COE}$ [-]	Objective function of cost of energy
$f_{LCOE}$ [-]	Objective function of levelized cost of energy
$f_P$ [-]	Objective function of power
$f_d$ [-]	Objective function of deformation
$f_m$ [-]	Ratio between blade mass and that of the original AOC 15/50 blade
$F$ [N]	Aerodynamic force acting on the blade section
$F$ [-]	Prandtl correction factor
$F_{lat}$ [N]	Forces from pressure distribution on the lateral surface
$F_{pres}$ [N]	Axial component of pressure forces
$F_{pres*}$ [N]	Forces from the net pressure distribution
$F_{ext}$ [N]	External forces
$FRC$ [%]	Fixed Charge Rate
$G_{LT}$ [MPa]	In-plane shear modulus
$G_{TZ}$ [MPa]	Out-of-plane shear modulus
$G_{LZ}$ [MPa]	Out-of-plane shear modulus
$i_A$ [-]	Penalty function for the area
$i_m$ [-]	Penalty function for the mass
$i_P$ [-]	Penalty function for the power
$I_{XX}$ [kg * m <sup>2</sup> ]	Bending stiffness of the airfoil
$I_{XX,rel}$ [-]	Ratio between the bending stiffness of the profile and of the baseline airfoil
$k$ [-]	Shape parameter of Weibull distribution
$L$ [N]	Lift force
$LCOE$ [\$/kWh]	Levelized Cost Of Energy
$LCOE_0$ [\$/kWh]	Levelized Cost Of Energy of the reference turbine
$m$ [m]	Mass of the blade
$m_0$ [m]	Mass of the original AOC 15/50 blade
$\dot{m}_{side}$ [kg/s]	Side mass flow rate
$M$ [Nm]	Bending moment acting on each blade cross section
$O\&M$ [\$/kWh]	Operation and Maintenance costs
$OpEx$ [\$/kW]	Operational Expenditures
$p$ [Pa]	Atmospheric pressure

$p_0$ [Pa]	Pressure value in the rotor plane
$p_N$ [N]	Normal force to the rotorplane
$p_T$ [N]	Tangential force to the rotorplane
$P$ [kW]	Aerodynamic power generated from the rotor
$P_0$ [kW]	Aerodynamic power generated from the original AOC 15/50 rotor
$P_{avail}$ W]	Aerodynamic available power
$q$ [–]	Generation number
$q_{max}$ [–]	Maximum generation number
$r$ [m]	Local radius
$R$ [m]	Radius of the rotor
$R$ [m]	Blade radius
$Re$ [–]	Reinolds Number
$t$ [mm]	Thickness of the layer
$u$ [m/s]	Velocity value in the rotor plane
$u_1$ [m/s]	Velocity value in the wake
$T$ [N]	Thrust
$TC$ [\$/kW]	Turbine cost
$V$ [m/s]	Unperturbed wind velocity
$V_m$ [m/s]	Weibull distribution wind speed mean value
$V_{rel}$ [m/s]	Local velocity
$V_{rel,1}$ [m/s]	Relative velocity upstream the blade
$V_{rel,2}$ [m/s]	Relative velocity downstream the blade
$V_{rot}$ [m/s]	Rotational velocity
$w$ [m/s]	Total induced velocity
$x$ [m/s]	Local rotational speed, non-dimensionalized
$x_{CM}$ [m]	X-coordinate of the airfoil centroid
$y_{CM}$ [m]	Y-coordinate of the airfoil centroid
$\alpha$ [°]	Section angle of attack
$\alpha_P$ [°]	Blade pitch angle
$\alpha_T$ [°]	Section twist angle
$\theta$ [°]	Section twist angle
$\frac{d\theta}{dz}$ [–]	Rate of rotation of the blade section
$\Delta p$ [Pa]	Pressure drop

$\lambda$ [-]	Tip speed ratio
$\nu_{LT}$ [-]	In plane Poisson's ratio
$\nu_{TZ}$ [-]	Out-of-plane Poisson's ratio
$\nu_{LZ}$ [-]	Out-of-plane Poisson's ratio
$\omega$ [rad/s]	Angular velocity
$\phi$ [°]	Flow angle
$\psi$ [°]	Angle between the plane of rotation and the relative velocity
$\rho$ [kg/m <sup>3</sup> ]	Density of fluid/material
$\rho_A$ [kg/m <sup>3</sup> ]	Blade surface density
$\rho_{eq}$ [kg/m <sup>2</sup> ]	Blade equivalent surface density
$\sigma$ [-]	Solidity of the blade
$\theta$ [°]	Twist angle of the blade
$\theta_P$ [°]	Pitch angle of the blade
$\theta_T$ [°]	Local twist angle of the blade



## Part III

# Development of an Optimization Environment for the Vertical Axis Wind Turbine Design



# Introduction and Background

Nowadays, the renewable energy sources are constantly increasing the market share compared to the conventional production and the wind energy is playing an increasing important role. According to the European Wind Energy Association a prediction for the year 2020 indicates a scenario of an 85% increase in installed capacity and a coverage of 17% of the total UE power demand [91].

Specifically, Horizontal Axis Wind Turbines have experienced a large diffusion in the last decades, due to their high efficiency in the conversion of wind energy. However, they present some disadvantages because of the need of big rotors and towers, to be installed in order to produce a consistent amount of energy. In addition, for the offshore or isolated sites, the connection to the electrical grid can be very expensive. Furthermore, HAWT are highly dependent on the wind direction.

For many applications as urban environments or installation sites characterized by an irregular wind distribution, the Vertical Axis Wind Turbines represent a valid alternative to HAWT. Since they are not dependent from the wind direction, there is no need of pointing the turbine to be efficient, so yaw drive and pitch mechanism is not required. Furthermore, there is no need of strong supporting towers and gearbox and other components are placed on the ground; hence the production and maintenance costs are lower. For these reasons VAWT play an increasing role in the wind energy market. The most common type of Vertical Axis Wind Turbine is the Darrieus model, a lift-type wind turbine activated by the aerodynamic forces of the wind, more efficient the drag-types (Savonius). Symmetric profiles are usually adopted for the blades since they need to be efficient in both the upstream and downstream zones [92].

In the past the studies of the VAWT airfoils were influenced by the HAWT design; the aim was to increase the maximum power coefficient (see Maydev and Klimas [93] and Asywill [94]), however the structural aspects of the blade are also important in order to decrease the cost of energy. Berg analyzed the impact of the customized airfoils on the cost of energy [95] and the same topic has also been analysed by Klimas [96]: the effects of stall regulation and low drag are studied in order to determine the best airfoil sections that decrease the COE. A more recent work of Wang et al. [97] coupled



---

the optimization, using genetic algorithms, with a structural FEM analysis of the blades, focusing on the determination of the best layout of the composite blades of a VAWT. A similar analysis has been conducted by Dal Monte et al. [54] for the HAWT model, work on which Part II of the thesis is based. Examples of optimization of Vertical Axis Wind Turbines can be also found in Literature. Yamazaki and Arakawa [98] used the Kriging response surface model approach in order to perform an aerodynamic shape optimization of VAWT airfoil. The thrust/pitching moment terms of the implemented fitness function were also calculated with a multi-objective optimization. Posteljnik et al. [99] proposed a multi-objective particle swarm algorithm for the design of small VAWT (Darrieus type): they employed a double-multiple stream-tube model coupled with a finite element analysis in order to improve the aerodynamic performances and design the structural main parameters of the turbine. Bedon and Benini [100] presented an efficient aero-structural design optimization, using genetic algorithms, of Darrieus vertical axis wind turbine. In the analysis the aerodynamic tool is represented by a Blade Element-Momentum algorithm while the structural model is based on the Euler-Bernoulli beam theory.

Ferreira and Geurts [101], proposed an alternative function to evaluate the aerodynamic performances of a VAWT, starting from the optimization of the shedding of the wake of the turbine, which determines the energy conversion from the flow. The optimizations suggested in Chapter 8, led by an open source genetic algorithm, are based mainly on that work and one of its applications, studied by Horst [104]. The considered objective functions are the ratio of average curve slope over the average drag coefficient over a rotation and the bending stiffness of the airfoil. Furthermore, the performances of the optimized airfoils are calculated with the 2D unsteady panel method P2DiWA, developed by Ferreira [102].

Finally, in Chapter 9, a numeric validation of the aerodynamic of a VAWT, against experiments conducted in the Open Jet Facility (OJF) of TU Delft [103], is presented. The OpenFOAM analysis has been implemented as a module of the optimization environment. An automatic procedure allows to generate geometry, mesh and set the unsteady 2D CFD simulation.

## Chapter 8

# Parametric Aero-Structural Optimization of a VAWT Airfoil

The analysis presented in the current chapter have been conducted in collaboration with TU Delft. The purpose is to develop an optimization procedure for the determination of the best airfoil shape of a Vertical Axis Wind Turbine. The optimization environment consists in the assembly of different engineering tools for the structural and aerodynamic analysis, optimization tools and in-house functions.

The work represents the final step of the development of the optimization environment and, differently from the previous chapters, it completely involves *open source* codes (CAE and optimization tools).

### 8.1 Case Study

The Vertical Axis Wind Turbine model, which characteristics are reported in Table 8.1, was considered the baseline model for the further optimization. The turbine is a 2 blade VAWT with a solidity  $\sigma$  of 0.1, tip speed ratio  $\lambda$  of 4.5, rotor radius  $R$  of 0.6 m and chord  $c$  of 0.06 m. The airfoil adopted in the baseline model is the symmetric NACA0015.

Airfoil	$\alpha$ range	$V_\infty$	$\lambda$	$\sigma$	$N_B$	$c$	$R$	$\varphi$
NACA0015	$-15^\circ, +15^\circ$	7.0 m/s	4.5	0.1	2	0.06 m	0.6 m	$0^\circ$

**Table 8.1:** Characteristics of the VAWT model considered for the analysis

The used Reynolds number  $Re$  for the aerodynamic analysis is 150000.

## 8.2 Analysis of the Airfoil Parametrization

In the current analysis a different Bezier parametrization technique has been examined. In Chapter 6, the suction and pressure sides of the airfoils were reconstructed as separate Bezier curves. However, the proposed parametrization takes into account both the camber line and thickness distributions. In order to establish the best combination of parameters, few examples of parametrizations are presented below. The test-cases are represented by a symmetric profile (NACA0015) and by a chambered airfoil (S812): the analysis test the influence of the number of control points and their degrees of freedom on the profile reconstruction. The profile reconstructions have been calculated through a single-objective optimization: the parameter to be minimized was represented by the maximum distance between the original and the reconstructed airfoils.

### 8.2.1 Parametrization ParA (5 Variables)

In the first parametrization (named *ParA*), 3 and 5 control points have been adopted respectively for the camber and thickness line distributions, as reported in Table 8.2. The central point of the camber curve can be moved in both the x and y directions, the central control points of the thickness curve can be moved only in the y-direction.

Control points	Pt1	Pt2	Pt3	Pt4	Pt5
Camber line	(0 0)	(G1 G2)	(1 0)		
Thickness line	(0 0)	(0 G3)	(0.33 G4)	(0.66 G5)	(1 0)

**Table 8.2:** Variables adopted in parametrization *ParA*

Figure 8.1 shows the results of the parametrization of the test-case profiles.

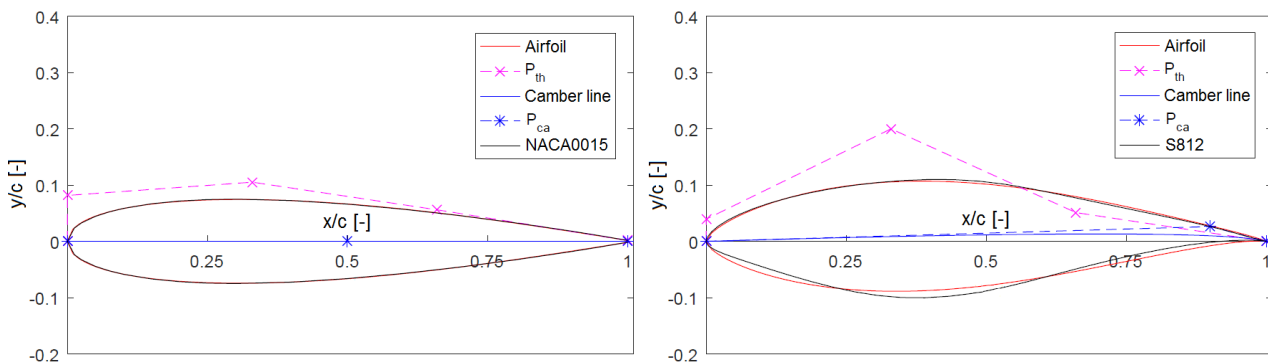


**Figure 8.1:** Results of the parametrization *ParA* on the NACA0015 (left) and S812 (right) airfoils

As can be observed, the parametrization of the NACA0015 airfoil shows a good accordance with the original geometry; however, the reconstruction of S812 airfoil presents marked differences in the leading

edge zone and in the suction side curve.

### 8.2.2 Parametrization ParB (8 Variables)

In *ParB*, the number of Bezier control points has been increased: 4 and 6 points regulate respectively the camber and thickness line distributions, as reported in Table 8.3. The central control points of the camber curve can be moved in both the x and y directions, the central control points of the thickness curve can be moved only in y-direction.

Control points	Pt1	Pt2	Pt3	Pt4	Pt5	Pt6
Camber line	(0 0)	(G1 G3)	(G2 G4)	(1 0)		
Thickness line	(0 0)	(0 G5)	(0.25 G6)	(0.50 G7)	(0.75 G8)	(1 0)

**Table 8.3:** Variables adopted in parametrization *ParB*

Figure 8.2 shows the results of the parametrization of the test-case profiles

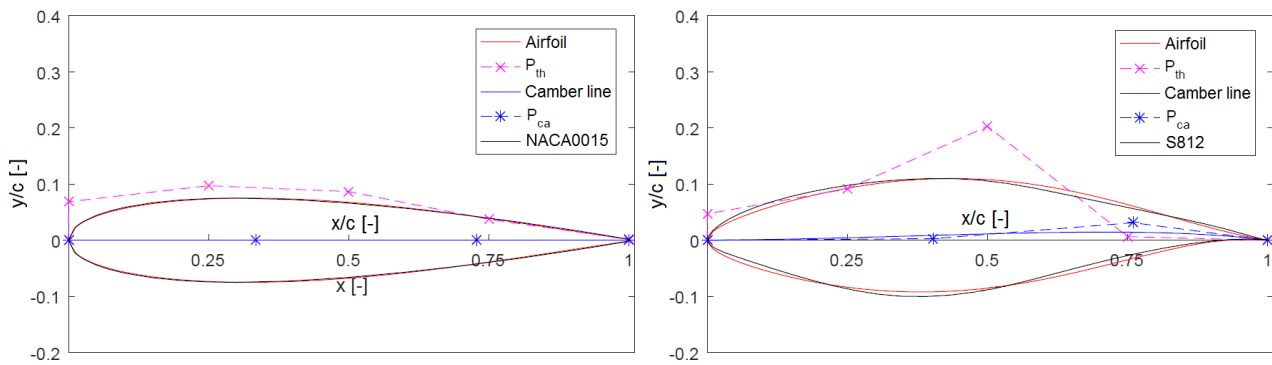


**Figure 8.2:** Results of the parametrization *ParB* on the NACA0015 (left) and S812 (right) airfoils

As can be seen, the parametrization of the NACA0015 airfoil shows a good accordance with the original geometry; the S812 reconstruction shows differences in the leading edge zone and in the suction side curve. The result is not totally satisfactory, the differences from the baseline profile still remain high.

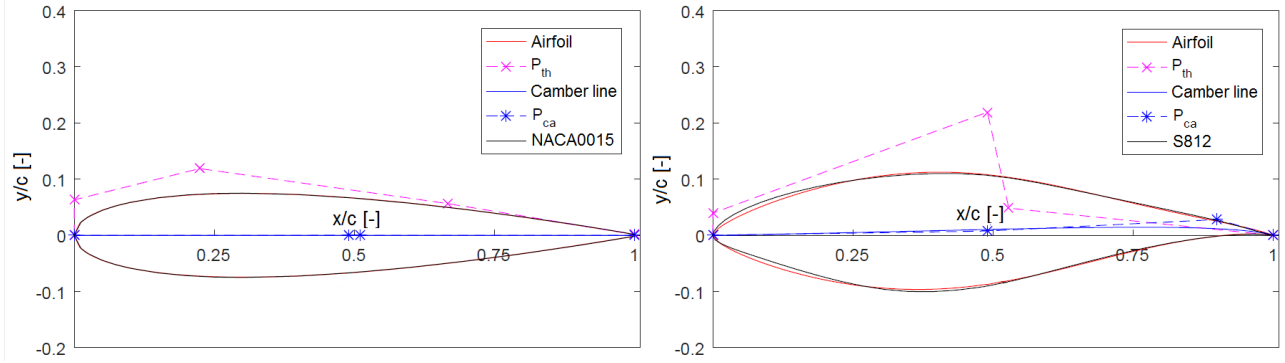
### 8.2.3 Parametrization ParC (9 Variables)

In the third proposed parametrization (indicated as *ParC*), 4 and 5 control points have been adopted respectively for the camber and thickness line distributions, as reported in Table 8.4. The degrees of freedom have been increased: the central points of every distribution can be moved in both the x and y directions.

Figure 8.3 illustrates the results of the parametrization for the test case profiles.

As can be observed, the parametrization of the NACA0015 airfoil is once again accurate. Regarding the S812 reconstruction, the differences between the curves have been reduced by increasing the number of

Control points	Pt1	Pt2	Pt3	Pt4	Pt5
Camber line	(0 0)	(G1 G5)	(G2 G6)	(1 0)	
Thickness line	(0 0)	(0 G7)	(G3 G8)	(G4 G9)	(1 0)

Table 8.4: Variables adopted in parametrization *ParC*Figure 8.3: Results of the parametrization *ParC* on the NACA0015 (left) and S812 (right) airfoils

variables and degree of freedom. However, slightly differences still remain between the original curve and its reconstruction.

### 8.2.4 Parametrization *ParD* (8 variables)

In *ParD*, the last proposed parametrization, 5 and 6 control points have been adopted respectively for the camber and thickness line distributions, as reported in Table 8.5. Only the central points of the camber distribution could be moved in both the x and y directions, the degrees of freedom of the other control points are represented by the y-coordinate. Specifically, the x-coordinate of Pt2 and Pt4 of the chamber line are maintained fixed respectively at  $0.1c$  and  $0.9c$ .

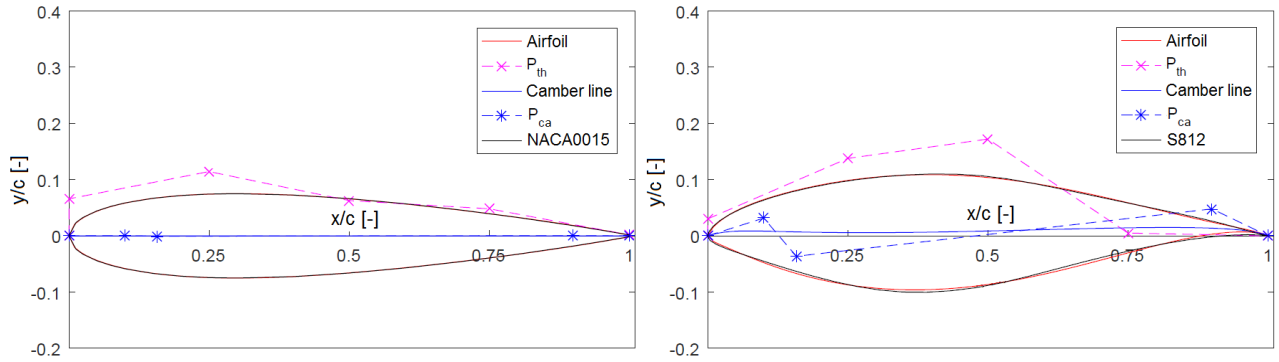
Control points	Pt1	Pt2	Pt3	Pt4	Pt5	Pt6
Camber line	(0 0)	(0.1 G2)	(G1 G3)	(0.9 G4)	(1 0)	
Thickness line	(0 0)	(0 G5)	(0.25 G6)	(0.50 G7)	(0.75 G8)	(1 0)

Table 8.5: Variables adopted in parametrization *ParD*

Figure 8.4 shows the results of the parametrization for the test case profiles.

As can be noticed, the parametrization of the NACA0015 airfoil once again shows a good accordance with the original geometry. The S812 reconstruction is more accurate compared the previous analysed parametrizations and slightly differences, compared to the original profile, are found in the leading edge zone.

*ParD* has confirmed to be the most accurate parametrization to describe the test-case airfoils and it represents a good compromise between the accuracy and the need to keep low the number of genes.



**Figure 8.4:** Results of the parametrization  $ParD$  on the NACA0015 (left) and S812 (right) airfoils

Therefore,  $ParD$  is adopted as the method to reconstruct and generate the airfoil geometries in the proposed optimization loop.

### 8.3 Airfoil Optimization for the Design Point (OptA)

The approach proposed in the optimization (named  $OptA$ ), consists in increasing the performances of a given configuration of vertical axis wind turbine. The geometrical parameters (radius  $R$ , chord  $c$ , number of blades  $N_B$ , pitch angle  $\varphi_P$ ) and the working conditions (tip speed ratio  $\lambda$ ) are set before the optimization loop, as reported in Table 8.1. Figure 8.5 illustrates the flowchart of  $OptA$ .

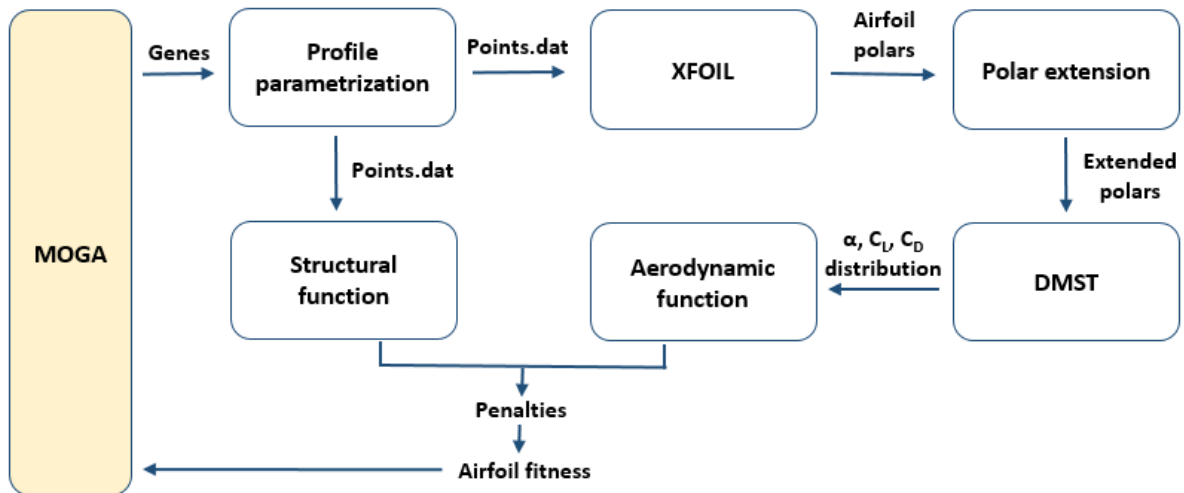


**Figure 8.5:** Flowchart of the  $OptA$  optimization process: the algorithm is based upon the coupling of the panel code XFOIL, the DMST model, functions for the parametrization and both the aerodynamic and structural analysis

The optimization is carried through the Multi-Objective Genetic Algorithm (MOGA) included in the Dakota optimization tool (described in Section 2.7.1). The evolutive algorithm leads the optimization:

it generates the individuals (defined by the genetic pools needed for the airfoil parametrization) and it gets, as input, their fitness (represented by the performances of the considered airfoil). Different parametrization techniques for the profile generation have been analysed, as reported in Section 8.2: the output of the *Parametrization module* is the *points.dat* file containing the coordinates of the points that describe the airfoil shape. The list of points is firstly used to evaluate the aerodynamic performances of the 2D airfoil (in the *XFOIL module*), for both free and forced transition conditions. The evaluated range of the angles of attack is  $\alpha = [-15^\circ, 15^\circ]$ , a wider range compared to the common angles of attack distributions of a VAWT. The polars of the profile are later extended in the range  $\alpha = [-180^\circ, 180^\circ]$  with the Viterna method [87].

The aerodynamic performances of the VAWT are calculated using the Double Multiple Stream Tube model (*DMST*), one of the first models proposed for the VAWT analysis [105]. The input of the *DMST module* is represented by the extended polar and the result of the evaluation consists in the performances of the wind turbine (in terms of angles of attack distribution  $\alpha$ ,  $C_T$ ,  $C_P$  and forces distribution). In particular, for the proposed optimization, only the angles of attack distribution is used for the determination of the aerodynamic objective function. The second analysis is carried in the *Structural module*: it reads the airfoil point list, as an input, and it evaluates the structural fitness function. Details of the two objective functions are further given in Section 8.5.

Finally, the two fitness of the individual are acquired by the optimization algorithm MOGA.

## 8.4 Description of the Genetic Pool and Adopted Constraints

The genetic pool of a generic individual is composed by a set of 8 decimal numbers representing the coordinates of the Bezier control points that can be modified in the adopted parametrization. In *ParD*, genes from *G1* to *G4* represent the control points of the camber line, genes from *G5* to *G8* regulate the thickness distribution. All the genes represent a movement in the y-direction of the Bezier control points, except the gene *G1* that represents a modification of the x-coordinate of the central control point of the camber line.

A set of boundary constraints is imposed to avoid infeasible and unusable solutions and to properly set the space of variables, after some preliminary analysis. The constraints adopted for the optimization variables are summarized in Table 8.6:

	<b>G1</b>	<b>G2</b>	<b>G3</b>	<b>G4</b>	<b>G5</b>	<b>G6</b>	<b>G7</b>	<b>G8</b>
<b>Lower Bound</b>	0.15	-0.10	-0.10	-0.10	0.02	0.00	0.00	0.01
<b>Upper Bound</b>	0.70	0.10	0.10	0.10	0.12	0.30	0.20	0.08

**Table 8.6:** Boundary constraints adopted in the proposed optimization

Figure 8.6 illustrates the allowed movements of the Bezier control points subject to the constraints of Table 8.6. Figure 8.7 shows the covered area resulting from the definition of the pressure and suction side curves, after the application of the extrema values of the boundaries.

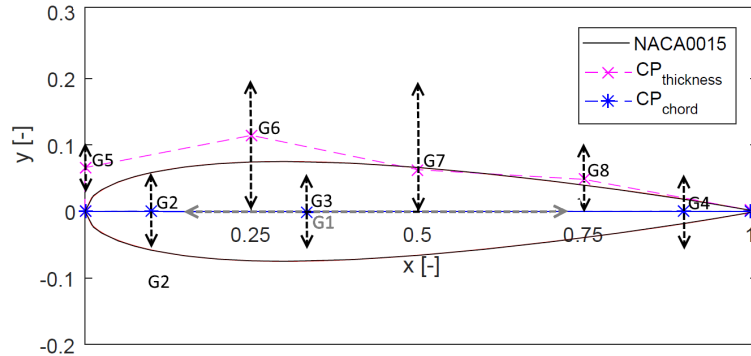


**Figure 8.6:** Range of the allowable movements of the *ParD* control points in *OptA*

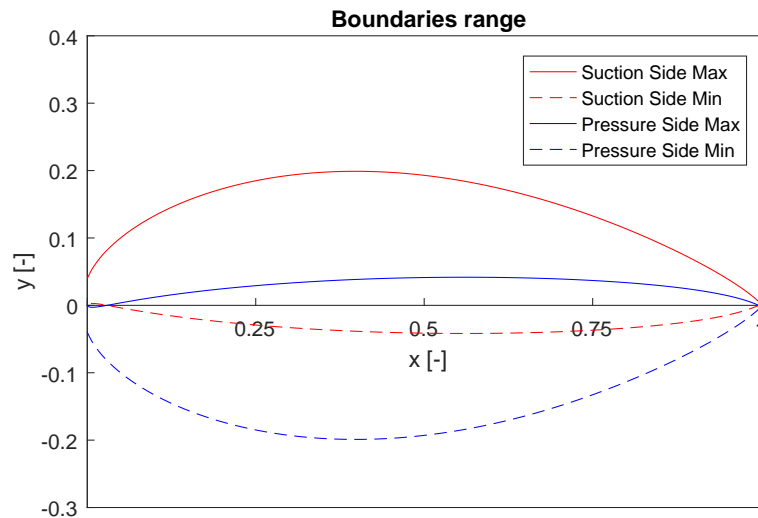


**Figure 8.7:** Upper and lower bounds for suction and pressure side curves on in *OptA*

## 8.5 Objective Functions

In order to identify the most suitable airfoils for the considered VAWT application and estimate the overall performance, two conflicting fitness functions should be maximized:

- Aerodynamic function

$$f_1 = \frac{\overline{C_{L\alpha}}}{\overline{C_D}} \quad (8.1)$$

- Structural function

$$f_2 = EI_{xx} \quad (8.2)$$



The procedure to calculate the aerodynamic function is now being illustrated; firstly the lift and drag polars, for both the free and forced transition, are computed using XFOIL. The solutions are then averaged, as shown in Figure 8.8 for the NACA0015 airfoil. The calculated polars are later extended in the range  $[-180^\circ 180^\circ]$  using the Viterna method [87], as shown in Figure 8.9.

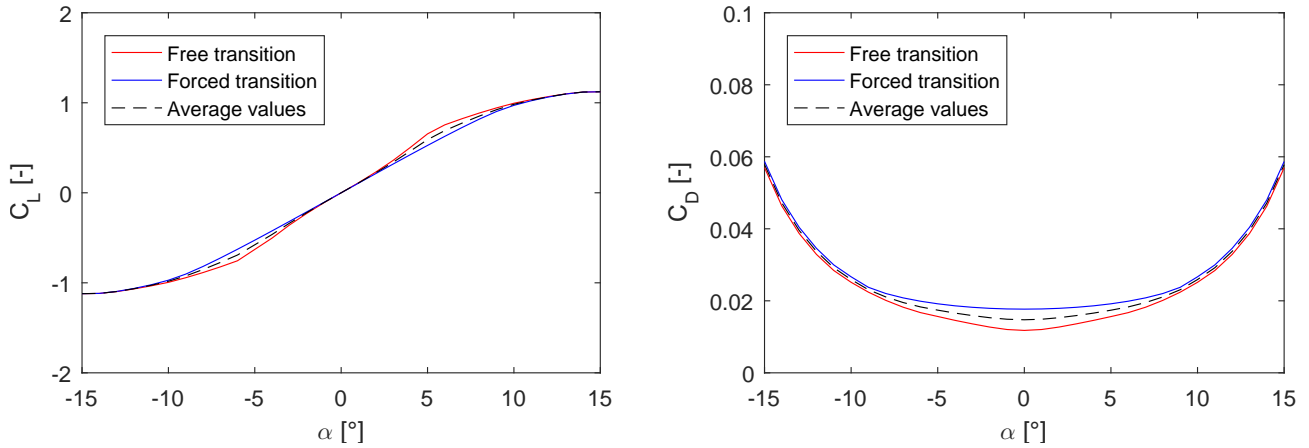


**Figure 8.8:** Aerodynamic polars of NACA0015, evaluated in XFOIL in both free and forced transition

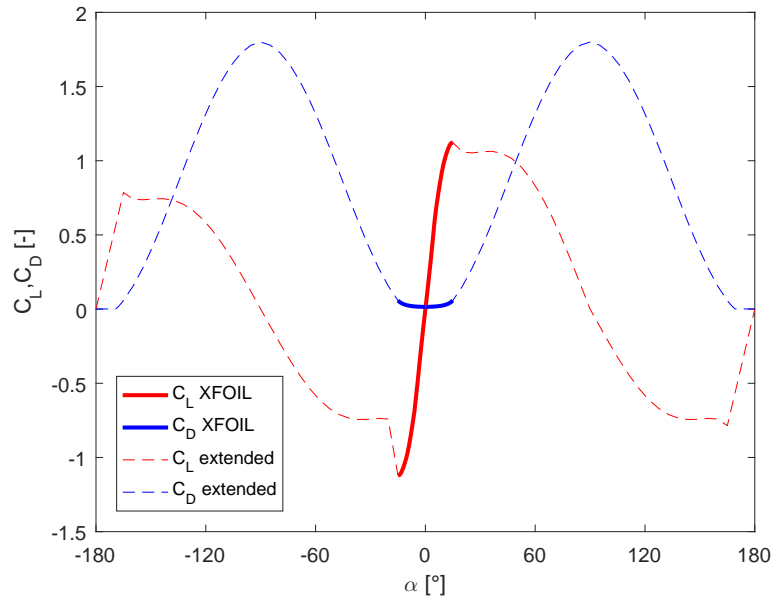


**Figure 8.9:** Extension of the aerodynamic polars using the Viterna method, for NACA0015

The  $f_1$  fitness function represents the ratio of the average lift curve slope over the average drag coefficient over a rotation. The optimal power output of the turbine is obtained by optimizing the shedding of the wake of the turbine, which determines the energy conversion from the flow. In order to optimize the related distribution of the loads on the blade, the ratio of the average lift curve slope over the average drag coefficient over a rotation should be maximized, as demonstrated by Ferreira et al. [101]: when the drag produced by the airfoil is contained, the value of  $f_1$  will increase.

To calculate the average lift curve slope  $\overline{C_{L\alpha}}$ , the range of assumed angle of attack  $\alpha$  (Figure 8.10a) is divided in  $n = 20$  intervals where the lift curve slope is computed. Finally, the average value is calculated as:

$$\overline{C_{L\alpha}} = \frac{\sum_{i=0}^n (C_{L\alpha,i})}{n} \quad (8.3)$$

In order to compute the mean drag coefficient  $\overline{C_D}$ , the frequency over a rotation is calculated as reported in Figure 8.10b. Then, the frequency is converted in a weight  $W$  to be applied in order to calculate the weighted average of the  $C_D$  distribution:

$$\overline{C_D} = \frac{\sum_{i=0}^n (C_{D,i} * W_i)}{\sum_{i=0}^n W_i} \quad (8.4)$$

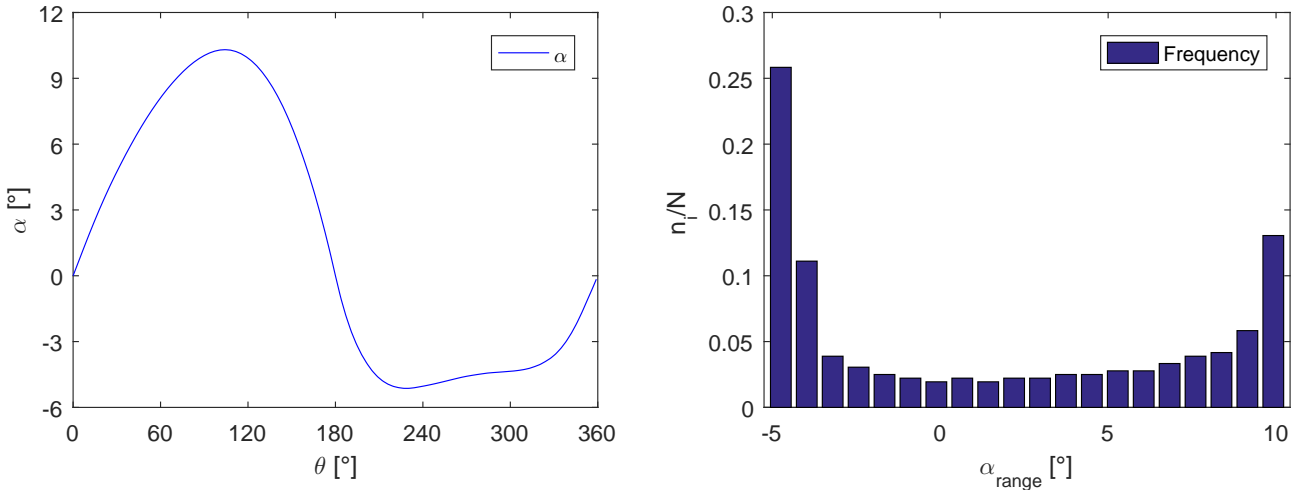


**Figure 8.10:** Angles of attack distribution during a revolution and related frequency for the NACA0015 airfoil

Finally, the aerodynamic fitness function can be computed as the ratio between  $\overline{C_{L\alpha}}$  and  $\overline{C_D}$ .

The structural function aims is to maximize the bending stiffness ( $EI_{xx}$ ) of the airfoil. The relationship between the bending moment  $M$  and the curvature of the blade  $k$  is:

$$M = EI_{xx}k \quad (8.5)$$

where  $E$  is the elastic module and  $I_{xx}$  represents the moment of inertia relative to the x-axis. To reduce the bending curvature is necessary to maximize the moment of inertia; the airfoil is hence divided in  $n$  segments and the moment of inertia relative to the x-axis is calculated as:

$$I_{xx} = \sum_{i=0}^n A_i * y_i^2 \quad (8.6)$$

where  $A_i$  represents the area of the  $i$ -segment (considering a small thickness  $th = 0.004$  for the normalized profile) and  $y_i$  is the distance between the segment and the neutral axis.

In order to run a multi-objective optimization using the MOGA algorithm included into DAKOTA, the objective functions should be minimized, hence the resulting fitness functions are normalized to NACA0015 airfoil performances ( $f_{1,0}$  and  $f_{2,0}$ ).

$$f_{Aer} = \min\left(\frac{f_{1,0}}{f_1}\right) \quad (8.7)$$

$$f_{Str} = \min\left(\frac{f_{2,0}}{f_2}\right) \quad (8.8)$$

## 8.6 Penalties Applied

The solutions characterized by bad aerodynamic performances and thick airfoils are unacceptable, hence the following penalties have been applied to the evaluated fitness.  $f_{Aer}$  and  $f_{Str}$  represent respectively the aerodynamic and structural objective functions, namely the performances normalized with respect to the NACA0015 airfoil, as described in 8.5.

$$f_{Aer} = \begin{cases} f_{Aer} & f_{Aer} < p_{a,1} \\ f_{Aer} * \left(1 + \frac{(f_{Aer} - p_{a,1})}{p_{a,1}}\right) & p_{a,1} \leq f_{Aer} \leq p_{a,2} \\ 1000 & f_{Aer} > p_{a,2} \end{cases} \quad (8.9)$$

$$f_{Str} = \begin{cases} f_{Str} & th_{max} < 0.33 \\ f_{Str} * \left(1 + \frac{(th_{max} - 0.33)}{0.33}\right) & th_{max} \geq 0.33 \\ 1000 & f_{Str} > p_{s,1} \end{cases} \quad (8.10)$$

The aerodynamic fitness function is made progressively worse when the calculated performances of the airfoil are lower than  $p_{a,1}$  times the performances of the NACA0015 profile. When the  $f_{Aer}$  value drops below  $p_{s,2}$  times the baseline value, the individual is rejected by assigning a high value of fitness. Similarly, the structural function  $f_{Str}$  is made progressively worse when the relative thickness of the airfoil  $th_{max}$  is above the 33%. Finally, if the value of  $f_{Str}$  is higher than  $p_{s,2}$ , the individual is rejected.

## 8.7 Setting of XFOIL for the Polars Evaluation

The calculated polars of the airfoil represent the input data for the further aerodynamic analysis. In the XFOIL computations, the used Reynolds number is 150000 and the critical flow amplification factor  $N_{crit}$  is set to 6 (typical VAWT condition). Two XFOIL evaluations are run for each considered profile: a free transition and a forced transition (where the *xtr* specification is added to the XFOIL command list) applied on both the upper and lower surfaces of the profile. The XFOIL analysis is carried for a range of angles of attack  $\alpha$  between  $-15^\circ$  and  $+15^\circ$  with steps of  $1^\circ$ . In order to avoid the instability and the occurrence of wrong results in XFOIL calculations, each analysis is sub-divided in two phases: first the negative angles of attack  $\alpha$  from  $0^\circ$  to  $-15^\circ$  are analysed, then the positive range of  $\alpha$ , from  $0^\circ$  to  $+15^\circ$ , is computed. The two polar are finally merged. For more information refer to Appendix C. Table 8.7 reports the XFOIL code to setup a forced transition analysis.

load points.dat	visc
mdes	150000
filt	pacc
exec	polare_points.txt
pane	aseq
oper	-15
vpar	15
n 6	1
xtr 0.1 0.1	pacc
	visc
iter	
70	quit

**Table 8.7:** An example of the XFOIL command list used to calculate the positive polar in forced transition conditions

## 8.8 Optimization Strategy

The Multi-Objective optimization algorithm (MOGA), included in Dakota, has been used for the present optimization. A population of 40 individuals has been random initialized and the optimization has run for a total number of 100 generations (4000 function evaluations in total).

Table 8.8 reports the main parameter setting of the optimization.

<b>Number of genes</b>	8	<b>Crossover rate</b>	0.8
<b>Population size</b>	40	<b>Mutation rate</b>	0.1
<b>Max generations</b>	100	<b>Shrinkage percentage</b>	0.9

**Table 8.8:** Main setting of the optimizer MOGA, used in *OptA*

## 8.9 Parallel Computing Implementation and Scalability Test

In order to simultaneously run several computations, involving different XFOIL analysis, a shell script (reported in Table 8.9) has been implemented; it checks the current process and it gets its PID. During the optimization setting phase, few issues have been found concerning the convergence of the XFOIL analysis: when non converging, the XFOIL process is not kill but it remains in standby, hence it needs to be constantly monitored during the running. The script checks the presence of XFOIL processes every 2 seconds and kills the XFOIL analysis, if still running, after 10 seconds.

The Dakota MOGA algorithm is run with the *asynchronous local parallelism* option as specified in the *Hybrid parallelism* section of the Dakota User Manual [29]. During the analysis, the template folder containing the function and the scripts is replicated for every individual and named with a cumulative number (e.g. Workdir1, Workdir2). An array of 8 doubles, containing the genes, is sent from Dakota to the main script, hence the local analysis is carried inside the temporary folder and the outputs are passed, as an array of 2 doubles, to Dakota MOGA. The temporary folder is finally deleted.

A preliminary test of the optimization algorithm has been set-up in order to determine the scalability of the analysis. The *scalability* is the capability of a system, network, or process to handle a growing amount of work, or its potential to be enlarged in order to accommodate that growth, as specified in [106]. The scalability can be defined in several ways, as illustrated by Hill et al. [107] and Duboc et al. [108]; for the scope of the current analysis the scalability is intended to measure how the increasing number of the simultaneous processes, improves the performances of the analysis in terms of computational time  $t$ . The optimization algorithm has been tested on an Ubuntu 14.04 operative system, the installed software for the optimization are Dakota v6.4 and XFOIL v6.99. The computer has 8Gb of RAM and the processor Intel® Core™ i7-4720HQ CPU @ 2.60GHz  $\times$  4. In order to guarantee the reproducibility of the results, a fixed *seeding number* has been imposed to the random number generator of the analysis. The optimization test case consists of 4 generations of 8 individuals, for a total number of 32 evaluations. As can be noticed in Figure 8.11, the total optimization time decreases while increasing of the number of simultaneous processes,  $Np$ . This represents a typical behaviour of the scaling analysis and allows to identify the best configuration for the parallel computing. For the considered case, running 4 analysis in parallel is sufficient: the computational time is reduced to 3.01

```

#!/bin/bash
rm polare_points.txt process.pid
xfoil points.dat < input_xfoil.txt &
echo "$!" > process.pid
pid=$(cat process.pid)
sleep 2
if [ "$(ps -o comm=-p "$pid")" = "xfoil" ]; then
    sleep 2
    if [ "$(ps -o comm=-p "$pid")" = "xfoil" ]; then
        sleep 2
        if [ "$(ps -o comm=-p "$pid")" = "xfoil" ]; then
            sleep 4
            if [ "$(ps -o comm=-p "$pid")" = "xfoil" ]; then
                kill -9 $pid
                echo "xfoil_killed_after_10_seconds"
            else echo "Myprocess_is_dead!_10_seconds"
            fi
        else echo "Myprocess_is_dead!_6_seconds"
        fi
    else echo "Myprocess_is_dead!_4_seconds"
    fi
else echo "Myprocess_is_dead!_2_seconds"
fi

```

**Table 8.9:** Shell script to check XFOIL processes and manage the parallel optimization

minutes that represents about one-third compared to the 8.51 minutes of the serial analysis. Adding more parallel processes does not provide significant improvements in terms of computational time.

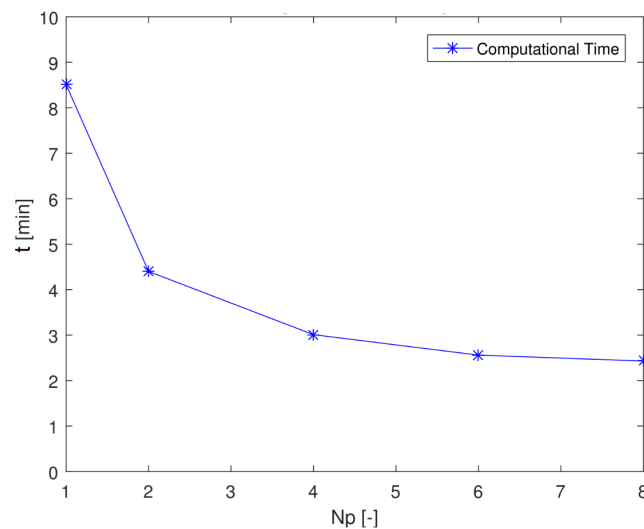


**Figure 8.11:** Results of the scalability test of the optimization algorithm

## 8.10 Results of Optimization A

The aim of *OptA* is to identify the best airfoils for a fixed design point of a VAWT.

First, the resulting Pareto front of the optimization is presented, then some solution are analysed.

The optimization problem has been set as described in the previous sections, a summary of the penalties adopted for *OptA* is reported in Table 8.10.

<b>Penalty coefficient <math>p_{a,1}</math></b>	1.2
<b>Penalty coefficient <math>p_{a,2}</math></b>	1.6
<b>Thickness limit</b>	0.33
<b>Penalty coefficient <math>p_{s,1}</math></b>	1.6

**Table 8.10:** Penalty coefficients adopted in *OptA* analysis

Figure 8.12 shows the resulting Pareto front of the optimization. Several individuals belonging to the front of best solutions have been analysed, Table 8.11 reports the genetic pool of the chosen solutions.

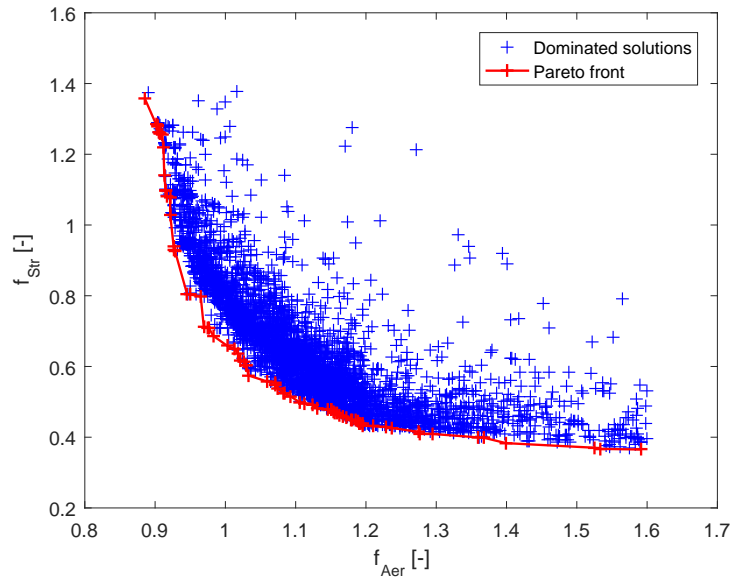


**Figure 8.12:** Resulting Pareto front for the *OptA* analysis

	Genes								Fitness	Max Thick
<b>Baseline</b>	0.500	0.000	0.000	0.000	0.658	0.114	0.063	0.048	1.00 1.00	15.0% 29.7%
<b>A101</b>	0.637	0.002	0.023	-0.006	0.041	0.181	0.002	0.020	0.90 1.28	15.1% 25.0%
<b>A102B</b>	0.678	0.014	0.004	-0.005	0.041	0.181	0.042	0.020	0.93 0.95	16.9% 27.3%
<b>A103B</b>	0.690	-0.020	0.004	0.004	0.054	0.181	0.024	0.051	0.96 0.82	17.2% 27.0%
<b>A104</b>	0.690	-0.045	0.004	0.032	0.084	0.181	0.060	0.020	1.00 0.66	20.0% 25.0%
<b>A105B</b>	0.690	-0.020	0.004	0.033	0.084	0.181	0.074	0.020	1.06 0.61	20.6% 26.1%
<b>A106</b>	0.659	0.002	-0.021	0.074	0.101	0.202	0.070	0.063	1.20 0.43	23.4% 27.3%

**Table 8.11:** *OptA*: considered individuals of the Pareto front

The characteristics of the considered solutions are illustrated below. The trends of the angle of attack  $\alpha$  during a rotation and the related frequency distribution are presented. A comparison between the polars, evaluated in XFOIL for both free and forced transition conditions, and their average, is also shown.

**Baseline NACA0015:** the characteristics of the symmetric profile are presented below.

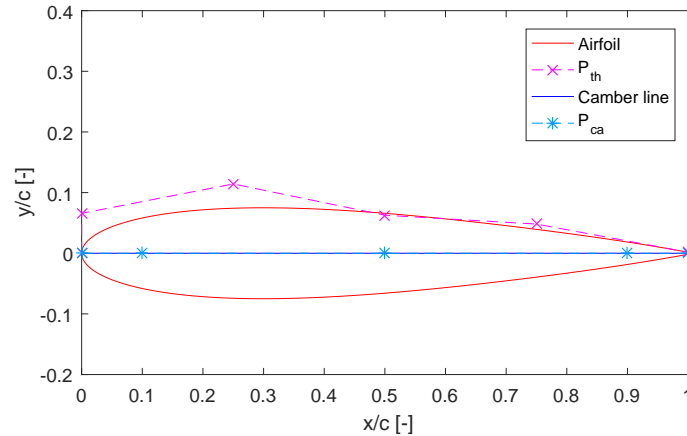


**Figure 8.13:** NACA0015: Bezier parametrization of the airfoil

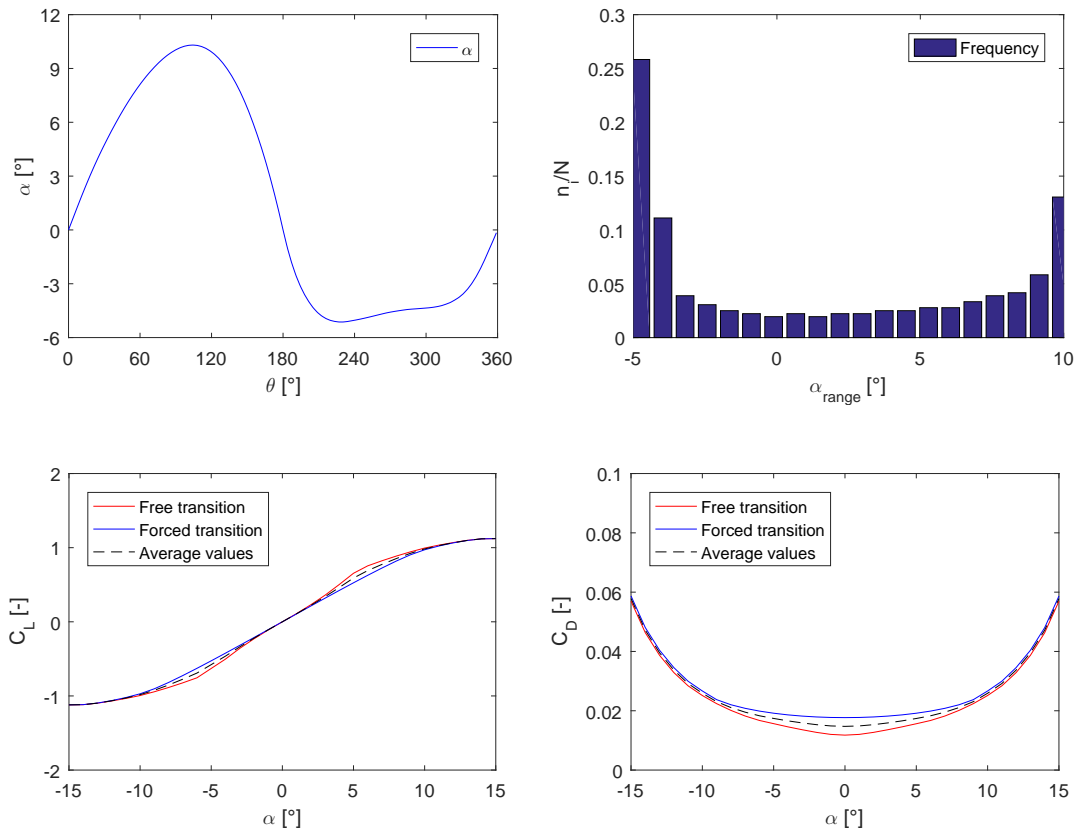


**Figure 8.14:** The trend of  $\alpha$  during a rotation, the related frequency distribution and the comparison between the polars in free and forced transition conditions are illustrated for NACA0015



**Airfoil A101:** the characteristics of the profile, belonging to the Pareto front, are presented below.

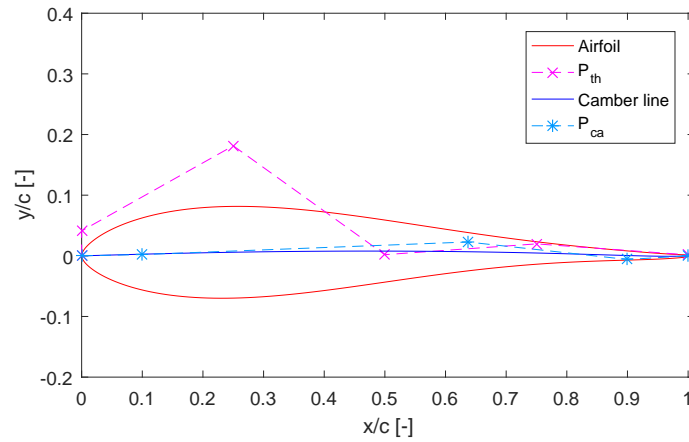


**Figure 8.15:** A101: Bezier parametrization of the airfoil

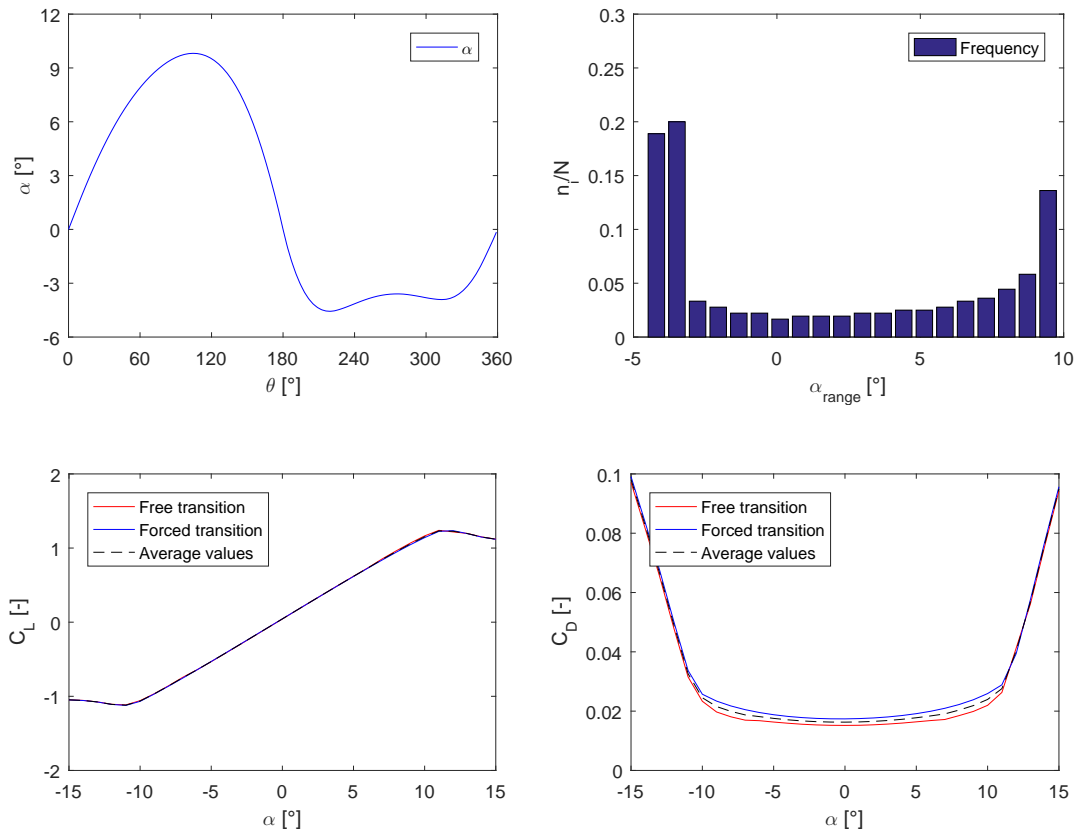


**Figure 8.16:** The trend of  $\alpha$  during a rotation, the related frequency distribution and the comparison between the polars in free and forced transition conditions are illustrated for A101 airfoil

**Airfoil A102B:** the characteristics of the profile, belonging to the Pareto front, are presented below.

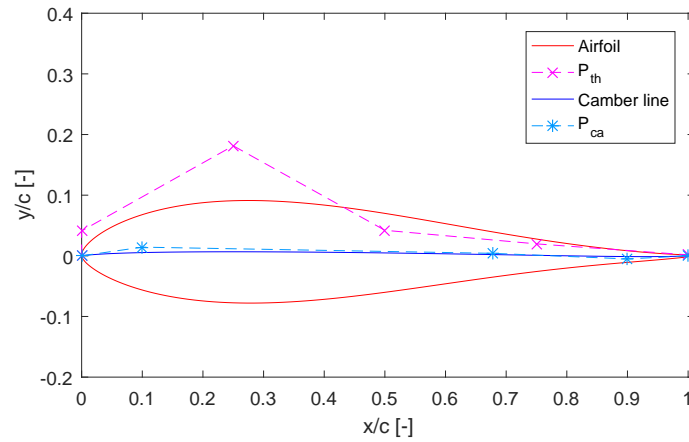


**Figure 8.17:** A102B: Bezier parametrization of the airfoil

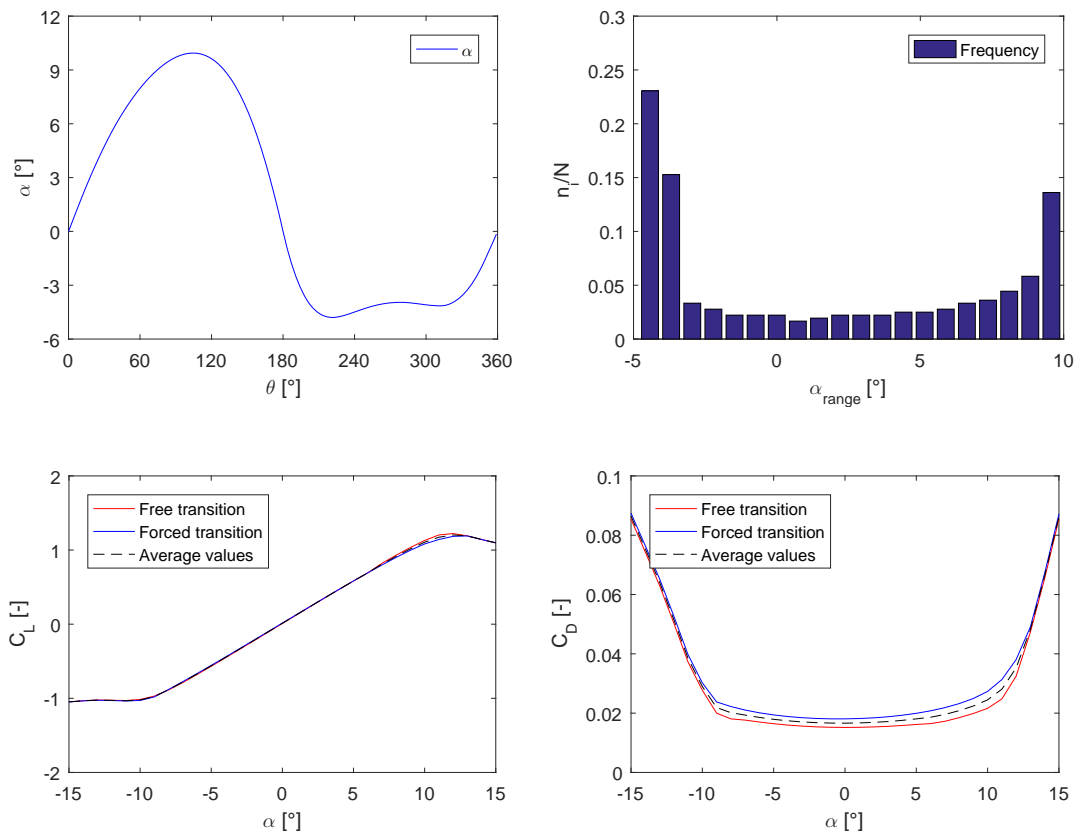


**Figure 8.18:** The trend of  $\alpha$  during a rotation, the related frequency distribution and the comparison between the polars in free and forced transition conditions are illustrated for A102B airfoil

**Airfoil A103B:** the characteristics of the profile, belonging to the Pareto front, are presented below.

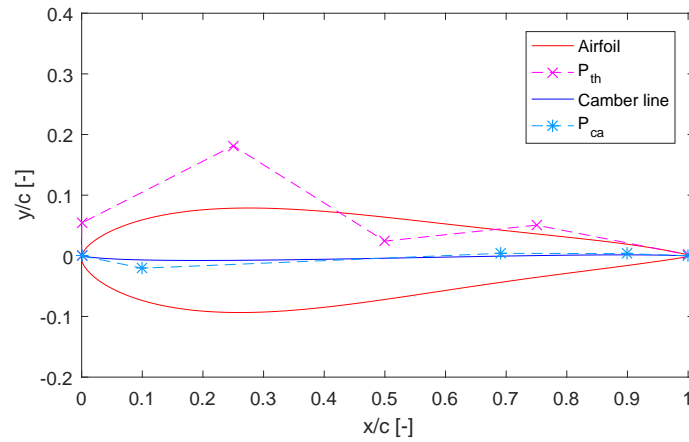


**Figure 8.19:** A103B: Bezier parametrization of the airfoil

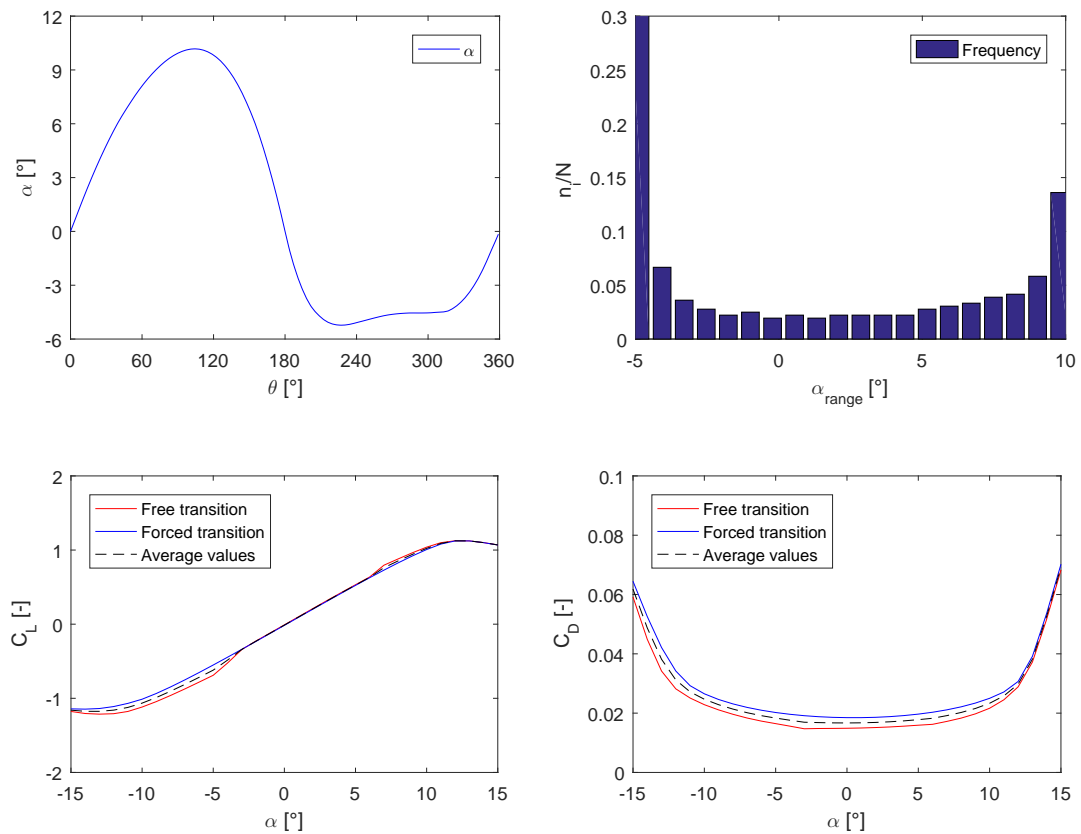


**Figure 8.20:** The trends of  $\alpha$  during a rotation, the related frequency distribution and the comparison between the polars in free and forced transition conditions are illustrated for A103B airfoil

**Airfoil A104:** the characteristics of the profile, belonging to the Pareto front, are presented below.

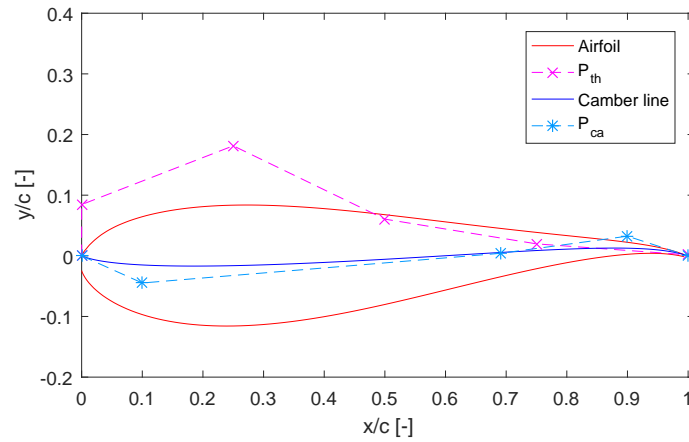


**Figure 8.21:** A104: Bezier parametrization of the airfoil

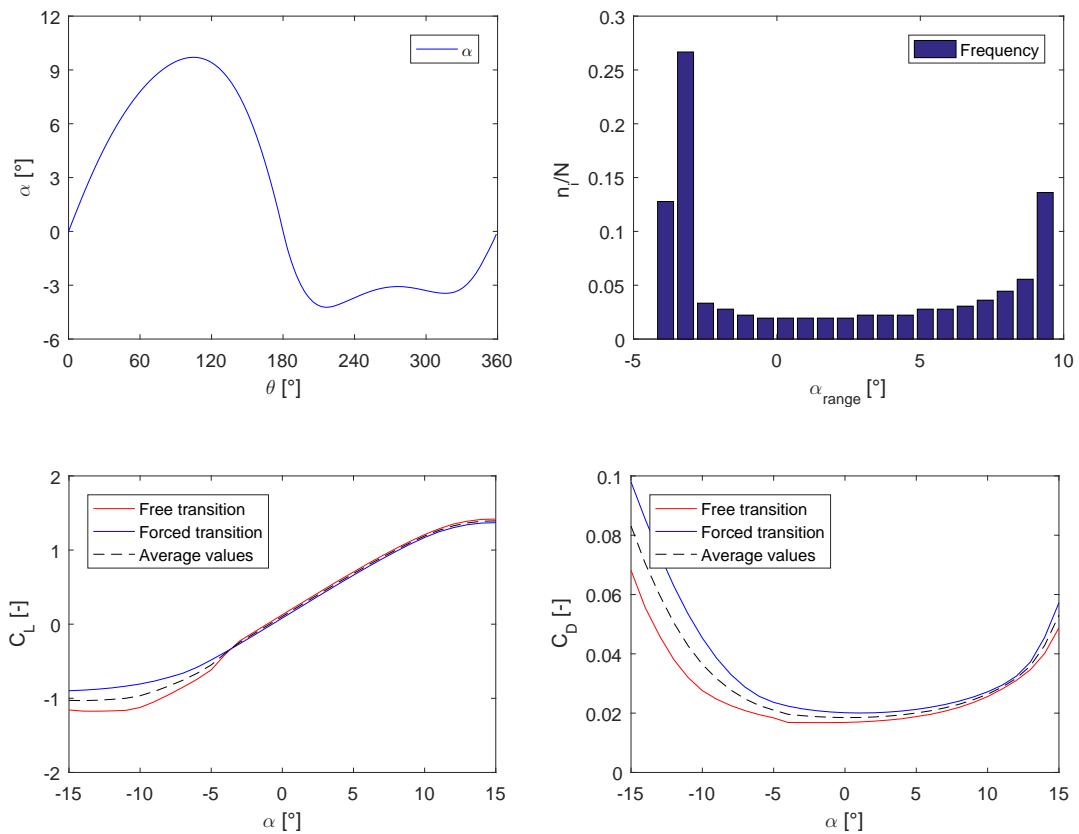


**Figure 8.22:** The trends of  $\alpha$  during a rotation, the related frequency distribution and the comparison between the polars in free and forced transition conditions are illustrated A104 airfoil

**Airfoil A105B:** the characteristics of the profile, belonging to the Pareto front, are presented below.

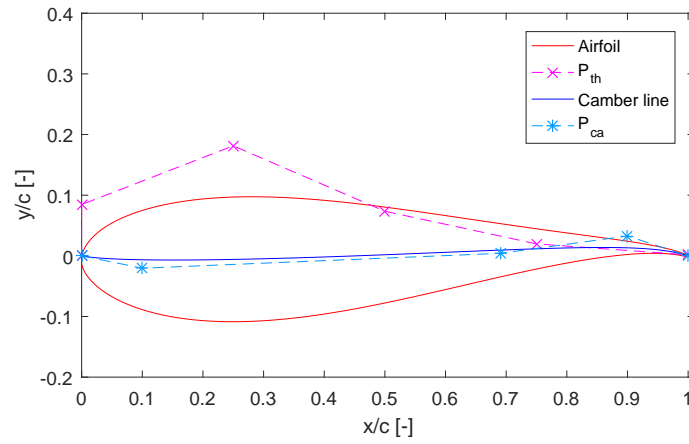


**Figure 8.23:** A105B: Bezier parametrization of the airfoil

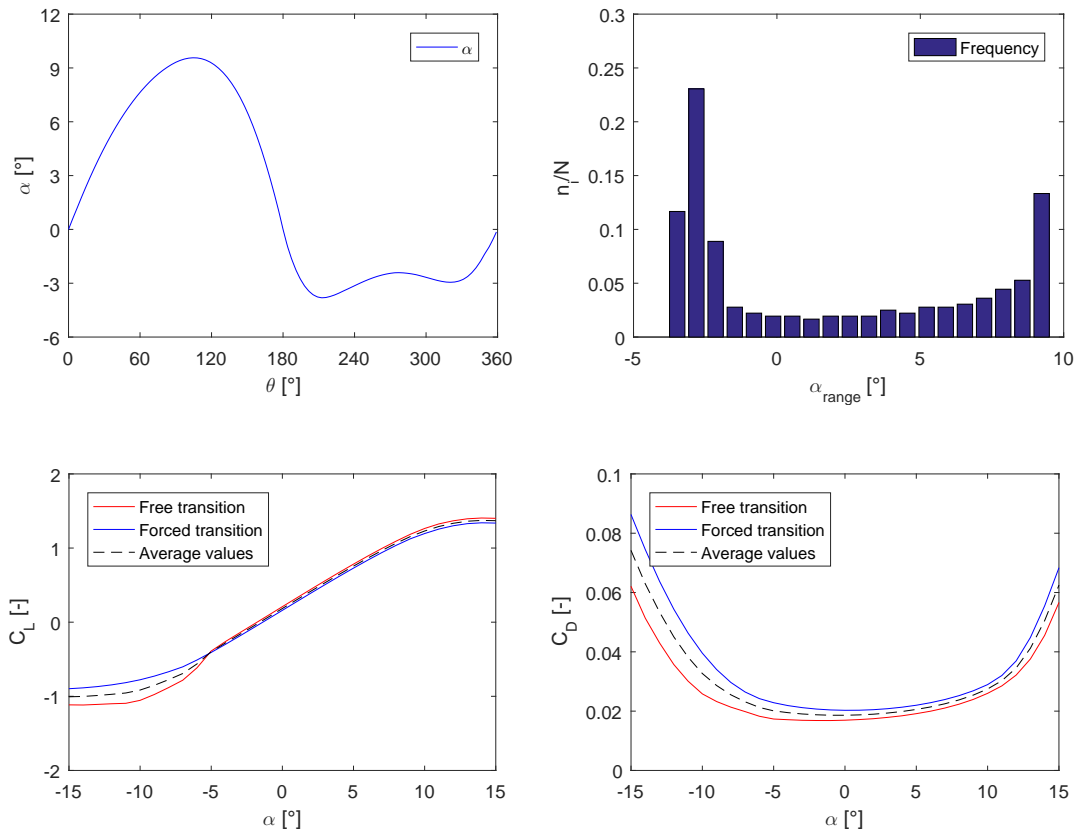


**Figure 8.24:** The trends of  $\alpha$  during a rotation, the related frequency distribution and the comparison between the polars in free and forced transition conditions are illustrated for A105B airfoil

**Airfoil A106:** the characteristics of the profile, belonging to the Pareto front, are presented below.

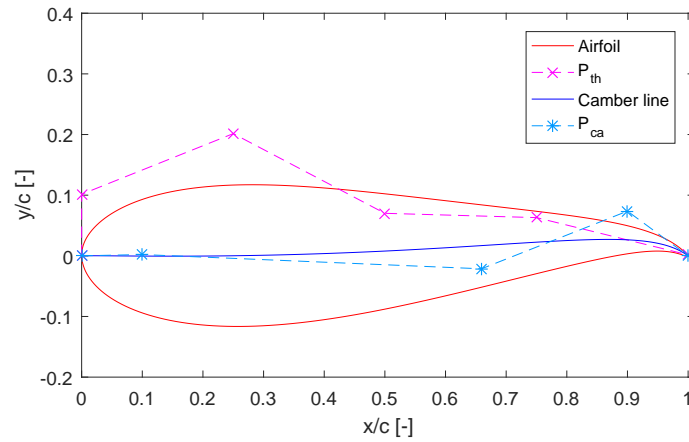


**Figure 8.25:** A106: Bezier parametrization of the airfoil

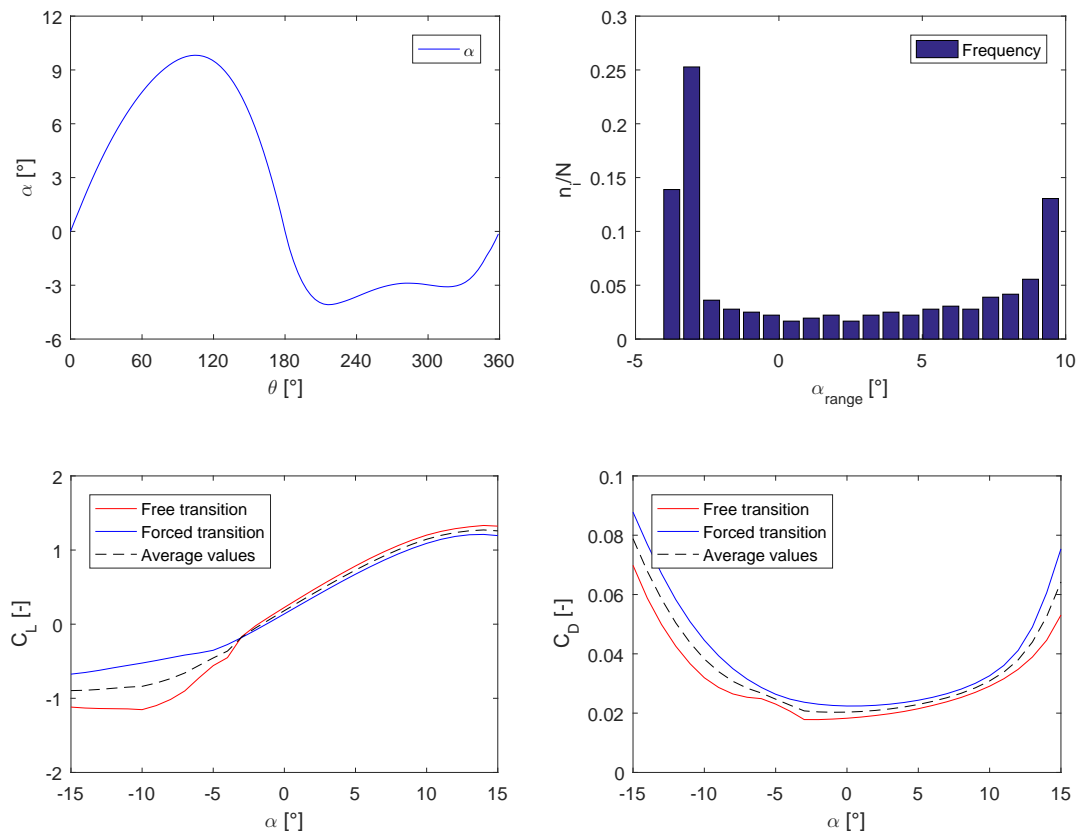


**Figure 8.26:** The trends of  $\alpha$  during a rotation, the related frequency distribution and the comparison between the polars in free and forced transition conditions are illustrated for A106 airfoil

The power and thrust coefficient maps are presented for the *A102B* and *A103B* airfoils and compared to the baseline *NACA0015*. The performances of the wind turbine have been evaluated using the P2DiVA panel code developed by Ferreira [102]. The zones with high solidity and tip speed ratio have been excluded from the plot because of wrong calculations in the used linear model.

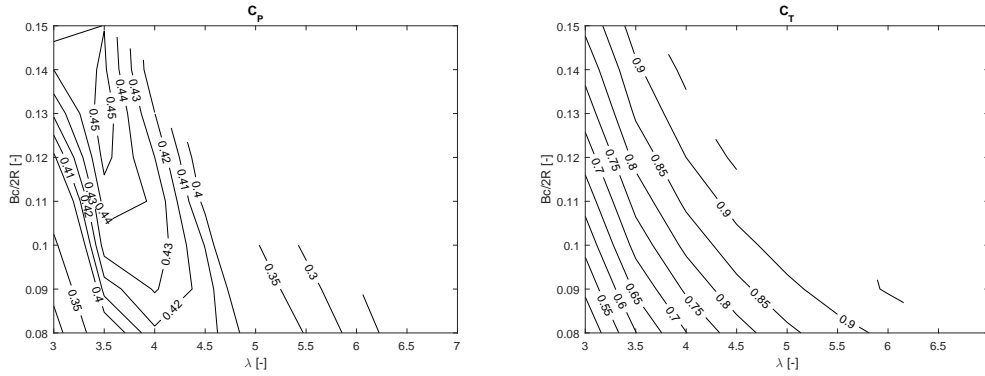


**Figure 8.27:** Power and thrust coefficients values of *NACA0015* airfoil for the considered range of tip speed ratio solidity

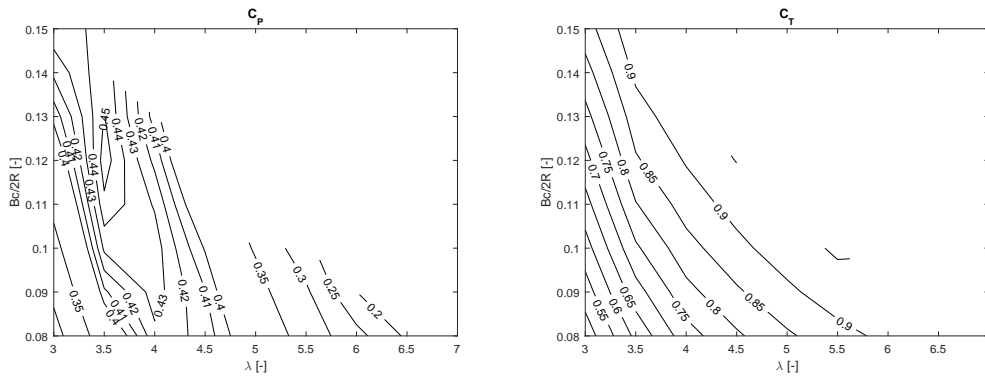


**Figure 8.28:** Power and thrust coefficients values of *A102B* airfoil for the considered range of tip speed ratio solidity

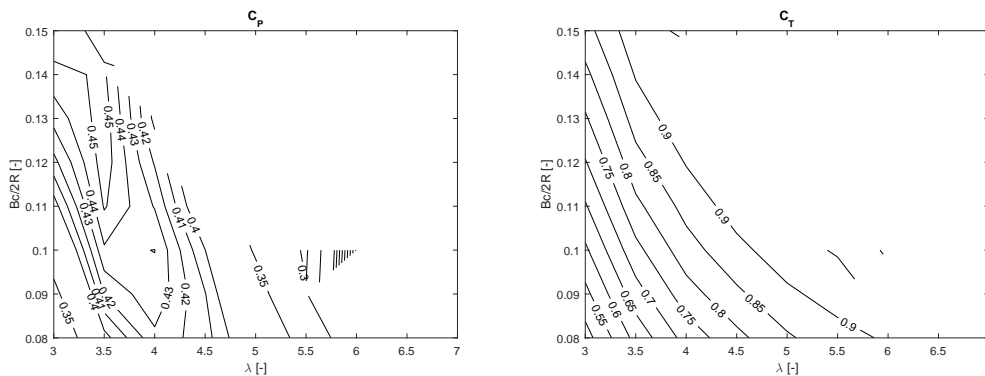


**Figure 8.29:** Power and thrust coefficients values of *A103B* airfoil for the considered range of tip speed ratio solidity

## 8.11 Discussion of Optimization A Results

The aim of *optA* is to identify the best airfoils suitable for a given VAWT geometry and working conditions. The considered case study is reported in Table 8.1. The optimization process allowed to identify a set of solutions belonging to the Pareto front. Solution *A101* presents the best aerodynamic efficiency, calculated as  $\overline{C_{L\alpha}}$  over  $\overline{C_D}$  for the studied configuration. The value has been increased by 9.45% compared to the NACA0015 airfoil, on the other hand the structural performance, in terms of  $f_{Str}$  function, results to be highly decreased of the 28.45%. Solution *A105B* belongs to the opposite side of the Pareto front and it is one of the best for the structural aspects of the analysis: the bending stiffness of the profile has been highly increased of the 38.74%, however the aero-dynamical performance has worsened of the 5.93%. The thicker airfoils, belonging to the Pareto front, for which the calculated  $f_{Aer}$  is higher than 1.20, present a highly curved trailing edge, as can be seen in Figure 8.25: their aerodynamic performances are very low.

The airfoils improved in both the optimization aspects can be found between the extreme cases. Solutions *A102B* and *A103B* represent profiles suitable for the analysed wind turbine: The identified *A102B* shape allows to increase the aero-dynamical performances of 6.53% and the structural properties of 5.03%. Profile *A103B* slightly improves the aerodynamic performances of 4.18%, however the bending stiffness is highly increase of 14.97%. The  $C_P$  values of the optimized profiles has not been increased in the design point, compared to the NACA0015 airfoil, however the Power Coefficient assumes higher values in the low solidity zones (Figures 8.28 and 8.29). In order to increase the performances of the design point, the power coefficient  $C_P$  should be considered as objective function. *OptA* has been completely run in an open source environment, using DAKOTA evolutive algorithm MOGA. The implementation of the procedure has allowed to identify numerical errors and problems due to the instability of the used codes. These issues have been fixed in the optimization *OptB* presented below.



## 8.12 General Airfoil Optimization (OptB)

The VAWT case study considered in Section 8.1, is analysed with a different approach in *Optimization B* using a slightly modified aerodynamic function. Figure 8.30 illustrates the flowchart of the algorithm schema adopted in *Optimization B*.

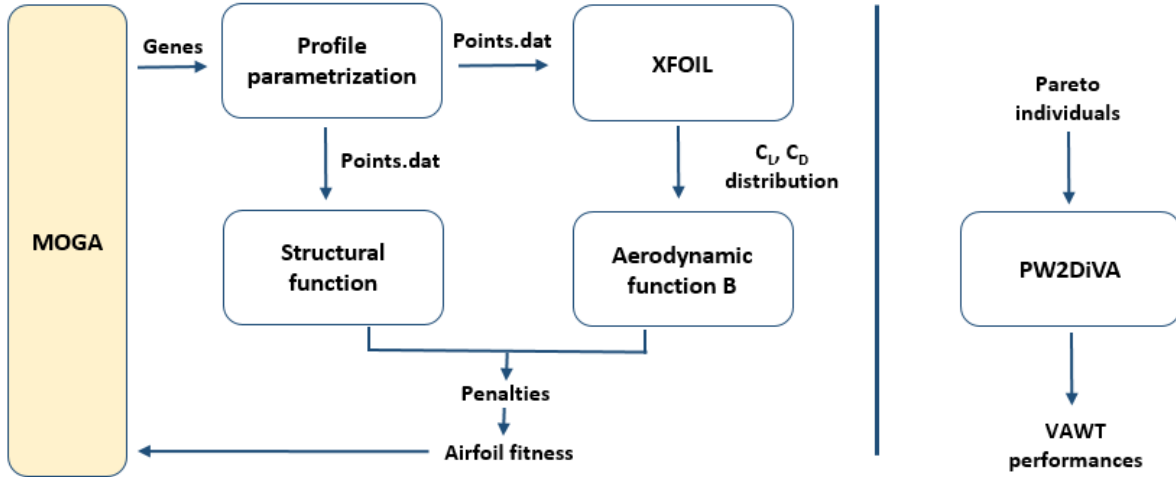


Figure 8.30: VAWT Optimization B Flowchart

The main difference consists in the implementation of the aerodynamic function. In *Optimization B*, the DMST model is not included in the optimization loop and used to calculate the distribution of the angles of attack  $\alpha$ . The polars computed in XFOIL (in terms of  $C_L$  and  $C_D$  distributions) are now directly used in the aerodynamic function, assuming the distribution of angles of attack calculated in Ferreira and Geurts [101]: the adopted distribution represents an average of the cases analysed in that paper, including different NACA airfoils and conditions. The used distribution of  $\alpha$  is shown in Figure 8.31. In the y-axis, the number of times  $n$  an  $\alpha$  value occurs during a rotation is non-dimensionalised with the total number of samples  $N$ . In the x-axis, the angles of attack  $\alpha$  non-dimensionalised and divided in bins using the  $\alpha_{min}$  and  $\alpha_{max}$  encountered during a rotation is reported.

The  $\alpha_{range}$  value is calculated as:

$$\alpha_{range} = 2 \left( \frac{\alpha - \alpha_{min}}{\alpha_{max} - \alpha_{min}} \right) - 1 \quad (8.11)$$

In *Optimization B* different penalties factors are adopted and more extended boundaries used, as reported in Tables 8.12 and 8.13.

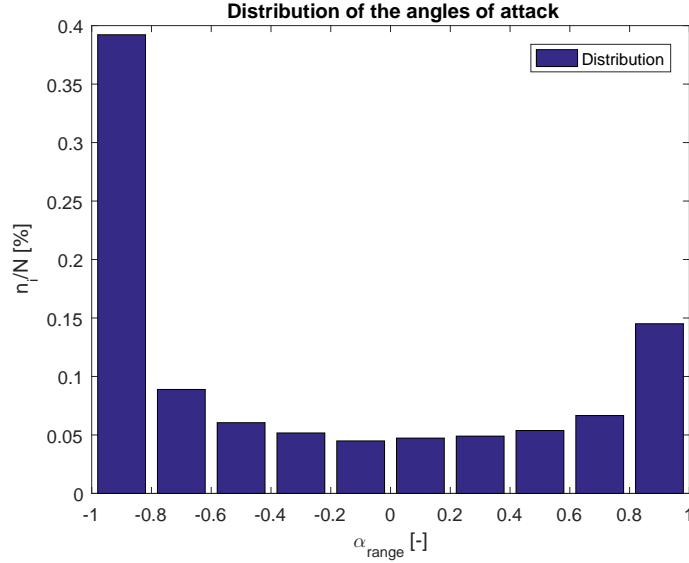


**Figure 8.31:** Distribution of the angles of attack adopted in *Optimization B*

<b>Number of genes</b>	8
<b>Population size</b>	40
<b>Max generations</b>	100
<b>Penalty A1</b>	1.50
<b>Penalty A2</b>	1.80
<b>Penalty thick</b>	0.33
<b>Penalty S1</b>	1.80

**Table 8.12:** Settings used in *Optimization B*

	<b>G1</b>	<b>G2</b>	<b>G3</b>	<b>G4</b>	<b>G5</b>	<b>G6</b>	<b>G7</b>	<b>G8</b>
<b>Lower bound</b>	0.150	-0.100	-0.100	-0.100	0.020	0.000	0.000	0.010
<b>Upper bound</b>	0.70	0.100	0.100	0.100	0.120	0.350	0.120	0.800

**Table 8.13:** *Optimization B* lower and upper extended boundaries

Once the Pareto front has been determined, the selected individuals are analysed in the post-processing phase, using the panel code PW2DiVA (Ferreira [102]), in order to compute the overall performances of the airfoils for different VAWT settings in terms of solidity  $\sigma$ , Tip Speed Ratio  $\lambda$  and pitch angle  $\phi$ .

## 8.13 Results of Optimization B

The results of three different cases with the *Optimization B* approach are presented in the following sections. In *OptB1* the calculated aerodynamic polars are the result of averaging the analysis in free and force transition conditions. In *OptB2* and *OptB3* only the free transition and force transition analysis have been respectively considered in the optimization.

### 8.13.1 OptB1 - Results of the Free+Forced Transition Analysis

In the first optimization, both free and forced transition polars are calculated using XFOIL. The average of the polars has been taken as the resulting polar for the individual in the optimization.

Figure 8.32 shows the Pareto front of the considered optimization.

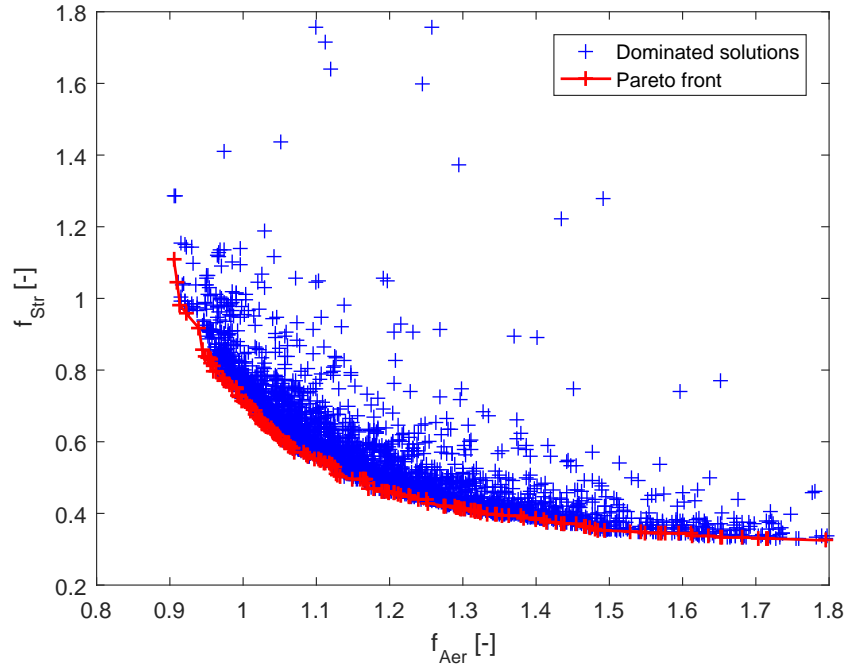


**Figure 8.32:** Resulting Pareto front of the free+forced transition analysis in Optimization B

In the post-processing phase, five solutions belonging to the Pareto front have been analysed with the PW2DiVA panel code, as reported in Table 8.14. In the following pages, the performances in terms of power coefficient  $C_P$  and trust coefficient  $C_T$  are presented for varying Tip Speed Ratio  $\lambda$  and rotor solidity  $N_{BC}/2R$ . The airfoil parametrization and the evaluated polars are also illustrated for the considered profiles.

	Genes								Fitness		Max Thick	
<b>baseline</b>	0.500	0.000	0.000	0.000	0.066	0.114	0.063	0.048	1.00	1.00	15.0%	29.7%
<b>B101</b>	0.638	0.023	0.019	0.008	0.059	0.159	0.031	0.017	0.90	1.11	15.8%	25.0%
<b>B102</b>	0.572	0.005	0.008	0.029	0.059	0.184	0.045	0.017	0.95	0.83	18.1%	26.1%
<b>B103</b>	0.426	0.011	-0.004	-0.020	0.059	0.184	0.048	0.046	1.00	0.71	18.7%	28.4%
<b>B104</b>	0.288	0.023	-0.004	-0.009	0.059	0.195	0.048	0.065	1.05	0.61	19.8%	29.7%
<b>B105</b>	0.275	0.005	0.019	-0.007	0.059	0.237	0.031	0.079	1.16	0.49	22.1%	28.5%
<b>B106</b>	0.275	0.005	-0.004	-0.007	0.088	0.237	0.045	0.079	1.30	0.41	24.2%	27.3%

**Table 8.14:** *OptB1*: considered individuals of the Pareto front

**Airfoil NACA0015:** the characteristics of the baseline profile are presented below.

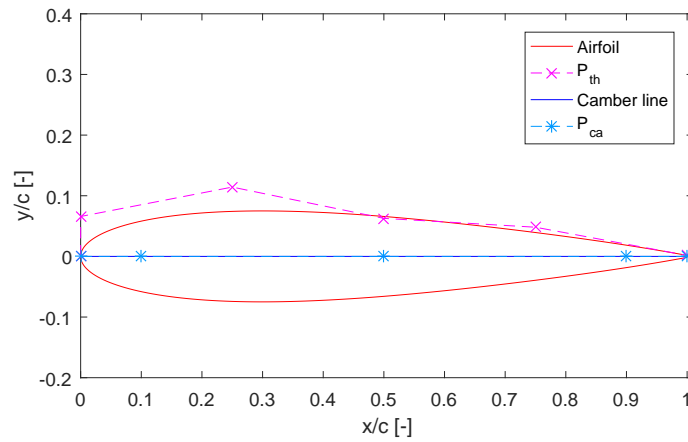


**Figure 8.33:** *OptB1*: NACA0015 airfoil parametrization

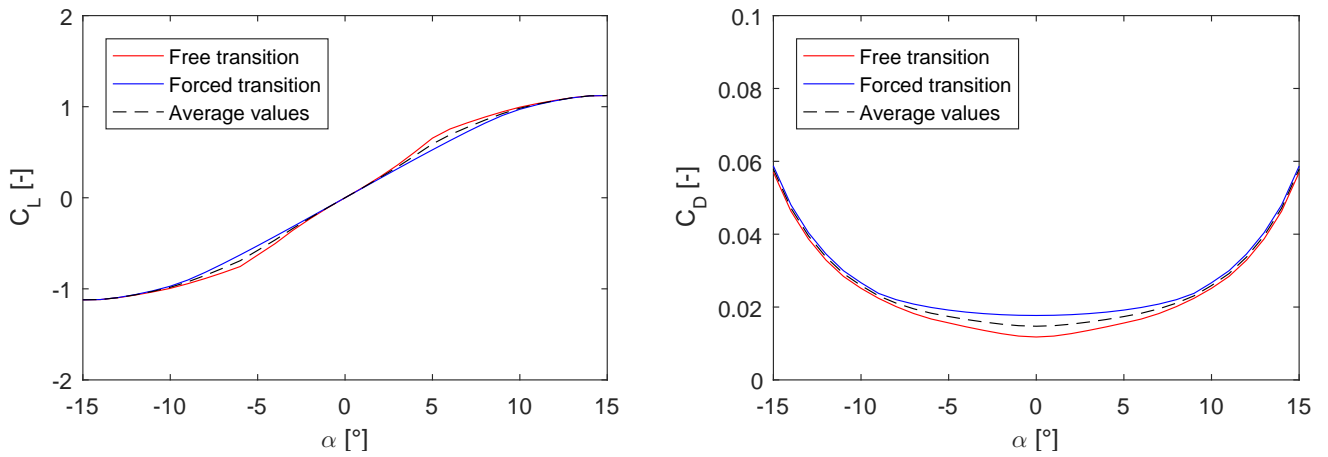


**Figure 8.34:** *OptB1*: NACA0015 airfoil, comparison of the polars for free and forced transitions

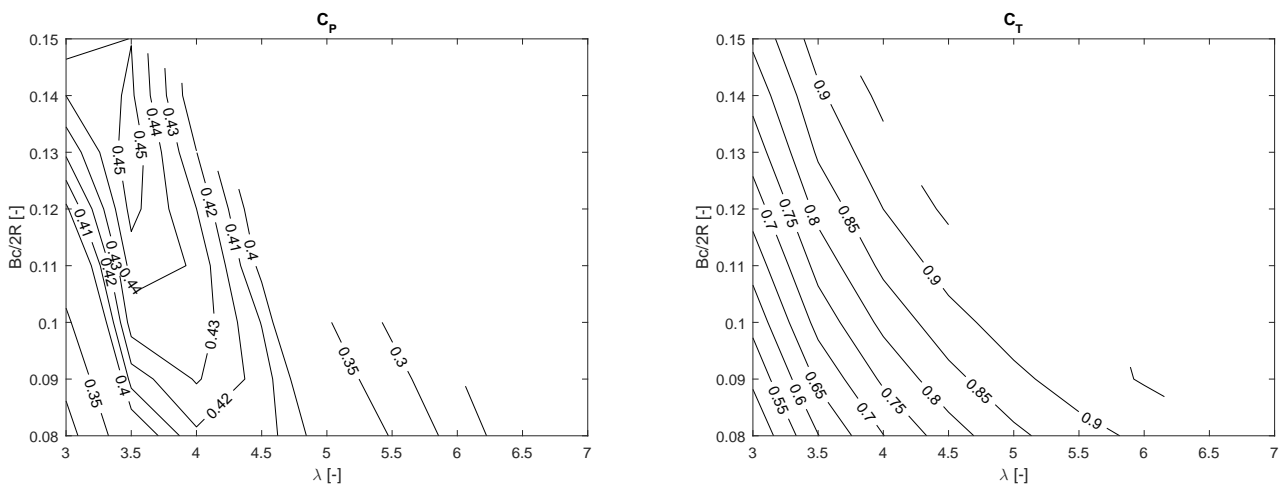


**Figure 8.35:** *OptB1*: NACA0015 airfoil, power and thrust coefficients

**Airfoil B101:** the characteristics of the profile, belonging to the Pareto front, are presented below.

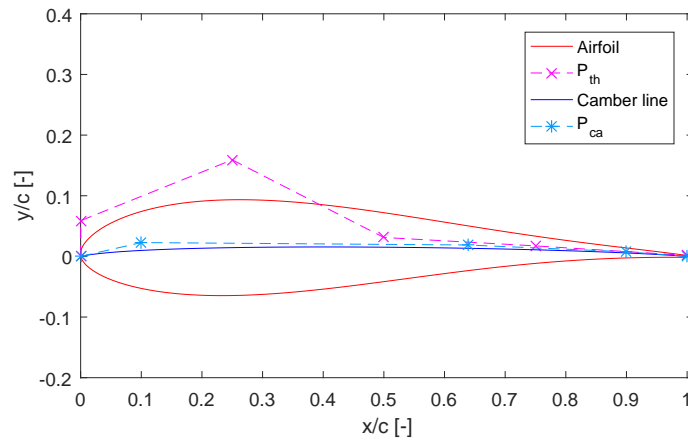


**Figure 8.36:** *OptB1*: B101 airfoil parametrization

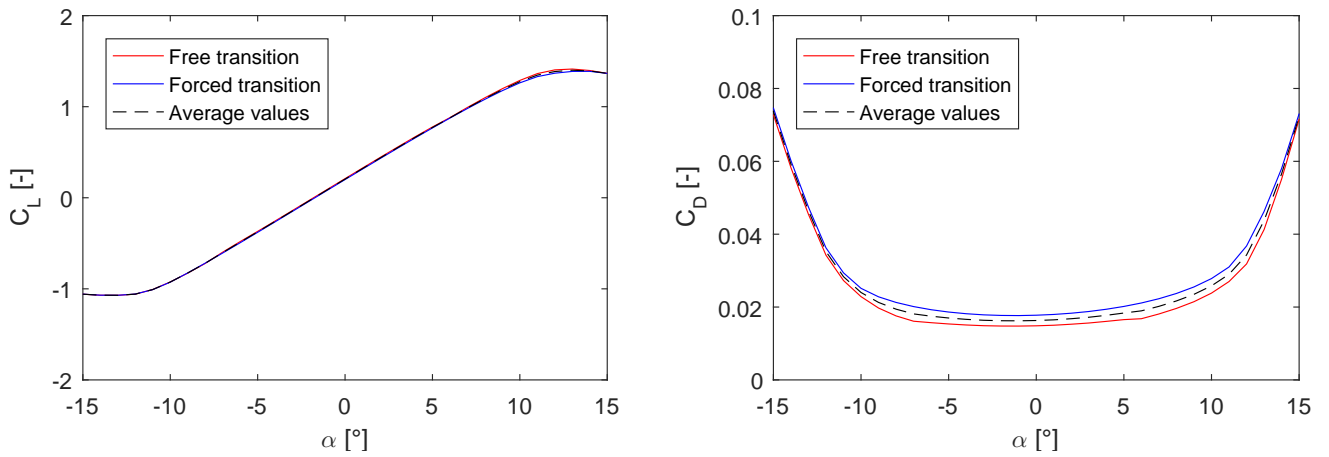


**Figure 8.37:** *OptB1*: B101 airfoil, comparison of the polars for free and forced transitions

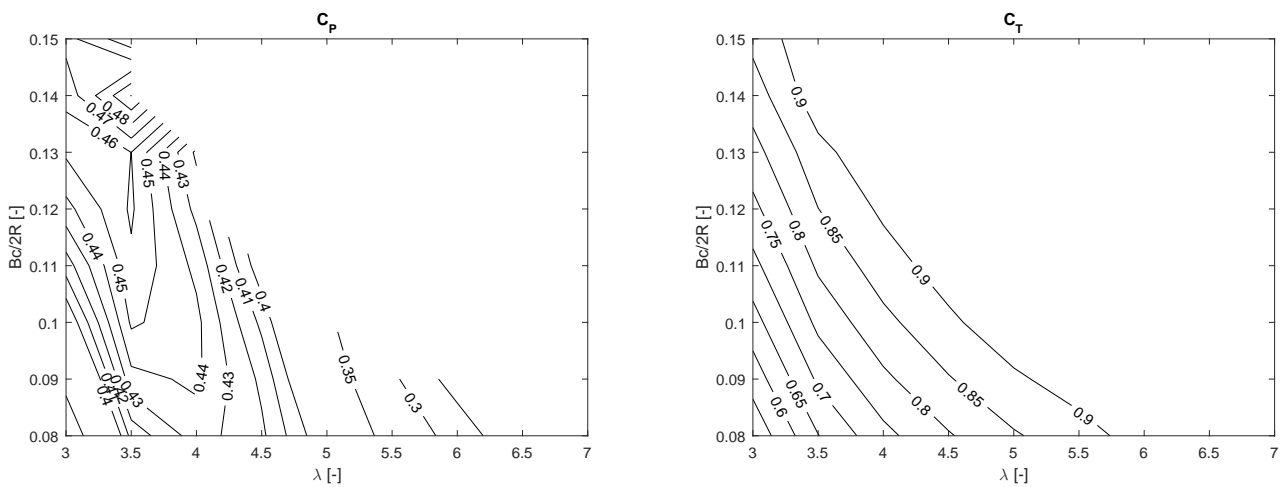


**Figure 8.38:** *OptB1*: B101 airfoil, power and thrust coefficients

**Airfoil B102:** the characteristics of the profile, belonging to the Pareto front, are presented below.

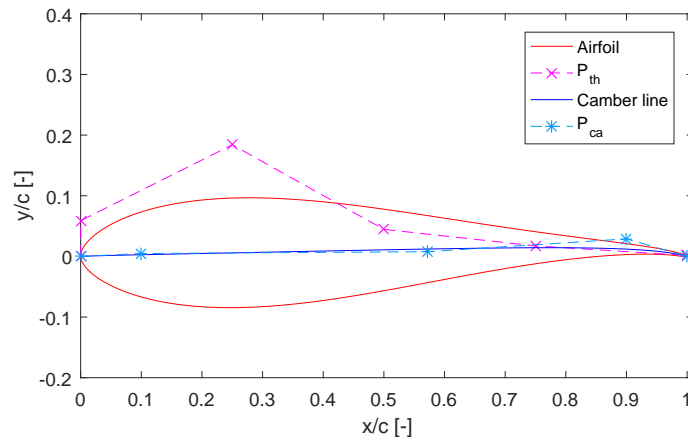


**Figure 8.39:** *OptB1*: B102 airfoil parametrization

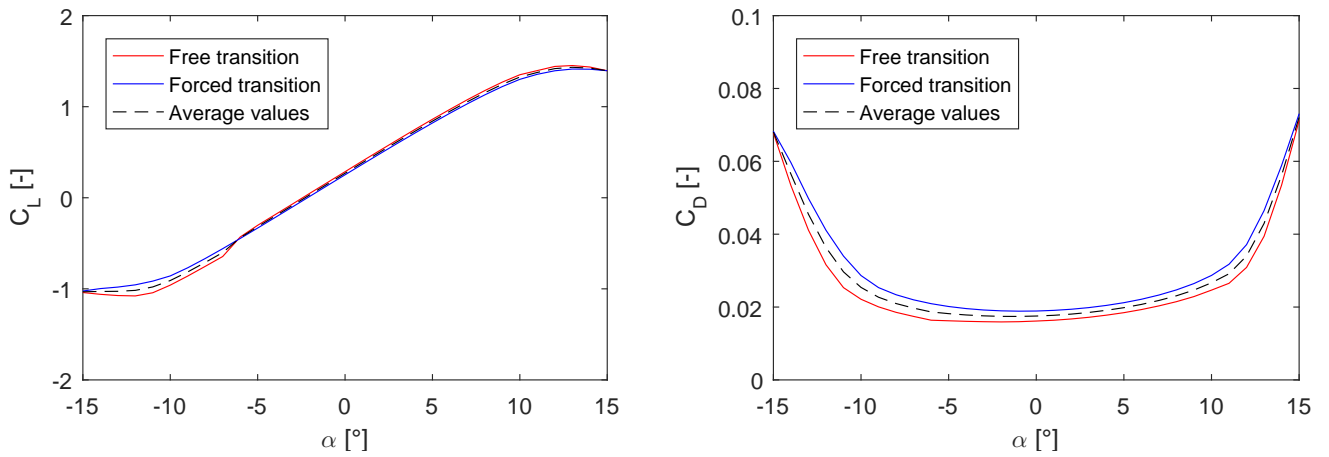


**Figure 8.40:** *OptB1*: B102 airfoil, comparison of the polars for free and forced transitions

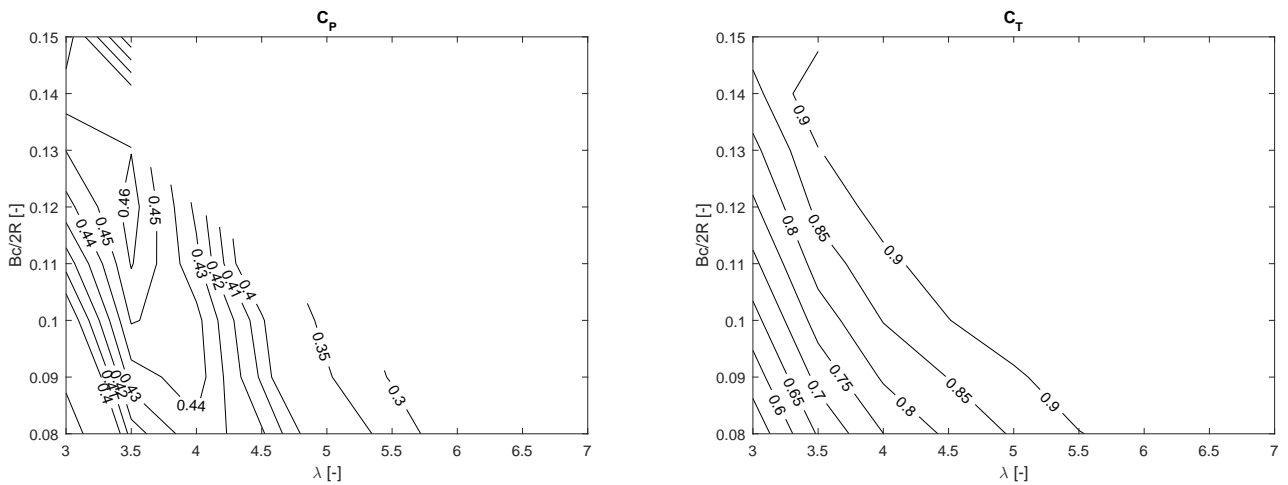


**Figure 8.41:** *OptB1*: B102 airfoil, power and thrust coefficients

**Airfoil B103:** the characteristics of the profile, belonging to the Pareto front, are presented below.

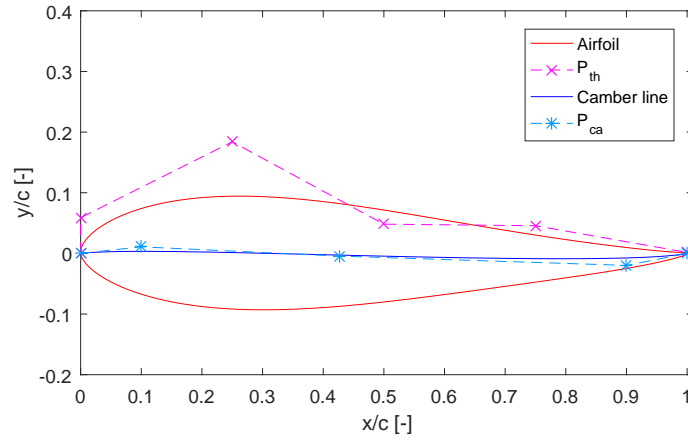


**Figure 8.42:** *OptB1*: B103 airfoil parametrization

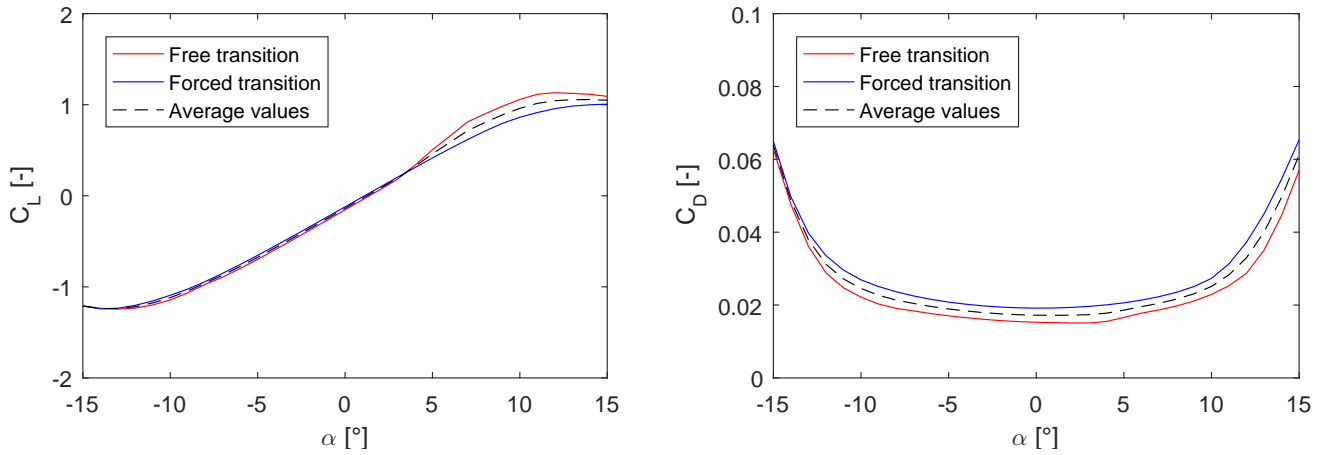


**Figure 8.43:** *OptB1*: B103 airfoil, comparison of the polars for free and forced transitions

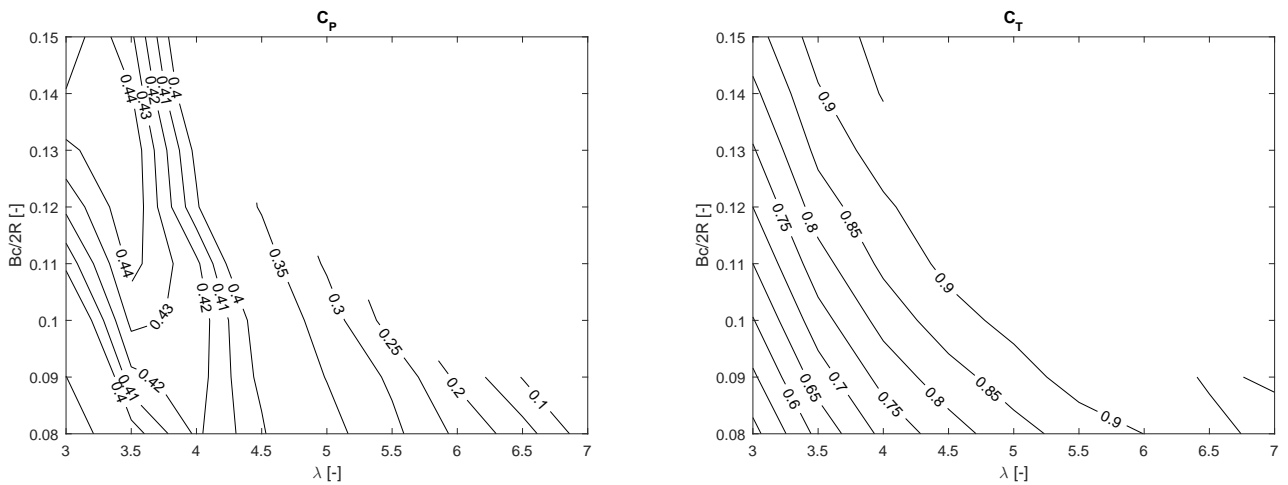


**Figure 8.44:** *OptB1*: B103 airfoil, power and thrust coefficients

**Airfoil B104:** the characteristics of the profile, belonging to the Pareto front, are presented below.

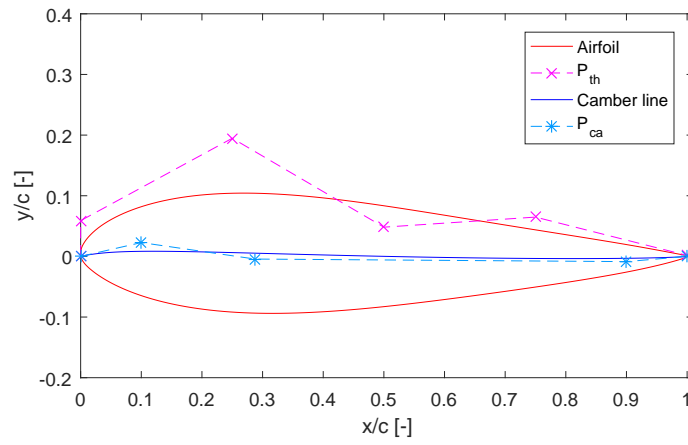


**Figure 8.45:** *OptB1*: B104 airfoil parametrization

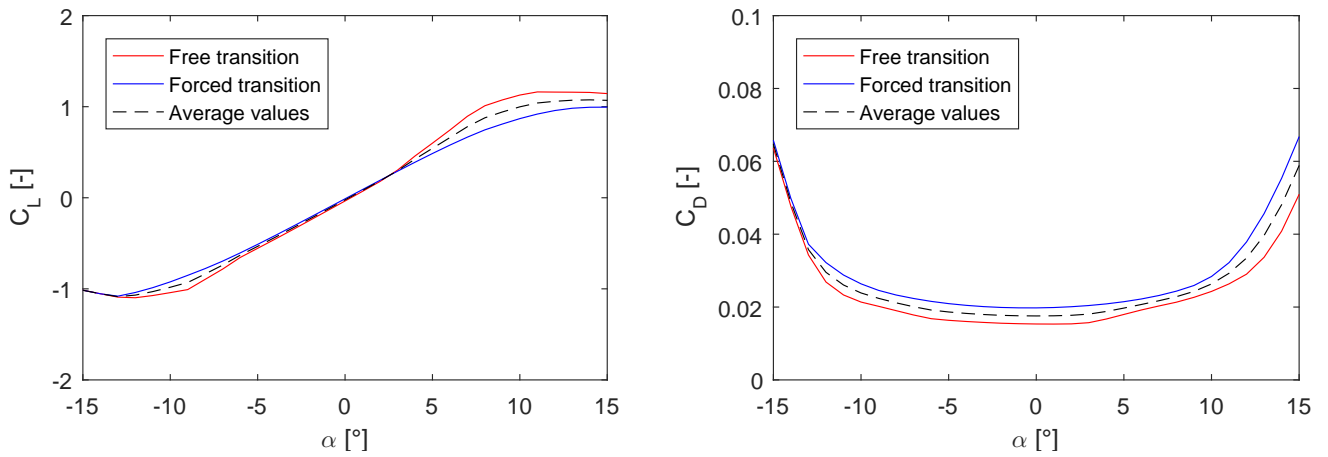


**Figure 8.46:** *OptB1*: B104 airfoil, comparison of the polars for free and forced transitions

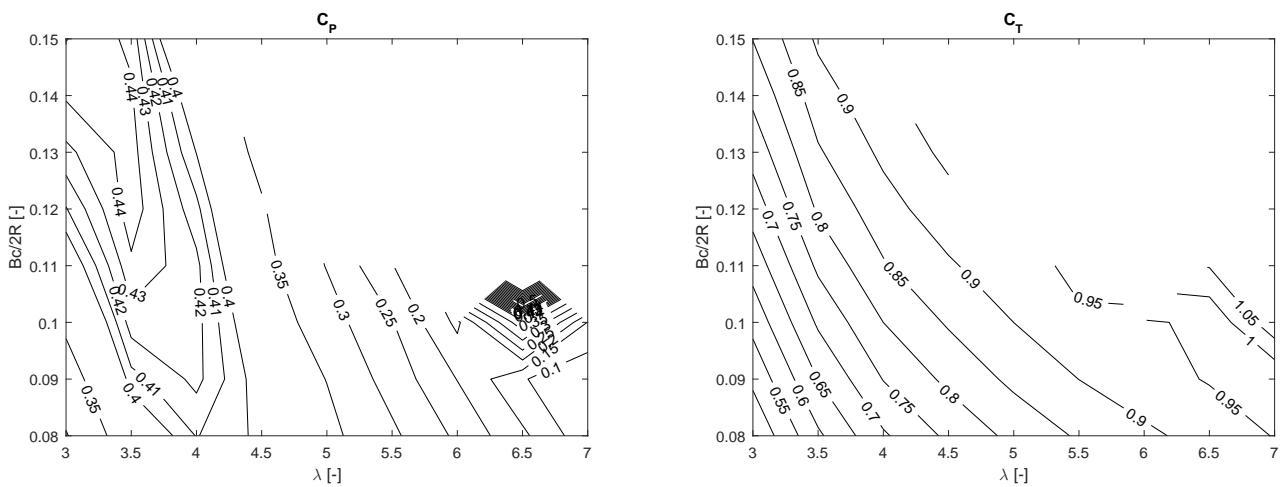


**Figure 8.47:** *OptB1*: B104 airfoil, power and thrust coefficients



**Airfoil B105:** the characteristics of the profile, belonging to the Pareto front, are presented below.

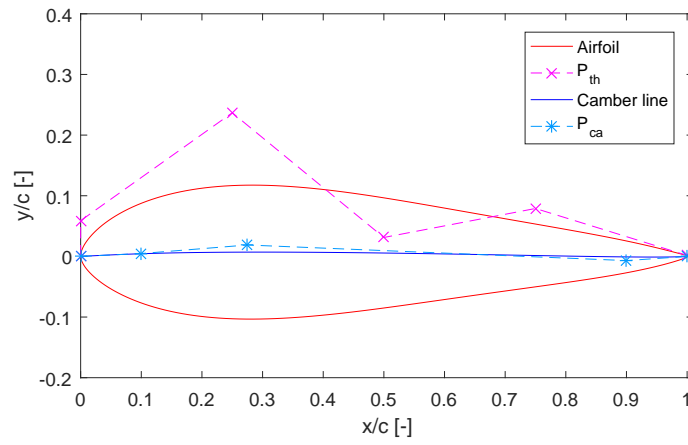


Figure 8.48: *OptB1*: B105 airfoil parametrization

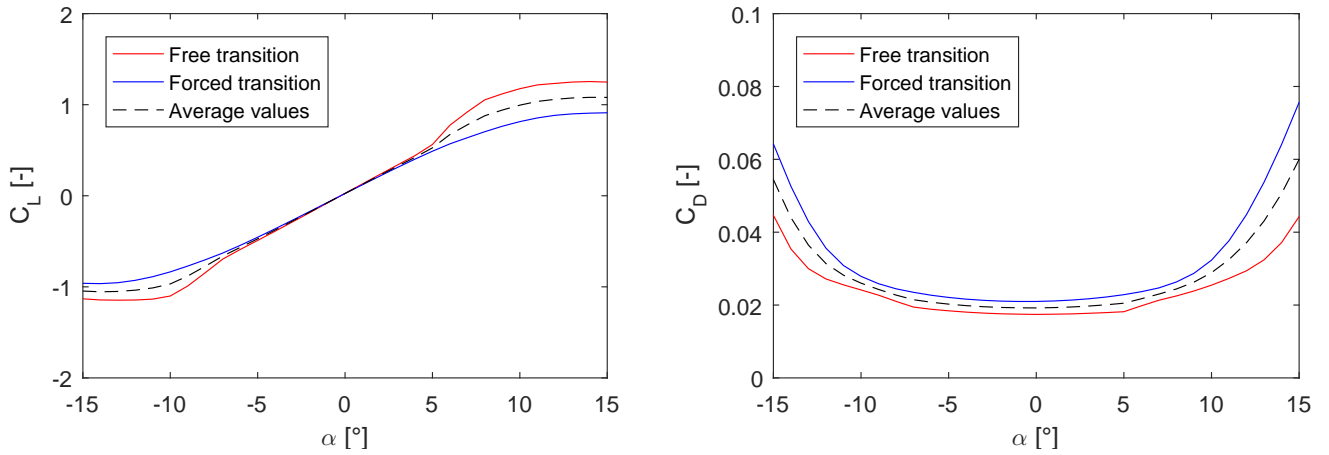


Figure 8.49: *OptB1*: B105 airfoil, comparison of the polars for free and forced transitions

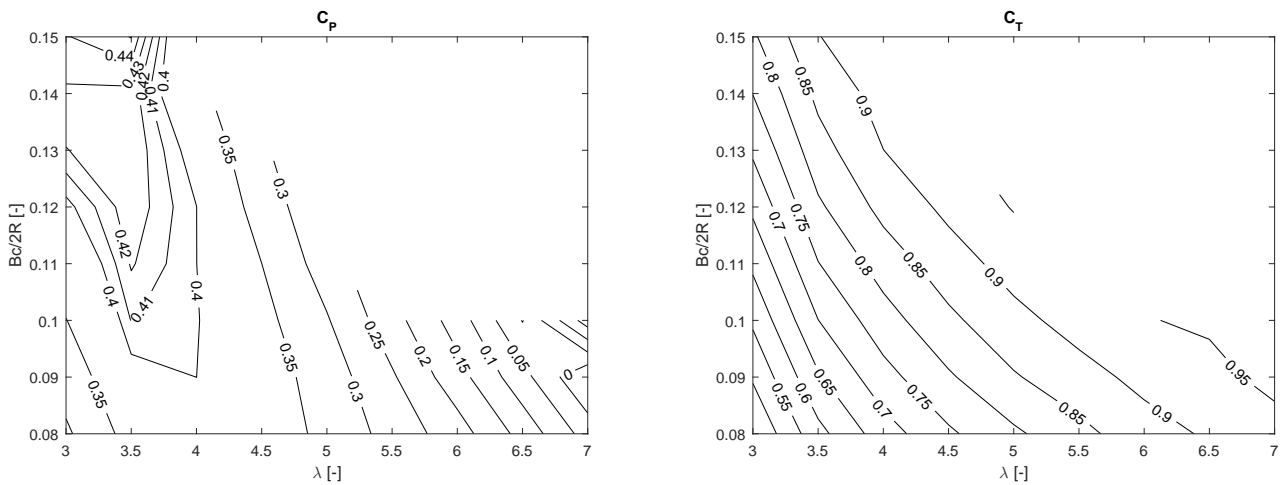


Figure 8.50: *OptB1*: B105 airfoil, power and thrust coefficients

**Airfoil B106:** the characteristics of the profile, belonging to the Pareto front, are presented below.

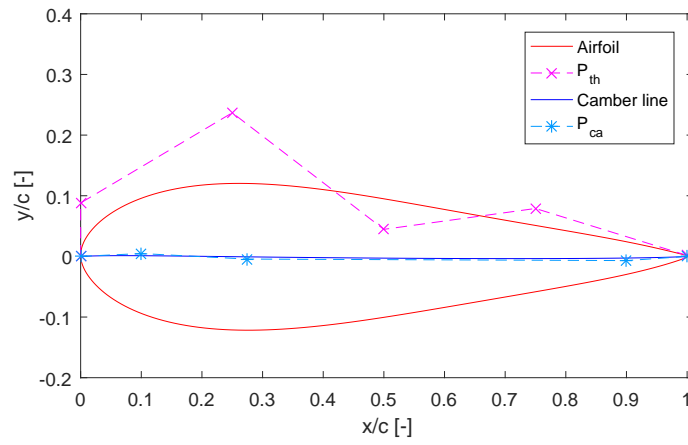


Figure 8.51: *OptB1*: B106 airfoil parametrization

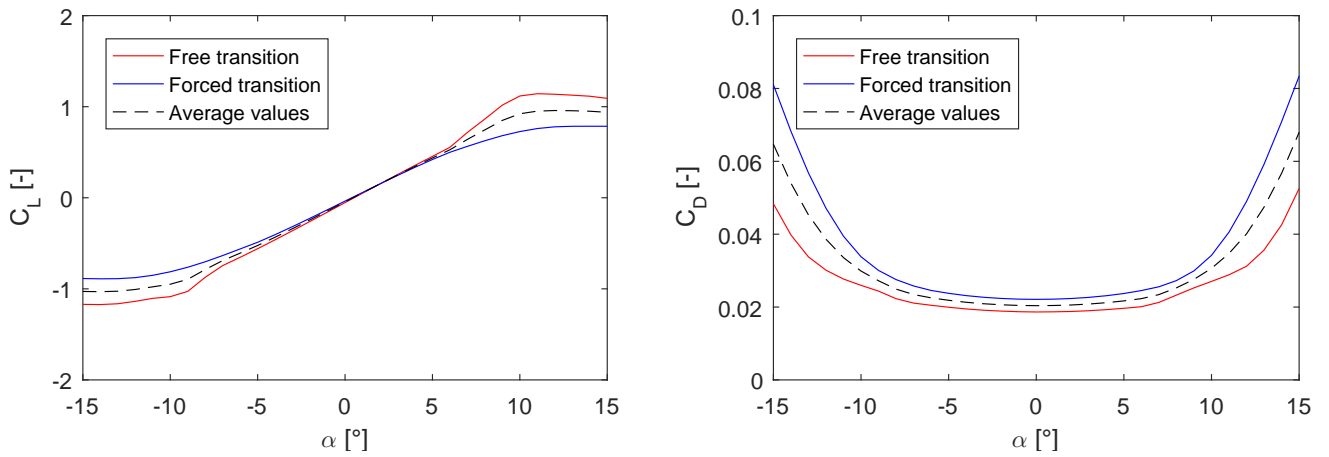


Figure 8.52: *OptB1*: B106 airfoil, comparison of the polars for free and forced transitions

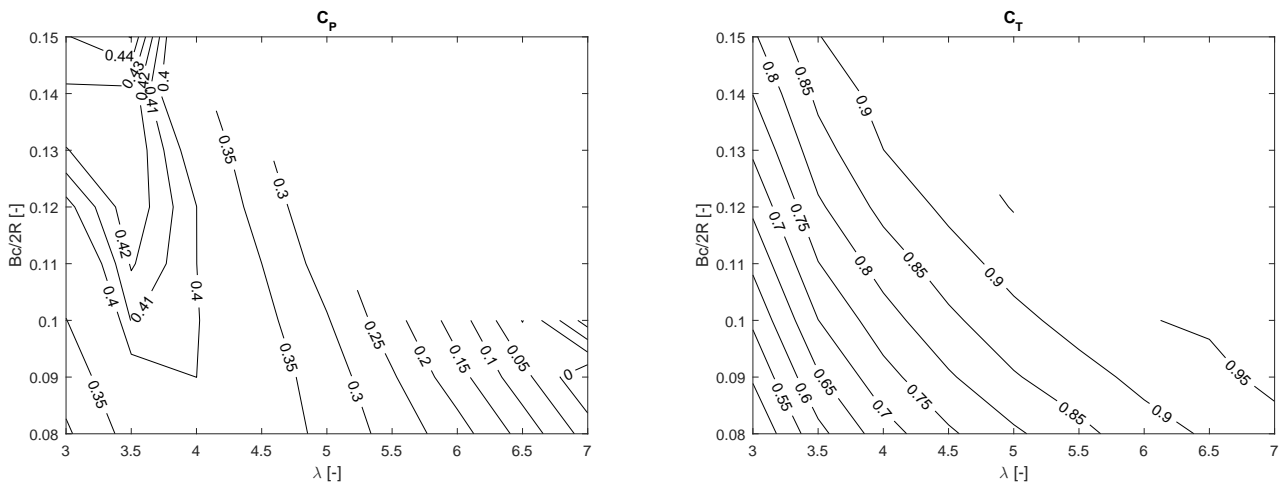


Figure 8.53: *OptB1*: B106 airfoil, power and thrust coefficients

### 8.13.2 OptB1 - Effects of the Angle of Pitch Variation

In the present section, the effects of the variation of the fixed angle of pitch  $\phi$ , for the airfoil B102 (Figure 8.39), is illustrated. From Figure 8.54 to Figure 8.58 the angle of pitch has been varied from  $\phi = -5^\circ$  to  $\phi = +5^\circ$ . The configuration with  $\phi = 0^\circ$  assumes the highest values of the power coefficient ( $C_P=0.5$ ) in the  $\lambda - \sigma$  space of solutions. The optimal performances value tends to be at  $\lambda = 3.5$  and  $\sigma = 0.12$  (Figure 8.56). A smooth low gradient of the  $C_P$  surface at the location of the optimum can also be observed; in the range of tip speed ratio  $3^\circ < \lambda < 4^\circ$ , the calculated value of  $C_P$  is still generally above 0.44.

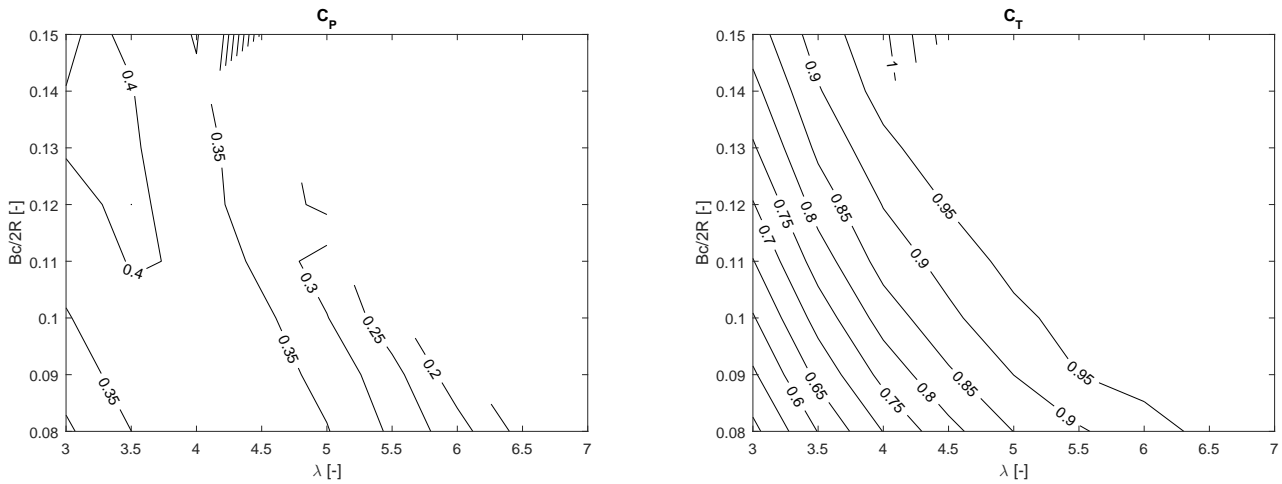


Figure 8.54: *OptB1*: B102 airfoil, power and thrust coefficients at  $-5.0^\circ$  fixed pitch

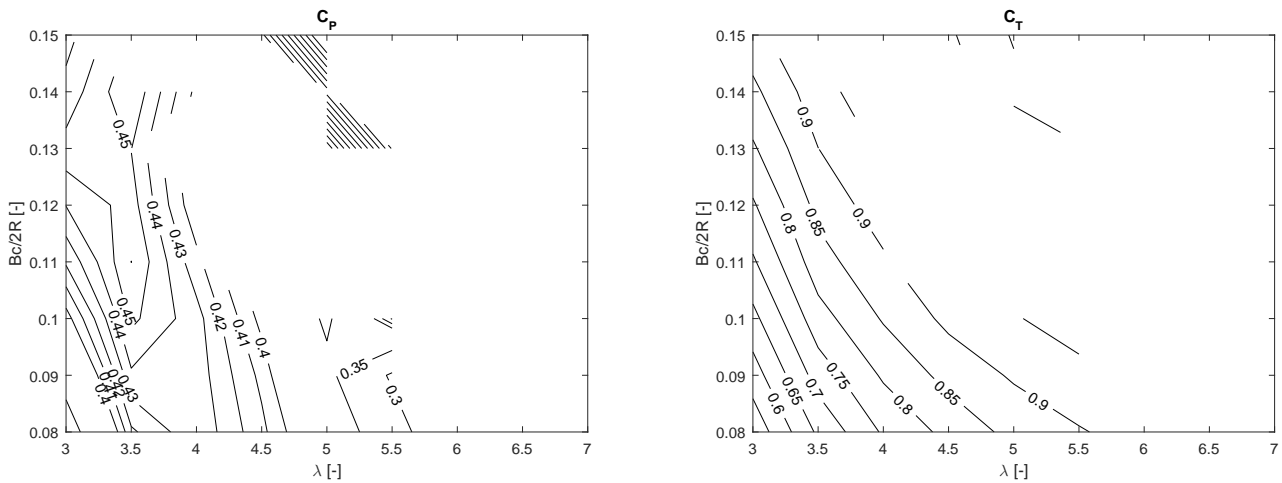


Figure 8.55: *OptB1*: B102 airfoil, power and thrust coefficients at  $-2.0^\circ$  fixed pitch

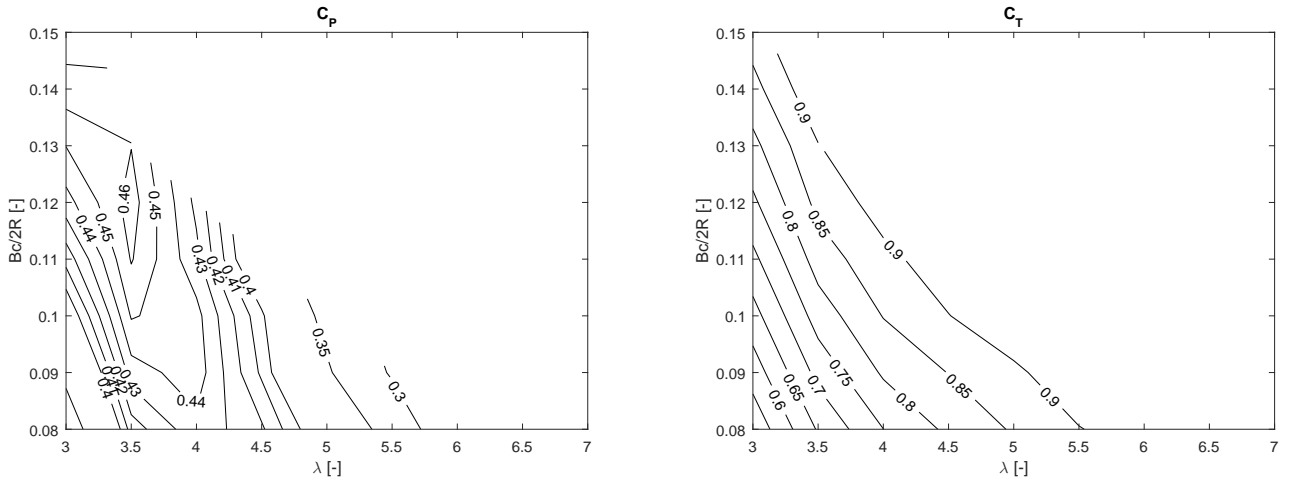


Figure 8.56: *OptB1*: B102 airfoil, power and thrust coefficients at  $0^\circ$  fixed pitch

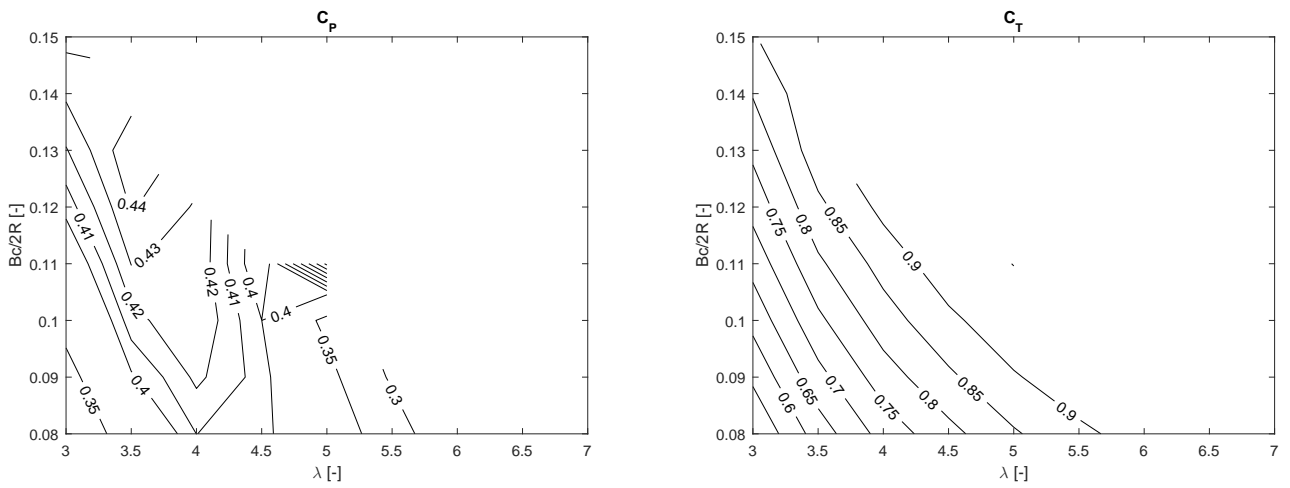


Figure 8.57: *OptB1*: B102 airfoil, power and thrust coefficients at  $+2.0^\circ$  fixed pitch

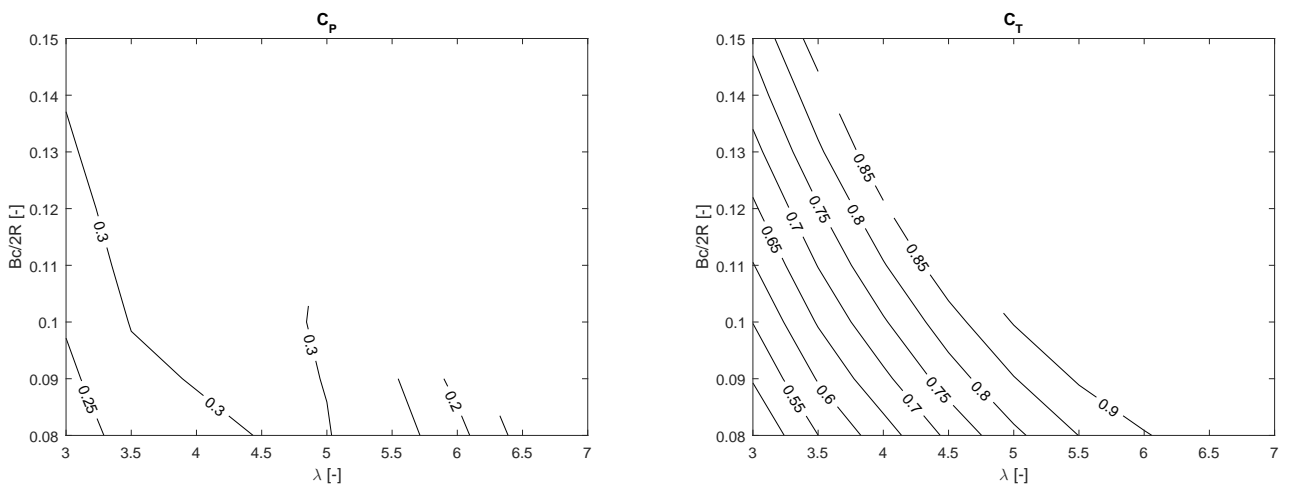


Figure 8.58: *OptB1*: B102 airfoil, power and thrust coefficients at  $+5.0^\circ$  fixed pitch

### 8.13.3 OptB1 - Pareto Front Analysis

The solutions belonging to the Pareto front (Figure 8.59) have been analysed with the P2DiWA panel code [102]. In Figure 8.60, the set of optimized individuals is plotted in the  $t_{max} - C_P$  space. For the analysis, the geometry parameters and the working conditions of the case study have been considered, as reported in Table 8.1.

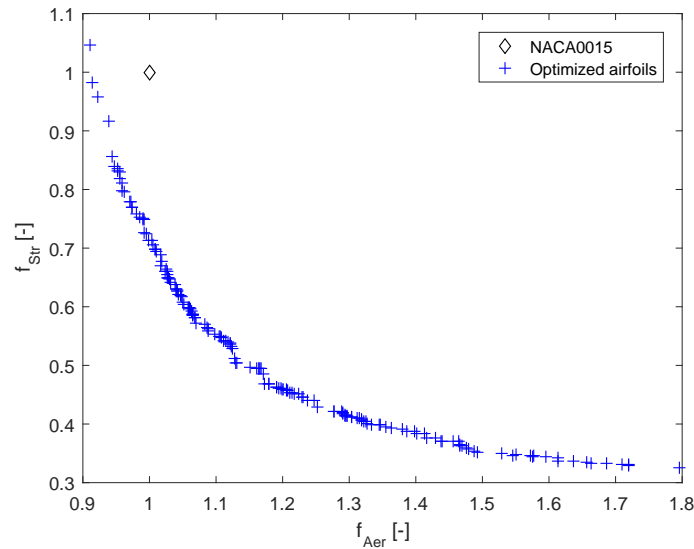


Figure 8.59: *Optimization B*: solutions belonging to the Pareto front

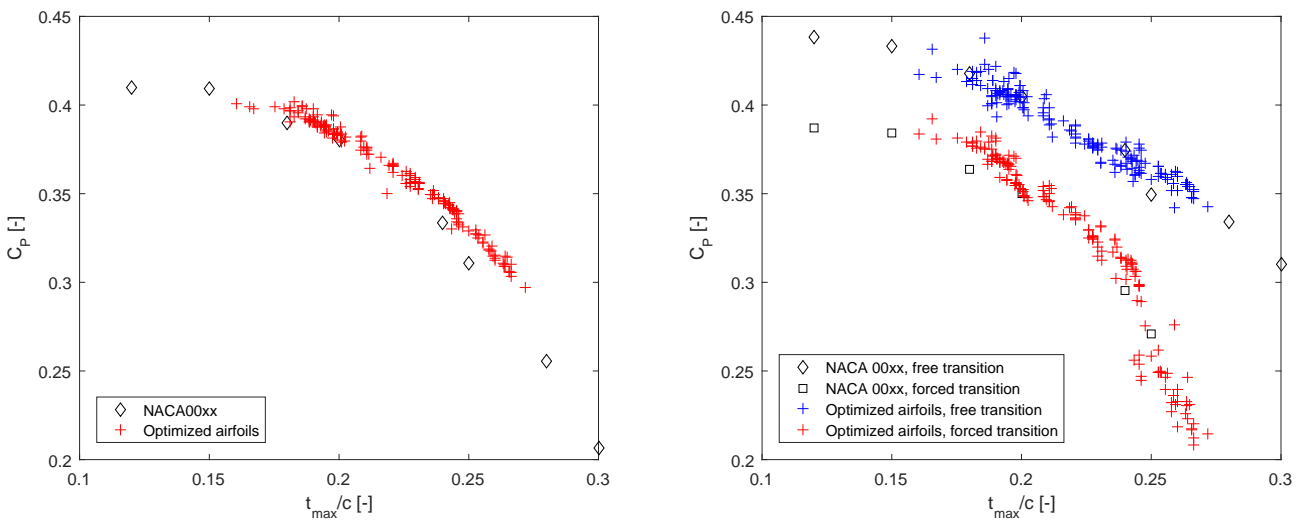
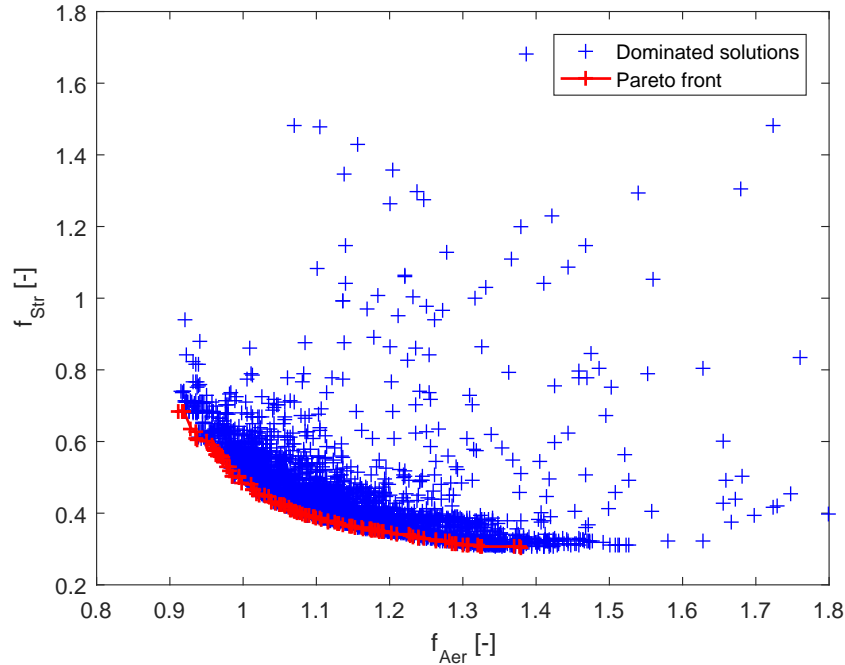


Figure 8.60: *Optimization B*: transposition of the considered solutions in the power coefficient - thickness space

As can be noticed, higher values of  $C_P$  are assumed by the profiles with low relative thickness  $t_{max}/c$  values. The power coefficient of the optimized profiles is also compared with several symmetric NACA four-digit series airfoils, as function of their relative thickness.

### 8.13.4 OptB2 - Results of the Free Transition Analysis

In a second analysis (*OptB2*), only the free transition condition is considered in the polars evaluation using XFOIL. Figure 8.61 shows the Pareto front of the proposed optimization.



**Figure 8.61:** Pareto front for the airfoil optimization in free transition conditions

Five points belonging to the Pareto front have been analysed with the PW2DiVA model, as reported in Table 8.15.

	Genes								Fitness		Max Thick	
<b>baseline</b>	0,500	0,000	0,000	0,000	0,066	0,114	0,063	0,048	1,00	1,00	15,0%	29,7%
<b>B201-FR</b>	0,412	0,009	-0,024	0,002	0,044	0,188	0,049	0,063	0,91	0,68	18,6%	30,9%
<b>B202-FR</b>	0,437	0,009	-0,024	-0,026	0,044	0,208	0,049	0,063	0,95	0,60	20,0%	29,7%
<b>B203-FR</b>	0,437	0,007	0,018	-0,026	0,044	0,222	0,073	0,063	1,00	0,49	22,2%	32,1%
<b>B204-FR</b>	0,437	0,020	0,018	-0,026	0,067	0,222	0,081	0,064	1,05	0,42	23,7%	30,1%
<b>B205-FR</b>	0,561	0,024	0,018	-0,055	0,097	0,222	0,093	0,063	1,15	0,36	25,7%	29,5%

**Table 8.15:** *OptB2*: considered individuals of the Pareto front

**Airfoil B201-FR:** the characteristics of the profile, belonging to the Pareto front, are presented below.

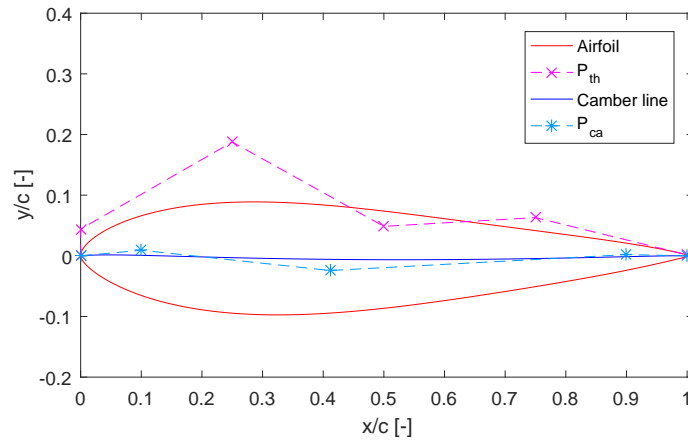


**Figure 8.62:** *OptB2*: B201-FR airfoil parametrization

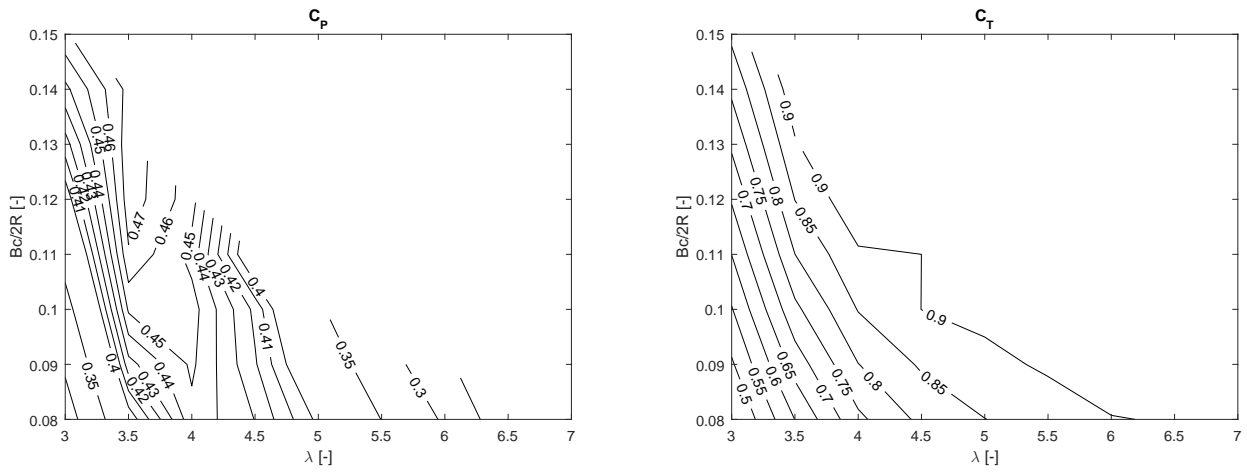


**Figure 8.63:** *OptB2*: B201-FR airfoil, power and thrust coefficients

**Airfoil B202-FR:** the characteristics of the profile, belonging to the Pareto front, are presented below.

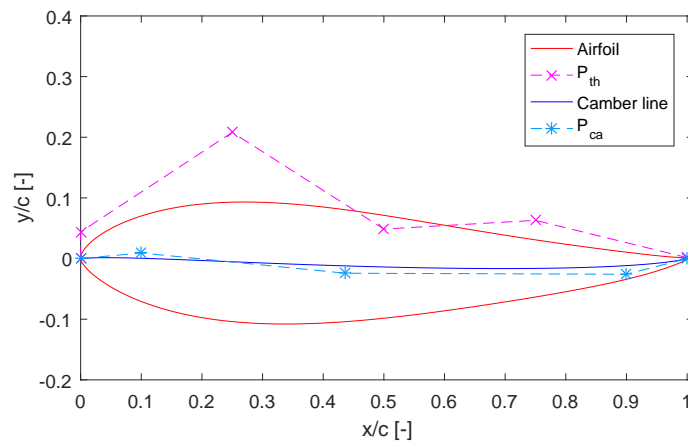


**Figure 8.64:** *OptB2*: B202-FR airfoil parametrization

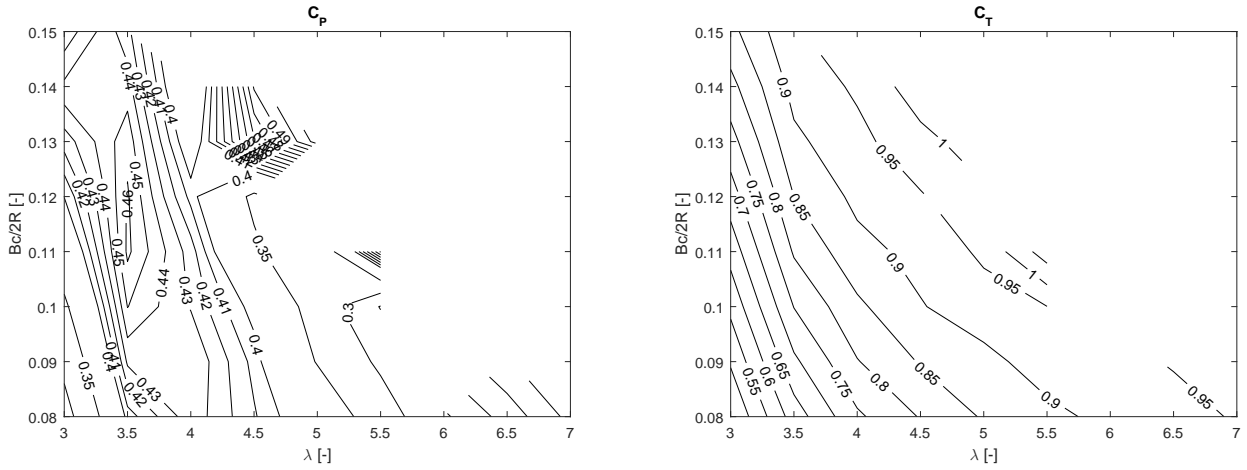


Figure 8.65: *OptB2*: B202-FR airfoil, power and thrust coefficients

**Airfoil B203-FR:** the characteristics of the profile, belonging to the Pareto front, are presented below.

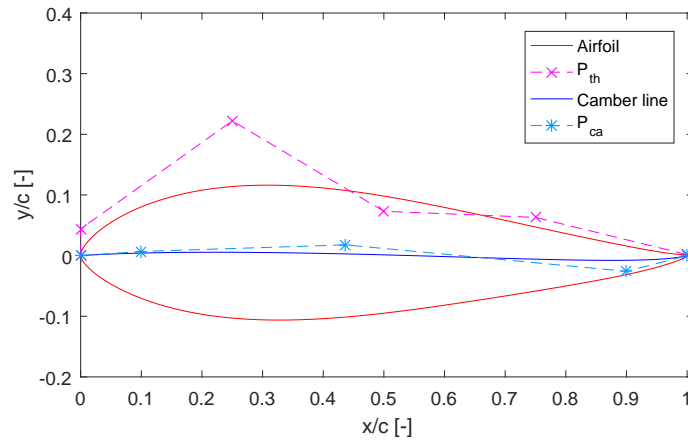


Figure 8.66: *OptB2*: B203-FR airfoil parametrization

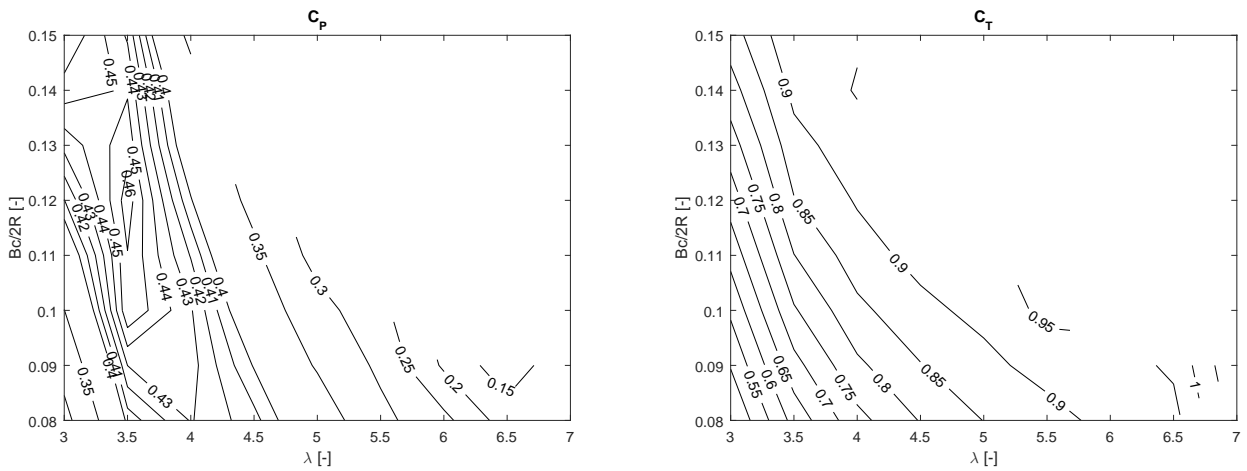


Figure 8.67: *OptB2*: B203-FR airfoil, power and thrust coefficients

**Airfoil B204-FR:** the characteristics of the profile, belonging to the Pareto front, are presented below.



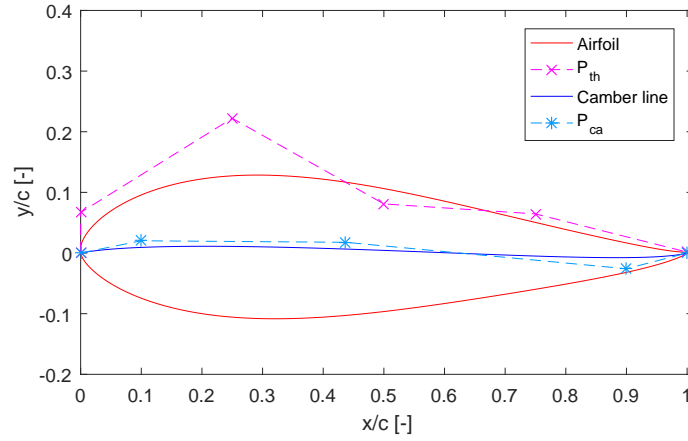


Figure 8.68: *OptB2*: B204-FR airfoil parametrization

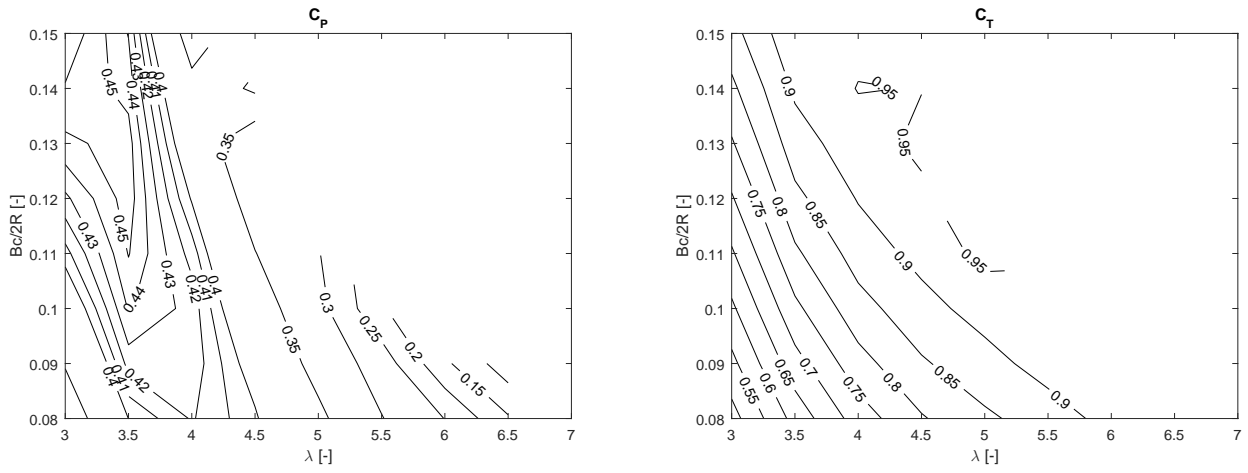


Figure 8.69: *OptB2*: B204-FR airfoil, power and thrust coefficients

**Airfoil B205-FR:** the characteristics of the profile, belonging to the Pareto front, are presented below.

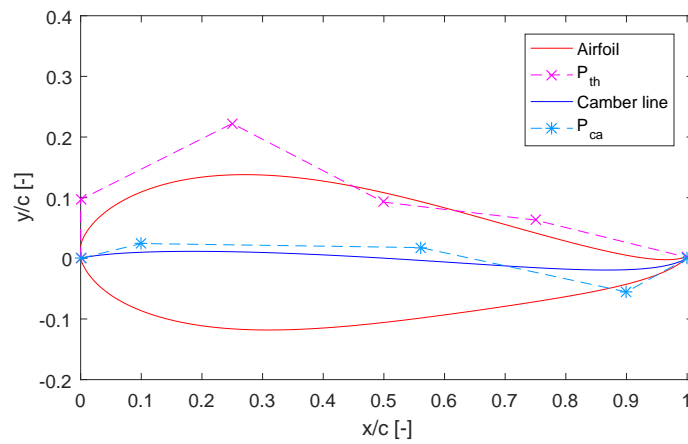


Figure 8.70: *OptB2*: B205-FR airfoil parametrization

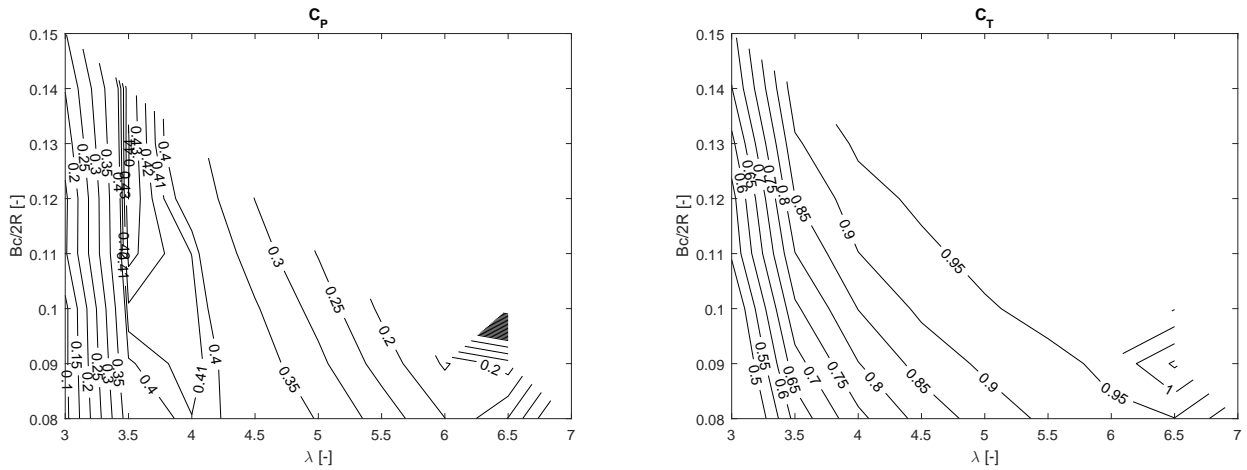


Figure 8.71: *OptB2*: B205-FR airfoil, power and thrust coefficients

### 8.13.5 OptB3 - Results of the Forced Transition Analysis

In the third analysis (*OptB3*), only the forced transition condition is considered in the polars evaluation using XFOIL. Figure 8.72 shows the Pareto front of the proposed optimization.

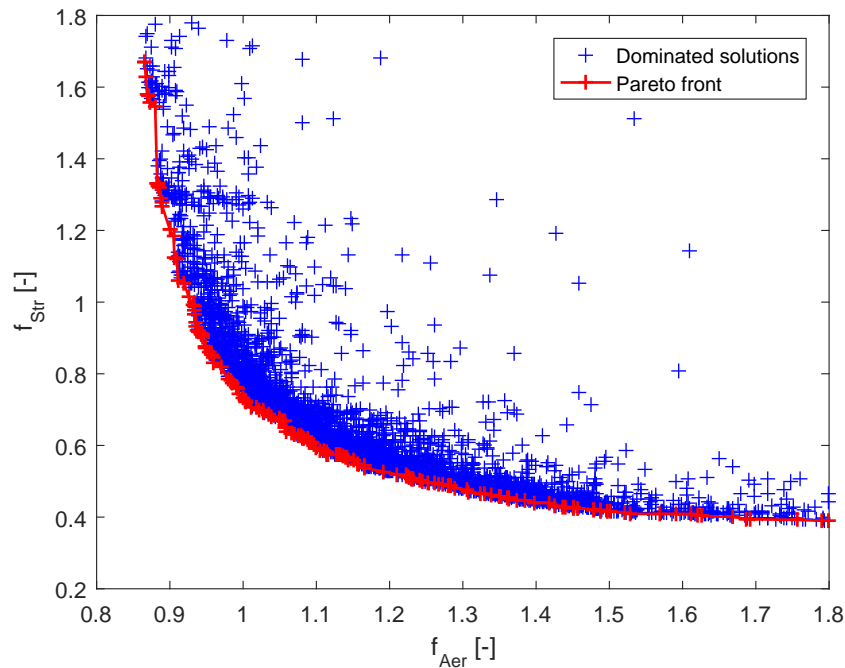


Figure 8.72: Pareto front for the airfoil optimization in forced transition conditions

Six points belonging to the Pareto front have been analysed with the PW2DiVA model, as reported in Table 8.16.

baseline	Genes								Fitness		Max Thick	
	0.500	0.000	0.000	0.000	0.066	0.114	0.063	0.048	1.00	1.00	15.0%	29.7%
<b>B301-FO</b>	0.513	0.024	-0.034	0.026	0.059	0.130	0.014	0.016	0.86	1.67	13.1%	22.8%
<b>B302-FO</b>	0.337	0.037	-0.034	0.026	0.080	0.130	0.037	0.017	0.90	1.18	15.3%	22.8%
<b>B303-FO</b>	0.386	0.037	-0.002	0.001	0.063	0.186	0.032	0.017	0.95	0.87	17.9%	25.0%
<b>B304-FO</b>	0.166	0.024	0.016	0.001	0.063	0.175	0.074	0.013	1.00	0.73	19.0%	28.5%
<b>B305-FO</b>	0.160	0.024	0.029	0.001	0.063	0.201	0.058	0.016	1.05	0.67	20.1%	27.3%
<b>B306-FO</b>	0.198	0.029	0.008	0.001	0.110	0.175	0.074	0.029	1.16	0.55	21.7%	25.0%

Table 8.16: *OptB3*: considered individuals of the Pareto front

Airfoil B301-FO: the characteristics of the profile, belonging to the Pareto front, are presented below.

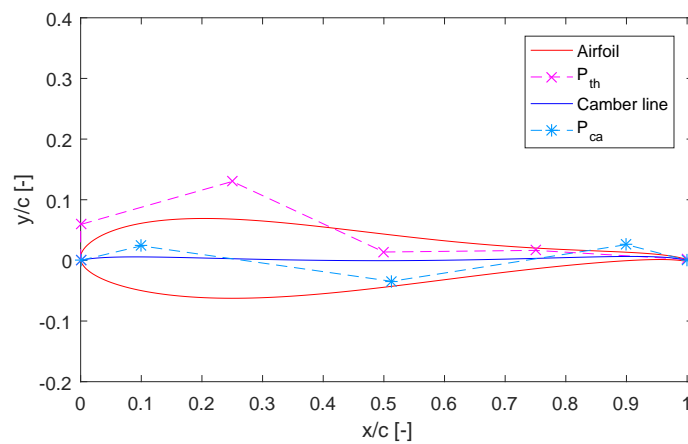


Figure 8.73: *OptB3*: B301-FO airfoil parametrization

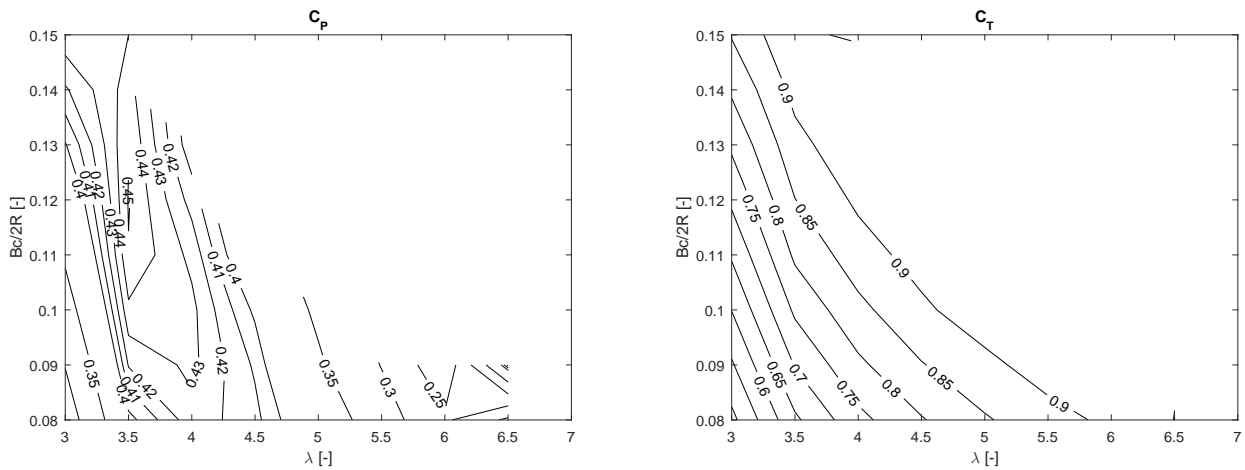
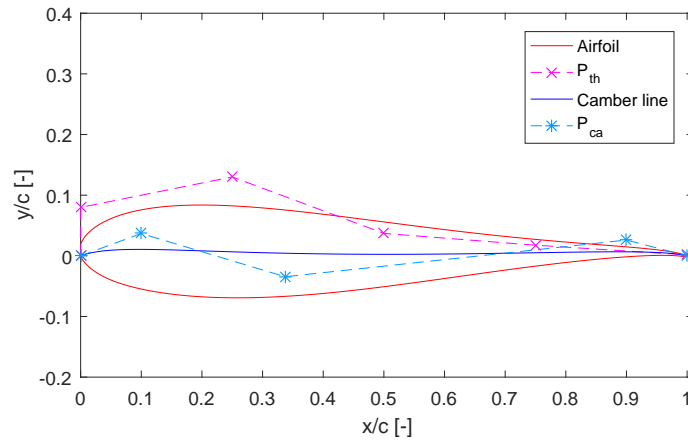
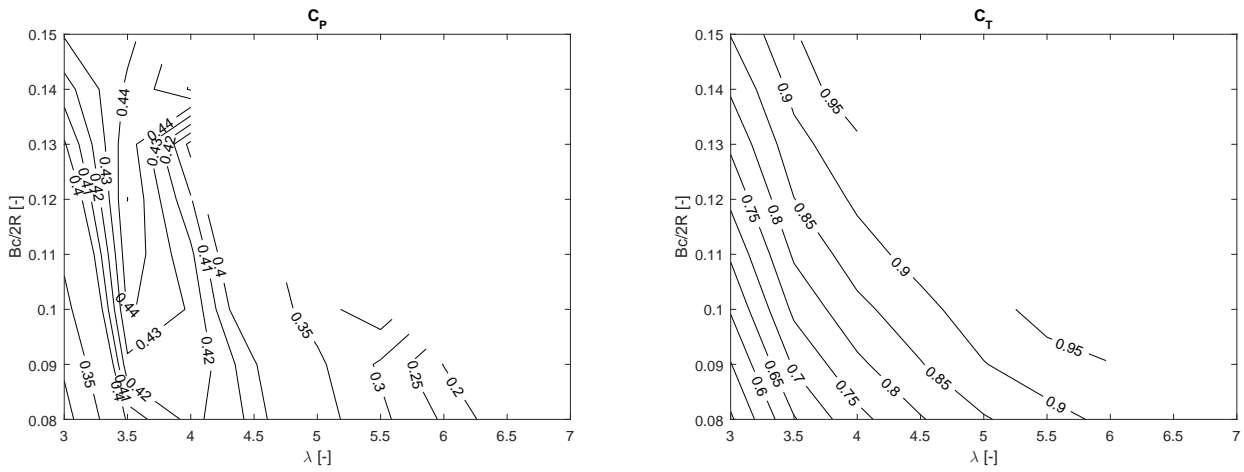


Figure 8.74: *OptB3*: B301-FO airfoil, power and thrust coefficients

**Airfoil B302-FO:** the characteristics of the profile, belonging to the Pareto front, are presented below.



**Figure 8.75:** *OptB3*: B302-FO airfoil parametrization



**Figure 8.76:** *OptB3*: B302-FO airfoil, power and thrust coefficients

**Airfoil B303-FO:** the characteristics of the profile, belonging to the Pareto front, are presented below.

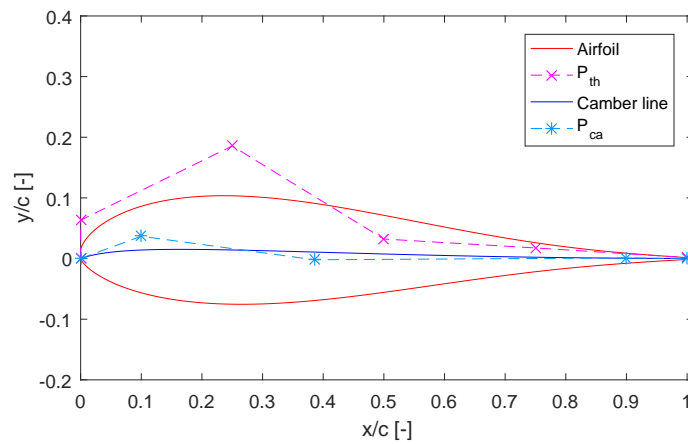


**Figure 8.77:** *OptB3*: B303-FO airfoil parametrization

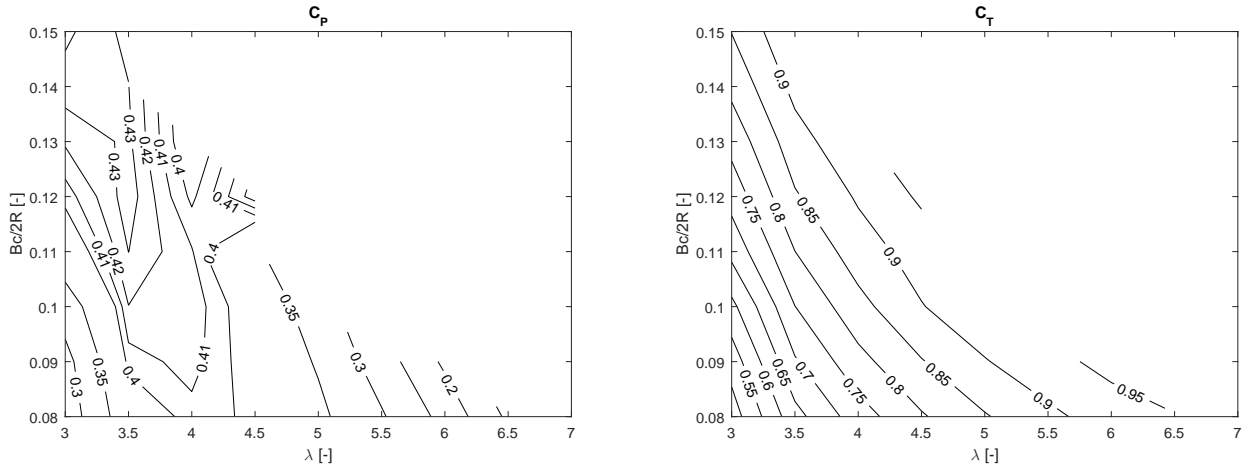


Figure 8.78: *OptB3*: B303-FO airfoil, power and thrust coefficients

**Airfoil B304-FO:** the characteristics of the profile, belonging to the Pareto front, are presented below.

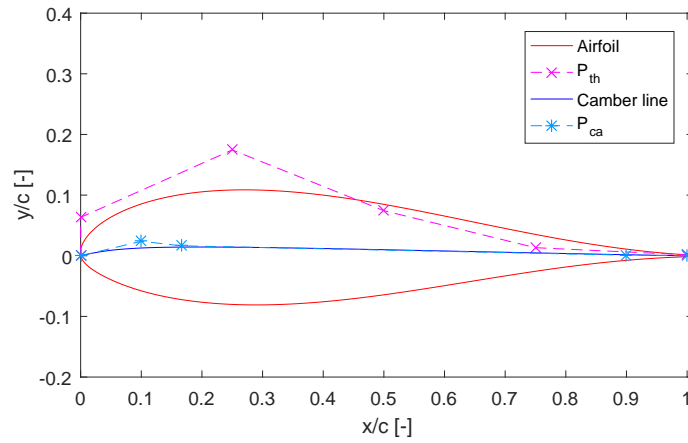


Figure 8.79: *OptB3*: B304-FO airfoil parametrization

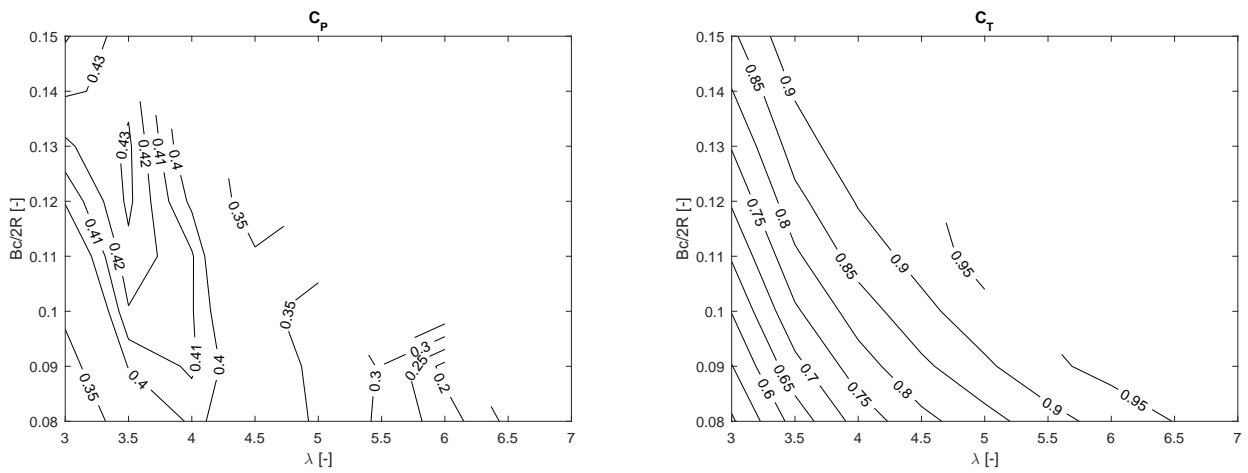
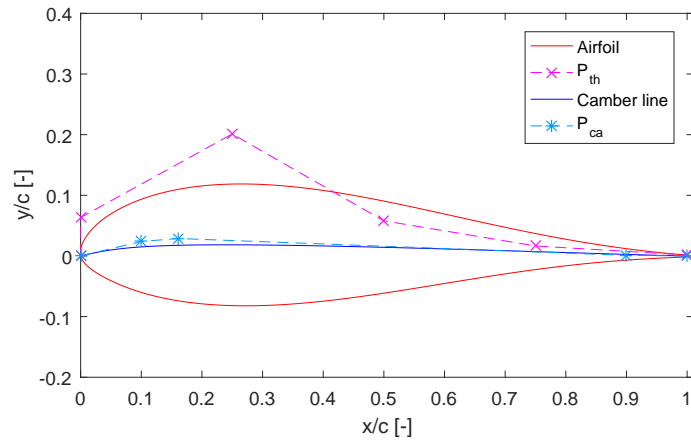
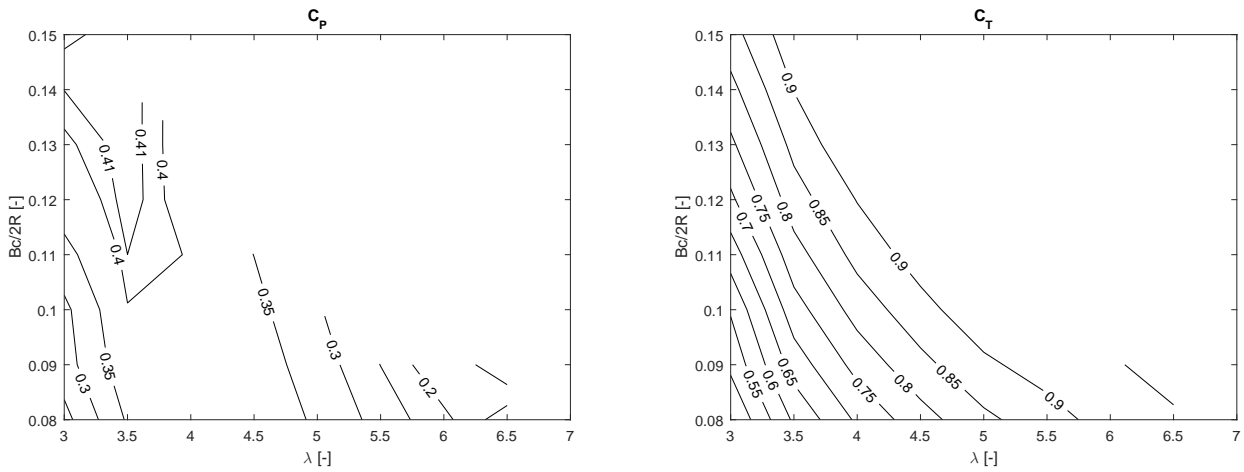


Figure 8.80: *OptB3*: B304-FO airfoil, power and thrust coefficients

**Airfoil B305-FO:** the characteristics of the profile, belonging to the Pareto front, are presented below.



**Figure 8.81:** *OptB3*: B305-FO airfoil parametrization



**Figure 8.82:** *OptB3*: B305-FO airfoil, power and thrust coefficients

**Airfoil B306-FO:** the characteristics of the profile, belonging to the Pareto front, are presented below.

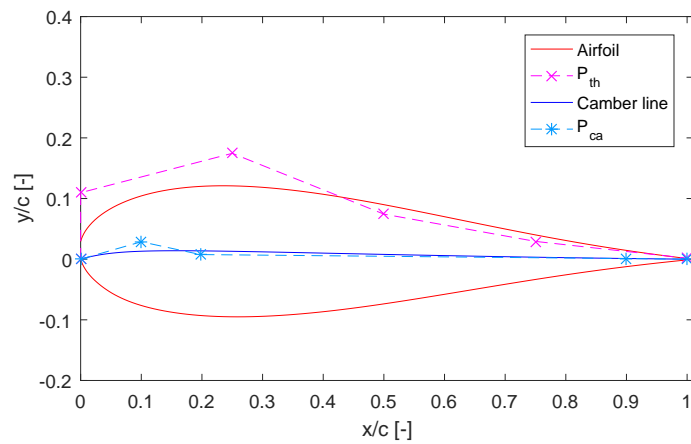


**Figure 8.83:** *OptB3*: B306-FO airfoil parametrization

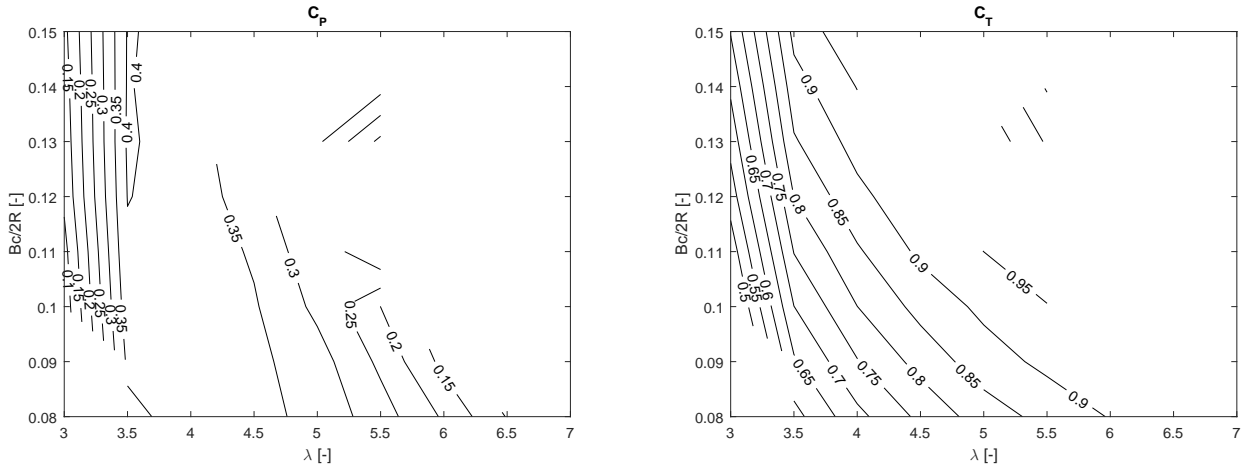


Figure 8.84: *OptB3*: B306-FO airfoil, power and thrust coefficients

## 8.14 Discussion of Optimization B Results

The aim of *Optimization B* is to maximize the aerodynamic (ratio between  $\overline{C_{L\alpha}}$  and  $\overline{C_D}$ ) and structural ( $EI_{xx}$ ) functions for a VAWT airfoil and chose, in a post-processing phase, the best working conditions in terms of tip speed ratio ( $\lambda$ ) and solidity ( $\sigma$ ) for the optimized profile. The considered case study is reported in Table 8.1.

The optimization process allowed to identify a set of solutions belonging to the Pareto front, as shown in Figure 8.32. Solution *B101* presents the best aerodynamic efficiency, calculated as the ratio between  $\overline{C_{L\alpha}}$  and  $\overline{C_D}$  for the studied configuration. The value has been increased by 9.46% compared to the *NACA0015* airfoil; on the other hand, the structural performance, in terms of  $f_{Str}$  function, results to be decreased of the 10.75%. Solution *B105* belongs to the opposite side of the Pareto front and is the best for the structural aspects of the analysis: the bending stiffness of the profile has been highly increased of the 50.45%, however the aerodynamic performance has worsened of the 15.96%. The improved airfoils in both the optimization aspects can be found between the extreme cases. Solution *B102* represents a profile suitable for the analysed wind turbine: the identified shape allows to increase the aero-dynamical performances of 4.84% and the structural properties of 16.49%. Finally *B103* has an aerodynamic function similar to the baseline *NACA0015* (-0.41%), however the structural properties have been highly increased of 28.7%.

Overall, the airfoils resulting from the optimization are not symmetric and the optimal performance values tend to be assumed for a tip speed ratio  $\lambda = 3.5$ . The optimal design point (highest value of  $C_P$ ) for *NACA0015* is found when the solidity is 0.13 ( $C_P=0.4570$ ). However, in the optimized airfoils with highest aerodynamic (*B101* and *B102*) the peak value of the power coefficient ( $C_P=0.4646$  in *B101*) is higher than *NACA0015* and is found at  $\sigma = 0.12$ . All the optimized airfoils present a smooth

low gradient of  $C_P$  at the location of the optimum. Furthermore, for the tip speed ratio in the range  $3 < \lambda < 4$ , the value of  $C_P$  is generally above 3.5.

Airfoil *B102* has also been chosen for an analysis regarding the effects of the variation of the pitch angle  $\varphi$  on the  $C_P$  and  $C_T$  distributions: as can be observed from Figure 8.54 to Figure 8.58, the configuration with  $\varphi = 0^\circ$  presents the widest area with high values of power production in the  $\sigma$ - $\lambda$  space.

A further analysis consisted in transposing the solutions, belonging to the Pareto fronts, to the  $C_P$ - $t_{max}/c$  space; it is possible to notice the linear proportionality between the power coefficient and the relative thickness of the considered profiles (Figure 8.60). The optimized profiles, belonging to the Pareto front, generally over-perform the symmetric airfoil of NACA four-series airfoils, in terms of  $C_P$ .

Finally, in order to understand the effects of the transition in the analysis, two further optimizations take into account only the free and force transition conditions respectively. From those analysis is possible to observe how considering the free transition condition only, in the calculation of the polars, leads to the determination of a set of solution that mainly improves the structural properties of the profiles (Figure 8.61); the best aerodynamic profiles are thicker than the NACA0015 baseline airfoil. On the other hand, the analysis in the force transition conditions identify the best profiles for aerodynamic as thin profiles (Figure 8.72).





## Chapter 9

# An Automatic Numerical Analysis of a VAWT

An automatic procedure to generate and simulate a 2D CFD model of a VAWT is presented in the current Chapter. The automated numerical analysis tool is integrated in the optimization environment described in Chapter 8. The model has been validated with PIV experiments conducted in the Open Jet Facility (OJF) of TU Delft [103].

### 9.1 Case Study

The considered test case for the validation of the numerical model is represented by a 2-blade H-type Vertical Axis Wind Turbine. The profiles of the blade are NACA0018 with a chord of 0.06 m; the turbine has a radius of 0.50 m and the blades are 1.00 m long. The wind turbine characteristics are summarized in Table 9.1.

<b>Airfoil</b>	<b><math>N_B</math></b>	<b><math>\sigma</math></b>	<b>R</b>	<b>c</b>	<b>L</b>	<b><math>\phi</math></b>
NACA0018	2	0.12	0.50 m	0.06 m	1.00 m	0°

**Table 9.1:** Case study considered in the analysis

Two analysis have been carried at different Tip Speed Ratios (2.0 and 4.5). Table 9.2 summarizes the operating condition for the two experimental analysis.

	<b><math>V_\infty</math></b>	<b><math>\lambda</math></b>	<b>Re</b>
<b>Test 1</b>	9.1 m/s	4.5	163300
<b>Test 2</b>	10.2 m/s	2	83063

**Table 9.2:** Operating conditions considered for the CFD analysis

## 9.2 Geometry Generation and Meshing Procedure

The numerical tool, integrated in the VAWT optimizer, allows to automatically generate the geometry and the mesh for the computational analysis and, to further run an unsteady analysis in OpenFOAM. The required input files are the *points.dat* (generated by the optimization tool and containing the coordinates of the airfoil points), the *geometry.dat* and the *mesh.dat*.

In *geometry.dat* the coordinates of the bounding box, radius of the rotor zone and extension of the structural mesh (in terms of radius and azimuth angle  $\theta$ ) are described. A python script converts the geometrical inputs into the geometry structure showed from Figure 9.1 to Figure 9.3. The script uses OCC libraries to generate the geometry and Salome tool as graphical interface.

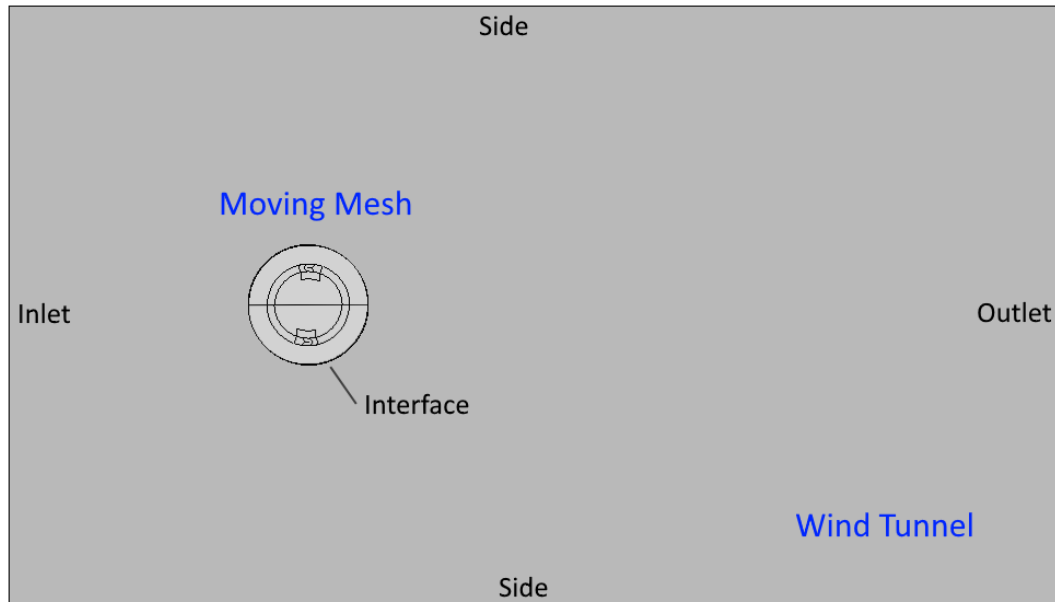


**Figure 9.1:** Domain of the computational analysis

The algorithm for the generation of the geometry includes the following operations:

- Import the airfoil points and create a polyLine;
- Split the airfoil polyLine into 4 edges;
- Create the vertices;
- Create the edges, arcs and wires;
- Create the faces;
- Generate the shell (from union of faces);
- Get the sub-shapes of the shell (edges and faces) and generate the groups-in-father entities.

Once the geometry creation process is completed, the mesh module is loaded by the script. The most important *open source* meshing methods are available in the module and they can be applied to edges, faces, shells and volumes created by the geometry module.

The different faces of the geometry represent different zones to which is possible to assign distinct meshing algorithms. The *Netgen 1D-2D* algorithm is applied, as general mesh, for edges and faces: it requires to specify the minimum and maximum size of elements, the grow-factor and the element shape preference (triangular or quadrangular). The mapped meshes have the priority on the general mesh and they are specified as *Sub-Meshes on Faces* in the structured zones of the mesh. The adopted algorithm is the *Quadrangle (Mapping)* and it requests to specify the desired element transition, if the number of the nodes in the opposite edges is not equal.

Finally, the edge nodes distribution is read from *mesh.dat* input file, where the *M-parameters* (illustrated in Figures 9.2 and 9.3) are specified. For the main edges of the mesh, a couple of values set the number of elements and the desired distribution (equidistant, scaled or with table density specification) of the *Wire Discretization* algorithm. A boundary layer is also applied to the compound of edges that represents the blade surface.

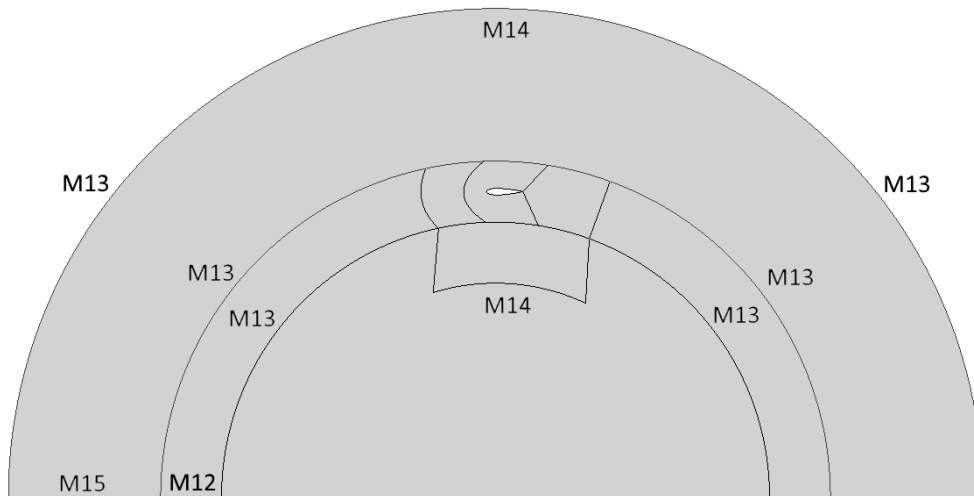


**Figure 9.2:** Domain of the rotating mesh zone (*Rotor*)

After the creation of half-rotor mesh, the second half is generated by operations of copy and rotate and, then, the two meshes are merged together. The wind tunnel mesh is also generated with similar operations. Since OpenFOAM, the used numerical CFD tool, deals only with 3D geometries, a 1-cell extrusion of the mesh, in the orthogonal direction, is required. Finally, the appropriate patches (illustrated in Figure 9.1) are also assigned and the meshes exported in UNV format.

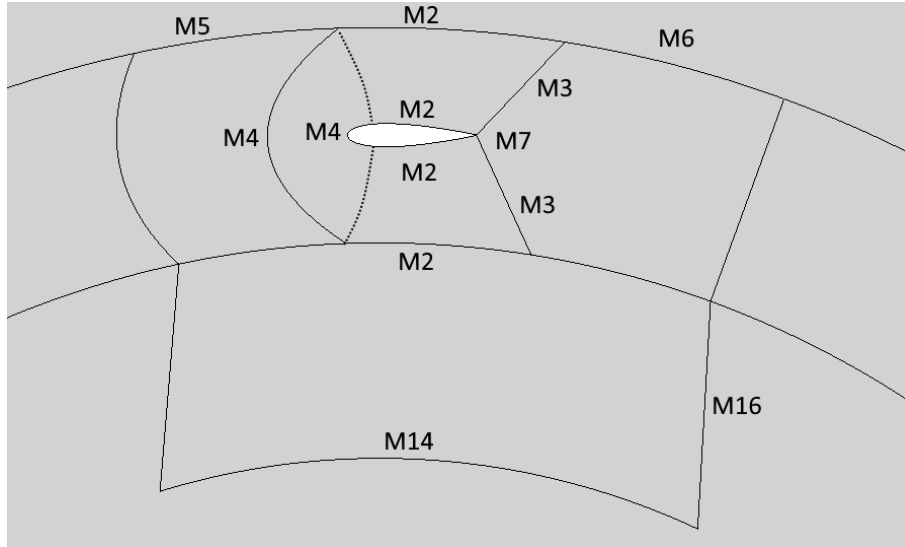


**Figure 9.3:** Detail of the structured mesh adopted around the airfoil

To summarize, the operation carried in the meshing module are:

- Import geometry and groups;
- Apply a general mesh to the shell face;
- Specify the mapped quadrangular mesh to faces;
- Specify edge nodes distribution;
- Specify the boundary layer parameters;
- Compute the rotor mesh;
- Copy and rotate the rotor mesh;
- Merge the 2-half rotor meshes using tolerance;
- Compute the wind tunnel mesh;
- Extrude the meshes;
- Specify the numerical patches;
- Export separately '*Rotor*' and '*WindTunnel*' meshes in UNV format.

Figure 9.4 illustrates some details of the generated mesh.

### 9.3 Setting of the CFD Numerical Model

The boundary conditions of the numerical analysis are illustrated in Table 9.3. A *Fixed velocity* value is imposed at the inlet, the relative pressure at the outlet and the side surface are computed as symmetry

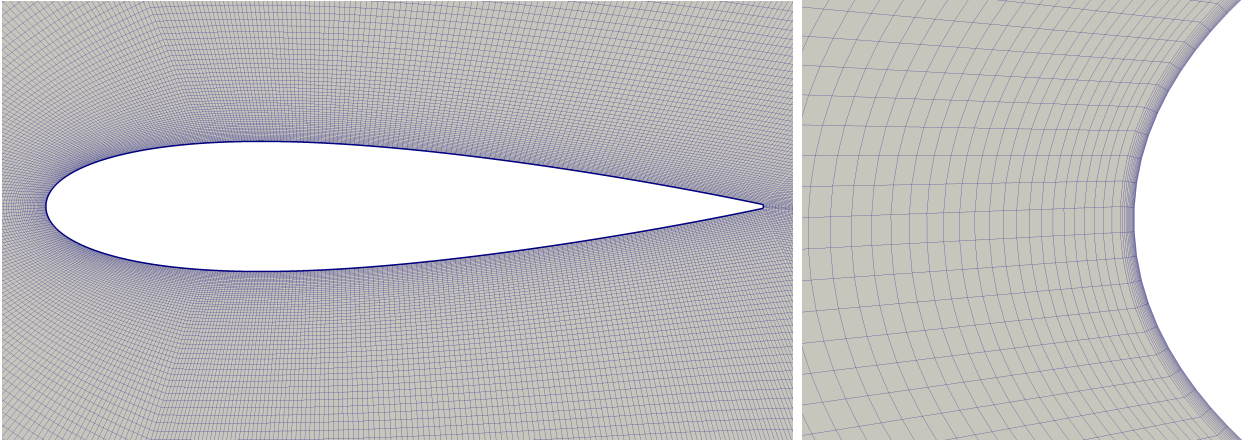


**Figure 9.4:** Details of the structured mesh

planes. Since the model is 2-Dimensional, the top and bottom surfaces of the bounding box are assigned as empty patches to avoid the fluxes in the orthogonal direction. The  $k\omega - SST$  has been adopted as turbulence model: the first cell height of the boundary layer has been fixed in order to calculate the values of the parameters in the viscous sublayer (and obtain a  $y^+$  value lower than 1 in the blade surface). The unsteady solver *pimpleDyMFoam* has been used in the analysis. The time step has been fixed in order to archive a *Courant Number* value close to 1. The main setting of the analysis are presented in Table 9.4.

Variable	Inlet	Outlet	Wall
$U$	FixedValue	zeroGradient	movingWallVelocity
$p$	zeroGradient	fixedValue	zeroGradient
$k$	fixedValue	inletOutlet	kqRWallFunction
$\omega$	fixedValue	inletOutlet	omegaWallFunction

**Table 9.3:** Setup of boundary conditions for the 2D CFD VAWT analysis

<b>Solver</b>	pimpleDyMFoam
<b>timeStep</b>	equivalent to $0.01^\circ$
<b>p solver</b>	GAMG
<b>U solver</b>	smothSolver
<b>nCorrectors</b>	2
<b>NonOrthogonalCorrectors</b>	1
<b>RelaxationFactors</b>	1

**Table 9.4:** Numerical setting of the 2D CFD VAWT analysis

The adopted solution strategy subdivides the simulation in three different phases. The fluid field is first initialized with the *potentialFoam* solver (12 iterations). Later, a simulation with first-order numerical schemes runs on a coarse mesh for 2 rotational period of the turbine ( $\theta = 720^\circ$ ). Finally

a simulation with second-order numerical schemes runs for further 8 rotations (until  $\theta = 3600^\circ$  is reached). Table 9.5 illustrates the numerical schemes adopted for the simulation.

<b>FirstOrder</b>	
<b>Gradient</b>	default: Gauss Linear k, $\omega$ : cellLimited Gauss linear 1
<b>Divergence</b>	default Gauss upwind div((nuEff*dev2(T(grad(U)))) Gauss linear
<b>Laplacian</b>	default Gauss linear limited 0.5 laplacian(DomegaEff,omega) Gauss linear limited 0.33
<b>Interpolation</b>	default linear
<b>SecondOrder</b>	
<b>Gradient</b>	default: Gauss Linear k, $\omega$ : cellLimited Gauss linear 1 U,p: cellMDLimited leastSquares 1
<b>Divergence</b>	default Gauss upwind div(phi,U),Gauss linearUpwindV grad(U) div((nuEff*dev2(T(grad(U)))) Gauss linear
<b>Laplacian</b>	default Gauss linear limited 0.5 laplacian(DomegaEff,omega) Gauss linear limited 0.33
<b>Interpolation</b>	default linear

**Table 9.5:** Numerical schemes adopted in the CFD analysis

## 9.4 The CFD Module

The meshing module generates the computational grids for the numerical analysis and exports them in the general UNV format [109]. The unsteady computational analysis is run with OpenFOAM and automatically prepared by a shell script through specific commands, as illustrated in Table 9.6.

First of all, the analysis folders are prepared and the meshes converted from the UNV to the OpenFOAM format (generation of the polyMesh folder with *ideasToFoam* command). The two meshes are merged into an unique mesh, consisting of two cell zones, using the *mergeMesh* command. The *checkMesh* instruction controls the quality of the mesh in terms of aspect ratio, skewness and non-orthogonality. A preliminary analysis, with first-order schemes, is run on a coarse mesh and, then, the solution is mapped as initial solution of the finest mesh (command *mapFields*). Finally, the second-order scheme analysis is run in parallel computing mode.

```

#!/bin/sh
echo "Salome_Mesh_Generator ..... "
salome AirFoil_MeshGenerator.py

echo "OpenFoam_Folder_Cleaning ..... "
rm -r OF_Rotor OF_WindTunnel
rm log.*
cp -r OF_VAWT OF_Rotor
cp -r OF_VAWT OF_WindTunnel

echo "OpenFoam_Folder_Preparation ..... "
cp mesh/AirFoil_Rotor.unv OF_Rotor/.
cp mesh/AirFoil_WindTunnel.unv OF_WindTunnel/.

echo "OpenFoam_Meshing_Conversion ..... "
cd OF_Rotor/
ideasUnvToFoam AirFoil_Rotor.unv >log.IdeasUnvToFoam
checkMesh >log.checkMesh
cd ../OF_WindTunnel/
ideasUnvToFoam AirFoil_WindTunnel.unv >log.ideasUnvToFoam
checkMesh >log.checkMesh
cd ..

echo "OpenFoam_Merge_Meshes ..... "
mergeMeshes -overwrite OF_Rotor/ OF_WindTunnel/ >log.mergeMe
cd OF_Rotor/
checkMesh >log.checkMesh_merged

echo "OpenFoam_Create_Patches ..... "
createPatch -overwrite >log.createPatch

echo "OpenFoam_Renumber_Mesh ..... "
renumberMesh -overwrite >log.renumberMesh

echo "OpenFoam_MapField ..... "
mapFields ../AirFoil_coarse_sol/ -latestTime -consistent \
>log.mapFields

echo "OpenFoam_Decomposition ..... "
decomposePar >log.decomposePar

echo "OpenFoam_Solver ..... "
mpirun -np 16 pimpleDyMFoam -parallel > log.pimpleDyMFoam&
pyFoamPlotWatcher.py log.pimpleDyMFoam

```

**Table 9.6:** Shell script to setup and run the CFD analysis



## 9.5 Discussion of the Numerical Analysis Results

The convergence criteria used to stop the simulation is based to the average torque value over a rotation; the simulation is considered converged when the changes between two consecutive rotational period are lower than the 1%. The results of the numerical analysis are compared with the experimental data reported in [103]. A first comparison concerns the trend of the radial and tangential forces on the blade over a rotation. In the presented figures, the forces are non-dimensionalised by  $(\frac{1}{2}\rho V_\infty^2 R)$ . Two reference frames have been used: the traversing system reference frame origins at the most upwind position at the rotor ( $\theta = 0^\circ$ ), the turbine reference frame lies in the centre of the turbine. The velocity field in proximity of the blades, resulting from the 2D CFD analysis, is also compared with the acquired velocity field of the PIV analysis. In the velocity field figures, the coordinates are non-dimensionalised with the radius  $R$  and the velocities are non-dimensionalised with the free stream velocity  $V_\infty$ .

### 9.5.1 Results for Tip Speed Ratio 4.5

The comparison of the radial forces trend (Figure 9.5) shows how the CFD model better fits the experimental results in the upwind zone while, in the downwind region, the DMST model follows quite nicely the wind tunnel data. Regarding the tangential forces, the DMST model seems to be closer to the experimental results in the upwind region (Figure 9.6), on the other hand, in downwind region, the CFD model is slightly more accurate. From the velocity plots is possible to observe how the turbine slows down the stream extracting energy from the flow. The results of the numerical analysis show a flow field similar to the experimental PIV analysis, as shown in Figures 9.7 and 9.8.

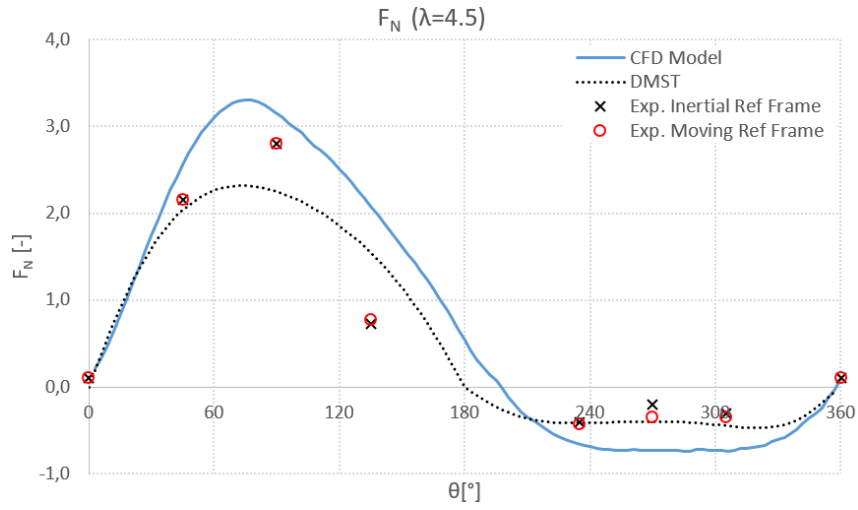


**Figure 9.5:** Comparison between normal forces calculated from CFD analysis, DMST model and experimental results for  $\lambda = 4.5$

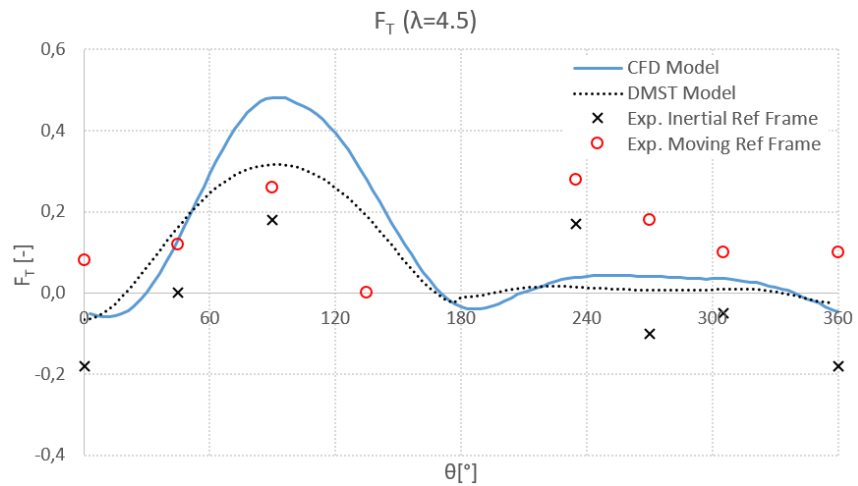


**Figure 9.6:** Comparison between tangential forces calculated from CFD analysis, DMST model and experimental results for  $\lambda = 4.5$

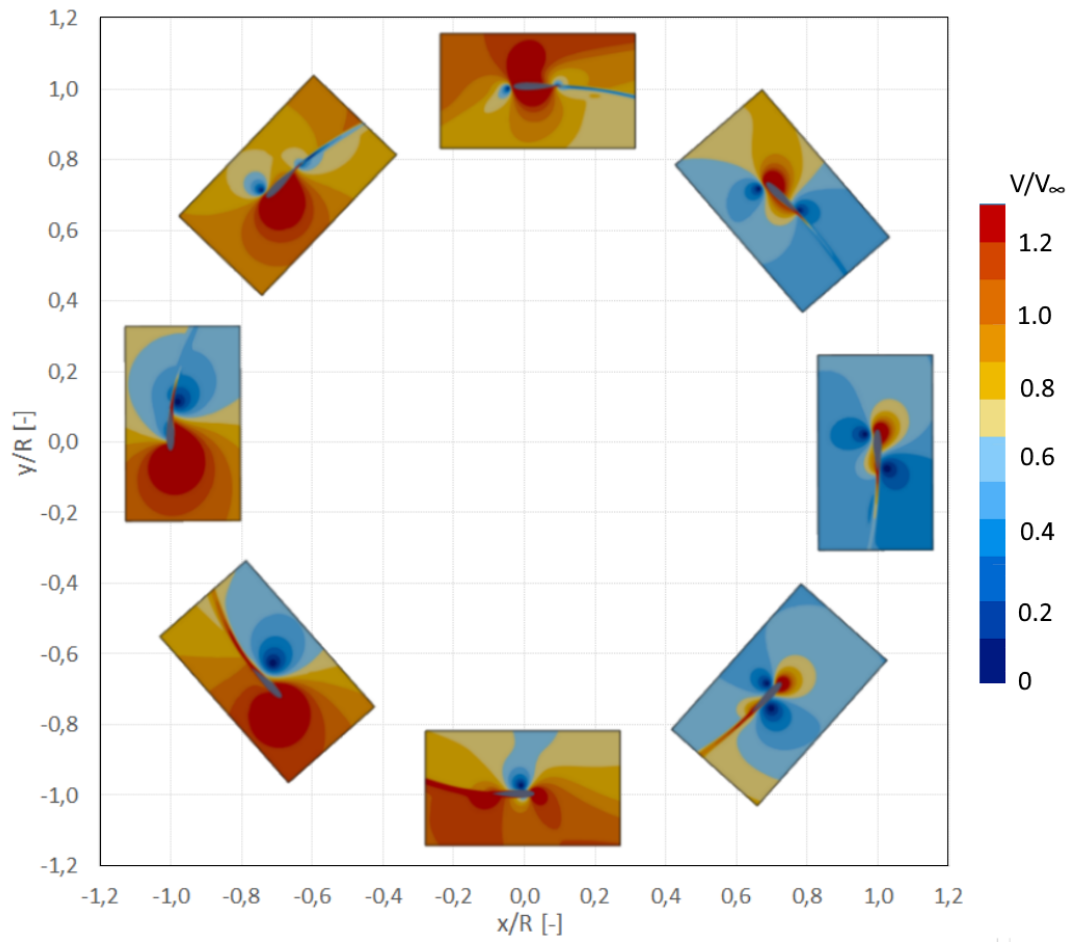


**Figure 9.7:** Numerical velocity field, calculated with OpenFOAM, for  $\lambda = 4.5$

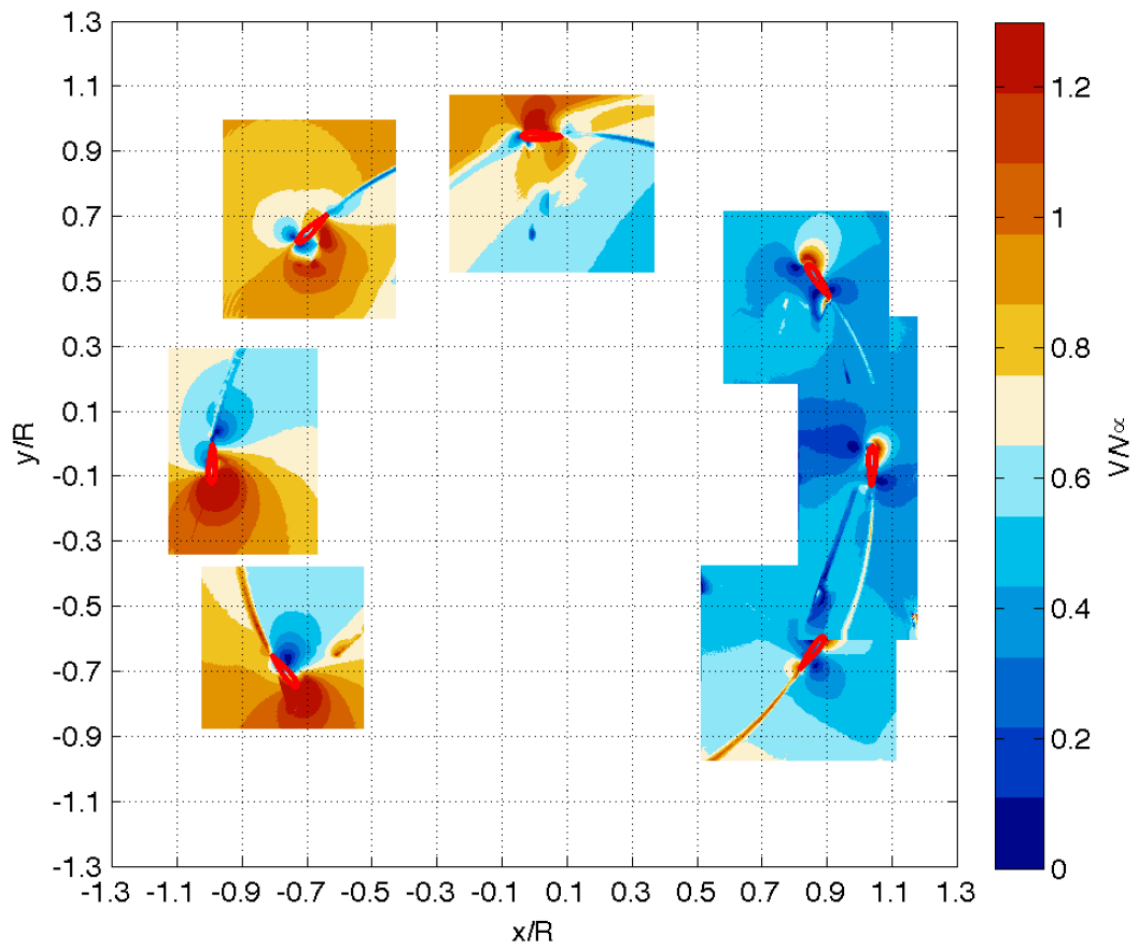
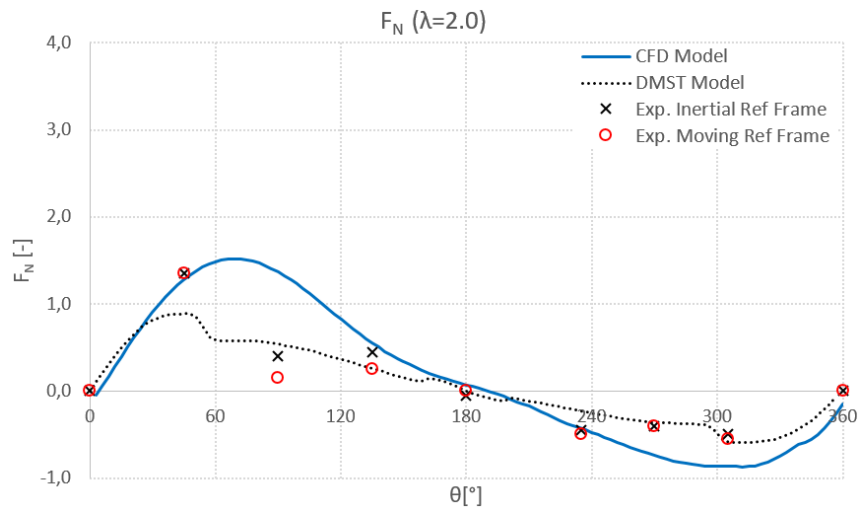


Figure 9.8: Velocity field resulting from the PIV analysis for  $\lambda = 4.5$ , [103] p. 60

### 9.5.2 Results for Tip Speed Ratio 2.0

In the analysis for a tip speed ratio condition of 2.0, the comparison of the radial forces trend (Figure 9.9 ) shows a good accordance for both the CFD and the DMST models to the experimental results during the most part of the rotation. However, in the first region of the upwind zone, the CFD model seems to be more accurate. The tangential forces are better calculated by the DMST model in the downwind zone and in the last part of the upwind region (Figure 9.11). The velocities field, resulting from the CFD analysis, is in a good accordance with the measured field also for the  $\lambda$  of 2.0, as shown in Figures 9.10 and 9.12.



**Figure 9.9:** Comparison between normal forces calculated from CFD analysis, DMST model and experimental results for  $\lambda = 2.0$

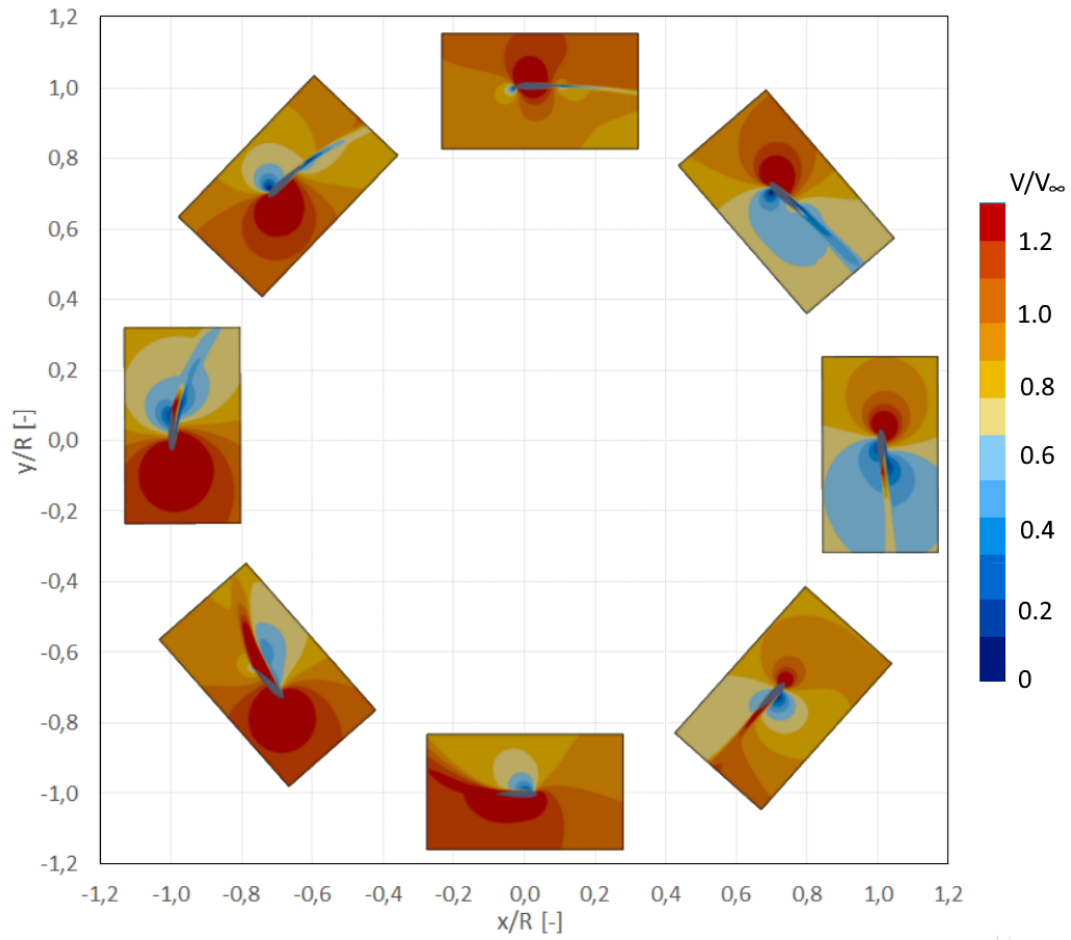


**Figure 9.10:** Numerical velocity field, calculated with OpenFOAM, for  $\lambda = 2.0$

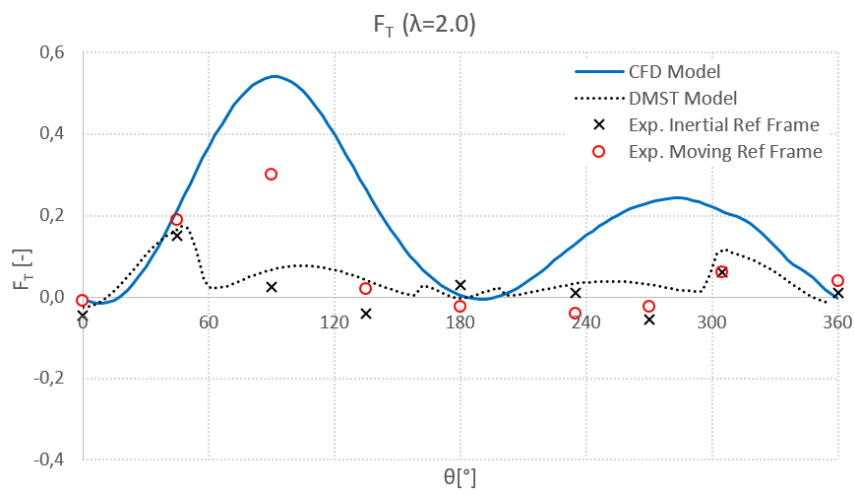


**Figure 9.11:** Comparison between tangential forces calculated from CFD analysis, DMST model and experimental results for  $\lambda = 2.0$

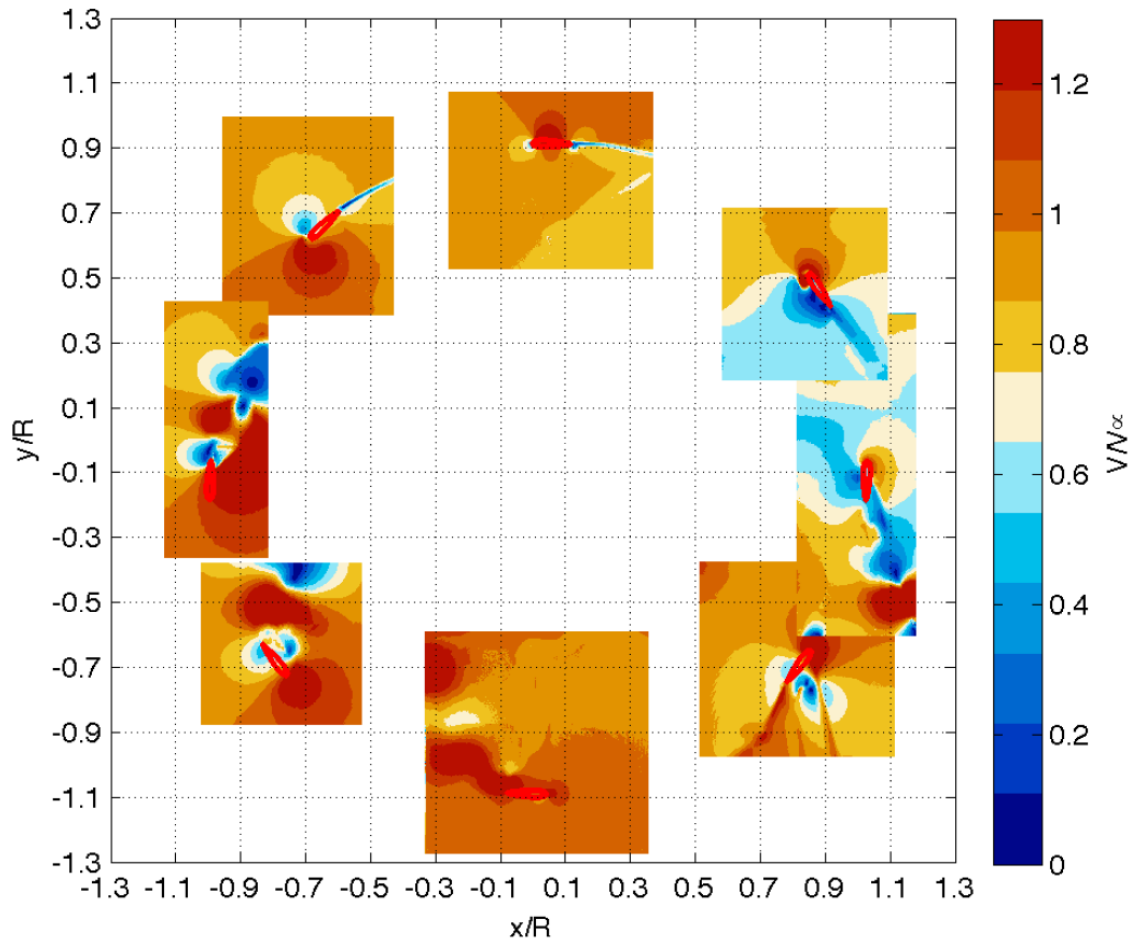


Figure 9.12: Velocity field resulting from the PIV analysis for  $\lambda = 2.0$ , [103] p. 61

# Conclusion

An open source optimization environment has been developed in order to compute the performances of the Vertical Axes Wind Turbines. The proposed environment couples the genetic algorithm MOGA of DAKOTA optimization tool, developed by Sandia, with several engineering tools for the aerodynamic and structural analysis. The aerodynamic analysis are performed with in-house functions based on the polar estimated with XFOIL panel code while some other in-house functions calculate the structural properties of the airfoils. The optimization environment allows to chose among 4 different Bezier parametrization techniques to reconstruct the aerodynamic profiles.

Two different optimization approach have been considered for the same objective functions; in *Optimization A* the shape of the airfoil is optimized for a fixed VAWT geometry and working conditions, in *Optimization B* the most suitable working condition, in terms of tip speed ratio ( $\lambda$ ) and solidity ( $\sigma$ ), is chosen in a post-processing phase. For both of the analysis the results are presented as a Pareto front set of individuals, where the most suitable solutions can be selected.

The considered aerodynamic function, to be maximized, is represented by the ratio between the lift coefficient slope and the averaged drag coefficient over a rotation ( $\overline{\frac{C_{L\alpha}}{C_D}}$ ). The bending stiffness property ( $EI_{xx}$ ) represents the structural function to be even maximized. The selected airfoil *B102*, resulting from *Optimization B* approach, presents improvements in both aero-dynamical performances (+9.46%) and the structural properties (+10.75%). This is also reflected in an higher value of the power coefficient ( $C_P=0.465$ ) compared to the maximum value of the NACA0015 airfoil ( $C_P=0.457$ ) assumed in a different design point of lower solidity.

The open source CFD tools OpenFOAM has also been integrated in the proposed optimization environment, in order to automatically setup a 2-Dimensional CFD analysis of the desired airfoil. The file containing the point coordinates of the airfoil is used first, to create the rotor and wind tunnel geometries and, later, to generate a predominantly structured mesh of the considered domain. Finally, an unsteady CFD analysis is set and run using the specified boundary conditions. The CFD model has been validated against the experimental results conducted on a 2 blade VAWT in TU Delft Facility.



The results show a good accuracy in the description of the velocity field, however, some discrepancies are found in the trend of the forces, probably due to the uncertainty related to the experimental measurements.

Further developments could consider different fitness functions, taking into account the inclusion of several materials properties for the structural analysis, and more complex aerodynamic fitness functions. In particular an aerodynamic objective function that considers the maximization of the power coefficient  $C_P$  in the desired design point should be implemented. The cost of energy calculation, related to the adopted materials, could also be implemented in the optimization environment. Regarding the CFD module, a more accurate estimation of the blade aerodynamic performances could be obtained by testing different type of meshes and numerical schemes. Finally, in order to better estimates the structural performances of the wind turbine blades, a FEM module (*Code\_Aster*) could be integrated in the optimization loop.

## Nomenclature Part III

$A_i$ [ $m^2$ ]	Area of the i-segment
$c$ [ $m$ ]	Chord length
$C_D$ [-]	Drag coefficient
$\overline{C_D}$ [-]	weighted average of the drag coefficient distribution over a rotation
$C_L$ [-]	Lift coefficient
$C_{L\alpha}$ [-]	Slope of $C_L$ - $\alpha$ curve
$\overline{C_{L\alpha}}$ [-]	Weighted average of the lift slope of the $C_L - \alpha$ curve distribution over a rotation
$C_P$ [-]	Power coefficient
$C_T$ [-]	Thrust coefficient
$E$ [ $Pa$ ]	Elastic modulus
$EI_{xx}$ [ $Nm^2$ ]	Bending stiffness
$f_1$ [-]	Aerodynamic function
$f_{1,0}$ [-]	Aerodynamic function for the baseline blade
$f_2$ [-]	Structural function
$f_{2,0}$ [-]	Structural function for the baseline blade
$f_{Aer}$ [-]	Aerodynamic function to be minimized
$f_{Str}$ [-]	Structural function to be minimized
$F_N$ [-]	Non-dimensionalized radial force
$F_T$ [-]	Non-dimensionalized tangential force
$I_{xx}$ [ $m^3$ ]	Moment of inertia relative to the x-axis
$k$ [ $m^{-1}$ ]	Curvature of the blade
$L$ [ $m$ ]	Length of the blade
$M$ [ $Nm$ ]	Bending moment
$n$ [-]	Number of time a value of $\alpha$ occurs
$N$ [-]	Number of samples
$N_B$ [-]	Number of blades
$N_P$ [-]	Number of cores in the parallel computing
$p_{a,1}$ [-]	First penalty coefficient for the aerodynamic function
$p_{a,2}$ [-]	Second penalty coefficient for the aerodynamic function
$p_{s,1}$ [-]	Penalty coefficient for the structural function
$R$ [ $m$ ]	Turbine radius

$Re$ [–]	Reynolds number
$t$ [ <i>min</i> ]	Computational time
$t_{max}$ [ <i>m</i> ]	Maximum thickness
$V_{\infty}$ [ <i>m/s</i> ]	Unperturbed wind velocity
$W$ [–]	Weight proportional to the occurrence frequency of an angle of attack range
$\alpha$ [°]	Angle of attack
$\alpha_{min}$ [°]	Minimum angle of attack encountered during a rotation
$\alpha_{max}$ [°]	Maximum angle of attack encountered during a rotation
$\alpha_{range}$ [°]	Range of angle of attack
$\lambda$ [–]	Tip Speed Ratio
$\sigma$ [–]	Solidity of the wind turbine
$\phi$ [°]	Blade pitch angle
$\rho$ [ <i>kg/m</i> <sup>3</sup> ]	Fluid density
$\theta$ [°]	Azimuth angle

# Conclusion and Future Work

The thesis presents sequentially the different analysis that, step by step, allowed the definition of the modules of the open source environment for the optimization of wind turbines. The evolutive algorithms have been chosen as optimization methods because of the characteristics of the analysed problems that potentially involve several local minima; furthermore, the evaluation of the considered functions (aerodynamic, structural, cost) is not expensive in terms of time.

A first analysis (Part I) concerned the comparison between commercial and open source fluid-dynamic codes. The topic is represented by the evaluation of the aerodynamic performances of a tiltrotor in wind tunnel conditions: the results revealed a similar behaviour of the codes in predicting the performances in terms of lift, drag and moment coefficients, field of velocity and vorticity. The accuracy of the open source analysis has been demonstrated by the comparison of the results with the wind tunnel experimental data.

In Part II, several models have been coupled in order to set the optimization of an Horizontal Axis Wind Turbine design. In the proposed analysis, a BEM code has been developed and included in the overall analysis in order to estimate the aerodynamic performances of the wind turbine. Inside the optimization environment it is possible to set all the main geometrical characteristics, the internal structure of the blade and the working conditions as parameters to be optimized. The objectives of the optimization are multi-disciplinary and include functions of the aerodynamic, structural and economical fields. The first proposed optimization coupled the BEM code with a FEM analysis made in ANSYS Mechanical: the resulting solution improved both the chord and twist angles distributions and redefined the composite layout of a HAWT blade in order to maximize the nominal power and minimize the tip displacements of the blade. In the second analysis the structural module has been replaced with a module for the evaluation of the Cost of Energy: the optimization succeeded in maximizing the Annual Energy Production and minimizing the Cost Of Energy by properly optimizing the twist angle distribution and the shape of the three airfoils of the blade. In Part II, both the optimization algorithm and FEM module are implemented by coupling analysis carried with commercial software.

In the final phase of the thesis (Part III), the optimization environment has been completely developed as open source. The optimization is led by DAKOTA MOGA tool and it involves the coupling of in-house functions, panel codes and CFD software. The topic of the optimization concerns the design of a Vertical Axis Wind Turbine airfoil. Two different approaches have been proposed: the first focused on the design point, the second is general. The average lift coefficient slope over the average drag coefficient over a rotation represents the aerodynamic objective function while the bending stiffness is the considered structural function. The optimization succeeded in identifying the best airfoil shapes for the desired working conditions. In addition a module for the computational fluid-dynamic analysis, linked to the optimization environment, has been included in the environment. The module consists in shell and python scripts; for a selected airfoil, it is capable to automatically create a geometry (using OPEN CASCADE libraries), generate a mainly structured mesh (through open source meshing algorithms) and set a 2D CFD analysis (with OpenFOAM).

Further developments could consider different objective functions belonging to several engineering fields such as modal analysis or include more complex economical, structural and aerodynamic functions. The generation of a database of materials and costs could be useful for a complete choice of parameters in the turbine optimization. Furthermore, the CFD analysis has been included as standalone module of the optimization environment for VAWT analysis, however it could be inserted in the optimization loop, taking fully into account all the limitation in the use of a computationally expensive CFD analysis in an optimization process. Finally, the proposed structural analysis are carried through the coupling of the optimization algorithm with a commercial software in batch mode or through the implementation of simple functions. A further module for the Finite Element Analysis will be included by coupling the definition of the geometry with OPEN CASCADE, the mesh generation with NETGEN libraries and the linear system solution with the open source software *Code\_Aster*.

# Bibliography

- [1] Marten D., Wendle, J., Pechlivanoglou G., Nayeri C. N., Paschereit C. O. , *Qblade: An Open Source Tool for Design and Simulation of Horizontal and Vertical Axis Wind Turbines* Int. J. Emerging Technol. Adv. Eng., 3(special issue 3), pp. 264–269, 2013.
- [2] Jonkman J. M., Buhl Jr. M. L., *FAST User's Guide NREL* Technical Report No. EL-500-38230, 2005.
- [3] Laino D. J., Hansen A. C., *User's guide to the wind turbine aerodynamics computer software AeroDyn*. Windward Engineering, Salt Lake City, 2002.
- [4] Ponza R., Benini E., *DREAM-TILT Proposal*, JTI-CS-2012-03.
- [5] Benini E., Ponza R., *CODE-Tilt Proposal*, JTI-CS-2010-1-GRC-02-004.
- [6] Campanardi G., Zanotti A., Macchi C., *Final Complete Wind tunnel Test Database for Aircraft Sizing, Suitable for Use by the Codes of the Partners*, NICETRIP/POLIMI/WP4.TR007/4.0, Version 4.0, September 2008.
- [7] Ponza R., Benini E., *CODE-Tilt Report 1.2*, “Report on near-stall characterization of the model scaled tiltrotor using Fluent®”, CS/CT/HIT09/WP1.1/R1.2/A, September 2012.
- [8] Campanardi G., Gibertini G., Lanz M., *Tilt-Rotor Stall Wind Tunnel Test*, GRC Technical Report no. 737, September 2011.
- [9] Gasparella E., Ponza R., Benini E., *Report on CFD assessment using OpenFOAM®*, CS/C-T/HIT09/WP1.1/R1.1/A. (CODE-Tilt Report R1.1).
- [10] De Gregorio F., Ragni A., Notarnicola N., *Test Report of DREAM-TILT PIV Test Campaign*, CIRA-CF-14-2082.
- [11] Anderson J. D., *Computational Fluid Dynamics – The Basics with Applications*, McGraw-Hill, Inc., New York.
- [12] Versteeg H. K., *An Introduction to Computational Fluid Dynamics – The Finite Volume Method*, 2nd ed., Prentice Hall, 2007.
- [13] ANSYS, INC, *Ansys Fluent 16.0 theory guide*, pp. 19-25, 2016

- [14] Free Software Foundation website, (2016, November 1), <https://www.fsf.org/>
- [15] GNU website - GPL license, (2016, November 1), <https://www.gnu.org/copyleft/gpl.html>
- [16] Reilly M., *Interview: Richard Stallman, one of the founders of 'free software'*, Volume 198, Issue 2651, pp. 42–44, 12 April 2008.
- [17] GNU Operating System website, (2016, November 1), <https://www.gnu.org/philosophy/free-sw.en.html>
- [18] GNU website - LGPL license, (2016, November 1), <https://www.gnu.org/copyleft/lgpl.html>
- [19] The 3-Clause BSD License website, (2017, January 9), <https://opensource.org/licenses/BSD-3-Clause>
- [20] Drela M., *XFOIL: An Analysis and Design System for Low Reynolds Number Airfoils*, Lecture Notes in Engineering, vol. 54, pp. 1–12, 1989.
- [21] XFOIL website, (2016, November 1), <http://web.mit.edu/drela/Public/web/xfoil/>
- [22] Energy research Centre of the Netherlands, (2016, November 1), <https://www.ecn.nl/>
- [23] TU Delft: Delft University of Technology, (2016, November 1), [www.tudelft.nl/](http://www.tudelft.nl/)
- [24] Van Rooij R., *Modification of the boundary layer calculation in RFOIL for an improved stall prediction*, Tech. Rep. IW-96087R, TU Delft, 1996.
- [25] Schlichting H., *Lecture series 'Boundary Layer Theory', Part I - Laminar Flows*, No. 1217, NACA, April 1949.
- [26] Ramanujam G., Ozdemirx H., Hoeijmakers H. W. M., *Improving Airfoil Drag Prediction*, 34th Wind Energy Symposium, San Diego, California, USA, 4-8 January 2016.
- [27] Dakota website, (2016, November 1), <https://dakota.sandia.gov/>
- [28] Eddy J. E., Lewis K., *Effective generation of Pareto sets using genetic programming*, Proceedings of ASME Design Engineering Technical Conference, 2001.
- [29] Adams B. M., Bohnhoff W. J., Dalbey K. R., Eddy J. P., Ebeida M. S., Eldred M. S., Hough P. D., Hu K. T., Jakeman J. D., Maupin K. A., Monschke J. A., Ridgway E. M., Rushdi A., Swiler L. P., Stephens J. A., Vigil D. M., Wildey T. M., *Dakota, a multilevel parallel object-oriented framework for design optimization, parameter estimation, uncertainty quantification, and sensitivity analysis: Version 6.4 users manual*, Technical Report SAND2014-4633, Sandia National Laboratories, Albuquerque, NM, May 2016.
- [30] OpenFOAM website, (2016, November 1), <http://www.openfoam.com/>
- [31] Salome website, (2017, January 9), <http://www.salome-platform.org/>
- [32] ParaView website, (2017, January 9), <http://www.paraview.org/>
- [33] VTK libraries website, (2017, January 9), <http://www.vtk.org/>

- 
- [34] Simioni N., Pellegrini A., Benini E., Ponza R., *Blind test CFD analysis of the wind tunnel models*, CS/DT/HIT09/WP1/5.1/1/B
- [35] Venturelli G., *CODE-Tilt D1 part I, Report on the baseline tiltrotor fuselage properties*, CS/C-T/HIT09/WP1.1/1/A, July 2011.
- [36] Hauser A., *Large Wind Tunnel Emmen LWTE Facility description*, RUAG Technical Report, TB-TA-2505, August 2012.
- [37] Menter F. R., *Two-Equation Eddy-Viscosity Turbulence Models for Engineering Applications. s.l.*, AIAA Journal, Vol. 32, pp. 269-289, 1994.
- [38] Steiling D., *Test Program L1394 - Low Speed Wind Tunnel Test DREAM-TILT, TPH-TA2014-0091 rev. B*, RUAG Aviation, Emmen, 2014.
- [39] Huber S., *CLEAN SKY - Grant Agreement CSJU-GAM-GRC Amendment 2014-1 Annex IB - Description of Work from Period 7 to 9 - ANNEX 2: Activity plan for GRC2 - Drag Reduction of Airframe and Non Lifting Rotating Systems*.
- [40] De Gregorio F., *TiltRotor Drag Reduction. Technical Specification of DREAM-TILT PIV Test Campaign* CIRA-CF-14-0730.
- [41] Hansen M. O. L., *Aerodynamics of Wind Turbines*, Earthscan, Second Edition, 2008.
- [42] Glauert H., *Airplane Propellers*, in Durand, W. F. (Ed) *Aerodynamic Theory*, Vol.4, Division L, Julius Springer, Berlin, pp. 169-360.
- [43] Spera D. A., *Wind Turbines Technology*, ASME Press, New York.
- [44] Troen I., Petersen E. L., *European Wind Atlas*, Roskilde: Risø National Laboratory, 1989
- [45] Burton T., Jenkins N., Sharpe D., Bossanyi E., *Wind Energy Handbook*, John Wiley & Sons, 2001.
- [46] Liu S., Janajreh I., *Development and application of an improved blade element momentum method model on horizontal axis wind turbines*, International Journal of Energy and Environmental Engineering, Vol. 3, 2012.
- [47] Refan M., Hangang H., *Aerodynamic Performance of a Small Horizontal Axis Wind Turbine*, Journal of Solar Energy Engineering, Vol. 134(2), 2012.
- [48] ElQatary I., Elhadidi B., *Comparison of CFD with BEM Technique for Wind Turbine Simulation of Thin and Thick Rotor Blades*, 31<sup>st</sup> AIAA Applied Aerodynamics Conference, San Diego, CA, June 24-27 2013.
- [49] Kong C., Bang J., Sugiyama Y., *Structural investigation of composite wind turbine blade considering various load cases and fatigue life*, Energy, Vol. 30, Issues 11-12, pp. 2101-2114, August-September 2005.



- [50] Mendez J., Greiner D., *Wind Blade Chord and Twist Angle Optimization Using Genetic Algorithms*, Proceedings of the Fifth International Conference on Engineering Computational Technology, Civil-Comp Press, Stirlingshire, UK, 2006.
- [51] Winter G., Periaux J., Gal n M., Cuesta P., *Genetic Algorithms in Engineering and Computer Science*, Jhon Wiley and Sons, 1995.
- [52] Benini E., Toffolo A., *Optimal Design of Horizontal-Axis Wind Turbines Using Blade-Element Theory and Evolutionary Computation*, Journal of Solar Energy Engineering, Vol. 124(4), pp. 357-363, November 2002.
- [53] Cai X., Zhu J., Pan P., Gu R., *Structural Optimization Design of Horizontal-Axis Wind Turbine Blades Using a Particle Swarm Optimization Algorithm and Finite Element Method*, Energies, Vol. 5, pp. 4683-4696, Nov 2012.
- [54] Dal Monte A., Raciti Castelli M., Benini E., *Multi-objective structural optimization of a HAWT composite blade*, Composite Structures, Vol. 106, pp. 362-373, December 2013.
- [55] Hu W., Han I., Park S. C., Choi D. H., *Multi-objective structural optimization of a HAWT composite blade based on ultimate limit state analysis*, Journal of Mechanical Science and Technology, Vol. 26, Issue 1, pp. 129-135, January 2012.
- [56] Pourrajabiana A., Afsharb P. A. N., Ahmadizadehc M., Woodd D., *Aero-structural design and optimization of a small wind turbine blade*, Optimization Methods in Renewable Energy Systems Design, Vol. 87, Part 2, pp. 837-848, March 2016.
- [57] Bottasso C. L., Campagnolo F., Croce A., *Multi-disciplinary constrained optimization of wind turbines*, Multibody System Dynamics, Vol. 27, Issue 1, pp. 21-53, January 2012.
- [58] Ashuri T., Zaaiker M. B., Martins J. R. R. A., van Bussel G. J. W., van Kuik G. A. M., *Multidisciplinary design optimization of offshore wind turbines for minimum levelized cost of energy*, Renewable Energy, Vol. 68, pp. 893-905, August 2014.
- [59] Grujicic M., Arakere G., Pandurangan B., Sellappan V., Vallejo A., Ozen M., *Multidisciplinary Design Optimization for Glass-Fiber Epoxy-Matrix Composite 5 MW Horizontal-Axis Wind-Turbine Blades*, Journal of Materials Engineering and Performance, Vol. 19, Issue 8, pp. 1116-1127, November 2010.
- [60] Zhu J., Cai X., Gu R., *Aerodynamic and Structural Integrated Optimization Design of Horizontal-Axis Wind Turbine Blades*, Energies 2016,9,66, January 2016.
- [61] Wang Y. Z., Li F., Zhang X., Zhang W. M., *Composite Wind Turbine Blade Aerodynamic and Structural Integrated Design Optimization Based on RBF Meta-Model*, Materials Science Forum, Vol. 813, pp. 10-18, 2015.

- [62] Ghommema M., Colliera N., Niemib A.H., Caloa V. M., *On the shape optimization of flapping wings and their performance analysis*, Aerospace Science and Technology , Vol. 32, Issue 1, pp. 274-292, January 2014.
- [63] Gillebaart E., De Breuker R., *Low-fidelity 2D isogeometric aeroelastic analysis and optimization method with application to a morphing airfoil*, Computer Methods in Applied Mechanics and Engineering , Vol. 305, pp. 512-536, June 2016.
- [64] Zingg D. W., Nemec M., Pulliam T. H., *A comparative evaluation of genetic and gradient-based algorithms applied to aerodynamic optimization*, European Journal of Computational Mechanics , Vol. 17, Issue 1-2, pp. 103-126, 2008.
- [65] Jacobson R., Meadors M., Jacobson E., Link H., *Power Performance Test Report for the AOC 15/50 Wind Turbine, Test B*, National Wind Technology Center, National Renewable Energy Laboratory, Colorado, 2003.
- [66] McKittrick L. R., Cairns D. S., Mandell J., Combs D. C., Rabern D. A., Van Luchene R. D., *Analysis of a Composite Blade Design for the AOC 15/50 Wind Turbine Using a Finite Element Model*, SAND2001-1441, May 2001.
- [67] Seaforthenergy website, (2014, June 1), *AOC 15/50 Detailed Specification*, <http://seaforthenergy.com/wp-content/uploads/2010/12/AOC1550-Specification-Sheet.pdf>
- [68] NREL website, *NREL FAST software*, (2014, June 1), <https://nwtc.nrel.gov/FAST>
- [69] Manwell J. F., McGowan J. G., Rogers A. L., *Wind Energy Explained: Theory, Design and Application*, John Wiley & Sons Inc., 2002.
- [70] Clifton-Smith M. J., *Wind Turbine Blade Optimisation with Tip Loss Corrections*, Wind Engineering, Vol. 33, pp. 477-496, 2009.
- [71] Lanzafame R., Messina M., *Power curve control in micro wind turbine design*, Energy, Vol. 35, pp. 556-561, 2010.
- [72] Pratumnopharat P., Leung P. S., *Validation of various windmill brake state models used by blade element momentum calculation*, Renewable Energy, Vol. 36, pp. 3222-3227, 2011.
- [73] Drela M., *XFOil: An Analysis and Design System for Low Reynolds Number Airfoils*, Technical Report, MIT Dept. of Aeronautics and Astronautics, Cambridge, Massachusetts, 1989.
- [74] Timmer W. A., van Rooij P. R. J. O. M., *Summary of the Delft University Wind Turbine Dedicated Airfoils*, Journal of Solar Energy Engineering, Vol. 125(4), pp. 488-496, 2003.
- [75] Lindenburch C., *Investigation into Rotor Blade Aerodynamics - Analysis of the stationary measurements on the UAE Phase-VI rotor in the NASA-AMES wind tunnel*, ECN-C-03-025, July 2003.
- [76] Yu G., Shen X., Zhu X., Du Z., *An insight into the separate flow and stall delay for HAWT*,

- Renewable Energy, Vol. 36, pp. 69-76, 2011.
- [77] Lanzafame, R., Messina, M., *Advanced brake state model and aerodynamic post-stall model for horizontal axis wind turbines*, Renewable Energy, Vol. 50, pp. 415-420, 2013.
- [78] *Enercon blade models*, (2016, November 1), <http://www.enercon.de/>
- [79] Wang L., Tanga X., Liu X., *Optimized chord and twist angle distributions of wind turbine blade considering Reynolds number effects*, International Conference on Wind Energy: Materials, Engineering and Policies, November 2012.
- [80] Mendez J., Greiner D., *Wind blade chord and twist angle optimization using genetic algorithms*, Fifth international conference on engineering computational technology, Las Palmas de Gran Canaria (Spain), 2006.
- [81] Dal Monte A., Benini E., *Validation of a numerical model of a Horizontal Axis Wind Turbine with experimental data using two CFD codes*, Analysis of Operating Wind Farms 2016 – 3rd edition, Bilbao, April 2016.
- [82] Rahimi H., Medjroubi W., Stoevesandt B., Peinke J., *Navier-Stokes based prediction of the aerodynamic behaviour of stall regulated wind turbines using OpenFOAM*, Progress in Computational Fluid Dynamic. An International Journal (PCFD), Vol. 16, No. 6, 2016.
- [83] Dal Monte A., Raciti Castelli M., Benini E., *Multi-objective structural optimization of a HAWT composite blade*, Composite Structures 106, pp. 362-373, 2013.
- [84] Dal Monte A., De Betta S., Raciti Castelli M., Benini E., *Proposal for a Coupled Aerodynamic-Structural Wind Turbine Blade Optimization*, Composite Structures, Vol. 159, pp. 144–156, January 2017.
- [85] Airfoiltools website, (2016, November 1), <http://airfoiltools.com/>
- [86] Giguere P., Selig M. S., Tangler J. L., *Blade Design Trade-Offs Using Low Lift Airfoils for Stall-Regulated Hawt*, NREL/CP-500-26091, National Renewable Energy Laboratory, Golden, CO.
- [87] Viterna L. A., Janetzke D. C., *Theoretical and Experimental Power from Large Horizontal-Axis Wind Turbines*, NASA TM-82944, September 1982.
- [88] Benini E., Ponza R, Iannelli P., Strüber H., Hrnčir Z., Moens F., Kühn T., *Multi-Point Shape And Setting Optimization Of High-Lift Airfoils In Both Take-Off And Landing Conditions*, European Congress on Computational Methods in Applied Sciences and Engineering (ECCOMAS 2012), Vienna, Austria, September 2012.
- [89] Compositex, carbon fiber technology, (2016, November 1), <http://www.compositex.com/>
- [90] Moné C., Stehly T., Maples B., Settle E., *2014 Cost of Wind Energy Review*, National Renewable Energy Laboratory report, 2014.

- [91] Moccia J., *Wind energy scenario for 2020*, European Wind Energy Association, 2014.
- [92] Sutherland H. J., Berg D. E., Ashwill T., D., *A retrospective of VAWT thecnology*, Sandia National Laboratories Technical Report, SAND2012-0304, January 2012.
- [93] Maydev R. C., Klimas P. C., *Aerodynamic performances of vertical and horizontal axis wind turbine*, Journal of energy, Vol. 5, pp. 189-190, 1981.
- [94] Ashwill T. D., *Measured data for the Sandia 34-meter vertical axis wind turbine*, Sandia National Laboratories Technical Report, SAND91-2228, 1992.
- [95] Berg D., E., *Customized airfoils and their impact on VAWT cost of energy*, Windpower '90, September 1990.
- [96] Klomas P. C., *Tailored aifoils for vertical axis wind turbines*, Sandia National Laboratories Technical Report, SAND84-1062, 1984.
- [97] Wang L., Koliosa A., Nishinoa T., Delafina P. L., Birdb T., *Structural optimisation of vertical-axis wind turbine composite blades based on finite element analysis and genetic algorithm*, Composite Structures, Vol. 153, pp. 123–138, October 2016.
- [98] Yamazaki W., Arakawa Y., *Numerical-Experimental Investigation of Airfoil Shape for Small VAWT*, 34th Wind Energy Symposium, pp. 1733, 2016.
- [99] Posteljnik Z., Stupar S., Svorcan J., Peković O., Ivanov T., *Multi-objective design optimization strategies for small-scale vertical-axis wind turbines*, Structural and Multidisciplinary Optimization, Vol. 53, pp. 277-290, 2016.
- [100] Bedon G., Benini E., *Aero-structural design optimization of vertical axis wind turbines*, Wind Energy ,2016.
- [101] Ferreira C. S., Geurts B., *Aerofoil optimization for vertical-axis wind turbines*, Wind Energy 18, pp. 1371-1385, May 2014.
- [102] Ferreira C. S., *The near wake of the VAWT: 2D and 3D views of the VAWT aerodynamics*, PhD thesis, Delft University of Technology, 2009.
- [103] Castelein D., *Dynamic stall on vertical Axis Wind Turbine*, Master Thesis, TU Delft, 2015.
- [104] Horst, S., *Airfoil design for vertical axis wind turbines*, Master Thesis, TU Delft, 2015.
- [105] Lapin E., *Theoretical performance of vertical axis wind turbines*, In American Society of Mechanical Engineers, Winter Annual Meeting, Houston, Texas, 1975.
- [106] Bondi A. B., *Characteristics of scalability and their impact on performance*, Proceedings of the second international workshop on Software and performance - WOSP '00, p. 195, 2000.
- [107] Hill, M. D., *What is scalability?*, ACM SIGARCH Computer Architecture News, Vol. 18, Issue 4, pp. 18-21, 1990.

- [108] Duboc L., Rosenblum D. S., Wicks T., *A framework for modelling and analysis of software systems scalability*, Proceeding of the 28th international conference on Software engineering - ICSE '06. p. 949, 2006.
- [109] UNV file format for exchange mesh-data, (2016, November 1),  
<http://www.sdrl.uc.edu/sdrl/referenceinfo/universalfileformats/file-format-storehouse/>

# Appendices



## Appendix A

# PIV Results for the Optimized Tiltrotor Configuration

The results of the external aerodynamic analysis of Erica tiltrotor are below presented for the optimized configuration case and compared to the PIV experimental data, [40]. Three different angles of attack ( $\alpha = -2^\circ, 0^\circ, +2^\circ$ ) have been considered and the velocity contours are presented for four section in the wake zone.

The same conclusions discussed in Section 3.7 can be drawn for the second configuration.



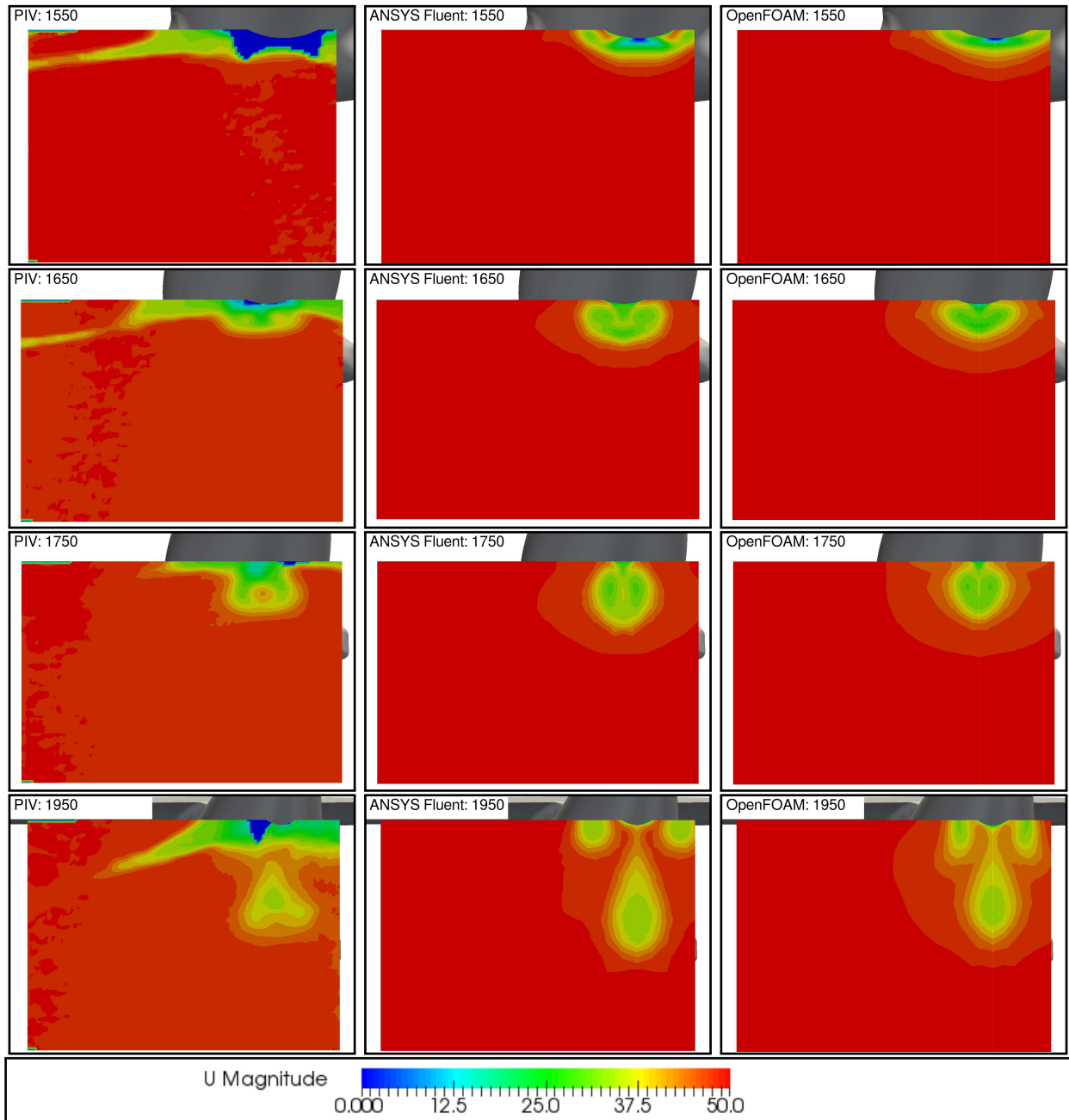


**Figure A.1:** Velocity contours in the wake of the optimized model, case  $\alpha = -2^\circ$ : the comparison among PIV data, ANSYS Fluent and OpenFOAM analysis is illustrated for the considered planes

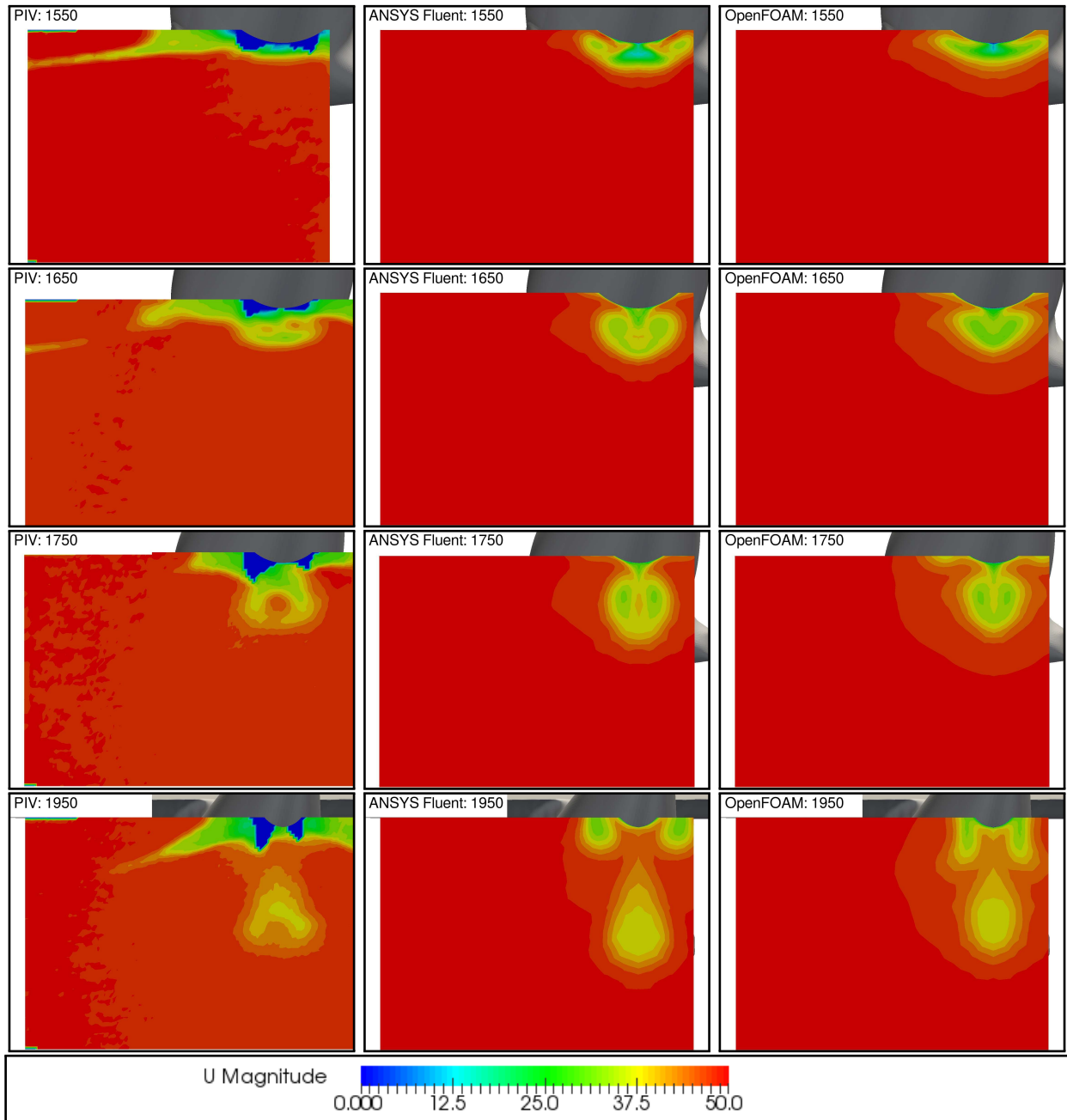


**Figure A.2:** Velocity contours in the wake of the optimized model, case  $\alpha = 0^\circ$ : the comparison among PIV data, ANSYS Fluent and OpenFOAM analysis is illustrated for the considered planes

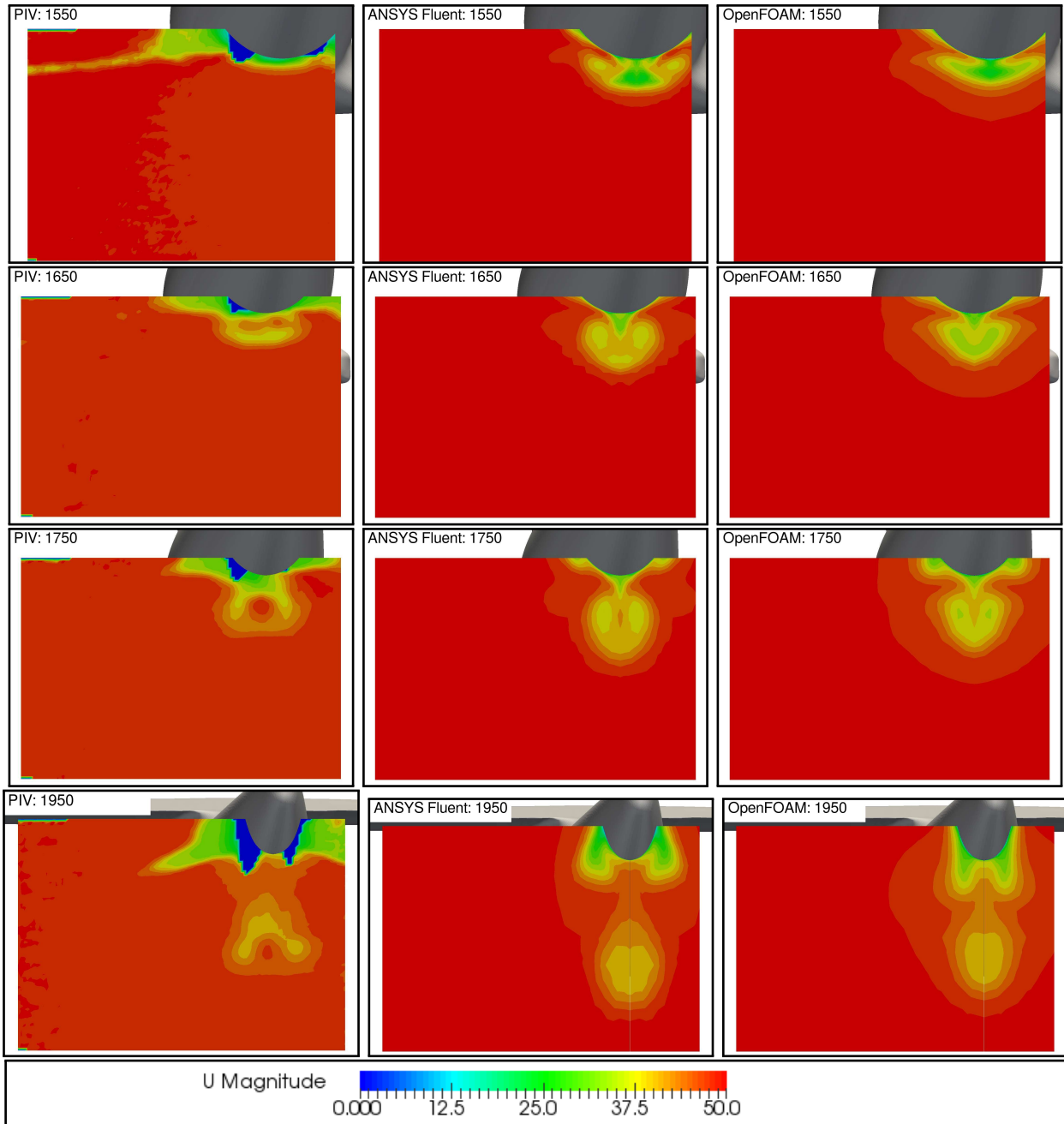


**Figure A.3:** Velocity contours in the wake of the optimized model, case  $\alpha = +2^\circ$ : the comparison among PIV data, ANSYS Fluent and OpenFOAM analysis is illustrated for the considered planes

## Appendix B

# HAWT: Global Shape Optimization

In order to properly set the parameters for the optimization of the HAWT and to test the robustness of the code, a preliminary global optimization (denoted by *Wb1Opt0*) has been, at first, run for the first considered Weibull distribution (mean velocity: 7 m/s). In *Wb1Opt0* the genes represent the variation in y-direction of the control points from the baseline values, as specified in 6.3. The values of the 10 genes move, at the same time, the corresponding control points of the three profiles of the blade. The movement is imposed to be proportional to the maximum thickness of the considered profile, normalized respect to the first profile (Profile1=100%, Profile2=86,92%, Profile3=66,21%). The population size has been set in 100 individuals and the maximum number of generations is 85. Figure B.1 shows the results of the optimization process: the Pareto front can be considered converged after the 40th generation and the results can be analysed.

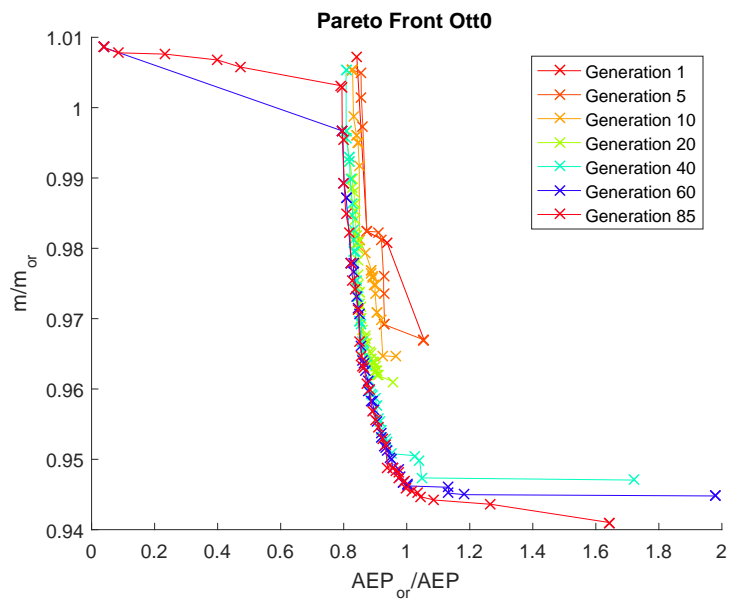


Figure B.1: Wb1Opt0: Pareto front of the global optimization

### B.0.1 Global Optimization Results

Three different solutions, belonging to the Pareto front, are analysed in the present Section: the genetic pool and the calculated fitness values of three possible solutions are reported in Table B.1.

	Genetic Pool										Fitness	
<b>Sol1</b>	-0.0241	0.0763	0.0959	0.0861	0.0357	0.0490	0.0439	0.0287	0.0642	0.0394	0.47	1.01
<b>Sol2</b>	-0.0044	0.0763	0.0961	0.0864	0.0273	0.0193	0.0209	-0.0148	-0.0618	0.0376	0.82	0.8
<b>Sol3</b>	0.0054	0.0852	0.0908	0.0806	-0.0273	-0.0043	-0.0792	-0.0624	-0.0772	-0.0219	1.64	0.94

**Table B.1:** Genetic pool and fitness values of the considered solutions belonging to the Pareto front of *Wb1Opt0*

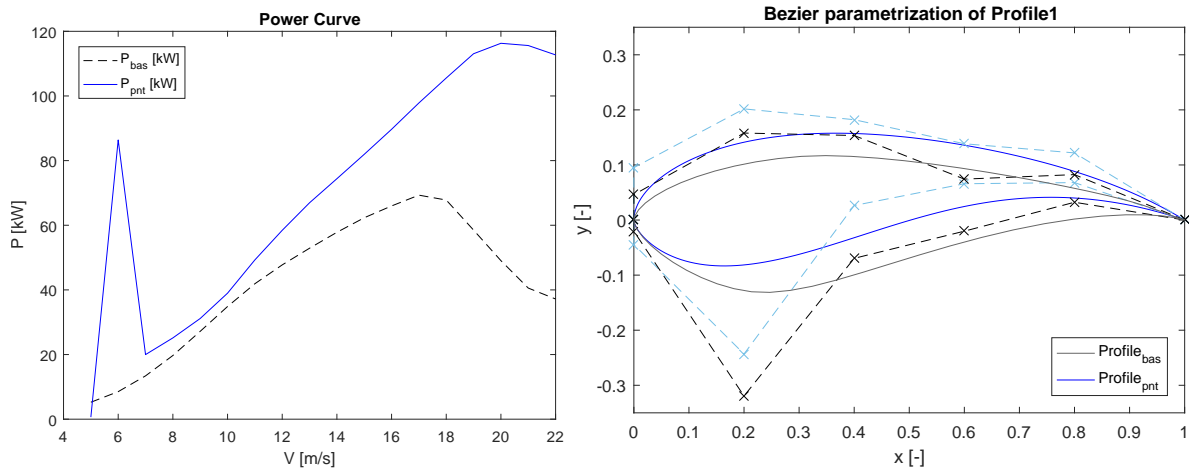


**Figure B.2:** *Wb1Opt0*, Solution 1: power curve and airfoil 1 shape

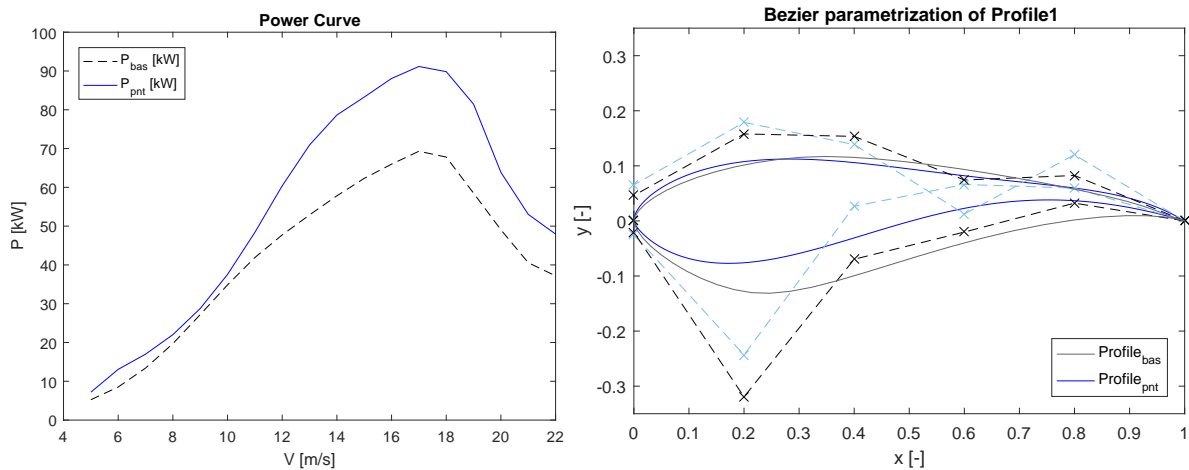


**Figure B.3:** *Wb1Opt0*, Solution 2: power curve and airfoil 1 shape

Figures from B.2 to B.4 illustrate the evaluated power curve and the root airfoil shape of the considered solutions. *Sol1* is an example of a great improvement of the  $f_{AEP}$  fitness function. As can be seen in the power curve plot, the *AEP* has been overestimated due to a wrong calculation

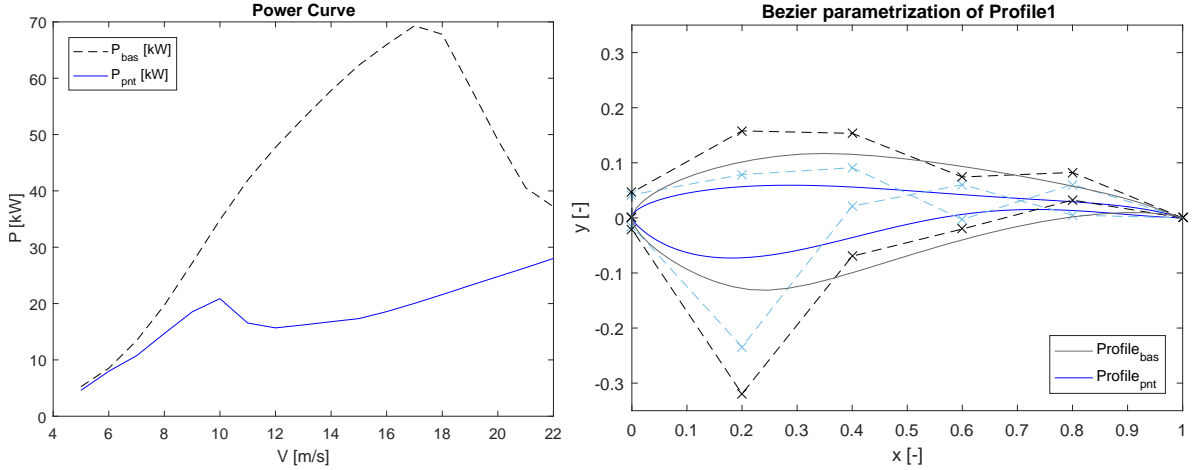


Figure B.4: *Wb1Opt0*, Solution 3: power curve and airfoil 1 shape

corresponding power at 5 m/s and 6 m/s velocities. This is due to a wrong numerical convergence found in the BEM code as further explained in Section B.1.1. *Sol2* also shows a slightly irregular path of the optimized power curve at low velocities, this behaviour is due to the same reason of *Sol1*. Finally *Sol3* represents the solution with the maximum improvement in the blade mass reduction at the cost of an unacceptable reduction of the *AEP*.

## B.1 Corrections to the Optimization Process

The analysis of *Wb1Opt0* results has highlight the need of include few arrangements in order to correct the numerical errors of the BEM code and to better fit the experimental power curve.

### B.1.1 Robustness of the BEM Code

As shown in Figure B.2 and in B.3, the BEM code has proved to be unstable and inaccurate in the calculation of the power curve at low wind velocities for few geometries. An incorrect convergence of both the *axial induction factor*  $a$  and the *tangential induction factor*  $a'$  in few zones of the blade has be found after a deep examination of the algorithm. The wrong convergence was due to the initialization of the values that caused the calculated loads the loads  $p_N$  and  $p_T$  to tend to very high values. In other sections, both the wrong initialization and the application of the Glauert 3D correction causes an interruption in the airflow (values of  $a$  and  $a'$  tends respectively to 1 and -1). This convergence errors have been solved using a re-initialization of the values of the problematic section with the values of the closest correct section.

### **B.1.2 Additional Constraints**

Further constraints must be set in the optimization loop in order to avoid non-realistic solutions. First, the pressure side y-coordinate values are imposed to be lower than the suction side y-coordinate values. Second, for feasibility reason, in order to avoid too thin profiles towards the trailing edge, the maximum thickness of the normalized profile at the 95% of the chord is imposed to be highest than 0.008. Finally, the correction for the start-up inertia of the wind turbine has been included, as explained in Section 6.7.2.

## Appendix C

# Incorrect Settings of the XFOIL Analysis

The optimization process makes possible to analyse an enormous amount of different airfoil configurations and shapes. During the setting phases of the VAWT optimization (Part III), few XFOIL incorrect calculations have been found as illustrated in the current Appendix.

For several profiles, the polars, evaluated with XFOIL v6.99, significantly changes with adopted setting; the number chosen number of iterations, the range of angles of attack to be evaluated and the adopted angle step seem to influence the calculation of the aerodynamic performances.

The most significant difference is found in the drag polar estimation: the calculated drag coefficient tends to assume unreal low values. Since the  $C_D$  term is the denominator of the aerodynamic function  $f_{AER}$ , it leads to the definition of the best aerodynamic functions of the population and their characteristics are used (crossover operator) and preserved (elitism operator) through the generations of the optimization. The overall results are hence influenced by the wrong fitness values of these individuals. Figure C.1 shows the Pareto front resulting in two preliminary optimizations.

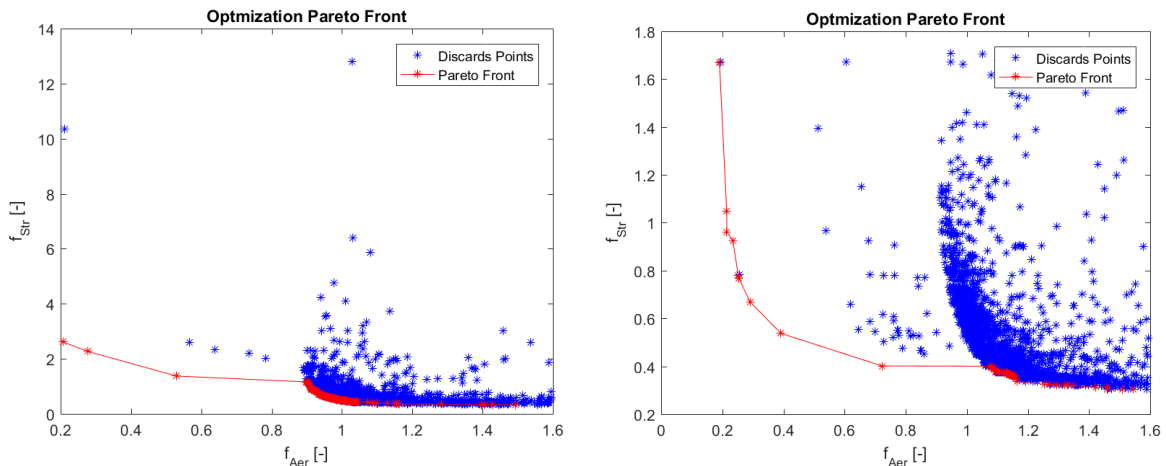


**Figure C.1:** Pareto front resulting in the preliminary phase of optimization setting



A thorough XFOIL analysis of some of the individual that showed the wrong calculation issue has been run. The genetic pools of the considered individuals are reported in Table C.1.

	Genes							
<b>A251</b>	0.4444	0.0503	0.0001	0.0098	0.0379	0.1063	0.0575	0.0127
<b>A253</b>	0.6693	0.0536	0.0362	0.0010	0.0379	0.1397	0.0849	0.0153
<b>A254</b>	0.5562	0.0536	-0.0424	0.0098	0.0379	0.1397	0.0849	0.0250
<b>A255</b>	0.3375	0.0536	0.0362	0.0010	0.0379	0.1709	0.0849	0.0127
<b>A256</b>	0.5562	0.0991	-0.0424	0.0098	0.0533	0.2081	0.1433	0.0220

**Table C.1:** Airfoils that present issues in the XFOIL calculation

Several XFOIL analysis have been run in order to determine the impact of the setting parameters that most influence the results. These parameters have been identified as:

- Number of iterations for the single step of calculation;
- Range of the considered angles of attack;
- Step of variation of the angles of attack.

The characteristics of the airfoil geometries and their polars are presented in the following pages. In the presented Figures, the polars ( $C_L$  and  $C_D$ ) are evaluated using different XFOIL settings, varying the most influential parameters. The red curves represent the setting used in the preliminary analysis, a XFOIL calculation of 70 iteration per step, in the range of angle of attack  $\alpha = [-15^\circ + 15^\circ]$  with steps of  $\alpha = 1^\circ$ .

An unique setting to fix all the wrong calculations of XFOIL has not been identified: the proposed settings generally don't works for all the considered airfoils. The expedient of increase the number of iterations to 100, fixed only one of the considered cases (Figure C.9). In the same way, the reduction of the considered steps of  $\alpha$  to  $0.5^\circ$ , in one case, worsened the calculation (Figure C.5).

Best results have been obtained when the considered range of  $\alpha$  is divided in 2 sub-ranges, starting the analysis from  $\alpha = 0^\circ$ ; in some cases, this setting fails to calculate the  $C_D$  values at negative angles of attack (Figure C.3), however it overall represents the most reliable setting.

For these reasons, the XFOIL analysis implemented in the optimization loops is divided in two different calculations, both starting from  $\alpha = 0^\circ$ , the angle of attack where the airfoil is supposed to not present stall conditions or phenomena of boundary layer separation. Additionally, a check on the  $C_D$  value at  $\alpha = 0^\circ$  has been implemented in order to reject the airfoil for witch the wrong XFOIL calculation has determined a  $C_D$  with values close to 0. The cause of the wrong calculations of XFOIL analysis has to be further investigated: it seems to be related to the starting angle, if it is close to stall conditions, it could affect the analysis of following angles of attack.

**Airfoil A251:** the  $C_D$  polar evaluated with XFOIL assumes unreal small values. The calculation is fixed using a limited  $\alpha$  range and splitting the analysis in two ranges.

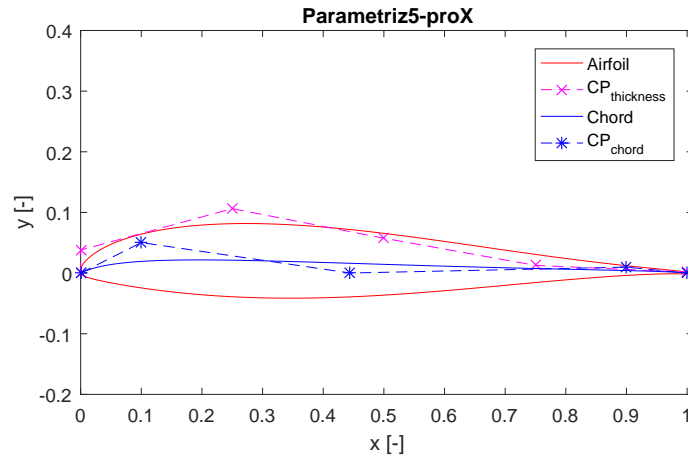


Figure C.2: A251: Bezier parametrization of the airfoil

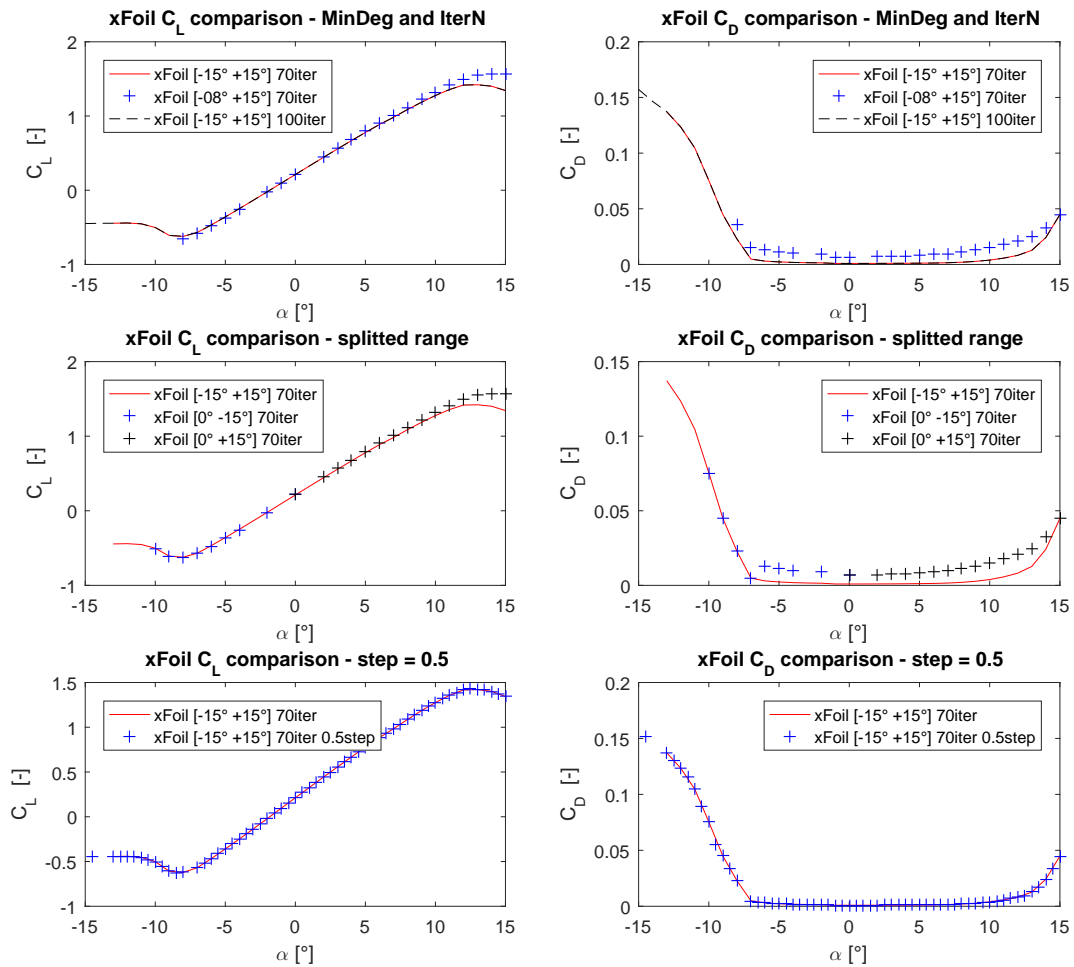


Figure C.3: A251 airfoil. The variation of  $C_D$  and  $C_L$  polars is presented for different setting of the XFOIL analysis

**Airfoil A253:** The  $C_D$  polar evaluated with XFOIL assumes unreal small values. The analysed settings don't improve the results, the adoption of a lower step of  $\alpha = 0.5^\circ$  makes the analysis worse.

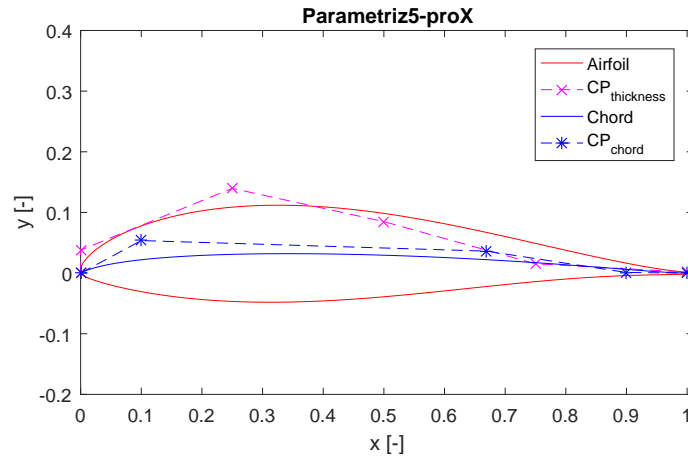


Figure C.4: A253: Bezier parametrization of the airfoil

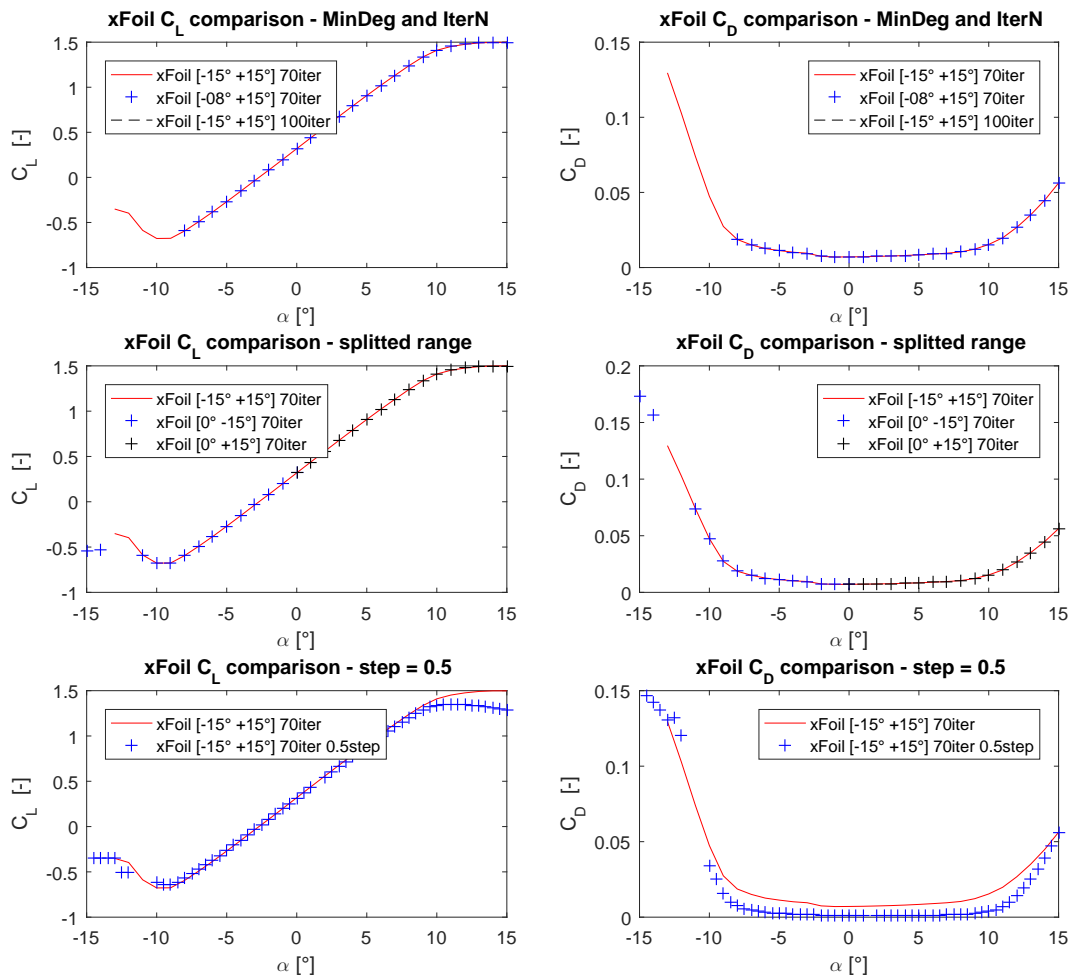


Figure C.5: A253 airfoil. The variation of  $C_D$  and  $C_L$  polars is presented for different setting of the XFOIL analysis

**Airfoil A254:** The  $C_D$  polar, assumes unreal small values. The proposed configurations fix the results, except for the reduction of the  $\alpha$  step (the calculation fails after the first evaluation).

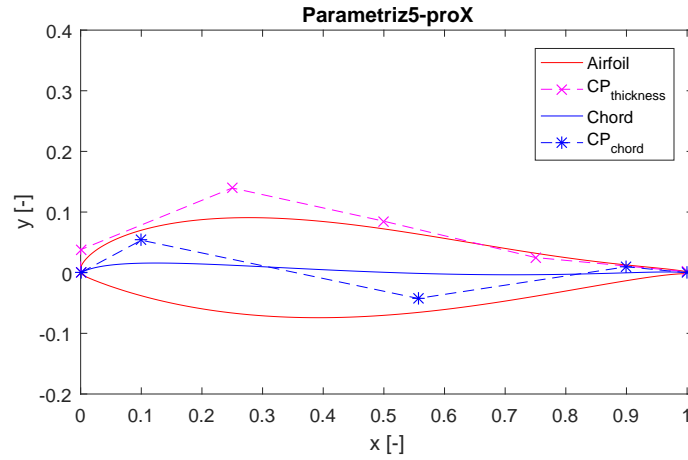


Figure C.6: A254: Bezier parametrization of the airfoil

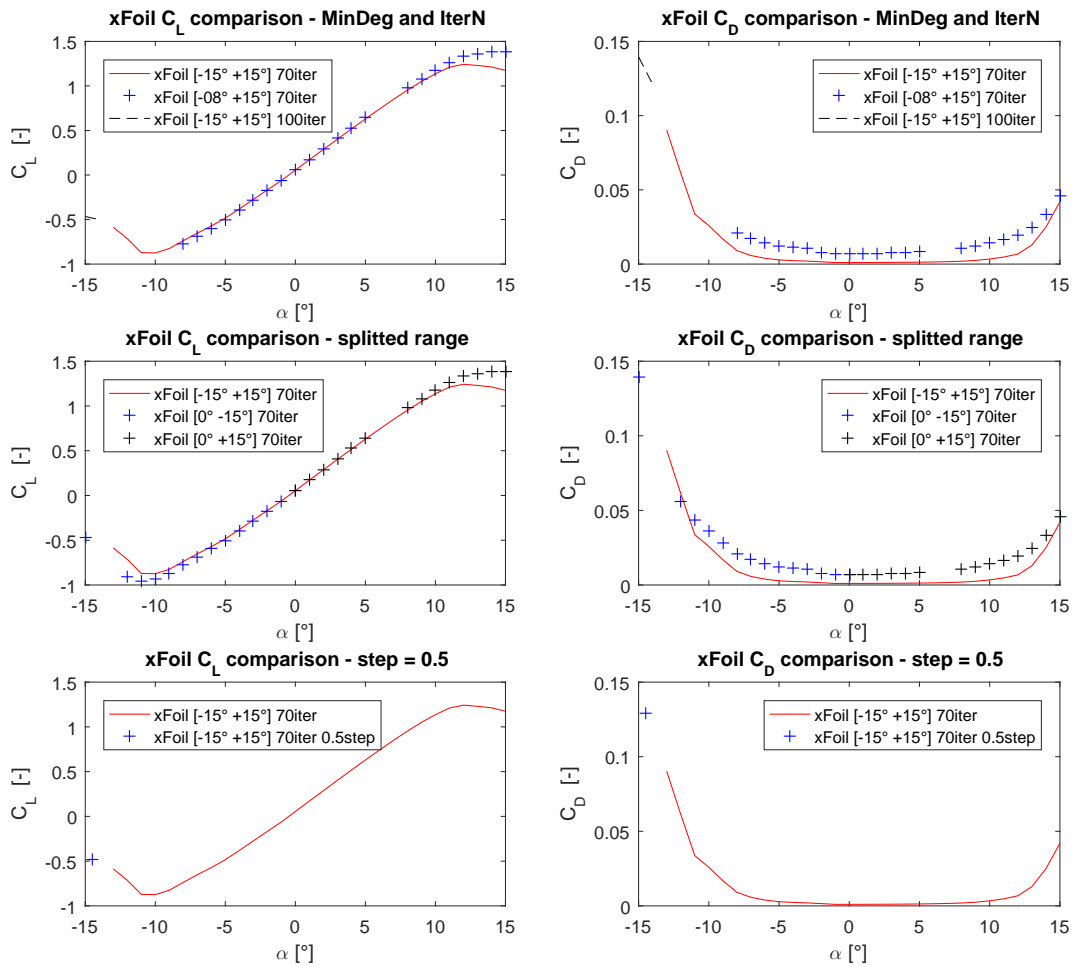


Figure C.7: A254 airfoil. The variation of  $C_D$  and  $C_L$  polars is presented for different setting of the XFOIL analysis

**Airfoil A255:** The  $C_D$  polar assumes unreal small values. In this case, also the configuration with 100 iterations fixes the results; the reduction of the  $\alpha$  step fails, again, to correctly calculate the polars.

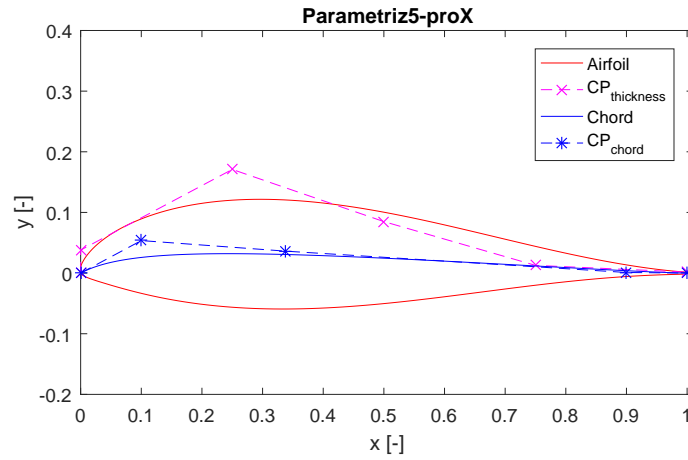


Figure C.8: A255: Bezier parametrization of the airfoil

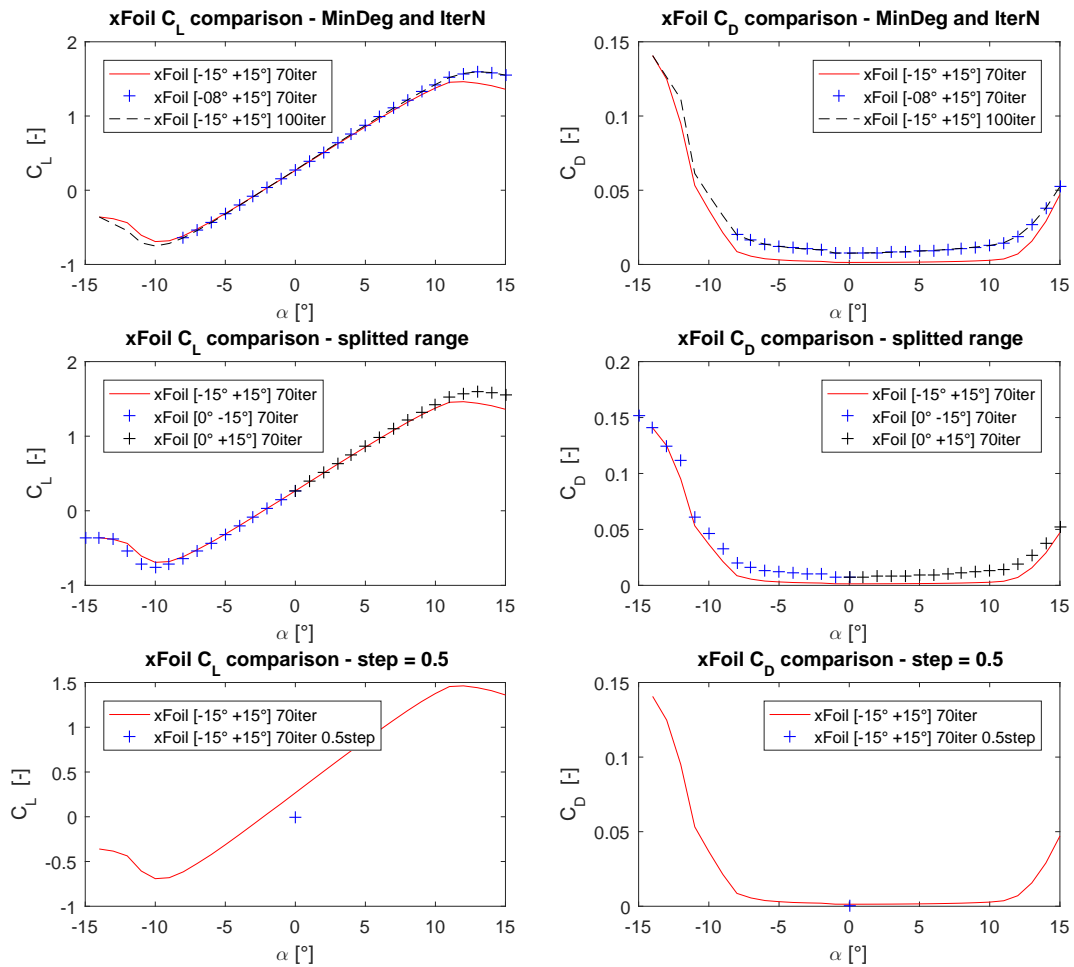


Figure C.9: A255 airfoil. The variation of  $C_D$  and  $C_L$  polars is presented for different setting of the XFOIL analysis

**Airfoil A256** - The  $C_D$  polar presents a jump when  $\alpha = -8^\circ$ . The alternative configurations don't fix the problem, increasing the number of iterations to 100 makes the drag lower.

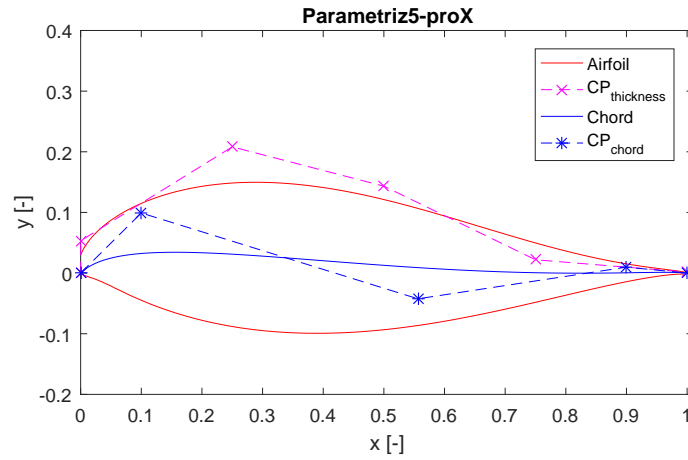


Figure C.10: A256: Bezier parametrization of the airfoil

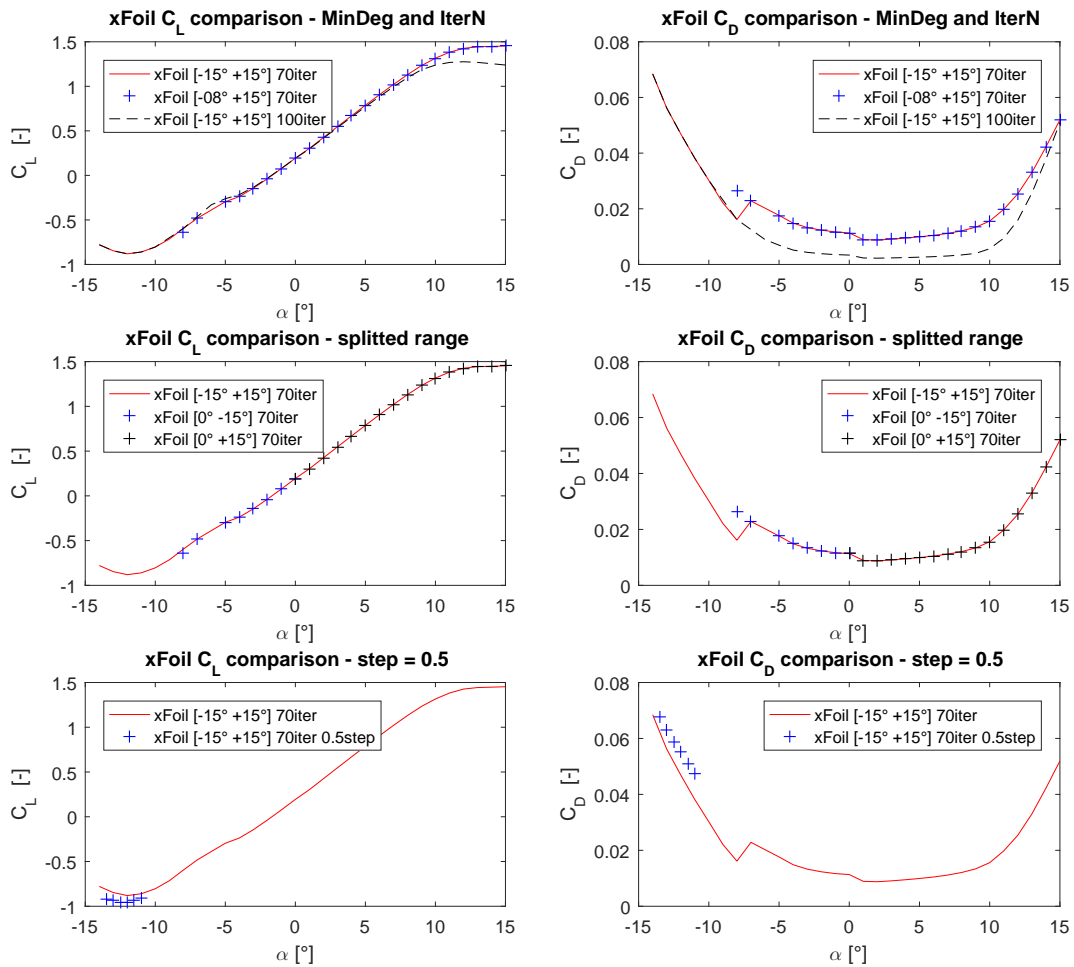


Figure C.11: A256 airfoil. The variation of  $C_D$  and  $C_L$  polars is presented for different setting of the XFOIL analysis



# Appendix D

## VAWT Optimization Tool - User Manual

In Chapter 8, the ultimate version of the open source environment for the wind turbine optimization has been used; the most important functions and commands to run and set the multi-objective optimization of a Vertical Axis Wind Turbine are summarized in the present Section. The Appendix is meant to be a sort of User manual that explains the structure of the code and the procedure to follow in order to setup an optimization.

### D.1 Structure of the code

The code is structured as shown in Figure D.1. The main folder contains the files needed for the optimization procedure, inside the *templatedir* folder are saved the files and of the considered analysis.

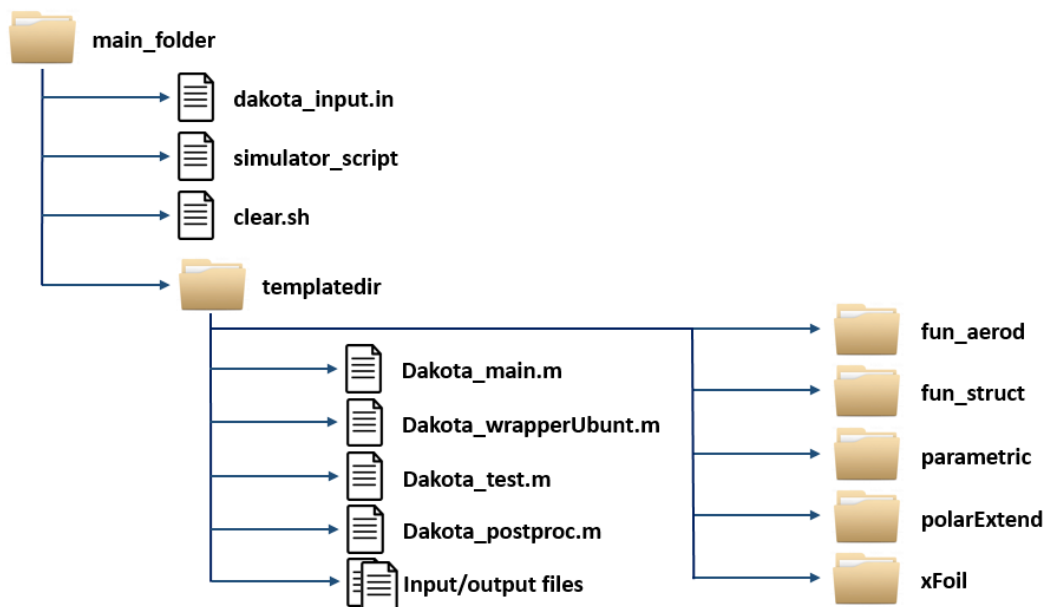


Figure D.1: Structure of the Optimization environment for Vertical Axis Wind Turbine



## D.2 Optimization files

The file that contains the setting of Dakota optimization with the MOGA algorithm is **dakota\_input.in**.

The principal parameters to be set are located in four different sections:

- method
  - *max\_function\_evaluations*: the maximum number of individuals to be simulated in the entire optimization process;
  - *initialization\_type*: it reports how to generate the initial population, in a random way or by specifying a set of individuals inside an external file;
  - *population\_size* : the number of individuals contained in the population;
  - *crossover\_type* : the rules for the crossover operator;
  - *mutation\_type* : the type of adopted mutation operator;
  - *convergence\_type* : the convergence stopping criteria.
  
- variables
  - *continuous\_design*: the number of design variables;
  - *upper\_bounds, lower\_bounds*: the equality constraints for the design variables;
  - *descriptors*: the labels of the design variables.
  
- interface
  - *system asynchronous evaluation\_concurrency*: the number of individuals to be simulated simultaneously (parallel mode);
  - *analysis\_driver*: the shell script that "drives" the evaluation functions.
  
- responses
  - *num\_objective\_functions* the number of expected fitness functions.

The other important files are **clear.sh**, an utility that clears the folder deleting the files of a previous analysis and **simulator\_script**, a shells script necessary for the input/output operations between Dakota and the considered functions.

## D.3 Analysis files

The analysis files are located in the template directory and they represent the functions to evaluate the performances of a single design. The main files to be set are:

**Dakota\_main.m**: it represents the main file of the optimization loop. It initializes the options of the different modules and the parameters of the case study, it sets the penalties to be used and it fixes the reference values. It takes, as input, the array of doubles containing the genetic pool from Dakota MOGA and it returns, as output, the fitness values of the individual. It consequentially calls the modules needed for the fitness evaluation: the parametrization function, the XFOIL polar evaluation, the aerodynamic and structural fitness functions. Finally, it applies the penalties and writes the result files.

The most important options to set in the file are divided in 4 main categories, defined as Matlab structures:

- *opt*: specifies the general options of the optimization. The main are as follows:
  - *opt.computer*: the option indicates the computer on which run the optimization, it sets the local paths depending on the O.S. (Windows or Ubuntu);
  - *opt.filterCD*, *opt.filterCDval*, *opt.checkFrFo*: options to filter the wrong XFOIL calculations. The first two are based on the drag coefficient value at  $\alpha = 0^\circ$ , the latter check if the forced transition polar exceeds the free transition one;
  - *opt.xfoilN*: it sets the XFOIL analysis using '*free+forced transition*', '*free transition only*' or '*forced transition only*' condition;
- *par*: sets the geometric parameters and the working conditions of the considered turbine;
- *xfoil*: sets the options for the XFOIL evaluation of polars;
- *pen*: sets the desired penalties values for the fitness functions.

**Dakota\_test.m** : the file is used to test the performances of a given individual. It needs the following options to be specified:

- *opt.opt*: it specifies the aerodynamic function to use;
- *opt.case*: runs the *only thickness* analysis or *camber+thickness* parametrization;
- *x*: vector containing the genes of the individual to be tested.

**Dakota\_postproc.m**: the file is used to post-process the result of an optimization. It reads the output files of Dakota optimization, *discards.dat* and *finaldata1.dat* and it plots the resulting Pareto front.

## D.4 Computer Setup

The required software to be installed to run an optimization are:

- *Dakota v6.4*: download from <https://dakota.sandia.gov/download.html>
- *XFOIL*: download from <http://web.mit.edu/drela/Public/web/xfoil/>
- *openFOAM 4.0*: install from Advanced Packaging Tool (apt) repository
- *Code\_Aster 12.6*: download from <http://www.code-aster.org/>
- *ParaView 5.2*: download from [www.paraview.org/download/](http://www.paraview.org/download/)
- *Salome 7.8.0*: download from <http://www.salome-platform.org/downloads/current-version>
- *NumPy*: install from <http://www.scipy.org/scipylib/download.html>
- *MATLAB*: install from <https://it.mathworks.com> with a valid license

## D.5 How to Run an Optimization

First, the main file governing the optimization, **dakota\_input.in**, has to be edited with the desired setting, as specified in D.2.

The input file refers to the main file for the wind turbine analysis, **dakota\_main.m**. MATLAB has been chosen as programming language, in the first version of the code, for reasons of speed of programming and simplicity of modification for a novice user. The code will be rewritten in C++ language in the further versions. The *analysis\_driver* parameter, in the interface section, contains the specification of the **simulator\_script** file. This shell script is necessary for the input-output operations between Dakota and the main function of code; the variable "1" represents the vector of the decision variables, "2" is the vector of the evaluated fitness. The *simulator\_script* calls the **dakota\_wrapperUbuntu.m** file: the wrapper file simply converts the input variables and sets them as input of **dakota\_main.m** function and, after the evaluation of the individual, converts the output fitness values in the format required by Dakota.

The optimization can be run both in single and in parallel mode; the input of the single mode is:

```
dakota -i dakota_input.in -o dakota_out.out
```

To use parallel mode, is necessary to input the following command:

```
mpirun -np 1 dakota -i dakota_input.in -o dakota_out.out
```

Once the optimization process is completed, the output is represented by two files, containing the information of the evaluated individuals and their fitness: **discards.dat**: it contains all the dominated individual **finaldata1.dat**: it contains the individual belonging to the Pareto front.

The output \*.dat files can be read and managed in order to analyse the results.